uOttawa

L'Université canadienne
Canada's university

FACULTÉ DES ÉTUDES SUPÉRIEURES ET POSTOCTORALES

uOttawa

L'Université canadienne
Canada's university

FACULTY OF GRADUATE AND POSDOCTORAL STUDIES

Scott Baker
AUTEUR DE LA THÈSE / AUTHOR OF THESIS

M.A.Sc. (Civil Engineering)
GRADE / DEGREE

Department of Civil Engineering
FACULTÉ, ÉCOLE, DÉPARTEMENT / FACULTY, SCHOOL, DEPARTMENT

Physical and Numerical Modelling of Wave Interaction
with a 3-D Submerged Structure

TITRE DE LA THÈSE / TITLE OF THESIS

Dr. Ioan Nistor
DIRECTEUR (DIRECTRICE) DE LA THÈSE / THESIS SUPERVISOR

Dr. Andrew Cornett
CO-DIRECTEUR (CO-DIRECTRICE) DE LA THÈSE / THESIS CO-SUPERVISOR

EXAMINATEURS (EXAMINATRICES) DE LA THÈSE / THESIS EXAMINERS

Dr. Paul Van Geel

Dr. C. Rennie

Dr. O. Seidou

Gary W. Slater
Le Doyen de la Faculté des études supérieures et postdoctorales / Dean of the Faculty of Graduate and Postdoctoral Studies

Physical and Numerical Modelling of Wave Interaction with a 3-D Submerged Structure

Scott Baker

Submitted under the supervision of
Dr. Ioan Nistor
Dr. Andrew Cornett

In partial fulfillment of the requirements
for the degree of
Master of Applied Science in Civil Engineering

Department of Civil Engineering
University of Ottawa
December, 2007

Your file Votre référence
ISBN: 978-0-494-50852-7
Our file Notre référence
ISBN: 978-0-494-50852-7

Acknowledgments

I sincerely thank my family and my beautiful girlfriend Kirsten for their loving support throughout my academic journey. Thank you for all your encouragement!

I extend my heartfelt appreciations to Dr. Nistor, Dr. Cornett, and Dr. Lomonaco for their invaluable support and guidance. Dr. Ioan Nistor, my thesis supervisor, was the first to introduce me to the world of Coastal Engineering, and I thoroughly enjoyed learning from and working alongside him throughout the course of my studies. Dr. Andrew Cornett, my co-supervisor, graciously allowed me to participate in research at the Canadian Hydraulic Centre and provided me with many helpful suggestions and directions throughout the course of my work. I sincerely thank Dr. Pedro Lomonaco for imparting me with so much Coastal Engineering knowledge and for his significant contributions to the physical experiments and the numerical simulations.

I want to thank all the staff at the Canadian Hydraulics Centre, especially David Hnatiw who contributed significantly to the physical experiments and provided me with much assistance performing data analysis; to Martin Serrer for answering my numerous queries about WaveSim; to all the floor staff who helped in the construction of the physical model; to Daniel Pelletier for his technical assistance, and finally to Dr. Etienne Mansard for permitting me to conduct research at CHC.

I want to thank Auður Atladóttir, a great friend, and all the other Water Resources graduate students with whom I studied. I also wish to thank Dr. Colin Rennie and all my undergraduate and graduate professors at the University of Ottawa.

I would like to acknowledge Dr. Okey Nwogu for answering a number of questions and his past contributions to the WaveSim numerical model used in this research.

Finally, I would like to thank CHC and COWI for allowing me to include data from their physical model study, and CHC for permitting me to use the numerical model WaveSim in my research.

Abstract

Submerged structures are frequently used in coastal engineering applications, such as tunnel and pipeline protection works, breakwaters, and artificial reefs. Although a significant number of research works have focused on low-crested structures, there is far less research into deeply submerged structures. In most research, lightly-sloped, uniform cross-sectioned submerged structures with specific crest elevations are considered.

The present thesis deals with the three-dimensional physical and numerical modelling of the interaction of irregular waves with a large-scale three-dimensional submerged structure. It aims to advance the understanding of the structure's influence on the irregular wave field, the wave-induced velocities along the structure crest, and the wave-induced currents. The ability of a nonlinear Boussinesq wave model to simulate these processes is also investigated and assessed.

Analysis was performed on a multitude of data, including – but not limited to – wave heights, wave periods, wave energy spectra, energy transfer functions, reflection analyses, and wave-induced velocities. In general, the analysis and comparison performed showed that the numerical model provided a modestly accurate representation of the physical modelling results.

Table of Contents

List of Tables

List of Figures

List of Symbols

Notes:

1. All units in this document are in the SI system unless otherwise stated.
2. Sea state parameters generally follow the definitions of IAHR (1986).

Symbol	Description
$_{(n)}$	Subscript 'n' denotes information pertaining to numerical data
$_{(p)}$	Subscript 'p' denotes information pertaining to physical data
a_i	Incident wave amplitude [m]
a_r	Reflected wave amplitude [m]
a_t	Transmitted wave amplitude [m]
a_0	Empirical constant [non-dimensional]
A_{00}	Mode of incident wave [m^2/s]
$A_{n+1,0}$	Mode of transmitted wave [m^2/s]
B	Width of structure crest [m]
B_{00}	Mode of reflected wave [m^2/s]
c_0	Velocity of wave propagation in deep water [m/s]
c_g	Wave group velocity [m/s], $c_g = 2\pi \partial f/\partial k$
c_w	Wave celerity [m/s], $c_w = 2\pi f/k$
C	Phase speed [m/s]
Ch	Chezy coefficient [non-dimensional]
Cr	Courant number [non-dimensional]
C_D	Coefficient of dissipation [non-dimensional]
C_r	Coefficient of reflection [non-dimensional]
C_t	Coefficient of transmission [non-dimensional]
d_s	Submergence depth [m] (MSL to breakwater crest)
D	Characteristic stone size [m]
$D_{n,50}$ (D_{50})	Nominal diameter of armour stone [m]
f	Wave frequency [Hz]
f_p	Spectral peak frequency [Hz], $f_p = 1/T_p$
f_1	Lower bound frequency [Hz]
f_2	Upper bound frequency of long-wave, lower bound frequency of main-wave [Hz]
f_3	Upper bound frequency [Hz]
F_p	Porous structure term [non-dimensional]
F_{du}	Wave energy damping term [non-dimensional]
$F_{d\eta}$	Wave energy damping term [non-dimensional]
Fr	Froude number [non-dimensional]
F_{wave}	Internal wave generation term [non-dimensional]
g	Gravitational acceleration [9.81 m/s^2]
G	Quadratic transfer function for weakly non-linear model [non-dimensional]

$G_{xy}(f)$	Coherence function of x(t) and y(t) [non-dimensional]
h	Water depth [m]
H	Wave height [m]
H_i	Incident wave height [m]
H_{m0}	Spectral estimate of the significant wave height [m], $H_{m0} = 4\sqrt{m_0}$
H_{max}	Maximum wave height [m]
$H_{max,d}$	Maximum zero down-crossing wave height [m]
$H_{max,u}$	Maximum zero up-crossing wave height [m]
H_r	Reflected wave height [m]
H_s	Significant wave height = $H_{1/3}$ [m]
H_t	Transmitted wave height [m]
$H_{xy}(f)$	Transfer function of a linear system [non-dimensional]
$H_{1/10}$	Average wave height of the $1/10^{th}$ highest waves [m]
$H_{1/100}$	Average wave height of the $1/100^{th}$ highest waves [m]
$H_{1/20}$	Average wave height of the $1/20^{th}$ highest waves [m]
$H_{1/3}$	Average wave height of the $1/3^{rd}$ highest waves [m]
H_{50}	Average wave height of the 50 highest waves [m]
$H_{av,d}$	Average zero down-crossing wave height [m]
i	Time step [s]
k	Wave number [rad/m], $k = 2\pi/L$
k_t	Turbulent kinetic energy [J]
K_D	Damage coefficient in rubblemound breakwater design [non-dimensional]
l_t	Turbulence length scale [m]
L	Wavelength [m]
L_d	Wavelength at depth d [m]
L_p	Spectral peak wavelength [m]
L_0	Deep water wavelength [m]
m_0	0^{th} moment of the water surface elevation time series [m^2/s^0] (record variance)
M	Mass [kg]
M_{10}	Stone mass for 10% sieve passing [kg]
M_{50}	Mean particle mass [kg]
M_{90}	Stone mass for 90% sieve passing [kg]
n	Porosity [non-dimensional]
N_{cells}	Number of cells in a histogram [non-dimensional]
N_w	Number of waves [non-dimensional]
P(x)	Probability distribution function [non-dimensional]
P(x)-95	Value of x corresponding to the 95% probability level [non-dimensional]
P(x)-99	Value of x corresponding to the 99% probability level [non-dimensional]
R(t)	Resultant vector in polar coordinates [m/s]
R_s	Relative submergence [non-dimensional], $R_s = d_s/H_i$
s	Wave steepness [non-dimensional], $s = H/L$
$S_{JONSWAP}$	JONSWAP wave spectrum [m^2/Hz]
$S_{lw}(f)$	Long wave variance spectrum [m^2/Hz]
$S_{lw-pwr}(f)$	Long wave power spectrum [(kW/m)/Hz]
$S_{pwr}(f)$	Wave power spectrum [(kW/m)/Hz]

S_r	Specific gravity of the armour material [non-dimensional]
$S_{xy}(f)$	Cross-spectral density between x(t) (input) and y(t) (output) [m^2/Hz]
$S_\eta(f)$	Wave variance spectral density function [m^2/Hz]
$S_{\eta,i}(f)$	Incident spectral density function [m^2/Hz]
$S_{\eta,r}(f)$	Reflected spectral density function [m^2/Hz]
$S_x(f)$	Auto spectrum of the input signal x(t) [m^2/Hz]
$S_{xy}(f)$	Cross-spectrum of input and output signals [m^2/Hz]
$S_y(f)$	Auto spectrum on the output signal y(t) [m^2/Hz]
t	Time [s]
T	Wave period [s], $T = 1/f$
T_{av}	Average of $T_{av,d}$ and $T_{av,u}$ [s]
$T_{av,d}$	Average period by zero down-crossing [s]
$T_{av,u}$	Average period by zero up-crossing [s]
T_p	Spectral peak period [s], $T_p = 1/f_p$
T_s	Significant wave period = $T_{1/3}$ [s]
T_z	Average wave period [s]
$T_{1/3}$	Average period of the 1/3rd highest waves [s]
u	Horizontal component of velocity in direction of wave propagation [m/s]
u_α	Horizontal velocity at the location z_α [m/s]
U_c	Current velocity [m/s]
U_r	Ursell number, $U_r = \frac{H \cdot L^2}{h^3}$ [non-dimensional]
v	Horizontal component of velocity perpendicular to direction of wave propagation [m/s]
w	Vertical component of velocity [m/s]
w_r	Unit weight of armour material [N/m^3]
W	Weight [N]
x	Horizontal cross-shore coordinate [m]
X_{max}	Maximum data value [m]
X_{min}	Minimum data value [m]
X_{12}	Distance between probes 1 and 2 (for reflection analysis) [m]
X_{13}	Distance between probes 1 and 3 (for reflection analysis) [m]
y	Horizontal alongshore coordinate [m]
z	Vertical coordinate, positive upwards [m]
z_α	Arbitrary distance from the still water level [m]
∇ (nabla)	Vector differential operator [non-dimensional]
α (alpha)	Variable term for linear dispersion relation [non-dimensional]
α_p	Phillips parameter [non-dimensional]
β (beta)	Free parameter [non-dimensional]
β_0	Empirical constant [non-dimensional]
γ (gamma)	Spectrum peak enhancement factor [non-dimensional]
Δt	Computational time step [s]
Δx	Grid size in x direction [m]
Δy	Grid size in y direction [m]

η (eta)	Water surface elevation [m]
η_{max}	Maximum water surface elevation relative to mean [m]
η_{min}	Minimum water surface elevation relative to mean [m]
η_{μ}	Average water surface elevation [m]
η_{σ}	Standard deviation of the input wave record [m]
θ (theta)	Slope of the structure [degrees]
$\theta(t)$	Direction of velocity vector [degrees]
λ (lambda)	Scale factor [non-dimensional]
μ (mu)	Damping strength [s^{-1}]
ξ (xi)	Iribarren number (Surf similarity parameter) [non-dimensional], $\xi = \tan\theta / \sqrt{H/L}$
π (pi)	pi constant [3.1415926535...]
ρ (rho)	Density [kg/m^3]
ρ_w	Density of sea water [1,030 kg/m^3]
σ (sigma)	Standard deviation [non-dimensional]
σ_i	Standard deviation of the incident wave train [non-dimensional]
σ_r	Standard deviation of the reflected wave train [non-dimensional]
σ_J	Constant for the JONSWAP wave spectra equation [non-dimensional]
τ (tau)	Bed shear stress [N/m^2]
τ_{br}	Wave breaking term [non-dimensional]
τ_{bf}	Bottom friction term [non-dimensional]
υ (upsilon)	Kinematic viscosity [St]
υ_t	Eddy viscosity [Pa·s]
φ (phi)	Phase spectrum [degrees]
$\varphi(f)$	Phase lag of cross-spectrum $S_{xy}(f)$ [non-dimensional]
χ^2 (chi)	Chi-square distribution for goodness-of-fit [non-dimensional]
ω (omega)	Angular frequency [rad/s], $\omega = 2\pi f$

List of Abbreviations

Abbreviation	Description
2-D	Two-Dimensional
2-DH	Two-Dimensional (Horizontal)
2-DV	Two-Dimensional (Vertical)
3-D	Three-Dimensional
ADV	Acoustic Doppler Velocimeter
ASCII	American Standard Code for Information Interchange
BNC	Bayonet Nut Coupling
BW	BreakWater
CDF	Cumulative Distribution Function
CEM	Coastal Engineering Manual
CFH	Cumulative Distribution Histogram
CHC	Canadian Hydraulics Centre
COBRAS	COrnell BReaking waves And Structure
CS	Cross-Section
CWB	Coastal Wave Basin
DELOS	environmental DEsign of LOw crested coastal defence Structures
ECM	Electromagnetic Current Meter
FFT	Fast Fourier Transform (FFT^{-1} is the inverse FFT)
GEDAP	Generalized Experiment control and Data Acquisition Package
GUI	Graphical User Interface
HHT	Hilbert-Huang Transform
JONSWAP	JOint North Sea Wave Analysis Project
LCS	Low-Crested Structure
MSL	Mean Sea Level
MWL	Mean Water Level
NDAC	(Windows) Nt Data Acquisition and Control
NRC	National Research Council
PDF	Probability Density Function
PDH	Probability Density Histogram
RANS	Reynolds Averaged Navier-Stokes
RMS	Root Mean Square
Sta.	Station (surveying)
SWL	Still Water Level
VARANS	Volume Averaged Reynolds Averaged Navier-Stokes
VOF	Volume Of Fluid
W + C	Wave and Current
WG	Wave Gauge
WL	Water Level
WM	Wave Machine
WT	Wavelet Transform

1 Introduction

Over the past 20 years, submerged structures have been extensively used in coastal management for protecting beaches against erosion. One of the advantageous properties of a submerged breakwater (BW) or low-crested structure (LCS) is that they do not interrupt a clear view from the beach out to the sea. The basic idea in the use of submerged structures is to provide a reduction in wave energy on its lee side, by triggering wave energy dissipation over the structure, and thus reducing sediment transport and the potential for coastal erosion. Low-crested structures are a growing interest due to their relatively low cost and capability of safe-guarding the coastal zone against erosion and also maintaining the quality of the coastal environment.

The effects generated by the combination of breakwater submergence, wave climate, distance of structure to shoreline, and crest width on wave and current hydrodynamics and morphological seabed and shoreline changes are not well understood (Cox & Tajziehchi, 2005). Functional knowledge for the design of submerged structures and their subsequent bearing on wave transmission, currents, sediment processes and shoreline response is still under development and additional research is necessary to elucidate the complex mechanisms governing these factors.

1.1 Significance and Novelty of the Study

As indicated by the author in the review of existing literature, there has been a substantial amount of experimental and numerical research into low-crested structures whose crests are located at or near the mean water level. One of the results of these research efforts is specifically the Environmental Design of Low-Crested Coastal Defence Structures (DELOS) research project currently under way in Europe (Zanuttigh, 2007). Research into deeply submerged structures is scarce in spite of an increase in their use and the lack of research impeaches on the proper design of such structures.

Moreover, a large part of the research on this topic was conducted in 2-D (two-dimensional) experimental flumes or using numerical models. Only a limited amount of research dealing with the 3-D (three-dimensional) behaviour of such structures has been performed. At the same time, almost all research projects consistently focused on the use of uniformly shaped structures with a specific *and constant* crest elevation.

The novelty of this research project is the use of a large-scale, three-dimensional model to study and analyze, both experimentally and numerically, the transformation of the waves and wave-induced velocities over a steeply sloped submerged structure, with a varying cross-section and a varying submergence depth.

1.2 Objective of the Study

The aim of this research project is to improve the understanding of wave and wave-induced velocity transformations in the presence of a steeply sloped, non-uniform depth submerged structure. These goals are accomplished in two main stages:

- Large-scale, 3-D laboratory tests,
- 3-D numerical modelling using a powerful numerical tool.

1.3 Scope of the Study

The physical and numerical modelling works undertaken in this research project have encompassed a wide array of coastal engineering research aspects. However, certain limitations imposed either by the tools or processes analyzed were not included in the present study. For instance, driven currents were included in several physical modelling tests. However since the numerical model used was not capable of handling currents, only the experimental features are briefly analyzed and discussed. A further discussion regarding wave-induced currents and the numerical model is found in Section 7.3.1. One of the main targets of the physical modelling work focused on damage and stability analysis of the outer protection of the submerged structure (refer to Section 3). This work is not considered within the scope of this research, but will be discussed briefly. The main focus of the present thesis is the complex interaction between the wave climate and the structure. Hence, this research project focuses primarily on the influence of the structure on the wave-induced hydrodynamics. The numerical model was also used to examine the general influence of the structure on the wave climate. Thus the objective was not to match the exact wave train used in the physical modelling series, but rather to reproduce the same statistical wave train parameters. Finally, morphological changes of the bed around the structure (bed erosion and deposition) were not the focus of this study.

1.4 Thesis Outline

The present work has been organized into nine main sections. A brief description of the content presented in each chapter follows.

Section 1 describes the significance of the study, describes the research objectives, and outlines the general framework of the thesis.

Section 2 reviews the state-of-the-art knowledge on the interactions of waves with submerged structures. An extensive literature review has been conducted by the author in relation to the main topics addressed in the present work.

Section 3 presents an introduction to the experimental project and provides the theoretical background and motivations for the present project.

Section 4 outlines the details of the physical modelling work, in particular the design, construction and experimental testing program together with data collection procedures.

Section 5 describes the numerical modelling work, in particular the theoretical framework of the numerical model, its adjustment, calibration and the sequence of numerical simulations performed by the author of this thesis.

Section 6 outlines the software and sub-routines used for experimental data analysis.

Section 7 presents the results of the physical and numerical modelling tests and provides a discussion on the work carried out (data analysis and interpretation, comparison of physical and numerical modelling results, etc.).

Section 8 briefly presents the conclusions and findings of the present work.

Section 9 finally makes recommendations for future works on the subject.

2 Literature Review

2.1 Introduction

Conducting an extensive and thorough literature review is a vital step in academic research. This process greatly guided the author in understanding the state-of-the-art with respect to the subject undertaken. The author was thus able to identify what has been already achieved by previous researchers and to identify the areas where further research is necessary or warranted. A thorough literature review has been conducted with regards to the physical and numerical modelling of the wave-breakwater interaction and related studies. A number of studies and results of several studies dealing with the topics studied are summarized from many sources, for both experimental and numerically based work, and a critical discussion follows.

2.2 Physical Modelling of Wave-Structure Interaction

Van der Meer & Daemen (1994) developed formulas to predict wave transmission over low-crested rubblemound structures, taking into consideration the crest height and width, wave height and wave steepness. The researchers classify low-crested rubblemound structures into three categories: dynamically stable reef breakwaters, statically stable low-crested breakwaters, and statically stable submerged breakwaters. It was concluded that the stability of submerged breakwaters depends significantly on the relative crest height, the damage level, and the spectral stability number. The formula described for wave transmission yielded a linear relationship between the wave transmission coefficient and the relative crest height.

d'Angremond *et al.* (1996) analyzed a database of wave transmission experiments for low-crested breakwaters and derived an expression for relating the transmission coefficient to structural parameters and wave parameters. This research provided the theoretical foundation for a number of other papers of several other researchers.

Brunone & Tomasicchio (1997) investigated the characteristics of the flow field produced by regular waves acting on a steep uniform slope, namely the temporal and spatial behaviour of surface elevation and the vertical distribution of the horizontal component of the local velocity. It was observed that due to the relationship between the variance of velocity distribution and the momentum flux correction coefficient, the second-order model proposed by the researchers can account for the shape of the velocity profiles in one-dimensional numerical models that describe the flow field due to the action of a wave on a steep slope.

Dean *et al.* (1997) conducted full scale monitoring of an experimental submerged breakwater in Florida, installed in an attempt to reduce beach erosion and wave impact on a protective seawall. Based on the results of the installation and other similar model studies, it was observed that a detached breakwater modifies both the wave and current fields landward of the breakwater, depending significantly on the crest elevation relative to the still water level. For higher relative crest elevations (i.e. emergent breakwaters), wave heights and currents on the lee side of the breakwater are both diminished. The study identified two significant mechanisms important in offshore breakwater design. The breakwater crest height is significant since a low crest height may allow so much water to flow over the breakwater that the resulting flows in the longshore direction will outweigh the benefits of the small reduction in wave height and still cause beach erosion landward of the breakwater. The effect of the offshore distance of the breakwater is also a factor. The research states that, based on numerical model results, the volume of water flow over the breakwater is only a secondary affect of the offshore location of the breakwater. However, the longshore currents are inversely varied with this distance.

Losada *et al.* (1997) conducted experiments in a wave flume to study the harmonic evolution of monochromatic waves as they propagate over a submerged impermeable step and a porous step under non-breaking conditions. It was observed that increasing porosity reduces reflection in general, although variations of porosity did not result in significant variations of reflection. The generation of harmonics over a submerged structure is related to water depth and wave height over the structure. It was also observed that an impermeable step induces not only a substantial growth of higher harmonics, but also substantially increases the energy carried at the first harmonic.

Seabrook & Hall (1998) conducted an extensive set of 2-D and 3-D model tests of wave transmission for submerged breakwaters. Their findings indicated that the transmission coefficient is most sensitive to the relative submergence (d_s/H_i) and that the relative crest width is an important factor that has not been accounted for adequately in previous design equations.

The researchers proposed a new equation for transmission that is well bounded over the range of test data; however upper and lower limits on the crest width are suggested as shown below.

$$C_t = 1 - \left(e^{-0.65\left(\frac{d_s}{H_i}\right) - 1.05\left(\frac{H_i}{B}\right)} + 0.047\left(\frac{B \cdot d_s}{L \cdot D_{50}}\right) - 0.067\left(\frac{d_s \cdot H_i}{B \cdot D_{50}}\right)\right)$$

$$0 \le \frac{B \cdot d_s}{L \cdot D_{50}} \le 7.08 \qquad (2\text{-}1)$$

$$0 \le \frac{d_s \cdot H_i}{B \cdot D_{50}} \le 2.14$$

Sutherland & O'Donoghue (1998) carried out random wave reflection experiments to characterize the form of the reflection coefficient spectrum from coastal structures. The tests were performed on smooth, impermeable walls, as well as rubblemound breakwaters. It was found that a frequency-dependent Iribarren number can be used to characterize the reflection coefficient spectra for sea states with different peak frequencies and significant wave heights reflecting off a structure. The reflection coefficient was found to be determined by wall slope, frequency, incident significant wave height and two fitted coefficients. A specific equation is recommended for prediction of reflection for smooth impermeable walls, however the rubblemound breakwater tests covered a limited range of parameters and thus no equation was recommended in the paper. However, the equation in this case is assumed to be similar to the smooth wall equation but with differently fitted coefficients.

Klopman & Van der Meer (1999) came to several conclusions with regard to the measurement of random waves in front of a reflective structure. A standing wave pattern was observed, extending over about two times the local spectral-peak wavelength. That meant that in laboratory experiments where only one wave gauge is used near the structure, it should be located far enough from the structure in order to keep it outside the region of significant oscillations. Measured and theoretical wave spectra displayed a pattern of nodal and antinodal frequencies, for which the distances between nodes decreased for increasing offshore distances.

Calabrese *et al.* (2002) present the results of large scale model tests on wave transmission at low-crested breakwaters, located in relatively shallow waters, where wave conditions ranged from shoaling to post breaking. The research showed that among existing formulae, d'Angremonde *et al.* (1996) gave the most reliable estimates of the transmission coefficient, especially for the case of wide crested structures. Some significant scatter was still observed between the data and predictions, due to two main reasons. Firstly, the breaker index should have an influence on wave transmission in the nearshore area; however it is typically not regarded in the presently used formulae. Secondly, the crest width should also affect the reduction rate of the transmission coefficient. A new equation was proposed that considerably reduced the differences between predicted and measured values, although further analysis is warranted to confirm and improve the proposed equation.

$$C_t = \left(\left(0.6957\frac{H_i}{h} - 0.7021\right)\cdot e^{\left(0.2568\frac{B}{H_i}\right)}\right)\cdot\frac{d_s}{B} + \left(\left(1 - 0.562\cdot e^{-0.0507\xi}\right)\cdot e^{\left(-0.0845\frac{B}{H_i}\right)}\right)$$

$$\begin{gathered} -0.4 \le d_s/B \le 0.3 \\ 1.06 \le B/H_i \le 8.13 \\ 0.31 \le H_i/h \le 0.61 \\ 3 \le \xi \le 5.20 \end{gathered} \qquad \textbf{(2-2)}$$

Briganti *et al.* (2003) collected a large database of more than 200 2-D laboratory tests on wave transmission behind low-crested structures. The gathered results were reanalyzed and used to improve the prediction of the transmission coefficient, with the outcome being the calibration of two design formulae based on d'Angremond *et al.* (1996). A preliminary analysis of the spectral shape changes was performed, based on the correlation of the energy shift induced by the low-crested structures and the same parameters used in estimating the wave transmission coefficient. The definition of a straightforward parameterization of the transmitted spectral shape, useful for design purposes, is the aim of the ongoing research on this topic.

Harris (2003) presented artificial reef structures as submerged breakwaters. These structures have the potential to assist with shoreline stabilization, while minimizing adverse impacts on nearby beaches. The artificial reef structures mimic natural reefs and sandbars by reducing the wave energy that reaches the shore. In addition to coastal erosion protection, artificial reefs provide environmental and recreational amenities, including increased habitat for marine life and recreational benefits. The study concluded that the design of any coastal protection system is extremely site specific and that not all locations may be suitable for the use of artificial reef for shoreline stabilization. During storm surge conditions, a submerged breakwater may be too deep to provide adequate erosion protection directly, but additional protection is afforded by the beach that has been maintained in its lee.

Lamberti *et al.* (2003) performed 3-D physical model tests with the aim of analyzing waves and currents around low-crested structures. The research presented a method for evaluating wave overtopping over low-crested structures from wave gauge records, verified through experimental data collected from the tests. The method can be applied to moderately submerged or emergent structures. The analysis of fluxes shows that runup is the most relevant process parameter for overtopping. For small runup values, overtopping for irregular waves is weak and most of the overtopping volume is lost due to percolation in the rubblemound. With increasing runup, overtopping discharge increases and the percolated volumes decrease. The proposed flux measurements and estimates satisfied a mass balance within 20%. Major discrepancies were however observed for cases of no relevant overtopping over emergent structures, where it is difficult to reconstruct the inshore discharge percolating and filtrating through the structure, and for deeply submerged structures due to a high return flow.

Lomonaco *et al.* (2003) performed a series of laboratory and prototype tests to measure the flow around and inside rubblemounds used to protect sea outfalls. The near-bed velocity profiles were measured on the slopes and over the crest of the structure, as well as the dynamic pressure around the protected pipeline. By applying a linear transfer function, the surface elevation and the incident wave height and period data were obtained. A statistical comparison was performed of the measured and computed cumulative distribution functions, as well as the Rayleigh distribution. The researchers found that although the measured pressure and velocity Cumulative Distribution Functions (CDF) followed the Rayleigh distribution, the largest waves deviated somewhat, yielding as a result that the computed horizontal velocity is 30% smaller than the measured one. Because the horizontal velocity at the crest of the structure is closely linked with the stability of stones composing the rubblemound breakwater, it is necessary to consider this underestimation during the design stage.

Van der Meer *et al.* (2003) performed a series of experiments on wave transmission for low-crested structures. It was observed that rubblemound structures behave quite differently from smooth structures, and wave transmission prediction formulas should consider both structures independently. Incident and transmitted wave angles are not always similar, and in general the transmitted wave angles do not exceed 45°. The influence of the wave angle on the transmission coefficient was found to be marginal for rubblemound structures, meaning the most recent and well calibrated formulae of Briganti *et al.* (2003) can be taken for 3-D situations.

Cox & Tajziehchi (2005) carried out 2-D laboratory experiments in a wave flume to investigate the effects of wave transmission, wave-induced setup and current over submerged breakwater/reef structures. The investigation found that mass flux is most influenced by the breakwater crest width and the incident wave height. The research also allowed for the improvement of a numerical model's predictive capability for calculating current passing over the breakwater/reef due to wave breaking by adjustment of the calibration factors.

Pinto & Neves (2005) performed measurements of the water elevation near a smooth and a rough submerged breakwater model to analyze the wave shoaling phenomenon. It was observed that total wave heights (incident plus reflected) can be larger than the incident ones, of importance for the stability of the breakwater components and their design parameters. In general, the measured shoaling coefficient obtained for the smooth model had a gentler variation than the rough one, partially explained by the wave dissipation process which is more turbulent in the rough model.

Sumer *et al.* (2005) performed an experimental study of scour around submerged breakwaters. It was determined that substantial toe scour may occur at submerged breakwater, irrespective of the breakwater's composition (impermeable or porous), and that the scour depth is of the same order as in the case of emergent breakwaters. The scour observed occurred on both offshore and onshore sides of the structure, both in the same order of magnitude. Scouring for roundheads at the offshore side is caused primarily by the combined effect of severe waves and the steady streaming, while at the back caused mainly by wave breaking and overtopping.

Wang *et al.* (2005) performed an experimental investigation of obliquely incident wave reflection at low-crested structures. The physical model tests were carried out with incident wave angles varying over a range of 0° to 60° in a multidirectional wave basin. Their research finding stated that, in addition to the fact that the reflection reduces if the crest height decreases, wave obliquities also contribute a further reduction of reflection. The data analysis also showed that in general, the reflected peak period is fairly close to the incident peak period, and in the spatial domain, the reflected waves from the low-crested structures are spread more widely than for the incident waves.

Burcharth *et al.* (2006) present a new design formula corresponding to the state of damage initiation for rock armoured low-crested structures attacked by depth-limited waves. The formula is valid for armour slopes of 1:2 and is based on 3-D model tests in short-crested waves. The formula also fits other test data gathered, for initiation of damage for low-crested structures with armour slope of 1:1.5 exposed to long-crested waves. The study revealed that the effects of crest width, wave steepness and obliquity are relatively small, but the influence of the freeboard is large. Submerged LCSs were observed to be much more stable than emerged ones under the same waves. For depth-limited waves, slightly submerged conditions are the most critical with respect to armour stability. The researchers also noted that armour hydraulic stability is not the only and most critical failure mode of LCSs, a proper (wide and stable) toe protection that blocks against regressive erosion at the bed, and a proper well-placed filter to avoid structure settlement in a sandy bed are equally important factors for long term stability.

Vidal *et al.* (2006) demonstrated that the wave height parameter H_{50}, defined as the average wave height of the 50 highest waves reaching a rubblemound breakwater in its useful life, was able to describe the effect of the wave height on the history of the armour damage caused by the wave climate throughout the life of the structure. Using data from previous physical experiments, it was shown that the H_{50} parameter can describe the damage on Rayleigh-distributed sea states of any length as well as presently existing formulae. The calculation of H_{50} requires detailed information of the incident wave statistics near the structure's toe, both for short term (sea states) and long term (wave regimes).

Zanuttigh & Lamberti (2006) present 3-D experiments on low-crested rubblemound structures under regular and irregular wave attack. The researchers presented a method for evaluating wave overtopping from wave gauge records, verified through experimental data collected that can be applied to emergent and moderately submerged structures (until $-F<0.7H_i$). Numerical simulations were also performed in comparison, and it was observed that the measured and computed circulation patterns were qualitatively similar, but setup and flow intensity were greater in the simulations than that found in the experiments.

2.3 Numerical Modelling of Wave-Structure Interaction

Madsen *et al.* (1991) derived a new form of the Boussinesq equations in order to improve the linear dispersion characteristics in deep water. This improvement was deemed important for studies of wave penetration, refraction and diffraction where the phase celerity and group velocity need to be accurately modelled. The newly derived equations made it possible to simulate the propagation of irregular wave trains travelling from deep water into shallow water. Nonlinearities were treated in the classical way by including convective terms and a nonlinear gravity term, and were seen to be proportional to the ratio of the wave height to the water depth; therefore in deeper water these terms become insignificant and the new equations became effectively linear. In shallower water, the nonlinear properties are similar to those obtained by the standard Boussinesq equations. This combination of a linear wave model in deep water and a nonlinear wave model in shallow water is justified by the researchers by the fact that waves which are non-breaking in shallow water will only be weakly nonlinear in deeper water.

Karambas & Koutitas (1992) used the eddy viscosity concept to incorporate wave breaking in a nonlinear wave propagation model, based on the Boussinesq equations. The turbulence model supports the Boussinesq model by providing reasonable values for the eddy viscosity coefficient. The developed model was tested against physical experimental data on wave transformation phenomena in the inshore zone, and was capable of reproducing the transformations with a high degree of accuracy.

Nwogu (1993) derived a new set of Boussinesq-type equations, using the velocity variable as the velocity at an arbitrary distance from the still-water level, instead of the commonly used depth-averaged velocity. In intermediate and deep water, the linear dispersion characteristics of these new equations were seen to be strongly dependent on the choice of the velocity variable. By selecting a velocity variable as the velocity close to mid-depth, a significant improvement in the dispersion properties was observed, allowing the model to be more applicable to a wider range of water depths. In comparison to laboratory data, good agreement was obtained for the shoaling of regular waves from intermediate to shallow water, and irregular waves from deep to shallow water. The model was also able to reproduce several nonlinear effects that occur during shoaling, such as the generation of longer and shorter period waves, an increase in horizontal and vertical asymmetrics, and the evolution of wave groups. The research represents a practical tool for the simulation of nonlinear transformation of non-breaking, irregular, multidirectional waves in water of varying depths. Further discussion is found in Section 5.2.

Ohyama & Nadaoka (1994) investigated the decomposition phenomenon of nonlinear wave trains passing over a submerged rectangular shelf by the use of a previously developed numerical model. The decomposition is triggered by the higher harmonic generation resulting from resonant interaction in the shallow-water region over a shelf. It was observed that in the trailing side of the shelf, the energy in bound harmonics is abruptly transferred into free higher harmonics which resulted in a drastic change of wave form and a greater height of transmitted waves than that predicted by the linear theory. For large amplitude incident waves, prominent wave decomposition was found to occur even when the shelf was deeply submerged.

Van Gent (1994) used a set of long wave equations for a numerical model in which the flow on a structure was described by a hydraulic model, and the flow inside the structure was described with a porous flow model. The combination of these parts resulted in an integrated model that was able to describe phenomena such as reflection, permeability, infiltration, seepage, and overtopping. The numerical model was found to give satisfactory results for conventional and berm breakwaters, and was suggested as a useful engineering tool, although further verification of the model would be necessary.

Wei & Kirby (1995) developed a high-order numerical scheme for the Boussinesq equations derived by Nwogu (1993). The scheme was tested with a number of examples to illustrate basic stability and to show that the new Boussinesq equations could be applied to a wider range of water depths than previous versions of the equation. The final example studied was a case with discrepancies between nonlinear effects in the Boussinesq approximation and corresponding effects in data or alternate analytical formulations. The researchers concluded that these limitations were most likely manifestations of the lowest order nature of the model which does not correctly represent either the nonlinearity of waves near the breaking point or the dominant cubic nonlinearity of intermediate depth waves. It was concluded that the model equations require extension to include higher order terms.

Vidal *et al.* (1995) examined the variability of extreme wave height parameters using the numerical simulation of sea states with the same spectral characteristics and duration. The research suggests that for correct interpretation of data resulting from model studies of rubblemound breakwaters, the wave height distribution of the measured incident time series and the number of repetitions of that time series should be given. The researchers propose a parameter, H_n, for use in breakwater stability formulas; the average height of the n largest waves in a sea state. The definition of the most suitable value for n is still a subject of continued study; however a value of around 100 was seen to be appropriate. A linear relationship was observed between the groupiness factor, defined as the standard deviation of the smoother instantaneous wave energy history, and wave height parameters related to the largest waves. The $H_{1/20}$ was shown to have the highest correlation with the groupiness factor among the different wave height parameters from the numerically simulated time series. Other parameters such as $H_{1/10}$ and $H_{1/100}$ also displayed high correlations. The research concluded that since there is a strong correlation between the groupiness factor and the statistics of large wave heights, future research on the effect of wave grouping should ensure that the time series have similar wave height statistics.

Losada *et al.* (1996a) used two models to study the influence of structure geometry, porous material properties and random wave characteristics, including oblique incidence, on the kinematics and dynamics over and inside a submerged permeable breakwater. It was observed that increasing wave obliqueness resulted in a reduction of wave reflection, taking a minimum value in the range of 50 to 60 degrees, although the reduction is strongly associated to relative depth, breakwater geometry and porous material characteristics. Transmission was not seen to be affected much by obliqueness of the incident waves, and remained almost constant for a given case until values near to 65 or 70 degrees where wave transmission was effectively zero. The analysis also revealed that the maximum pressure values are located at the front slope while velocities and accelerations take their maximum value at the beginning of the breakwater crest.

In a companion paper, Losada *et al.* (1996b) used the eigenfunction expansion model to evaluate random wave transformation for rectangular breakwaters, and an extension of the mild slope equation is applied to study the effects on trapezoidal breakwaters. The model was seen to reproduce the experimental results well and provides a tool to analyze several engineering problems such as breakwater efficiency, stability of armour units, bottom scour and determination of harbour tranquility. It was observed that in general, random waves (unidirectional or multidirectional) induced lower reflection and transmission coefficients than regular waves. Another general trend is that energy dissipation is more dependent on the spectral width parameters than on the spreading parameter.

Nwogu (1996) described the extension of a comprehensive numerical model for the simulation of ocean wave propagation and transformation in coastal regions and harbours, including the effects of wave breaking, runup, and breaking-induced currents. The fully nonlinear Boussinesq model was extended to the surf and swash zones by coupling the mass and momentum equations with a one-equation turbulent kinetic energy transport model. Waves are assumed to start breaking when the horizontal velocity at the wave crest exceeds the phase velocity of the waves. The numerical model was compared with experimental data for shoaling of regular and irregular waves on a beach with 1:25 slope. The model was able to reproduce with reasonable accuracy the frequency and time domain characteristics of waves in the surf zone. Further discussion is found in Section 5.2.

Bosboom *et al.* (1997) modelled the horizontal velocities in the near-bed zone in partially breaking waves using a frequency-domain Boussinesq model. By imposing a parabolic profile, the near-bed velocities were obtained from the depth averaged velocity. The computation of bottom velocities from the surface elevation yielded results with an accuracy comparable to that of predicted surface elevations. The velocity variance was also predicted fairly well. For longer wave periods, the velocity skewness was predicted well; however for shorter wave periods, an underestimation of velocity skewness was observed due to an underestimation of the crest values of the highest waves. Additional research is required in order to determine whether the discrepancies resulted from the water depth restrictions of the Boussinesq equations used, or from additional assumptions made in the derivation of the evolution equations underlying the model.

Kaihatu & Kirby (1998) derived a two-dimensional parabolic frequency domain wave transformation model based on the extended Boussinesq equations of Nwogu (1993). The researchers were able to begin from the (η, u) form of the equations of Nwogu and retain the original dispersion relation after the transformation into the frequency domain. A free parameter β was introduced as a means of circumventing the ambiguous nature of the first-order substitutions required to reduce the system of equations down to one. This parameter was optimized in two ways, what the authors refer to as "dispersion optimized" (DO) and "dispersion and shoaling optimized" (DSO). Both schemes demonstrated shoaling behaviour consistent with linear theory. The full model, with nonlinear terms included was compared to physical test data, with the results showing that both schemes had good agreement with the data in intermediate water depth, similar to other numerical models at the time.

Huang & Dong (1999) developed a numerical scheme to solve the Navier-Stokes equations and the exact free surface boundary conditions in order to simulate the wave deformation and flow fields in water waves propagating over a submerged dike. The scheme was found to be able to accurately predict wave deformation and the detailed flow fields, including separation and vortex generation. The research found that the first harmonic wave amplitude on the lee side of the dike becomes smaller as the Ursell number of the incident wave increases and the water depth ratio of the dike decreases. It was also found that the shape of the dike plays an important role. The amplitudes of higher harmonics on the lee side of a trapezoidal dike are smaller than those for a rectangular dike due to the gentler depth change.

Chawla & Kirby (2000) describe an alternate formulation for wave generation in weakly dispersive wave models using two spatially distributed source functions. Studies involving interaction of waves with a strong current could directly utilize this formulation that allowed for the existence of an underlying current field. The method was tested with an existing model in the presence and absence of strong currents and was observed to work well. Although the method used linear wave approximation, it was able to reproduce the larger wave heights with reasonable accuracy. The formulation generated waves traveling in one direction only, the advantage of which eliminates the non-physical backward propagating waves, thus greatly reducing the required damping layer behind the source region.

Kennedy *et al.* (2000) developed a surf zone model for the fully nonlinear Boussinesq equations of Wei *et al.* (1995) and extended Boussinesq equations of Nwogu (1993), using a modified eddy viscosity model and a slot technique to represent the moving shoreline and dry land. The model showed accurate predictions of wave transformation in the surf and swash zone, however some over-prediction was seen for monochromatic wave shoaling and breaking on a planar beach. In the companion paper, Chen *et al.* (2000) continued the extension of the same model to include numerical wave results, including spatial variation of Root Mean Square (RMS) wave heights and distribution of maximum runup heights. The model is capable of predicting the combined refraction and diffraction of nonlinear waves with wave breaking over rapidly varying bathymetry. Comparisons indicated that for shoaling and runup of solitary waves, the Boussinesq model gave better predictions than do nondispersive models based on nonlinear shallow water equations in literature.

Lee *et al.* (2001) sought whether the mass transport or the energy transport is the proper approach for internal wave generation in the extended Boussinesq equations of Nwogu (1993). In a horizontally one-dimensional domain, it was observed that the energy transport approach gave proper wave amplitudes; however, the mass transport approach gave wave amplitudes different from those desired. The researchers conclude that further theoretical investigation would be valuable.

Méndez *et al.* (2001) present two models, a 3-D model for permeable rectangular breakwaters and a 2-D model for permeable breakwaters of arbitrary geometry, in order to evaluate second-order magnitudes such as mass flux, energy flux, radiation stress, and mean water level. Both models were capable of reproducing the wave height transformation as well as mean water level variations along the breakwater with reasonable accuracy. In front of the structure, second-order magnitudes were seen to be modulated due to the reflection induced by the structure. It was observed that for non-breaking conditions, increasing the freeboard yields a higher energy flux transmission. Results indicated that the setup induced by a permeable submerged breakwater is due to the radiation stress gradients induced by the dissipation associated with both breaking and friction. The mean water level variations showed a modulation in front of the structure, with a maximum set-down at the beginning of the crest, and a progressive increase along the crest that reached its maximum value approximately at the back slope.

Nwogu & Demirbilek (2001) describe BOUSS-2-D, a comprehensive numerical model based on a time-domain solution of Boussinesq-type equations. The model is based on Nwogu's original work from 1993, which, despite improvements in the frequency dispersion characteristics, was based on the assumption that the wave heights were much smaller than the water depth, limiting the ability of the equations to describe highly nonlinear waves in shallow water. In 1996, Nwogu extended the fully nonlinear form of the Boussinesq equations to the surf zone, by coupling the mass and momentum equations with a one-equation model for the temporal and spatial evolution of the turbulent kinetic energy produced by wave breaking. The equations were also modified to include the effects of bottom friction and flow through porous structures, and were able to simulate most of the hydrodynamic phenomena of interest in coastal regions and harbour basins.

Shi *et al.* (2001) derived the fully nonlinear Boussinesq equations by Wei *et al.* (1995) in generalized curvilinear coordinates by using the contravariant velocity method. The numerical model was then developed further through the use of a high-order finite difference scheme in staggered grids. Testing the model showed that good convergence rates with both space and time discretization were obtained in the computation of wave evolution in a rectangular basin. The comparison between numerical results and measurements shows that the model has good accuracy in dealing with the computation of nonlinear wave propagation with complex lateral boundaries. Further development is required for incorporation of energy dissipation by wave breaking and wave run up on sloping beaches and structures.

Twu *et al.* (2001) performed studies on the improvement for the problem of wave transmission in deeply submerged breakwaters. The research showed that for a single-slice breakwater, the transmission coefficient could be effectively reduced to as low as 0.2 when the porosity of the structure material is as high as 0.8, and the thickness-depth ratio B/h = 20. For the deeply submerged breakwater case, the wave transmission problem could be effectively improved by adopting a multi-slice structure concept. In general it was found that the more slices of which the breakwater is composed, the more effective it is in reducing the transmission coefficient. Formulae were also derived for the calculation of the reflection and transmission coefficients as follows:

$$\begin{aligned} C_r &= \left|\frac{B_{00}}{A_{00}}\right| \\ C_t &= \left|\frac{A_{n+1,0}}{A_{00}}\right| \\ A_{00} &= \frac{ga_i}{\omega\cosh(kh)} \\ B_{00} &= \frac{ga_r}{\omega\cosh(kh)} \\ A_{n+1,0} &= \frac{ga_t}{\omega\cosh(kh)} \end{aligned} \tag{2-3}$$

Christensen *et al.* (2003) compared wave heights, instantaneous and mean water levels and flow velocities predicted by 2-DH (two-dimensional (horizontal)) and 3-D numerical models of varying complexity to measurements performed in a wave basin. In general, satisfactory agreements were obtained between measured and computed wave heights and instantaneous water levels; however the models consistently tended to overpredict mean water levels and flow velocities. The researchers gave a possible explanation for the observed mismatch based on the permeability of the structures, since this effect was not taken into account by the models used in the investigation.

Hur & Mizutani (2003) developed two numerical models to estimate the wave forces acting on a submerged breakwater. The models combine a Volume of Fluid (VOF) model and porous body model to simulate nonlinear wave deformation including wave breaking and its interaction with a porous structure. The first model is two-dimensional and associated with empirical wave force formulae such as the Morison equation. The second is three-dimensional and does not rely on empirical formula or coefficients. The two-dimensional model gave good estimations of the time variations of the water surface elevation, velocity and accelerations, and through substitution of these time profiles into the Morison equation confirmed good predictions of the wave force. The three-dimensional model demonstrated the ability to reproduce the wave forces for both non-breaking and breaking wave conditions and is seen as a powerful tool to evaluate wave forces.

Losada *et al.* (2003) investigated wave interaction with permeable low-crested breakwaters using data from small-scale laboratory experiments and numerical simulations using a 2-DV (two-dimensional (vertical)) VOF-type Reynolds-Averaged Navier Stokes model. The numerical model has been validated by comparing the computational results with experimental data of the free surface time series along the flume and mean velocity profiles at the offshore slope of the structure. The breaking and post-breaking wave transformation processes were observed to be adequately reproduced by the model. Production and dissipation energy processes associated to wave breaking and internal porous flow were also correctly simulated. The influence of the crest width on the energy dissipation and thus on the breakwater performance has been confirmed, with an observed wave height decay and attenuation of the mean flow field that was greater in the case of wide-crested structures.

Shi *et al.* (2003) used an improved curvilinear Boussinesq model based on the fully nonlinear equations to simulate nonlinear waves at an inlet. The model was able to resolve the complex geometry and predict nonlinear wave transformation in the large computational domain. Fairly good agreement was observed in the wave height comparisons. Spectral analysis showed the wave energy transfer from the original peak frequencies to the corresponding harmonic frequencies. An indicator of wave nonlinearity observed in the research was the probability distributions of wave surface elevations, which showed similar deviations from the Gaussian distribution for both the measured data and numerical results. Difficulties were encountered with the generation of large incident waves in the numerical model, and further improvement was deemed necessary.

Avgeris *et al.* (2004) combined a 2-DH Boussinesq-type model with a depth-averaged Darcy-Forchheimer equation to simulate wave propagation over submerged porous breakwaters. The model was tested against experimental measurements undertaken in a wave flume and a wave basin. The analysis demonstrated that the model was able to simulate relatively well the wave evolution at the regions before and over the breakwater. Behind the breakwater, the decomposition of the leading wave component into higher frequency waves was also predicted with reasonable accuracy. A deficiency noted in the model that affected the results was that the linear dispersion relationship was not accurate enough. Model performance was also noted to be influenced by the fact that the wave energy dissipation rate due to porous resistance and wave breaking was not exactly predicted.

Bredmose *et al.* (2004) dealt with the possibility of using methods and ideas from time domain Boussinesq formulations in the corresponding frequency domain formulations, termed "evolution equations". It was demonstrated that the computational efficiency of evolution equations can be significantly improved by calculating nonlinear terms by the aid of Fast Fourier Transforms. An attempt to improve the traditional wave breaking formulations, the surface roller breaking model, was adapted similarly. Even though the new breaking model was based on direct processing of time series for the surface elevation, the quality of the resulting wave profiles was not found to improve the results, and thus it was not recommended in the present form. The embedded amplitude dispersion of the evolution equations was also analyzed. It was observed that the dispersion can be twice as large as the reference solution of Stokes waves on a zero mass flux and more than three times larger than for the corresponding time domain model. Further analysis showed the difference was due mainly to the neglect of spatial derivatives of the wave amplitudes in the nonlinear terms of the evolution equations. Although the Fourier series representation is ideal for describing a spectrum of linear waves, the representation of coherent bound waves like nonlinear breaking waves was not accurate.

Figueres & Medina (2004) presented a modification to the time-domain method for separating incident and reflected waves, involving the use of a fully nonlinear wave model for the local approximation. Laboratory experiments were carried out to test the new method, and the results were quite good. The researchers concluded further study is needed to expand the model with pressure or velocity records or 3-D models.

Garcia *et al.* (2004) investigated the capability of the VOF-type Cornell Breaking Waves And Structure (COBRAS) model, resolving the Reynolds Averaged Navier-Stokes (RANS) equations in the vertical plane, to simulate wave interaction with low-crested rubblemound breakwaters in large scale laboratory tests. The numerical model was able to correctly reproduce the time series of free surface displacement and dynamic bottom pressure at the different sections of measurement. The processes of wave deformation, breaking over the crest of the breakwater, and post-breaking evolution were also well captured. The numerical model was proven to adequately simulate the performance of the breakwater in terms of reflection, dissipation, and transmission of the incident wave energy. The results were seen to be useful in support of measured data to explore breakwater functionality and stability.

Sørensen *et al.* (2004) presented a numerical model for solving a set of extended time domain Boussinesq-type equations including the breaking zone and the swash zone, based on the unstructured finite element technique. The work has shown the new model to be an accurate tool for prediction of wave conditions in large coastal areas that include the surf zone. The use of unstructured meshes offers the possibility of adapting the mesh resolution to the local physical scale, and compared to the use of structured meshes, unstructured may significantly reduce the number of nodes in the spatial discretization, especially where the breaking and surf zone are included. The main drawback found was the computational effort required to solve the linear system of equations at each time step, and more efficient solvers need to be investigated.

Weston *et al.* (2004) presented a numerical model based on weakly non-linear Boussinesq-type equations, discretized with a finite volume framework, and using an empirical breaking criterion to predict the onset of breaking and simulates the subsequent breaking waves as the propagation of a discontinuous bore. This technique was shown to be valid, accurate, and robust method for simulating breaking waves. The case of a wavegroup propagating over a shoal was investigated, and it was found that as the wavegroup passed over the shoal, higher order bound harmonics within the group were generated as expected and subsequently released as free waves as the wavegroup returned to deeper water.

Woo & Liu (2004a) describe a new 2-D finite-element method developed for Nwogu's (1993) modified Boussinesq equations. Boundary treatment and the possibility of extension to include higher-order nonlinear terms were considered for the choice of auxiliary variables used for the treatment of the third-order spatial variables in the governing equations. A physically and mathematically consistent treatment for a perfect reflective wall boundary condition has been developed and implemented in the model. Good agreements were obtained between present numerical results and existing analytical and other numerical solutions. In the companion paper, Woo and Liu (2004b) apply the model to linear and nonlinear harbour oscillation problems. Comparisons with experimental data demonstrate the applicability of the presented model for studying and analyzing nonlinear harbour resonance problems. The researchers noted that the computational efficiency required improvement, and furthermore different dissipation mechanisms such as wave breaking, bottom friction, and partial reflection were needed to improve the model.

Bruehl & Oumeraci (2005) performed a comparative analysis of the Fast Fourier Transform (FFT), Wavelet Transform (WT) and the Hilbert-Huang Transform (HHT) as applied to the example of regular and irregular wave trains transmitted over an impermeable reef. It was observed that the peak frequency of the incident waves was reliably identified, and that energy transfer from the incident peak frequency to higher frequencies within the transmitted wave spectrum was well confirmed by all three methods. Although WT and HHT proved somewhat superior to FFT, a key limitation observed in all three methods is the linearity of the applied methods themselves. To better understand the nonlinear processes which are particularly associated with shallow water waves and wave structure interaction, the researchers suggest a nonlinear analysis method using nonlinear waves as the basis components, and accounting for their nonlinear interaction is required.

Cáceres *et al.* (2005) evaluated the hydrodynamic influence of different design parameters for a submerged breakwater by using a set of numerical models. The research found that the behaviour of submerged barriers is mainly controlled by setup gradients and nearshore current pattern as well as the effect of wave mass fluxes over the barrier and the resulting diverging fluxes. The filtering effect on incident waves, associated to differing freeboards, was mainly apparent in the wave field and the induced circulation pattern. It is remarked that varying the freeboard will act as a filter of wave transmission over the structure. In this way, higher waves will be more filtered than smaller ones. This filter will occur by wave breaking giving as a result a mass flux over the structure that will control or modify the wave-induced circulation pattern.

Johnson *et al.* (2005) used two approaches, phase-averaged and phase-resolving, for the simulation of waves, changes in the mean water level, and currents in the vicinity of submerged breakwaters. In the phase-averaged approach, a wave model was used to simulate wave transformation and calculate radiation stresses; while a 2-D depth averaged flow model was used to calculate the resulting mean wave driven currents. In the phase-resolving approach, a 2-DH Boussinesq-type model combined with a depth averaged Darcy-Forchheimer equation was used to calculate the waves and intra-wave flow. Both models showed reasonably good agreement in the prediction of wave heights; however the phase-averaged model required that the wave breaking sub-model was appropriately tuned for wave dissipation over the breakwater. The phase-averaged model was able to predict flow circulation patterns in qualitatively good agreement, but the predicted current speeds and wave setup leeward of the breakwaters were higher than measured. The case was similar for the phase-resolving model. It predicted the flow circulation patterns in qualitatively good agreement, however the calculated currents speeds were low compared to the measurements, whereas the calculated wave set-down was too large. It was observed that the absorbing lateral boundaries in the lee of the breakwater were mainly responsible for the deviation between measurements and calculations, thus giving some confidence in the ability of the models to reproduce waves and currents in the vicinity of submerged breakwaters. Kramer *et al.* (2005) is a companion paper presenting the series of experimental tests on low-crested structures relating to the Johnson *et al.* (2005) paper. The physical experiments focused on wave obliquity, flow velocities inside and close to the surface of the structure, structural stability, and wave transmission.

Losada *et al.* (2005) used two numerical models to the study the effects of the breaking process on the functional design as well as on the velocity and turbulence distribution around and inside low-crested structures. Both numerical models originate from the Navier-Stokes equations: a two-dimensional model based on the Volume Averaged Reynolds Averaged Navier-Stokes (VARANS) equations (COBRAS), and a three-dimensional model based on a Large Eddy Simulation approach. Validation of the 2-D model for two crest widths was carried out under breaking conditions, and it was observed that the model performs well, showing good comparisons with the experimental records of velocity and free surface. For the 3-D model, the flow on the leeside of the breakwater is more chaotic and turbulent and therefore it was more difficult to achieve a good comparison in this area.

Johnson (2006) describes a simple method for modelling wave breaking over submerged structures. A dominant mechanism for dissipating wave energy over a submerged breakwater is depth-limited wave breaking. In the research, wave breaking was split into two parts: depth-limited breaking and steepness limited breaking. It was observed that a parabolic refraction/diffraction model with a modified description of wave breaking can be used to adequately predict wave transmission over submerged breakwaters. The parameter γ_2, governing the maximum wave height at incipient breaking, is found to vary mainly with the relative submergence depth (ratio of submergence depth at breakwater crest to significant wave height). It was also observed that the calculated transmission coefficients using the numerical model compared favourably with empirical expressions.

Lynett (2006) employed a slightly modified version of the eddy viscosity breaking model in a two-layer high-order Boussinesq-type model. Comparisons were made between this model and a one-layer highly nonlinear Boussinesq-type model. The over-shoaling observed in the one-layer model for regular waves is shown to be better captured in the two-layer model, which demonstrated closer agreement with experimental data for both monochromatic and cnoidal waves. For wave breaking over a step, it was observed that the two-layer model showed better accuracy for waves propagating behind the step.

Madsen *et al.* (2006) derived new equations for fully nonlinear and highly dispersive water waves interacting with a rapidly varying bathymetry, an extension of a recent high order Boussinesq-type formulation valid on a mildly sloping bottom. Numerical solutions were obtained and the model was verified on a wide range of test cases involving various rapidly varying bathymetries. Reflection from a plane shelf with steepness varying from 1/16 to 1.0 showed accurate results. Reflection and transmissions for a shelf of 0.5 steepness showed computed results in very good agreement. Reflection from two Gaussian trenches in shallow and intermediate waters again showed excellent agreement. Reflections from three trenches with sloped transitions with steepness 0.2, 0.5 and 1.0 were performed, with excellent agreement on the first two cases, however minor discrepancies were observed for the slope of 1.0.

Buccino & Calabrese (2007) present a prediction method for wave transmission based on an extremely simplified modelling of phenomena that rule wave energy transfer behind breakwaters, namely wave breaking, wave overtopping, and seepage through the body of the barrier. As was expected, in the proposed method the wave transmission process is dominated by wave breaking for submerged breakwaters, by mass flux through the barrier for structures with crests well above the Mean Water Level (MWL), and by wave runup and overtopping for barriers whose crest lies around the sea surface (slightly emerged or slightly submerged). The design equations arrived at seem to give reasonable predictions of transmission for a wide spectrum of engineering conditions, however the work is considered exclusively for 2-D structures, and 3-D situations should be handled with caution.

Kobayashi *et al.* (2007) developed a numerical model based on time-averaged continuity, momentum, and energy equations to predict the mean and standard deviation of the free surface elevation and horizontal fluid velocities above and inside a porous submerged breakwater. Four empirical parameters associated with irregular wave breaking, porous flow resistance and bottom friction were calibrated using experimental tests. The calibrated model was found to predict the cross-shore variations of the mean and standard deviation of the measured free surface elevation reasonably well. However the semi-empirical model will need to be extended in order to predict the vertical velocity variation.

2.4 Discussion

The review of existing literature with regards to the physical modelling of wave-breakwater interactions has shown that a significant amount of study has been undertaken, especially for the case of low-crested structures which have crests at or near to the mean water surface (Van der Meer & Daemen (1994), d'Angremond *et al.* (1996), Calabrese *et al.* (2002), Van der Meer *et al.* (2003), Wang *et al.* (2005), Burcharth *et al.* (2006)). However, research into submerged structures specifically is much sparser (Dean *et al.* (1997), Lomonaco *et al.* (2003), Cox & Tajzichchi (2005), Pinto & Neves (2005)). Most experimental work is 2-D, undertaken in narrow wave flumes often using a uniformly-shaped structure (Brunone & Tomasicchio (1997), Seabrook & Hall (1998), Calabrese *et al.* (2002), Cox & Tajzichchi (2005), Pinto & Neves (2005)). Although some experiments have been conducted in larger wave basins, they generally use much smaller scales such that the measured wave heights are of only a few centimetres (Seabrook & Hall (1998), Lamberti *et al.* (2003), Van der Meer *et al.* (2003), Wang *et al.* (2005), Zanuttigh & Lamberti (2006)).

With regards to the numerical modelling of wave-breakwater interaction, much of the current research for low-crested or submerged structures has dealt with models that can accurately predict the exact wave transformations for each particular wave versus matching statistics of an entire wave train from experimental observations. Quite a few of these models proved quite capable of this task, however they are somewhat limited since they are essentially primarily built for 2-D setting (in a long, narrow flume) (Bosboom *et al.* (1997), Kennedy *et al.* (2000), Lee *et al.* (2001), Losada *et al.* (2003), Lynett (2006)). In general wave heights simulated with these models are generally quite small since they are making direct comparisons to wave flume or wave basin experiments (Karambas & Koutitas (1992), Losada *et al.* (1996b), Kaihatu & Kirby (1998), Huang & Dong (1999), Hur & Mizutani (2003), Figueres & Medina (2004), Kobayashi *et al.* (2007)). Numerical models also predominantly deal with less aggressive slopes since their formulae are only capable of handling mild slopes. It is quite difficult to develop a steady reliable model that can deal with steep bottom slopes and nonlinear wave transformation.

Few large-scale 3-D physical model studies of wave interaction with submerged structures are reported in literature (Dean *et al.* (1997), Seabrook & Hall (1998)). Also, the author could find no cases dealing with submerged structures of longitudinally varying shape. As most numerical modelling deals with transformations of individual waves, there appears to be far less research into the longer term wave field development over the course of an entire storm.

As outlined in Section 1.2, this study attempts to fill some of these gaps in current research.

3 Project Introduction

3.1 Preamble

The physical experiments described in this report were conducted as part of an applied research study performed by the National Research Council (NRC) Canadian Hydraulics Centre for COWI, a large international engineering firm. The author of this thesis was a member of the team responsible for conducting the research project. Due to the confidential nature of this study, details of the project and the full study results cannot be presented and discussed herein. However, permission was obtained to analyse some of the experimental data as part of the academic research project the author undertook as a student at the University of Ottawa.

3.2 Project Description

The Canadian Hydraulics Centre was commissioned to perform a physical model study to investigate and verify the stability of the armour layer protecting a section of an immersed tunnel, part of an 8.2 kilometre motorway connecting several islands to the mainland.

The immersed tunnel is composed of 18 steel elements, each segment having general dimensions of 180 m long by 26.5 m wide by 9.75 m tall. The majority of the tunnel elements are to be buried below the seabed; however, several of the elements will be positioned at or above grade. These exposed elements need to be covered by a protection material to prevent scour and prevent movements due to hydrodynamic forces. Figure 3.1 (Hauge *et al.*, 2004) presents the plan and elevation between stations (Sta.) 5+000 and 5+500, the red box indicating the actual testing section from stations 5+100 at the left to 5+460 at the right. Figure 3.2 (Hauge *et al.*, 2004) depicts a typical tunnel element cross-section.

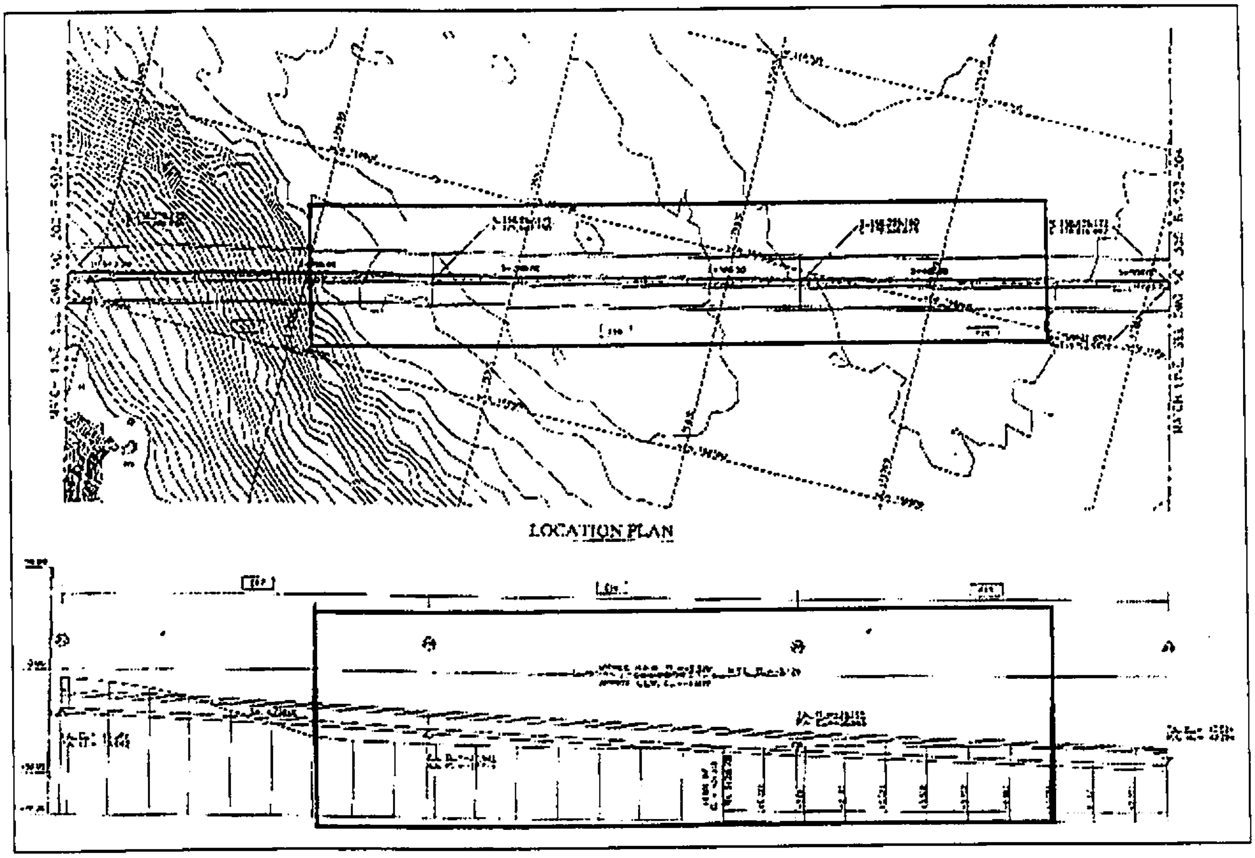

Figure 3.1 – Location plan and profile drawing of the immersed tunnel (Hauge *et al.*, 2004)

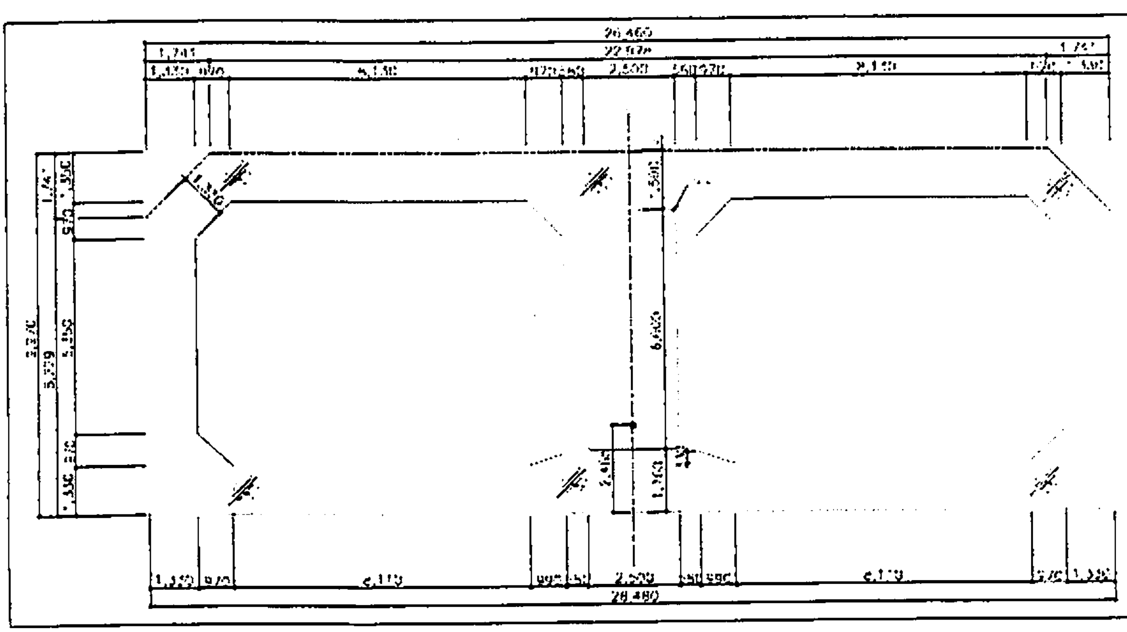

Figure 3.2 - Typical tunnel steel element cross-section (Hauge *et al.*, 2004)

3.3 Site Conditions

The site in question is subjected to strong tidal currents and severe wave action generated by typhoons. The local wave climate is strongly governed by waves incident from the SSW, S, and SSE directions. To illustrate these extreme conditions, Figure 3.3 shows the numerical simulation of the SSE waves heights with a 100-year return period (from Hauge *et al.*, 2004). The red box indicates the specific study area.

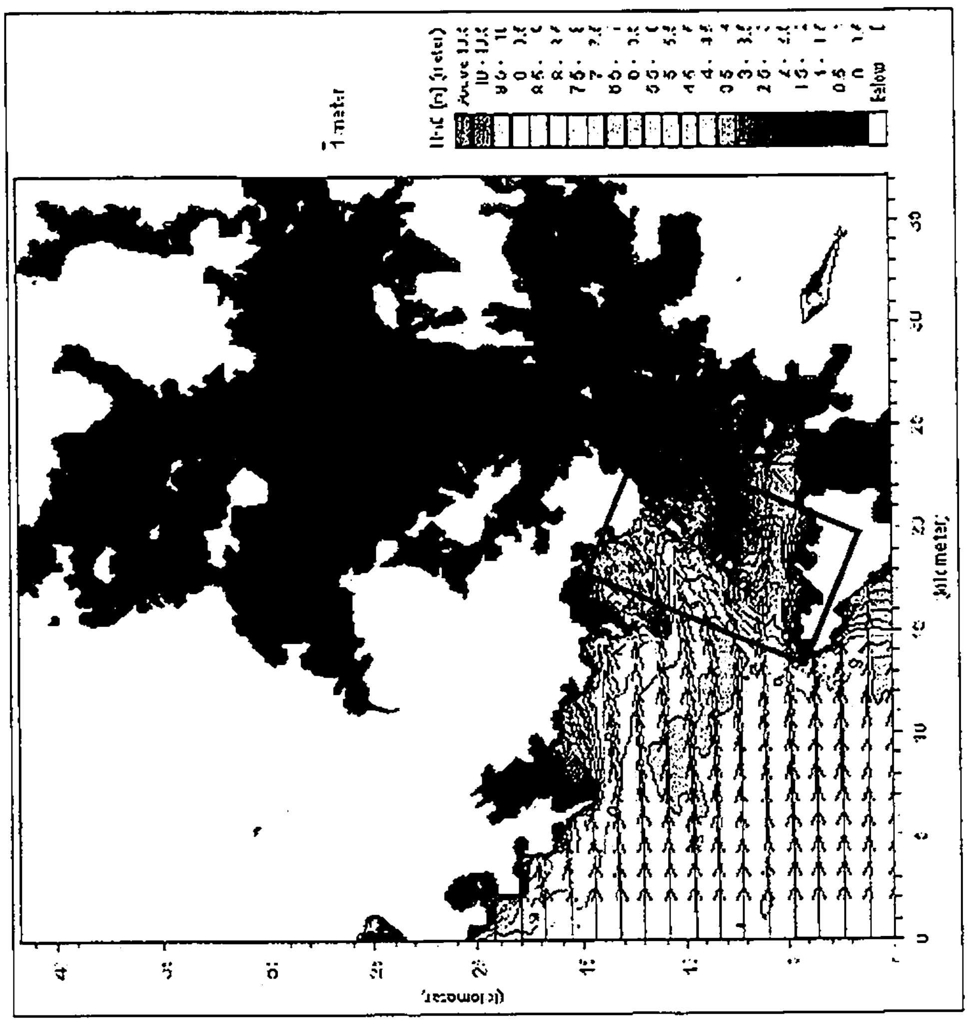

Figure 3.3 - Numerical simulation of SSE waves (Hauge *et al.*, 2004)

The design net sea conditions that were simulated in the physical model study are summarised in Table 3.1. More information on the test programs used for the physical experiments and numerical simulations can be found in Sections 4.10 and 5.7, respectively.

Table 3.1 - Design testing conditions

Condition	H_{m0} (m)	T_p (s)	U_c (m/s)	WL (m)
1:100 year	4.5	16.2	1.2	−1.55
1:10,000 year	5.0	20.1	1.2	−1.72
Overload (design + 20%)	6.0	20.1	1.2	−1.72

3.4 Units of Measurement

It should be noted that throughout this thesis, all model dimensions and measured quantities will be expressed in their equivalent prototype units, unless noted otherwise.

4 Physical Modelling

4.1 Introduction

Physical modelling studies play an important role in coastal engineering. Qualitatively, physical models are close simulations of the prototype. Also, viewing a physical model in operation adds to the physical understanding of the problem and physical models should be used, even if not all details of the relevant processes are clearly understood (Kamphuis, 2000). The behaviour of physical models is quite similar to prototype conditions; however certain aspects such as current circulations, refraction, and diffraction are more obvious in the model. Systems can be tested to observe their responses under extreme conditions and over long durations which can only be estimated for the prototype. Also, changes made by trial and error are cheap and easy to do with physical models which may be costly, if not impossible, in prototypes. Finally, complex nonlinear physical processes can be reproduced in a well-designed physical model.

The first phase of this research was the undertaking of a large-scale, three-dimensional physical modelling study. Section 4 provides a detailed account of the work.

4.2 CHC Coastal Basin

The Canadian Hydraulics Centre is home to a world-class coastal and hydraulics engineering laboratory, located in Ottawa as part of the National Research Council of Canada. The stability tests of the armour protection along a 360 m section of the immersed tunnel were performed in CHC's Coastal Wave Basin (CWB). This basin is 63 m long by 14 m wide and a water depth of 1.5 m deep. The facility is equipped with a powerful computer-controlled multi-mode wave machine capable of producing irregular long-crested waves with significant wave heights up to approximately 0.35 m (refer to Figure 4.1).

Specially designed wave generation software allows for the simulation of natural sea states. They can be defined by parametric or measured wave spectra, or measured wave records. The basin is equipped with large and efficient wave absorber modules in order to dissipate virtually all of the incident wave energy and prevent any unwanted reflections from occurring.

The coastal basin is typically used for projects where reproduction of near-shore bathymetry and coastal structures is required, and is easily accessed by heavy machinery used for model construction. The basin is also spanned by a mobile gantry crane and a mobile service bridge (CHC, 2007).

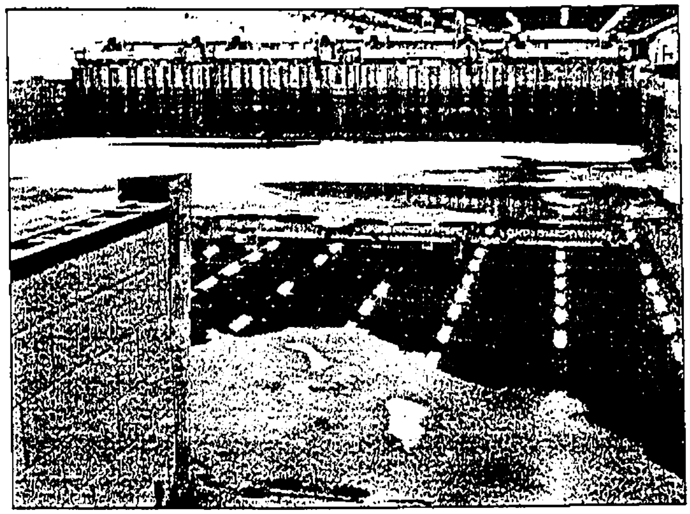

Figure 4.1 - CHC's Coastal Basin wave generator

4.3 Model Layout and Design

Selection of a suitable geometric scale is an important factor in the design of a physical model, even more so when a mobile bed is involved. Although many factors play in the decision, the key is establishing a middle ground between two important conflicting requirements:

- Minimizing scale effects, which requires as large a model scale as possible, and
- Minimizing boundary effects, which requires a smaller model scale to model as large an area as possible.

The physical model studies reported herein were conducted at an undistorted length scale of 1 to 50. At this size, a compromise is reached between the minimization of scale and boundary effects. All lengths in the model (horizontal and vertical) are 50 times less than the actual lengths at full scale.

The general layout of the model in the basin is shown in Figure 4.2 and a detailed 3-D close-up view of the tunnel is shown in Figure 4.3 (Lomonaco & Cornett, 2006). A 7.2 m wide central test channel was created by constructing two parallel solid vertical walls, leaving two 3.4 m wide side-channels on either side. A rigid model bathymetry was poured within the central channel as discussed in Section 4.7.1. This bathymetry included a 0.32 m deep by 6 m long trench which contained the fine sand used in the model to simulate the seabed around the tunnel corridor.

A number of undisturbed flow tests were performed before installing the model tunnel (simulating the natural conditions at the site) to calibrate and verify the waves and currents at the tunnel location.

To generate the required current at the test site, four variable speed electric thrusters were installed, two in each of the side channels. The current within the central test channel could be regulated by adjusting the speed of the thrusters. Flow guides transparent to the incident waves were placed up-wave and a small wave absorber module was placed down-wave of the tunnel to encourage straighter current streamlines along the test channel and to produce a consistent velocity distribution along the tunnel axis.

After completing the flow calibration tests, the proposed dredging works were replicated in the mobile sand bed while a scale model of the tunnel was fabricated and installed to simulate the prototype conditions. Model scale backfill, armour stone and scour protection was then placed in an accurate representation of the structure. Strict surveying methods and templates were used to ensure the precision of this delicate process.

In Figure 4.4 to Figure 4.9, the cross-sections of the immersed tunnel and armour protection are shown for selected stations. These sections were used to create the fibreboard templates, which were used as a guide for the accurate reproduction of the structure, described further in Section 4.7.2.

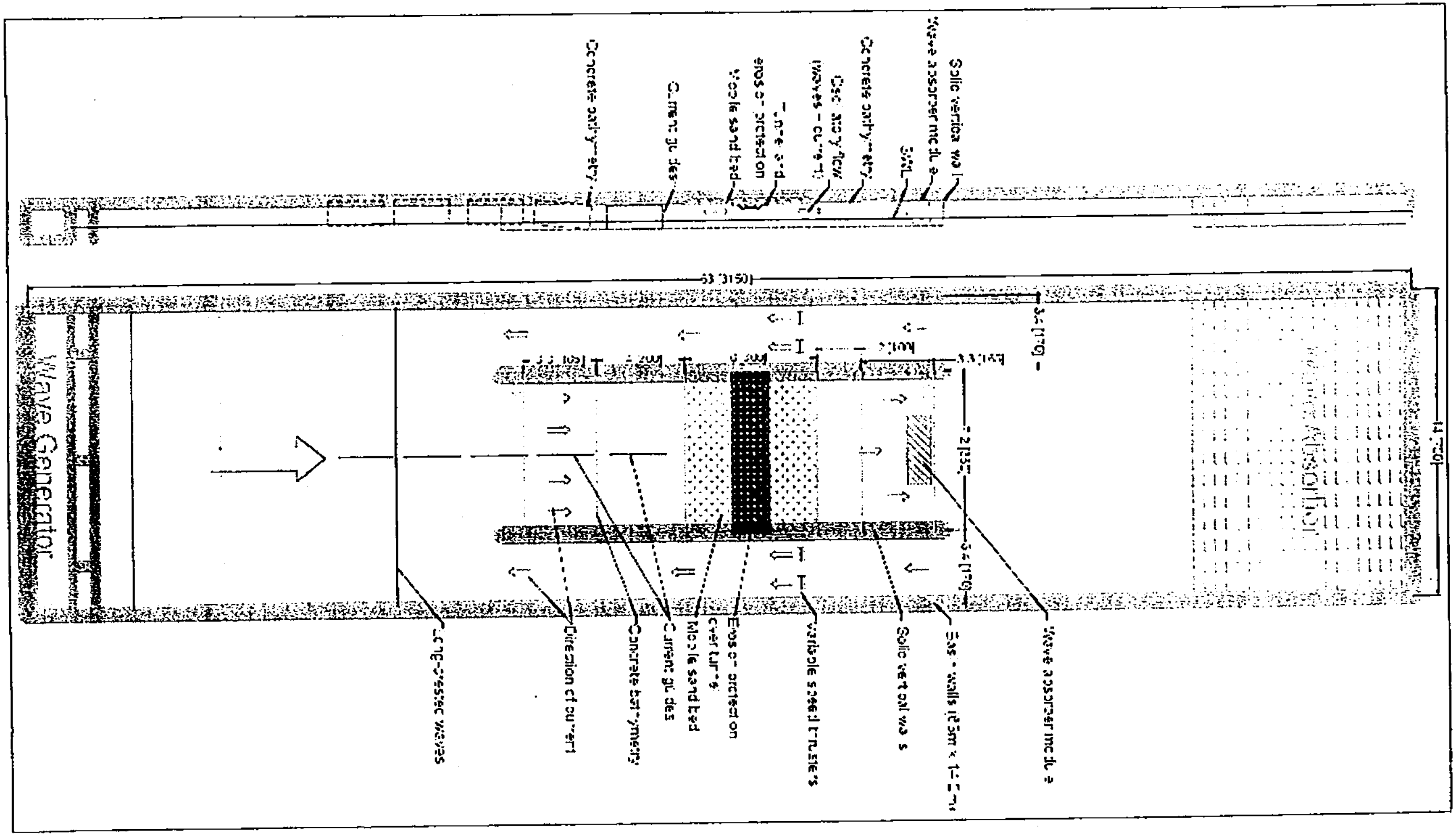

Figure 4.2 - Basic layout of the physical model in the Coastal Wave Basin
(Lomonaco & Cornett, 2006)

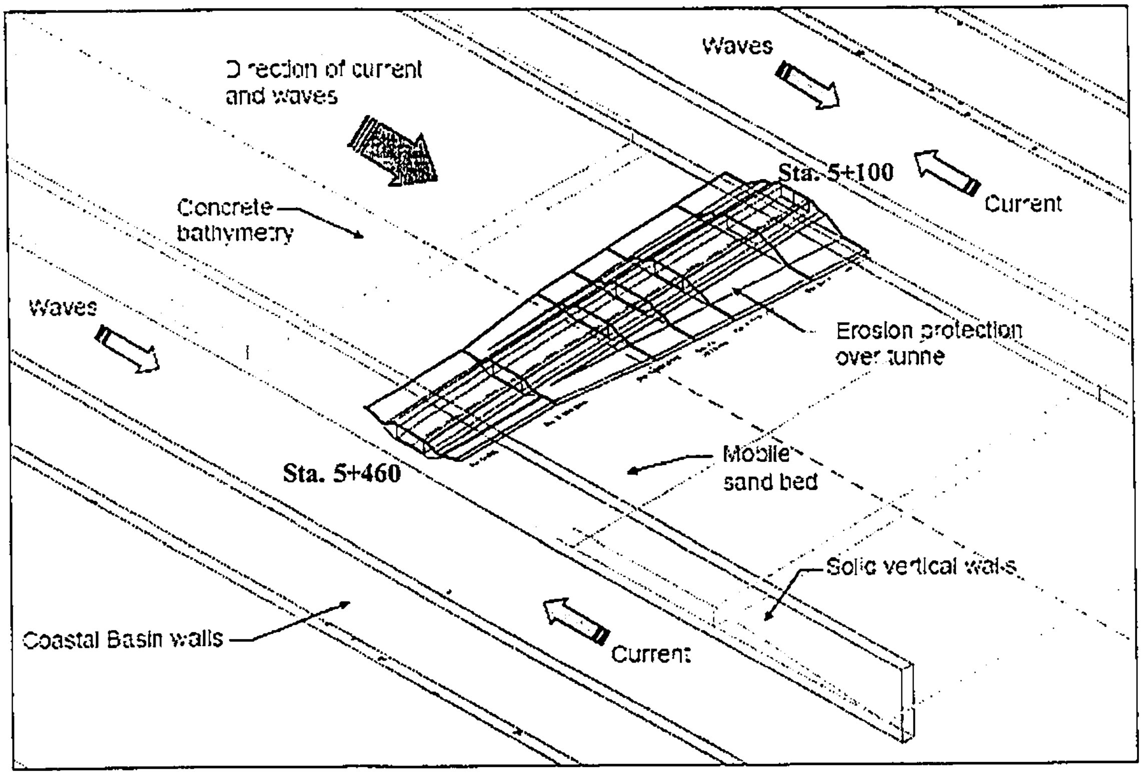

Figure 4.3 - Detailed 3-D close-up of the tunnel model (Lomonaco & Cornett, 2006)

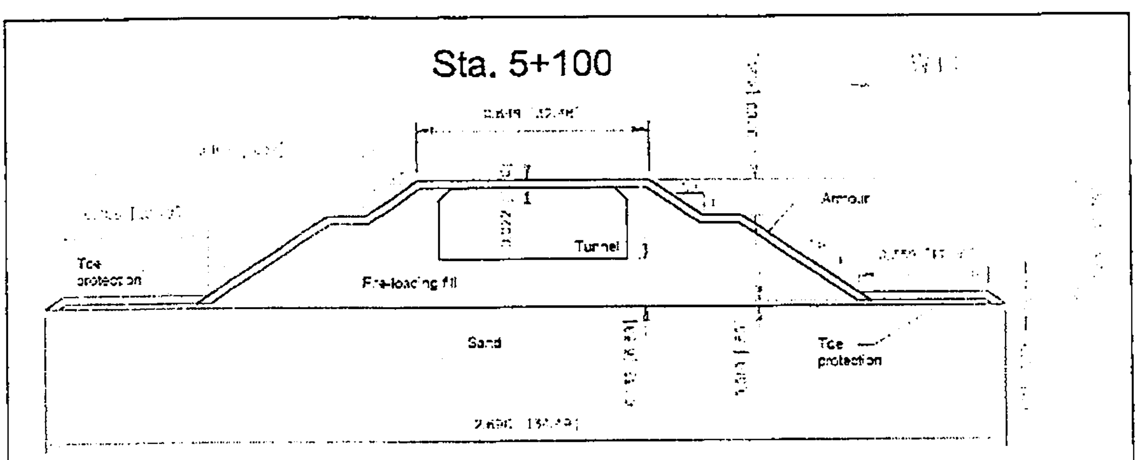

Figure 4.4 - Sta. 5+100, defined at the West limit of the model study

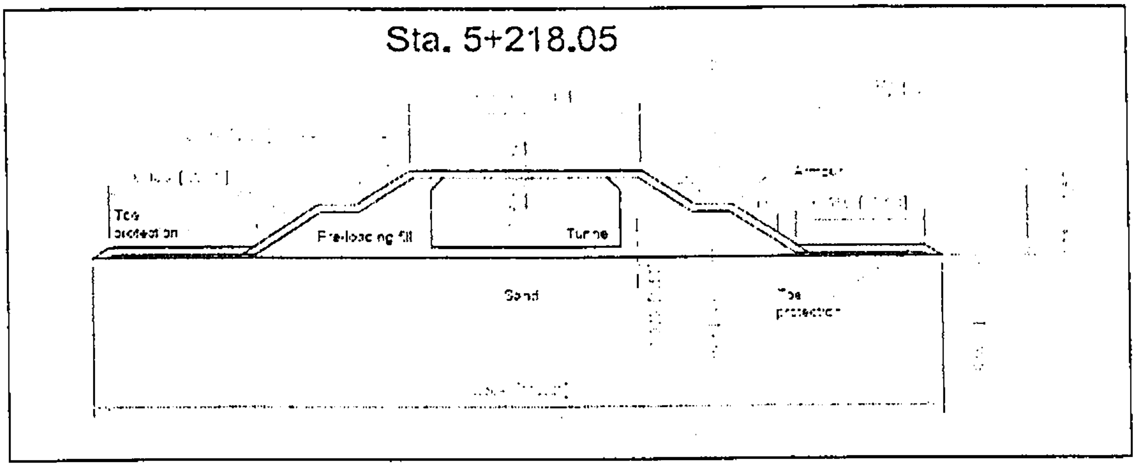

Figure 4.5 - Sta. 5+218.05, defined where the lower elevation of the gravel bed is at −34 m

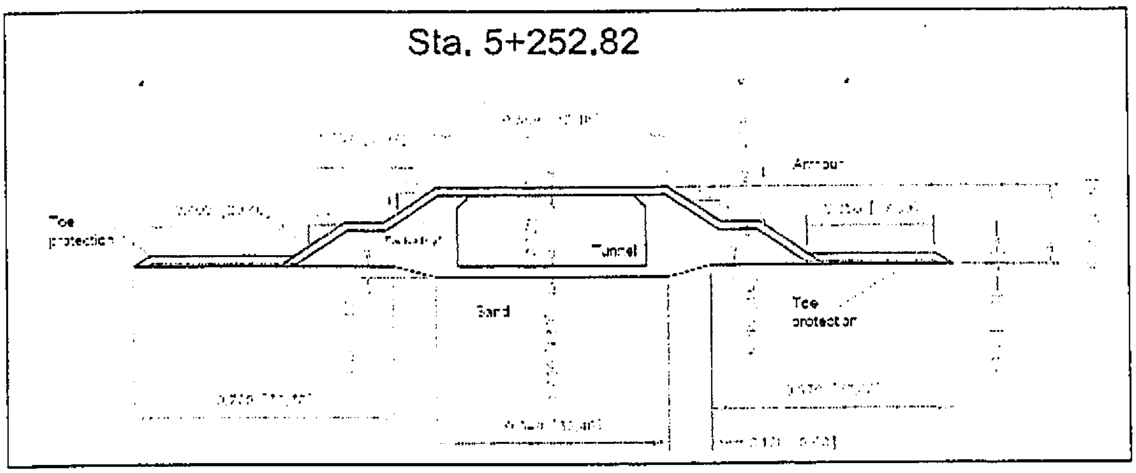

Figure 4.6 - Sta. 5+252.82, defined where the lower tunnel elevation is at bed level (−34 m)

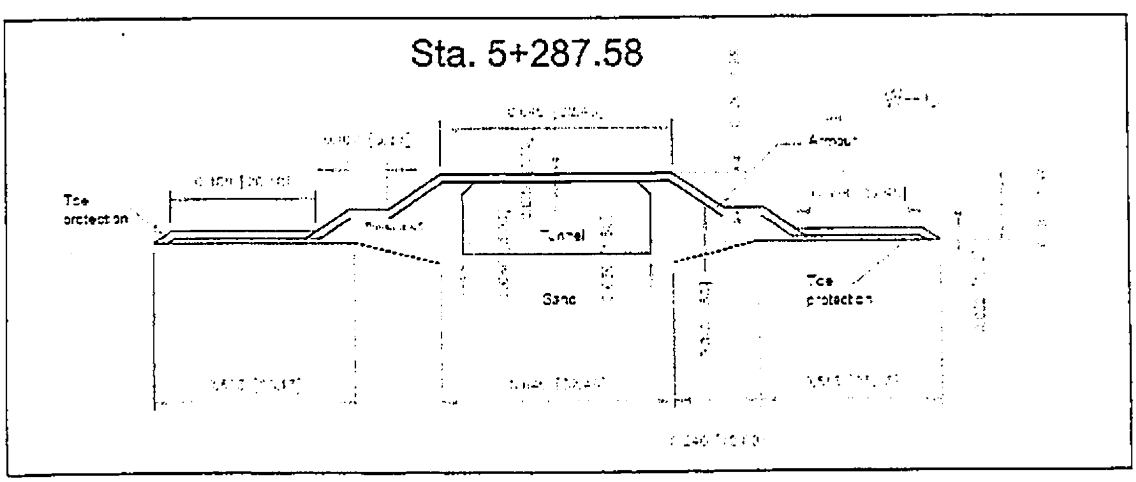

Figure 4.7 - Sta. 5+287.58, defined where the lower elevation of the gravel bed is at −37 m

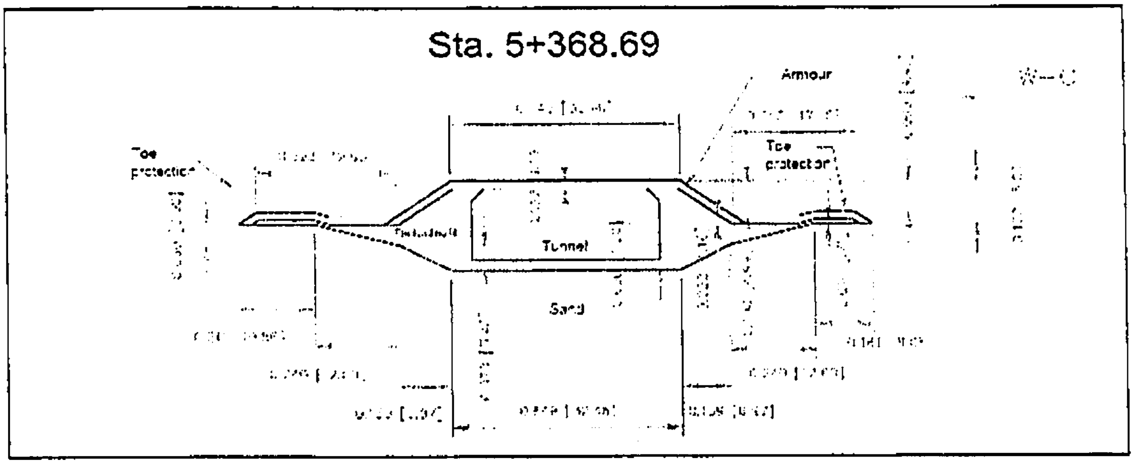

Figure 4.8 - Sta. 5+268.69, defined where the mid-height of the tunnel is at bed level (−34 m)

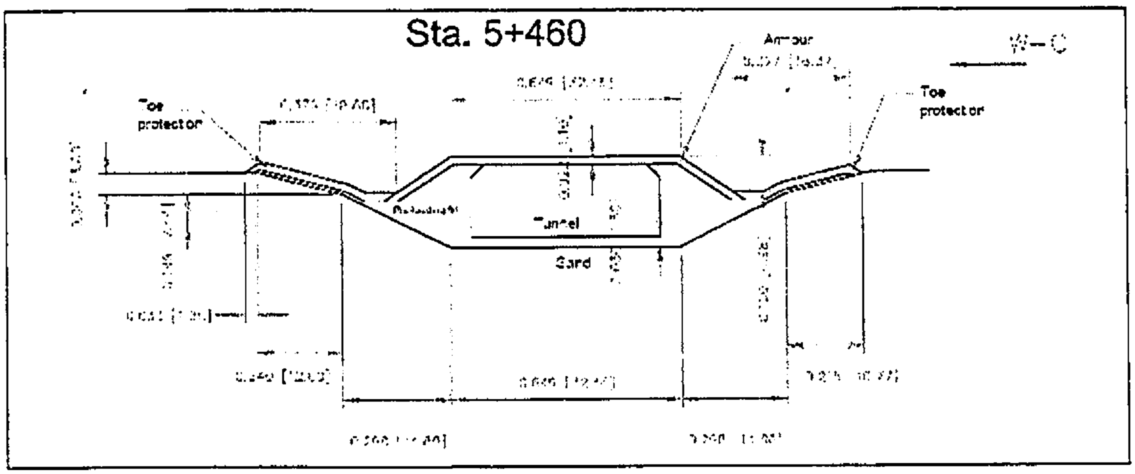

Figure 4.9 - Sta. 5+460, defined at the East limit of the model study

4.4 Scaling Relationships

Most aspects of the physical model, with the exception of the armour stone and the mobile-bed sediment (see Section 4.5.2 and Section 4.6 respectively), were designed using Froude scaling, which assumes that gravitational and inertial forces are dominant in comparison to viscous forces. Froude scaling provides a set of laws dictating the proper relationship between quantities measured at model scale and prototype scale. These scaling laws are derived from similarity of the Froude number, which represents the ratio between gravitational and inertial forces in the model and at full scale.

Setting the scale factor of the Froude number (λ_{Fr}) equal to unity makes certain that the relative inertial and gravitational forces involved are the same on both scales. The similarity of the

Froude number, combined with geometric similitude, ensures that the model provides a good simulation of the wave propagation and wave-structure interactions that occur in nature.

Table 4.1 presents the scale factors for selected quantities used in the model. Note the scale factor for water density is approximately 1.030 because fresh water was used in the model in lieu of seawater.

Table 4.1 - Scale factors

Quantity	Scale Factor	Typical value at full scale	Corresponding model value
Froude Number	$\lambda_{Fr} = \dfrac{\lambda_v}{\sqrt{\lambda_g \lambda_l}} = 1.0$	1.0	1.0
Length (x,y,z)	$\lambda_l = 50.0$	10 m	0.2 m
Time (time, period)	$\lambda_t = \sqrt{\lambda_l} = 7.071$	16 s	2.263 s
Velocity (length/time)	$\lambda_v = \dfrac{\lambda_l}{\lambda_t} = \sqrt{\lambda_l} = 7.071$	1.0 m/s	0.141 m/s
Acceleration (length/time^2)	$\lambda_v = \dfrac{\lambda_l}{\lambda_t^2} = 1.0$	9.81 m/s^s	9.81 m/s^s
Density of water	$\lambda_{\rho w} = 1.030$	1,030 kg/m^3	1,000 kg/m^3
Mass	$\lambda_M = \lambda_l^3 \lambda_\rho = 125{,}000 \lambda_\rho$	20 kg	0.16 kg

4.5 Armour Protection

4.5.1 Design Rock Protection Properties

Figure 4.10 (Hauge *et al.*, 2004) shows a typical cross-section of the protection works in the area of study.

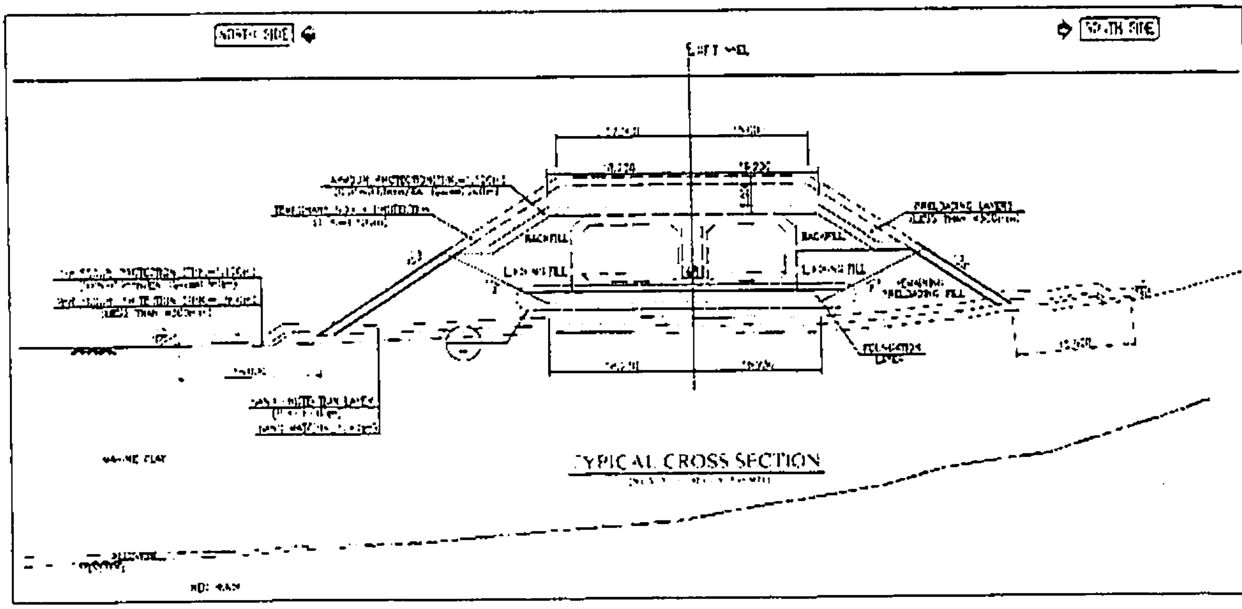

Figure 4.10 - Typical tunnel protection cross-section (Hauge *et al.*, 2004)

The different materials can be classified as follows:

- **Preloading Fill**: The tunnel elements in the study area are to be placed on a permanent embankment constructed of compacted fill material. The gradation of this material is shown in Figure 4.11.
- **Gravel Bed**: Underneath the tunnel, a 1.5 m thick layer of non-compacted gravel will be placed. The gradation of this material is shown in Figure 4.12.
- **Locking Fill**: The locking fill will laterally support the tunnel. It shall be non-liquefiable coarse material, dense and well-graded. The gradation of this material is shown in Figure 4.13.
- **Backfill**: The ordinary backing fill is placed along the tunnel on top of the locking fill. The gradation of this material is shown in Figure 4.14.
- **Armour Protection**: A protective cover 1.1 m thick is placed atop the backfill material to avoid erosion from waves and currents. The armour rock also serves to protect the tunnel structure against ship impacts and from falling or crawling anchors. The armour protection layer on the top of the tunnel also provides an additional weight against the uplift forces from waves. The nominal diameter of the armour is $D_{n,50} = 0.2$ m, with a particle range of $M_{10} = 10$ kg to $M_{90} = 50$ kg, and a mean particle mass of $M_{50} = 20$ kg. The 1.1m thick armour layer is equivalent to 5 to 6 layers of stones.

- **Scour Protection**: The scour protection, or toe protection, extends on both sides of the protection embankment, 15.5 m to the South and 18 m to the North. It is formed by two layers of rock, the first scour protection (exposed) is 1.1 m thick and made of 0.05 to 0.2 tonne rock ($D_{n,50}$ = 0.35 m), and is equivalent to 3 layers of stones. Underneath is found the second scour protection, 0.5 m thick and made of rock with diameters less than 0.3 m.

For practical reasons, and since the overall stability of the tunnel protection remains unchanged, only one type of rock material was used for the embankment fill (the preloading fill) during the construction of the physical model. This will be explained in further detail in Section 4.7.7.

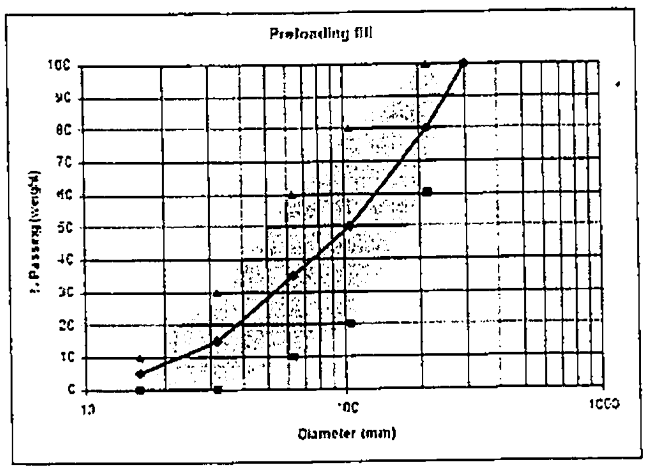

Figure 4.11 – Design gradation of preloading fill (with confidence intervals)

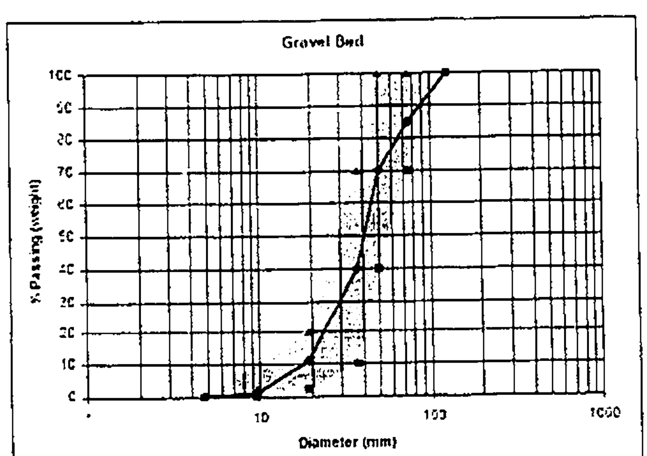

Figure 4.12 – Design gradation of gravel bed (with confidence intervals)

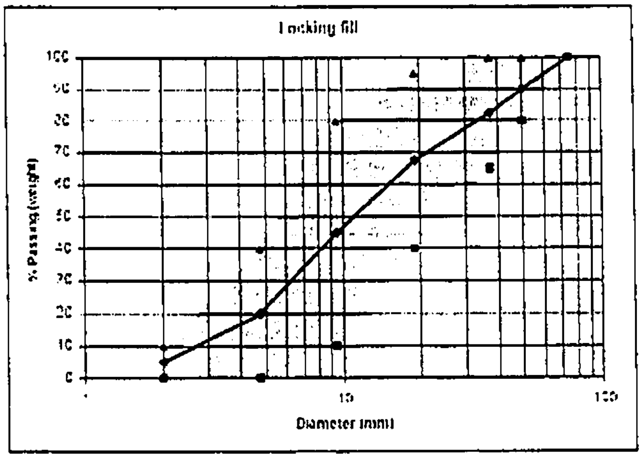

Figure 4.13 – Design gradation of locking fill (with confidence intervals)

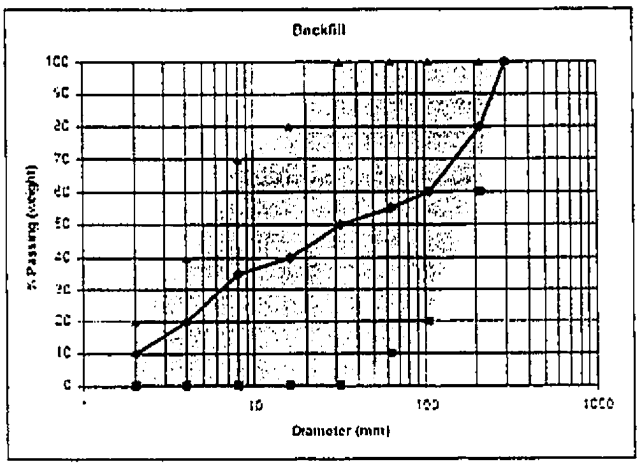

Figure 4.14 – Design gradation of backfill material (with confidence intervals)

4.5.2 Scaling of Rock Weight

The model scale factor of the armour stone needed to be carefully selected to ensure that the submerged stability of the stone was correctly reproduced. This is required in cases where the densities of the model stone and prototype stone are different, and where freshwater is used in the model to represent seawater (such as this case).

The Hudson formula is a widely accepted equation for predicting the stable weight of submerged armour material under wave attack. By scaling armour weights using this formula, it will yield a model stone or armour unit having the same stability as the prototype state. The Hudson formula is as follows:

$$W = \frac{w_r H^3}{K_D (S_r - 1)^3 \cot\theta} \tag{4-1}$$

where W is the weight of the armour material (N), w_r is the unit weight of the armour material (N/m³), H is the design wave height (m), θ is the slope of the armour material and K_D is the stability coefficient of the armour material. S_r is the specific gravity of the armour material and can be written as $S_r = w_r/w_w$, where w_w is the unit weight of water (N/m³). To scale for physical modelling purposes, the following relationship is used:

$$\lambda_W = \frac{\lambda_{w_r} \lambda_{H^3}}{\lambda_{K_D} \lambda_{(S_r-1)^3} \lambda_{\cot\theta}} \tag{4-2}$$

where λ is used to represent the ratio of prototype to model values of a quantity. Assuming that the model stone has the same approximate shape ($\therefore \lambda_{K_D} = 1$) and since the model is undistorted ($\therefore \lambda_{\cot\theta} = 1$), the above relationship is reduced as follows:

$$\lambda_W = \frac{\lambda_{w_r} \lambda_{H^3}}{\lambda_{(S_r-1)^3}} \tag{4-3}$$

The rock used in the model was chip stone having a unit weight of approximately 2650 kg/m³. Without any information of the locally available stone, it was assumed that the stone designated as appropriate for the construction of the protection would have the same density. Thus, the scale of the unit weight of rock becomes:

$$\lambda_{w_r} = \frac{2650}{2650} = 1.000 \tag{4-4}$$

Assuming a seawater density of 1030 kg/m³, the scale of the specific gravity term is:

$$\lambda_{(S_r-1)} = \lambda_{\left(\frac{w_r}{w_w}-1\right)} = \frac{\left(\frac{2650}{1030} - 1\right)}{\left(\frac{2650}{1000} - 1\right)} = 0.953 \tag{4-5}$$

The scale of the wave height is the model length scale (i.e. $\lambda_H = 50$), therefore the weight scale for the armour stone is:

$$\lambda_W = \frac{(1.000)(50)^3}{(0.953)^3} = 144{,}421 \approx 52.47^3 \tag{4-6}$$

In order to account for the freshwater used in the model, the weight of the stone used in the model should therefore be roughly 15.5% lighter than that given by standard Froude scaling (according to standard Froude scaling, the scale factor for rock weight would be $50^3 = 125{,}000$).

4.6 Mobile-Bed Material

Hughes (1993) provides a comprehensive review of the scaling requirements for mobile-bed physical models that are designed to investigate the wave-driven sediment transport processes. It is the belief of many researchers that using sand as the model sediment is the preferred approach for modelling coastal sediment transport.

Dean (1985) proposed three requirements for physical modelling of sedimentary processes:

- The model should be undistorted,
- Froude scaling laws should be applied to model both hydraulic and the sedimentary processes. In particular, the settling velocity of the sediment should be scaled according to the square root of the length scale, and,
- The model should be of sufficient size so that viscous and surface tension effects are negligible.

Fine silica sand with a median diameter of approximately 0.14 mm was used in the model to represent the native sediments. The particle size distribution of the model sand is shown in Figure 4.15 and images of the sand are shown in Figure 4.16.

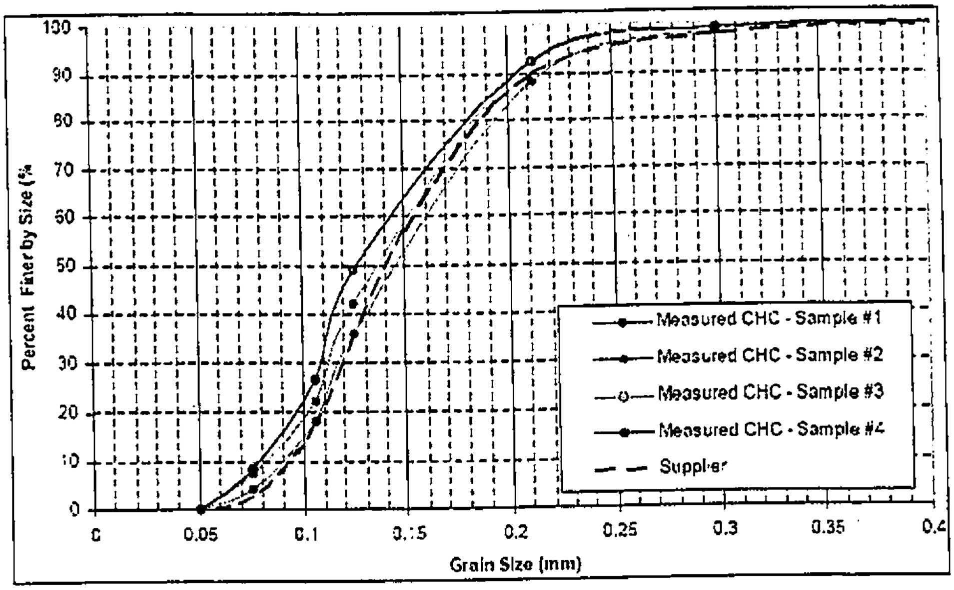

Figure 4.15 - Gradation of fine silica sand

Figure 4.16 - Images of the fine silica sand

According to the fall velocity relationships developed by Van Rijn (1993), the 0.14 mm model sand has a fall velocity of roughly 0.014 m/s. Applying the Froude scaling law for velocity, this material is representative of a prototype sediment with a fall velocity of 0.099 m/s, or a median grain diameter of approximately 0.76 mm. In other words, the model sand has a fall velocity equivalent to 0.76 mm sand at full scale.

The actual prototype seabed is made of marine clay. Because of this, the mobility and behaviour of the native sediments along the tunnel corridor cannot be accurately simulated in a physical model, and can only be represented in a qualitative manner.

It is reasonable to expect the model to exhibit the following behaviour in comparison with the prototype:

- The model will underestimate the amount of sediment in suspension and the rate and extent of suspended load transport.
- The bed forms in the model will be over-sized, resulting in an exaggeration of the bottom roughness.
- The time scale for sedimentary processes observed in the model may differ from the Froude time scale.

Regardless, the mobile-bed material allows the reproduction of the construction sequence of the tunnel, in particular where the tunnel is partially buried into the seabed.

4.7 Model Construction

This section describes the overall construction of the physical model in chronological order. A number of pictures are included to illustrate the process.

4.7.1 Solid Vertical Walls

Two parallel temporary solid vertical walls were erected using non-mortared masonry blocks to form a central channel in the basin. The walls, each 20 m long and 1.15 m high, were fastened to the basin floor using anchor rods that hold the entire length of wall by capping it with welded steel angles and brackets. The lateral stability of the walls was reinforced using a series of 45-degree braces. This lateral support was necessary since the waves in the central channel were often out of phase with those in the outer channels, and exerted lateral forces on the walls, especially for the bigger waves. This phase difference was caused by the different propagation depths and current flow directions in the central and lateral channels.

The walls were separated by 7.2 m, corresponding to 360 m in prototype scale, so that two complete tunnel elements could be tested in the central channel, with the current generation taking place in the side channels. Figure 4.17 presents a series of images recorded during construction of the walls.

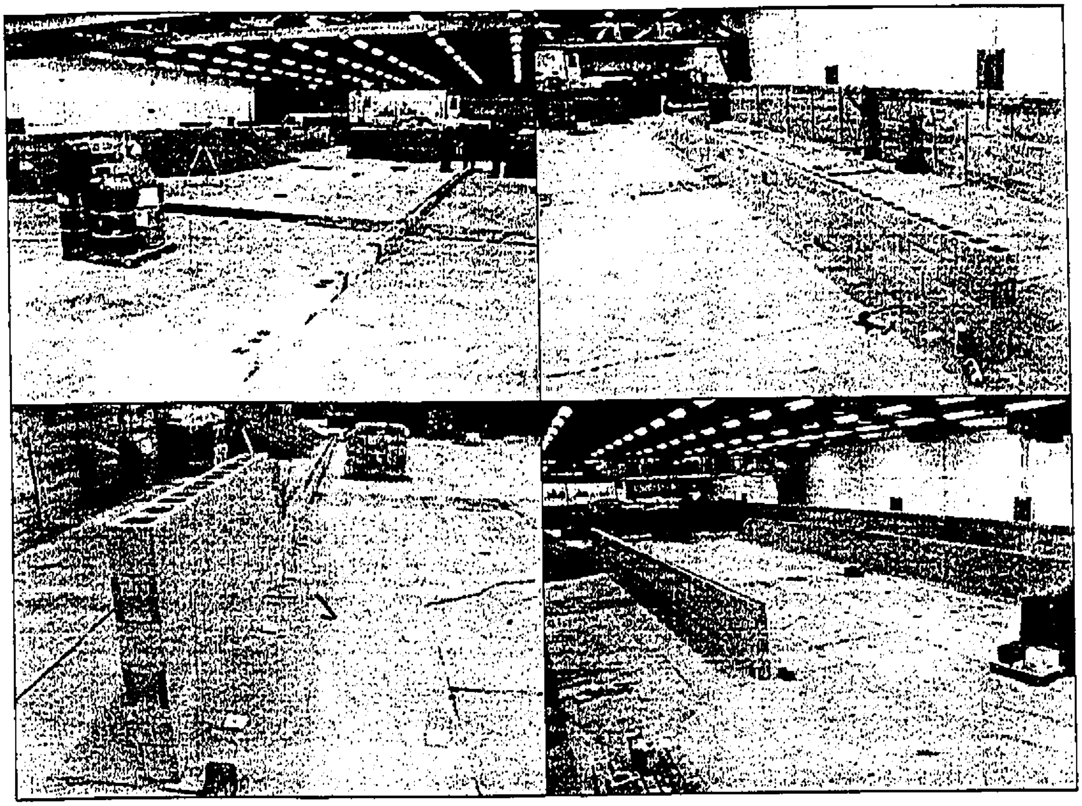

Figure 4.17 - Construction of the masonry block walls

4.7.2 Bathymetry

The model bathymetry was constructed using a framework of fibreboard templates placed at 1 m intervals. The templates themselves were cut with a ±2 mm tolerance, and were placed on a grid of wooden pads that were levelled to within ±2 mm using precise surveying techniques as illustrated in Figure 4.18. Once erected, the templates were backfilled with fine gravel and compacted using a vibrating plate compactor to approximately 5 cm below the top edge of the fibreboard templates, demonstrated in Figure 4.19 and Figure 4.20.

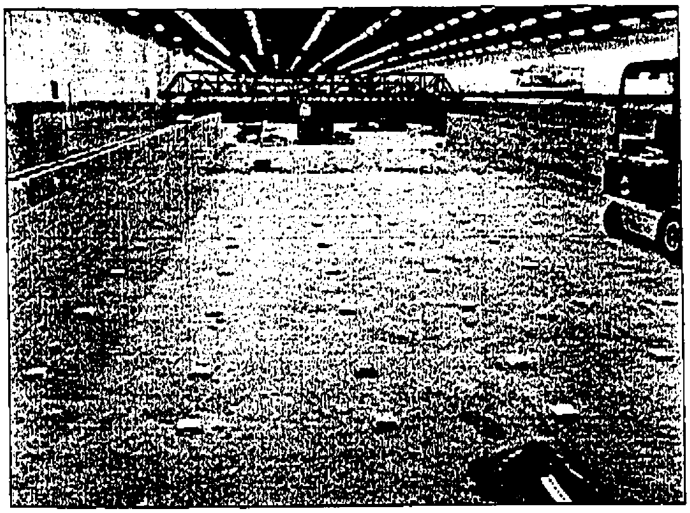

Figure 4.18 - Grid of pads levelled by precise surveying

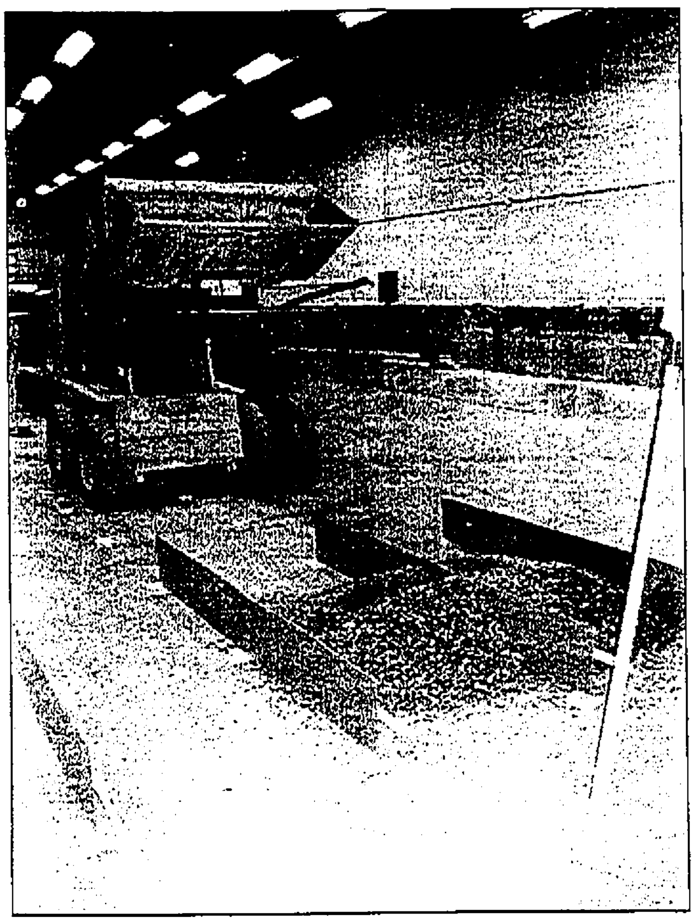

Figure 4.19 - Fibreboard template network backfilled with gravel

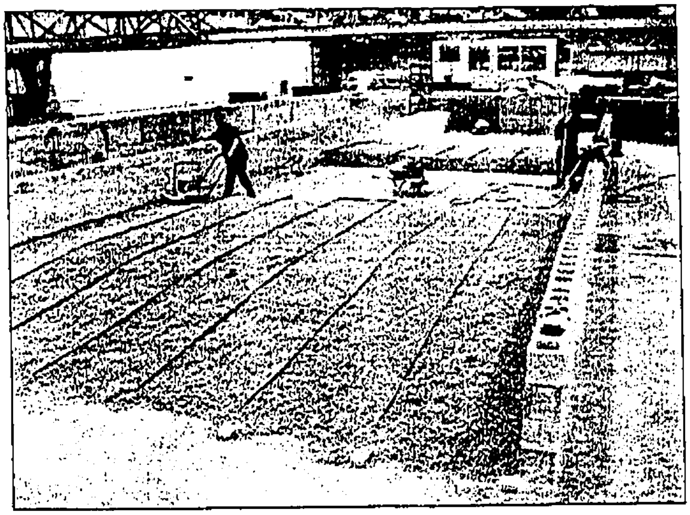

Figure 4.20 - Gravel compacted to 5 cm below top of templates

The remaining 5cm gap was filled with a skin of concrete that was screeded and later power-trowelled to match the elevation defined by the templates as seen in Figure 4.21. The resulting bathymetry is generally accurate to within ±5 mm, which is equivalent to ±25 cm at prototype scale.

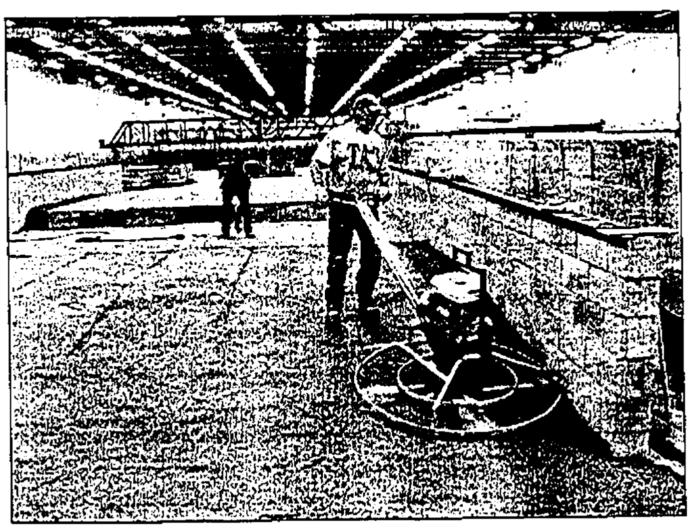

Figure 4.21 - Concrete skin finishing

The flat portion of the bathymetry represented the sea bottom with a reference elevation of −34 m. The sand pit and testing section are cast into the bathymetry, while two smooth 1:10 transition slopes were built on the outer sides to allow the waves and current approach smoothly to the structure, depicted in Figure 4.22.

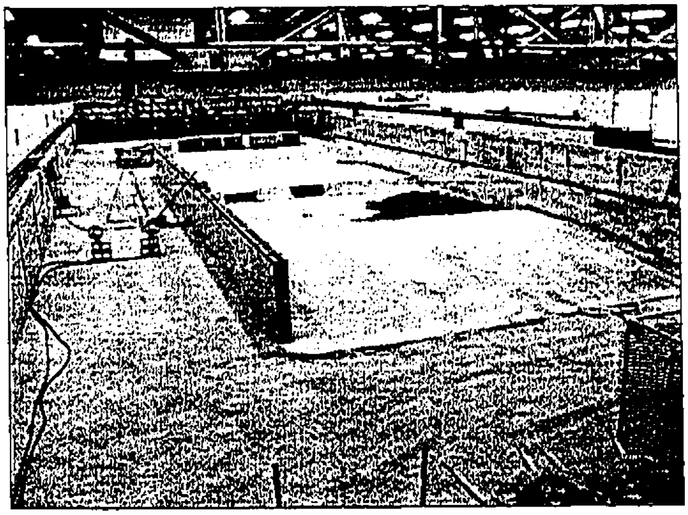

Figure 4.22 - Overview of constructed bathymetry

4.7.3 Sand Pit

A 6 m long, 7.2 m wide and approximately 33 cm deep trench was left open in the concrete bathymetry to contain the fine sand used to simulate the seabed along the tunnel corridor. The western portion of the trench (where the structure is highest above the seabed) was partially filled with gravel first, in order to reduce the required volume of sand. This gravel was kept separated from the sand by use of a geotextile. The trench was filled with the fine sand discussed previously ($D_{50} \sim 0.14$ mm) up to the −34 m level to match the concrete bathymetry. Figure 4.23 shows the construction of the sand pit.

During the physical modelling test series, small bedforms were observed throughout the sand pit due to the action of the waves and current. No significant erosion was observed in the sand bed along the toe of the structure, suggesting the scour protection was adequately designed. Minor deposition of sand was observed along the toe. This erosion and deposition would not have had any noticeable influence on the hydrodynamics highlighted in this study.

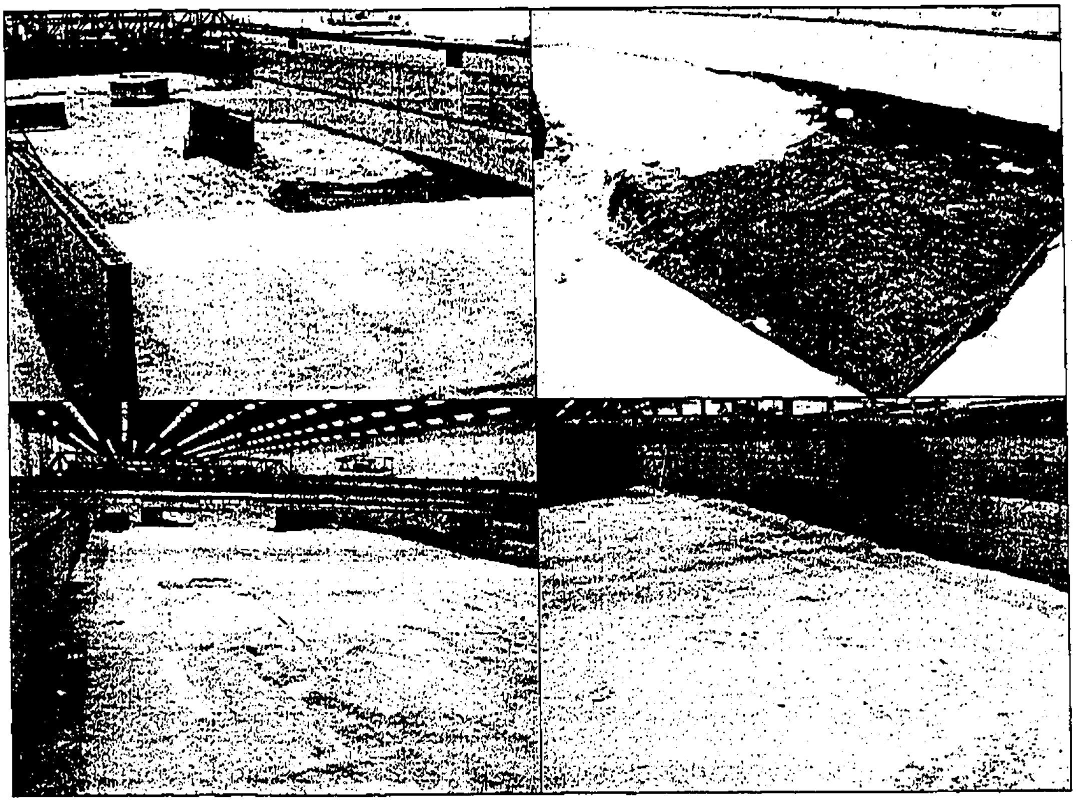

Figure 4.23 – Mobile seabed construction

4.7.4 Current Generation

The currents were generated in the physical model by means of four variable speed electric thrusters, two located in each of the lateral channels. The momentum imparted by the thrusters forced the water on the outer sides of the central test channel to flow towards the wave machine. By continuity, the central test channel conveys the same discharge flowing away from the wave machine.

The strength of the flow could be modified swiftly and easily by adjusting the settings of the controllers of each thruster. Due to the momentum of the flow, however, there was a modest time lag between this adjustment and the measured response of flow in the model. Various components of the current generation system are depicted in Figure 4.24.

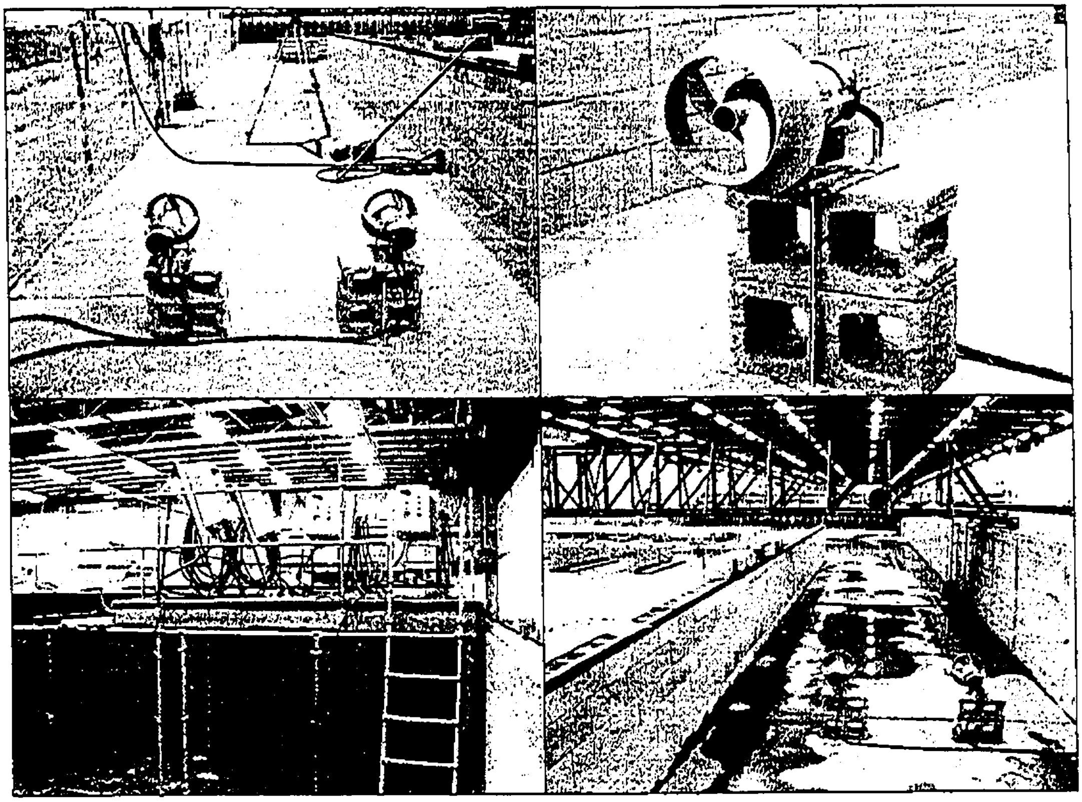

Figure 4.24 - Current generation system

4.7.5 Flow Guides

Several portable guide walls and a single portable wave absorber module were used to guide the current generated within the model basin in order to create a reasonably uniform and steady flow through the central test channel. The location of the guide walls and the absorber module were optimised by trial-and-error until the most favourable flow conditions were realized. The guide walls were installed in a row along the centreline of the basin, near the entrance to the center channel, shown in Figure 4.25. The wave absorber module was installed near the centreline of the basin, on the rear slope of the bathymetry behind the structure, depicted in Figure 4.26.

The undisturbed flow conditions (current alone, waves alone, combined waves and current) were fine-tuned and calibrated in a series of tests conducted on the bathymetry without the tunnel. These flow calibrations are described later in Section 4.10.1. The current along the tunnel corridor was uniform and steady, with observed spatial and temporal variations within 5% and 10% respectively. The final configuration of the flow guides and wave absorber module is shown in Figure 4.27.

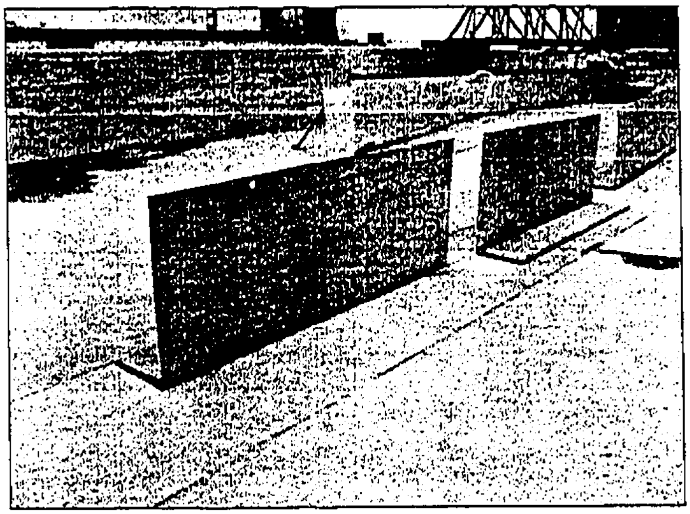

Figure 4.25 - Portable guide walls

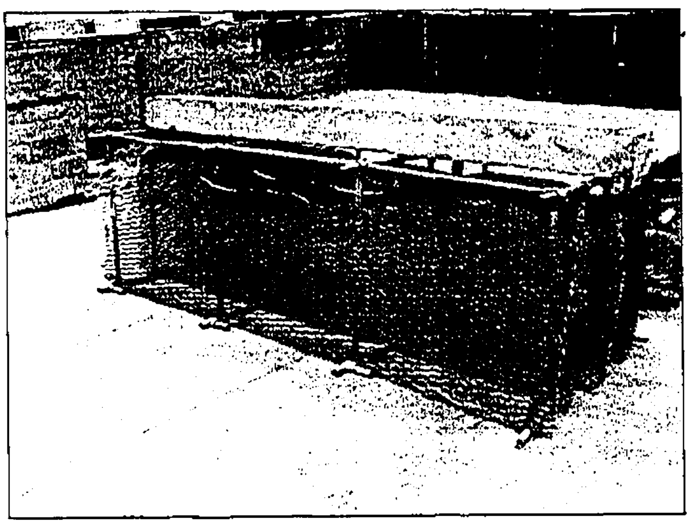

Figure 4.26 - Wave absorber module

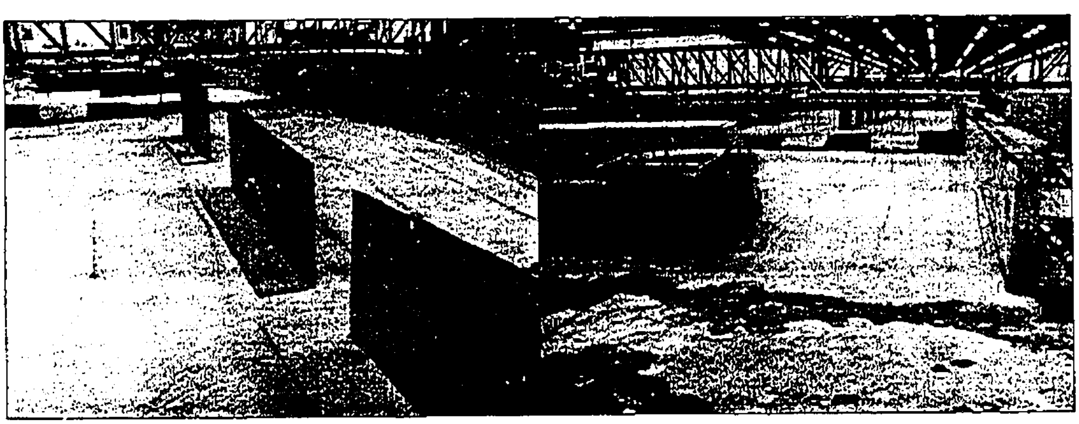

Figure 4.27 - Final layout of flow guides and wave absorber module

4.7.6 Model of the Immersed Tunnel

A 360 m long length of the immersed tunnel, Sta. 5+100 to Sta. 5+460, was reproduced in the physical model as a single structure constructed from marine plywood. The size and geometry of the model tunnel was controlled to replicate the prototype specifications. The tunnel cross-section was maintained constant, despite the fact that a short section of the tunnel in this area held a climbing lane, since this small change in the tunnel width was not expected to have any impact on the performance of the armour protection above. Several images showing various stages of the construction are depicted in Figure 4.28.

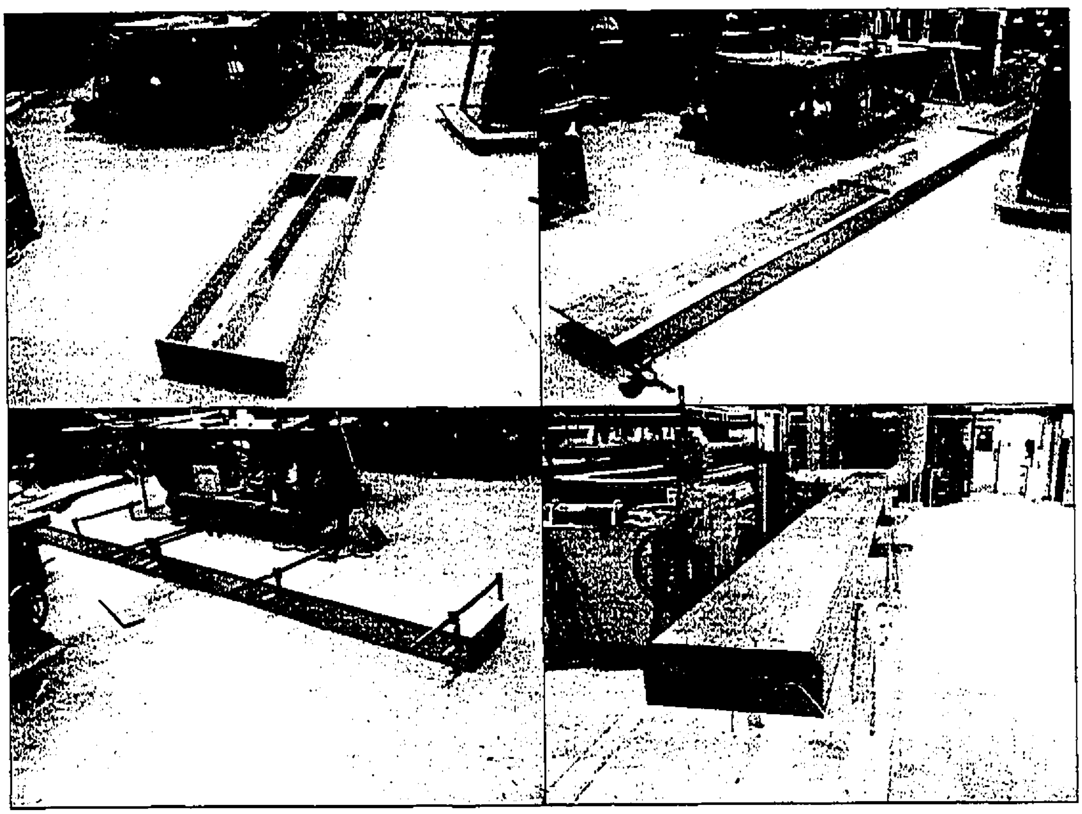

Figure 4.28 - Construction of the immersed tunnel model

Stationing was carefully marked over the top of the tunnel and on both sides, in order to identify the precise location should any section of the tunnel become exposed during the stability tests. In addition, a 2.5 cm x 2.5 cm (1.25 m prototype scale) chequered tape was also placed to be able to assess the damage area visually and, later also by post-processing the digital images taken after each test. Figure 4.29 gives a detailed view of the stationing and marks placed on the top of the tunnel.

Since the buoyancy and the pressure forces around it were not being studied in these tests, the tunnel was simply fastened to a steel frame and levelled into position, as described in Section 4.7.7.

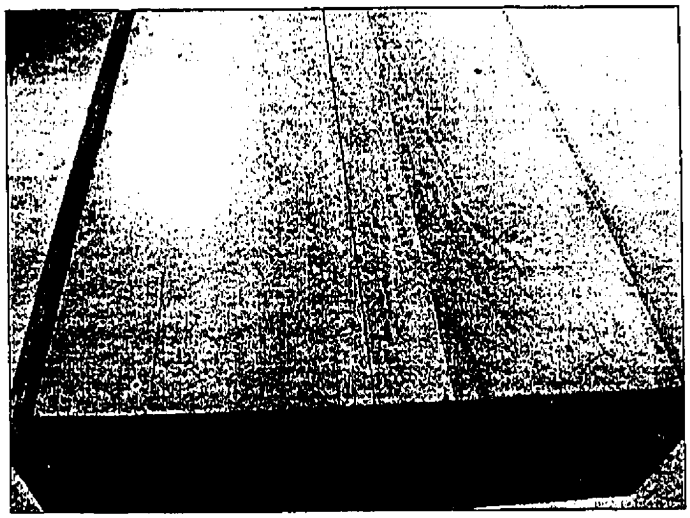

Figure 4.29 - Stationing on top of the tunnel for location and assessment of damage

4.7.7 Tunnel Installation and Embankment Fill Construction

After completion of the undisturbed flow tests, the basin was emptied and installation of the tunnel began. Dredging works were undertaken in the sand, and a sloping trench was excavated to receive the tunnel (see Figure 4.30).

Fine gravel was used to construct the embankment fill. This substitution of the gravel bed and locking fill materials was deemed appropriate since the stability of the armour and scour protection is not affected by the minor changes in the seepage flow within the structure, particularly for the case of a submarine structure protecting a rather large and impervious tunnel element.

The model tunnel was fastened to two steel angles that were in turn supported by 8 threaded rods grouted into the basin floor before the sand pit was filled. The steel angles were first surveyed to give a reference level to the embankment fill. Then, after the tunnel was placed and fastened to the frame, its top was again carefully surveyed, with an allowed tolerance of less than 1 mm. The tunnel was raised or lowered as required by means of the double nuts attached to the threaded rods.

After installing the tunnel, the embankment fill, armour and scour protection materials were installed. To accomplish this task, a series of fibreboard templates were used to guide the placement of the various rock materials. Elevations of the material were controlled using the tunnel as a reference. This technique allows the variable design section (both shape and elevation) to be constructed to a high degree of accuracy. Figure 4.31 and Figure 4.32 illustrate the installation of the model tunnel and the subsequent placement of the embankment fill.

Figure 4.30 - Dredged trench for installation of the immersed tunnel

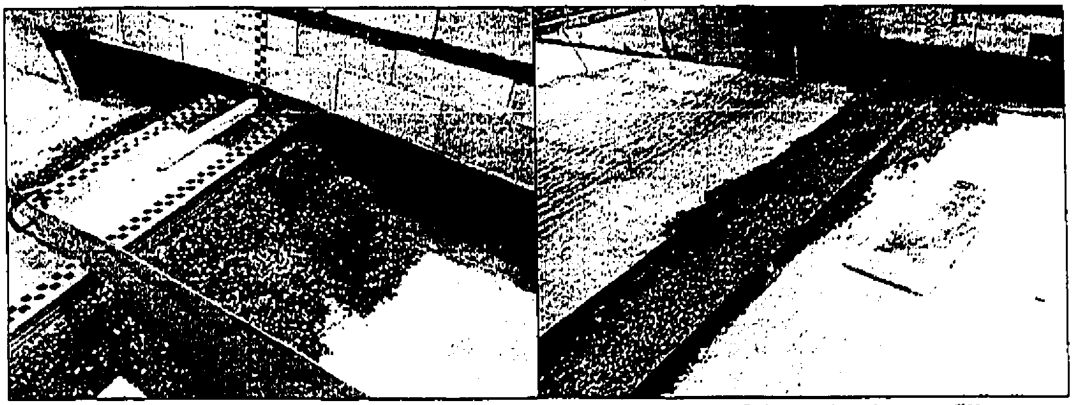

Figure 4.31 - Installation of the tunnel and construction of the embankment fill

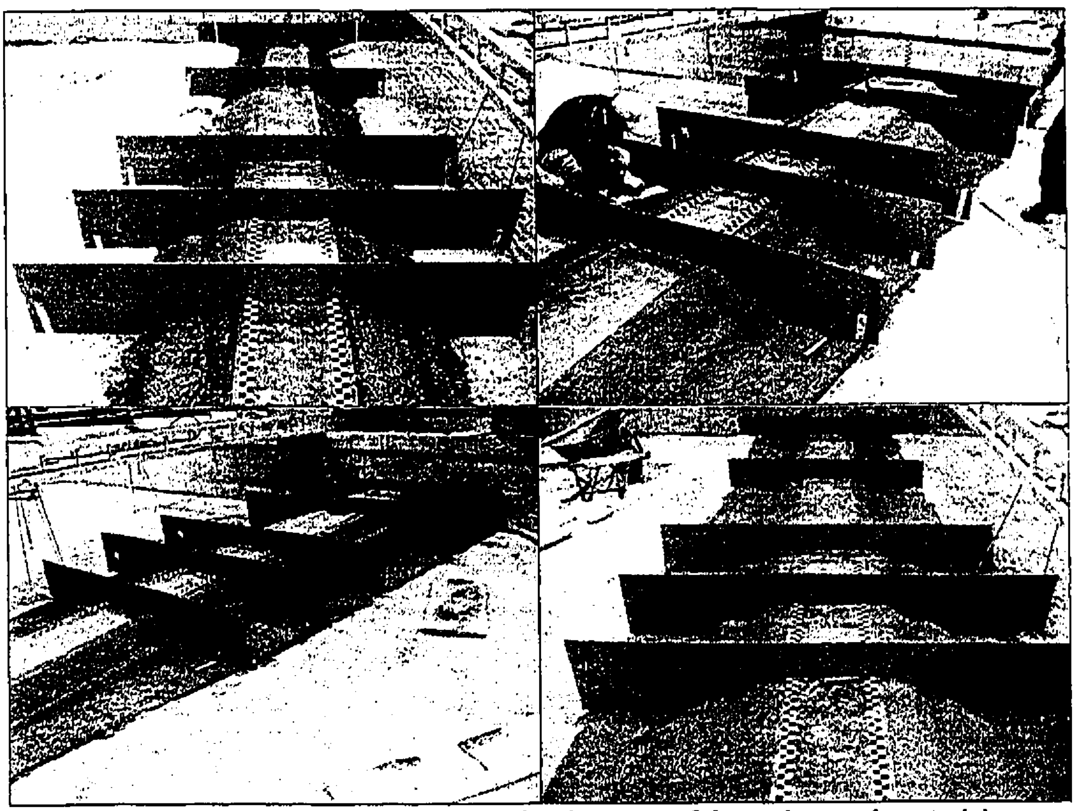

Figure 4.32 - Templates used to guide the placement of the various rock materials

Next, the underlayer material was placed and painted in a bright pink to clearly identify the layer should it become exposed. The use of paint is beneficial as it helps identify damage to the structure. In order for the paint to not affect particle mobility by inadvertently gluing the particles together, the painted structure was gently tapped in order to loosen any bonds formed between particles due to the paint. Figure 4.33 shows a portion of the model following placement of the preloading fill.

The particle size distribution of the material used for the underlayer is presented in Figure 4.34, where the prescribed preloading fill gradation and confidence intervals are also shown (refer back to Figure 4.11). An image of the fill material used is presented in Figure 4.35. The particle size distribution was obtained by means of weighing the material retained on a series of standard size sieves trays.

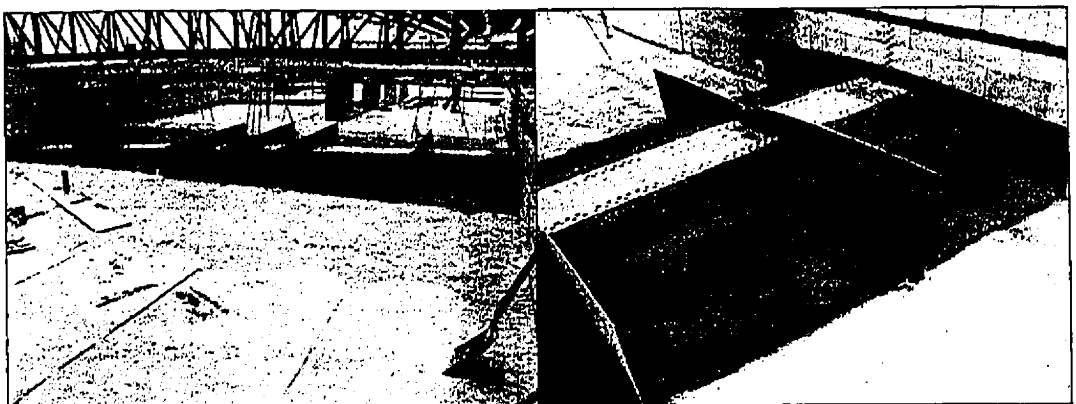

Figure 4.33 - Final configuration of the embankment fill

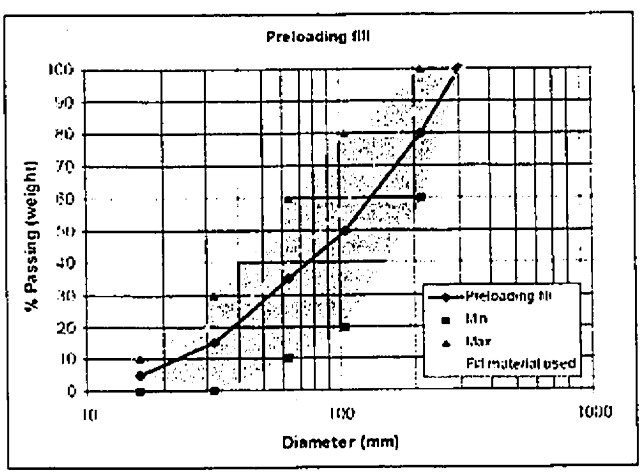

Figure 4.34 - Grain size distribution of the embankment fill material used in the model

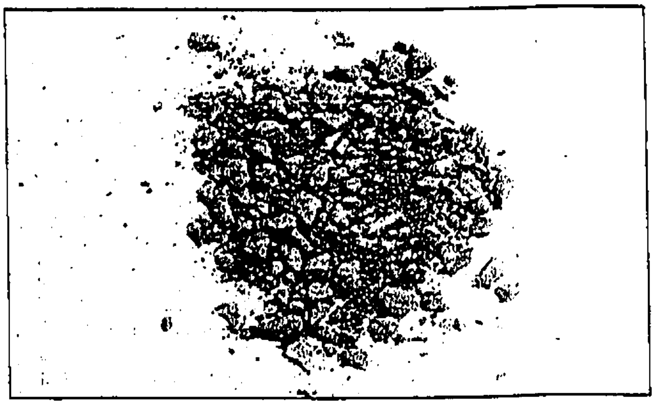

Figure 4.35 - Image of the embankment fill (on mm paper)

4.7.8 Armour and Scour Protection

Fibreboard templates were used to guide the placement of the armour and scour protection materials on top of the embankment fill. Similar to the embankment fill, the rock materials prepared for use in the construction of the model were sorted by sieve, and a small sample from each tray was weighed, and the number of stones counted. The rock materials were scaled by weight according to the relationships discussed earlier in Section 4.4. Several samples were randomly selected and sieved in the same fashion to detect any variance in the gradation. Moreover, there were additional samples collected from the armour and scour protection after the stability tests were completed to assess the final gradation of the tested material. The grading curves for the armour protection and the scour (toe) protection are shown in Figure 4.36 and Figure 4.37 respectively. Figure 4.38 and Figure 4.39 also show images of these rock materials. The armour protection material used for the model construction (refer to Figure 4.36)was slightly smaller than prescribed, however this was deemed acceptable by both the CHC researchers and the client since it meant the testing would be more conservative. This discrepancy may have yielded slightly more armour damage to the structure; however it would not have had any notable effect on the wave and current characteristics which are more the focus of this thesis.

Once the armour and scour protection materials were installed, the fibreboard templates were carefully removed prior to testing (refer to Figure 4.40). The minor damage caused by the removal of the templates was repaired and the outer surface of the armour and scour protection was lightly painted to aid in the visualization of any damage and the extent of any reshaping. The armour was painted in 50 m (prototype scale) long strips alternating in blue and white, whereas the scour protection was painted similarly using green and gold (refer to Figure 4.41).

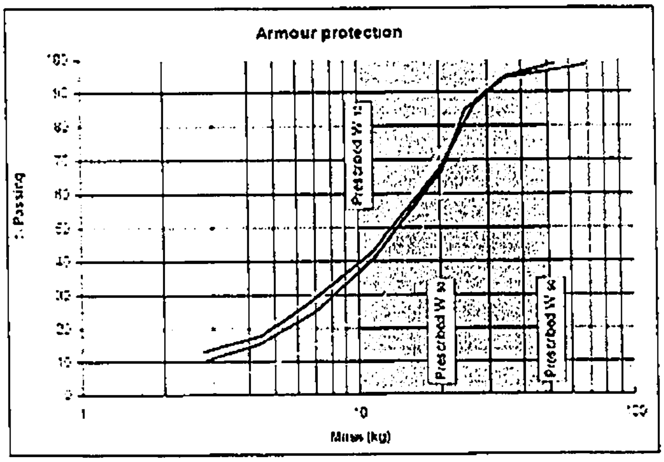

Figure 4.36 - Rock weight distribution of the armour protection used in the model (Blue lines correspond to samples taken before the stability tests, orange lines to samples taken from after the tests)

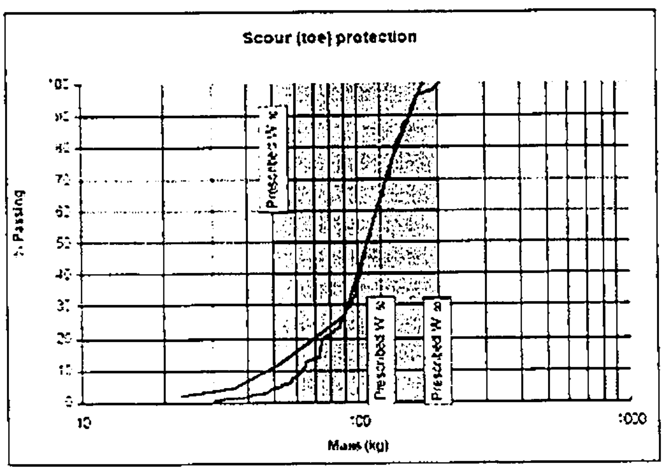

Figure 4.37 - Rock weight distribution of the scour protection material used in the model

Figure 4.38 - Image of the armour protection material (on mm paper)

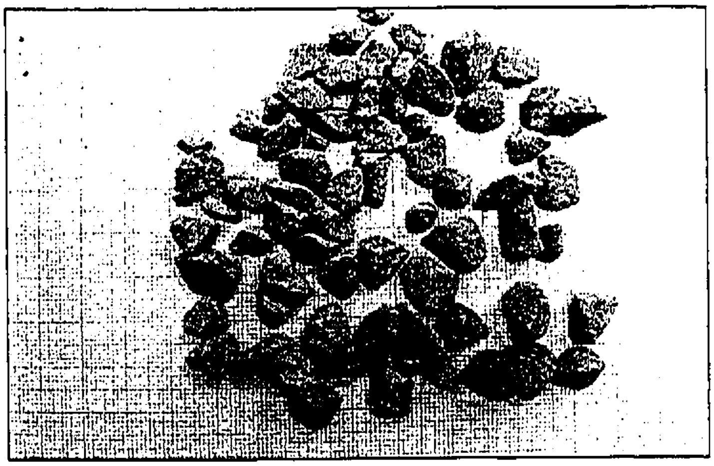

Figure 4.39 - Image of the scour protection material (on mm paper)

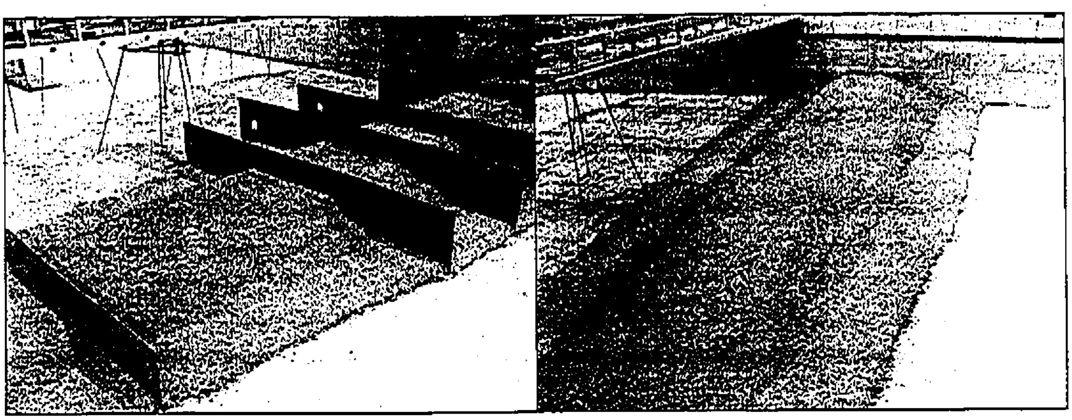

Figure 4.40 - Armour and scour protection during construction

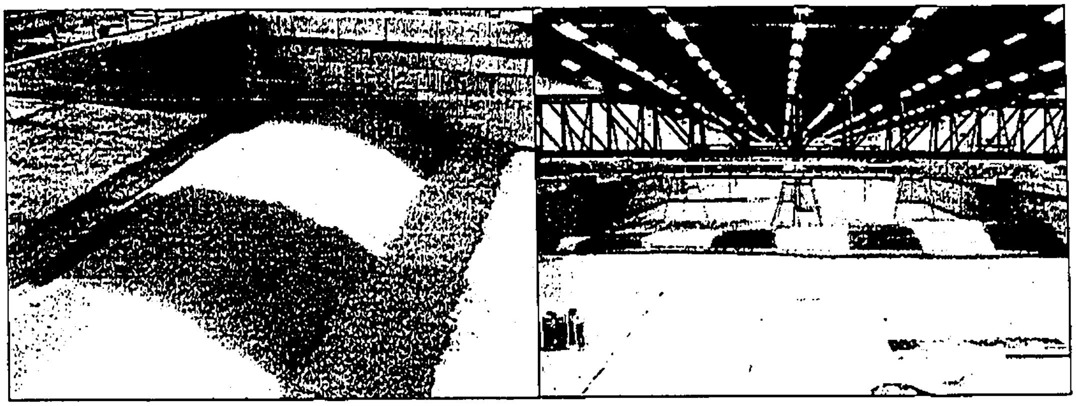

Figure 4.41 - Final configuration of armour and scour protection

4.8 Instrumentation, Data Acquisition and Video

4.8.1 Wave Gauges

Wave conditions in the physical model were measured at 10 locations through the use of capacitance wire gauges previously developed at CHC. The probes (see in Figure 4.42) operate by detecting the change in capacitance that occurs as a section of the insulated wire becomes wetted. The signal is directly proportional to the percentage of the wire that is wetted, regardless of whether the wetting is continuous (caused by "green water") or intermittent (as in the case of splash or spray). This type of wave gauge (WG) exhibits a highly linear and stable water level to voltage response. The gauges typically demonstrated calibration errors of less than 0.5% over a 100 mm calibration range. This error represents an accuracy of ±0.5 mm at model scale, or ±25 mm at prototype scale. The sample rate for all wave gauges was 25 Hz. Figure 4.43 shows an example of a wave gauge record.

The wave gauges were arranged in three rows, parallel to the tunnel axis. The first three gauges were located 150 m (full scale) to the South of the tunnel (up-wave) corresponding to approximately half a wavelength. The next four gauges were installed above the centerline of the tunnel. The final three gauges were located 150 m to the North of the tunnel (down-wave). This arrangement remained constant throughout the calibration and testing phases of this study, so comparisons of the impact of the structure on the wave field could be assessed. The layout of the instrumentation is presented in Figure 4.47, which also shows the location of the current meters.

The wave probes were calibrated on several occasions during the study, notably when there were changes in the water elevation between tests. This calibration was performed by changing the elevation of the probes with respect to a fixed water level. The calibration constants remained stable throughout the testing period.

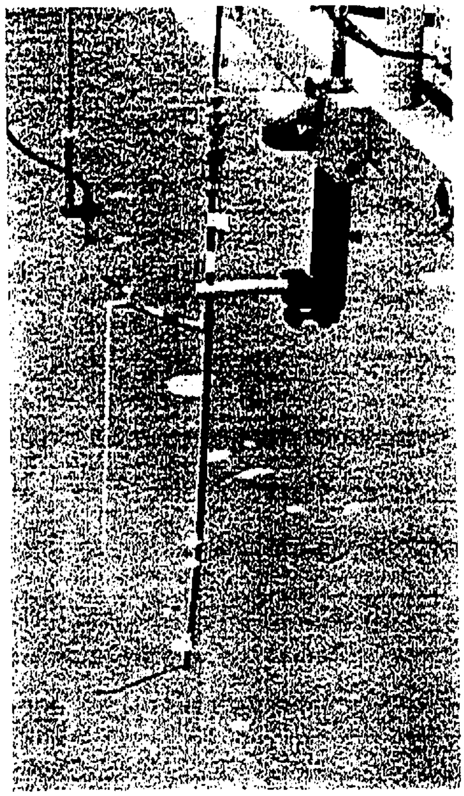

Figure 4.42 - Capacitance wave gauge measuring the water surface elevation

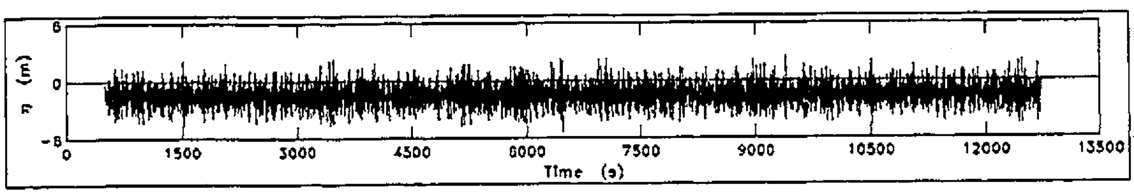

Figure 4.43 – Example of a measured wave train (WG05 from Case 0)

4.8.2 Current Meters

In addition to measurements of the water surface elevation, the magnitude and direction of the currents in the model were measured using two 2-axis electromagnetic current meters (ECM) and three 3-axis Sontek acoustic Doppler velocimeters (ADV).

The electromagnetic instruments, shown in Figure 4.44, measure the voltage resulting from the motion of a conductor (the water) through a magnetic field according to Faraday's law of electromagnetic induction. Simply stated, Faraday's law defines the voltage produced in a conductor as the product of the speed of the conductor (water flow velocity) times the magnitude of the magnetic field times the length of the conductor (the spacing between electrodes). The sampling rate of the ECMs was 25 Hz.

In contrast, the ADVs use sound waves to provide a continuous measure of the fluid velocities at a point located approximately 5 cm below the head of the instrument. This device, shown in Figure 4.45, uses the Doppler-shift principle, i.e. the apparent change in frequency or wavelength of a wave that is perceived by an observer moving relative to the source of the waves. The ADV emits an acoustic beam, and measures the Doppler shift in wavelengths of reflections from particles moving with the flow. This technique allows for measurements of the flow with high levels of precision at a high frequency, provided there are a sufficient number of fine particles in the flow. The sampling rate of the ADVs was 25 Hz.

The ECM flow meters were positioned along the central axis of the test channel (Sta. 5+280) on both sides of the structure axis (approximately 75 m North and South), corresponding to approximately 20 m from the toe of the structure and at an elevation of 16.5 m from the seabed (35 cm above the bed in model scale). The ADVs were placed along the axis of the structure. The elevation of the measurement depended on the test conditions and, in some cases, it was varied to capture the vertical velocity profile characteristics. As with the wave gauges, the location of the ECMs and ADVs remained constant throughout the calibration and testing program. Figure 4.46 shows an example of recorded data from ECM02 from one of the calibration tests. In this figure, the black and red lines indicate the readings of the x and y directions respectively. A diagram showing the layout of the instrumentation is presented in Figure 4.47.

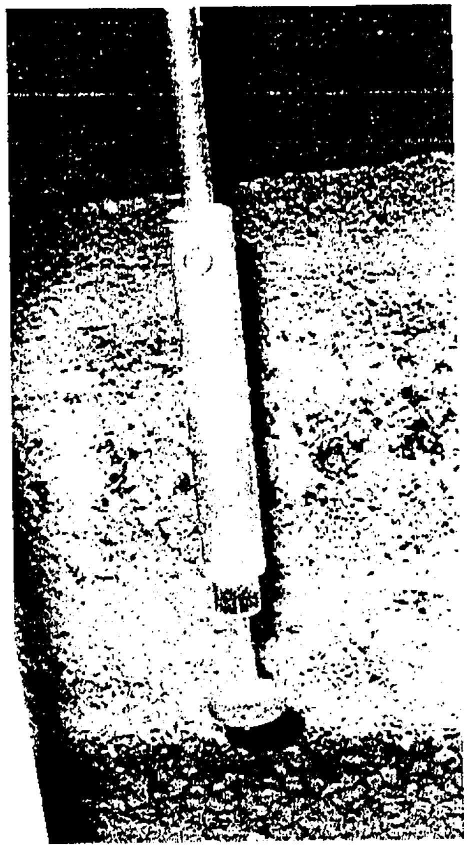

Figure 4.44 - Electromagnetic Current Meter giving 2-Dimensional velocity measurements

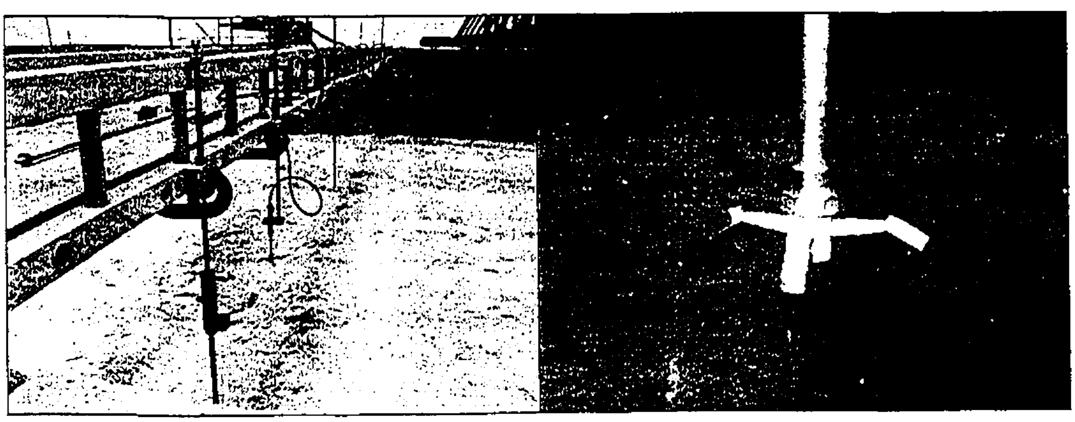

Figure 4.45 - Acoustic Doppler Velocimeter giving 3-Dimensional velocity measurements

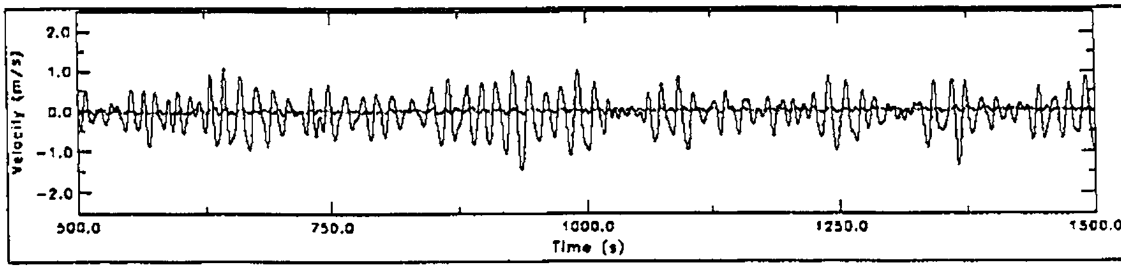

Figure 4.46 - Velocity gauge record example (ECM02 from Case 0)

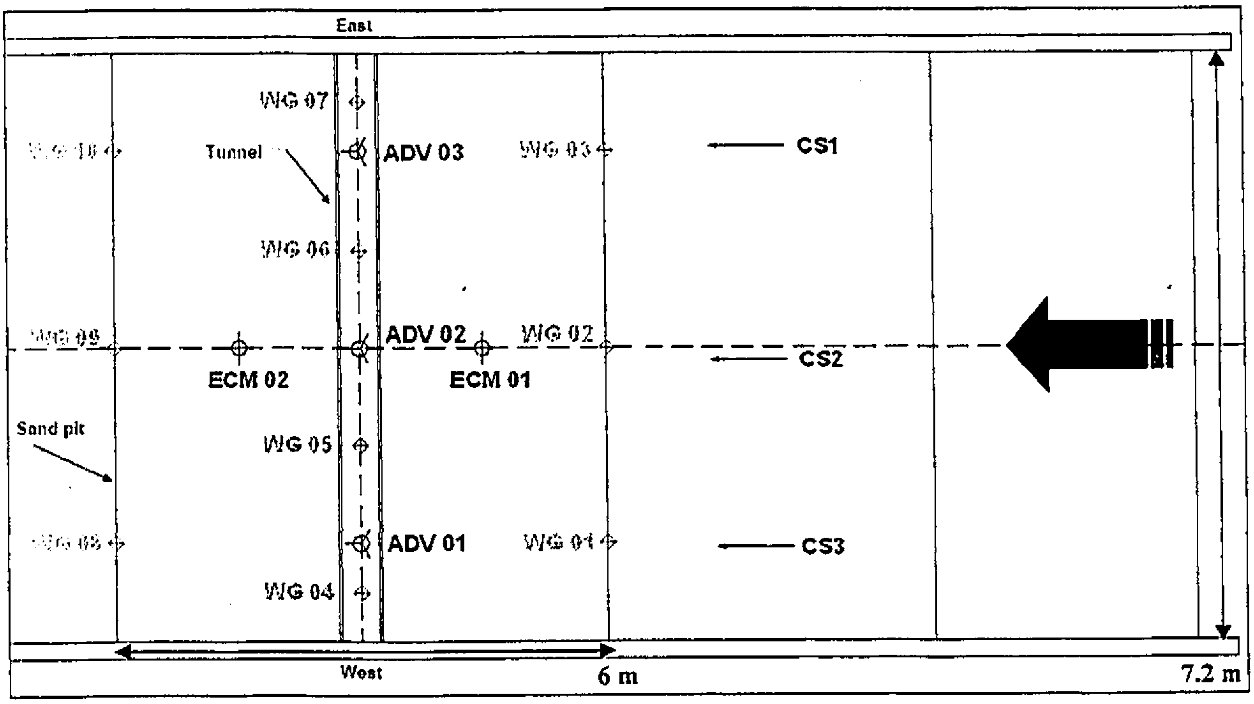

Figure 4.47 - Arrangement of the instrumentation in the physical model
WG = Wave Gauges, ECM = Electromagnetic Current Meter, ADV = Acoustic Doppler Velocimeter

4.8.3 Data Acquisition System

A data acquisition system converts the analog voltage signals from the various sensors deployed in the model into digital form for storage in a computer data file. Analog signals from each sensor were routed to a set of signal conditioning units equipped with separate amplifiers and anti-aliasing filters for each channel. From the signal conditioning units, the analog signals were routed through Bayonet Nut Coupling (BNC) Interface units to data acquisition cards housed inside a high-speed computer. Two model 6031E cards, supplied by National Instruments Inc., were used for the physical modelling study. Each card is capable of handling up to 32 channels of differential input, 16-bit resolution, and a maximum sampling rate of 1×10^5 samples per second. The data acquisition system was controlled through the use of the Windows NT Data Acquisition and Control (NDAC) software developed by CHC.

4.8.4 Video and Imaging

Throughout the model construction, calibration tests and stability tests, a digital and video camera were used to collect numerous images and video from various locations within the model. A number of the digital photographs have been included in this thesis. During the stability tests, a high-resolution underwater video camera was also used before and after each test. The digital images and the underwater video were used to aid in the assessment of the damage level to the armour and scour protection.

4.9 Wave Synthesis and Generation

Irregular long-crested waves were generated in the physical model using the powerful WM14 wave machine mentioned previously in Section 4.2 (see Figure 4.1). The wave machine is located in a water depth of 50 m at full scale, corresponding to the floor of the basin where no additional bathymetry is situated. The irregular waves were synthesized from a Joint North Sea Wave Analysis Project (JONSWAP) wave spectra $S_{JONSWAP}(f)$ defined as:

$$S_{JONSWAP} = \frac{\alpha_p g^2}{(2\pi)^4 f^5} \exp\left[-\frac{5}{4}\left(\frac{f}{f_p}\right)^{-4}\right]\gamma^a \tag{4-7}$$

$$a = \exp\left[-\frac{(f-f_p)^2}{2\sigma_J^2 f_p^2}\right], \quad \sigma_J = \begin{cases} 0.07 \text{ for } f \le f_p \\ 0.09 \text{ for } f > f_p \end{cases} \tag{4-8}$$

In these equations, f is the wave frequency and f_p is the peak frequency (the frequency at which $S_{JONSWAP}$ is maximum), while α_p and γ are parameters that control the scale and width of the spectrum. No specific information regarding spectral shapes at the site was available when testing began, thus a default value of $\gamma = 3.3$ was used, which corresponds to a fully developed sea state. For wave synthesis, a spectral estimate of the significant wave height H_{m0} is defined by (in which case α is scaled appropriately):

$$H_s \approx H_{m0} = 4\sqrt{\int_0^{\infty} S_{JONSWAP} df} \tag{4-9}$$

The various irregular wave trains were synthesized from the appropriate target spectrum by the random phase method, described by Funke and Mansard (1984). Each time series during the stability tests had a duration corresponding to 5 hours at full scale (nearly 43 minutes at model scale). Each signal contained more than 1000 unique waves.

This lengthy duration is important for stability testing, since it ensures that the structure will be exposed to a full distribution of large waves, since rubblemound structures are particularly sensitive to the few largest waves in a sea state.

These generated time series were converted to model scale and used to compute command signals for the wave generator using CHC's Generalized Experiment Control and Data Acquisition Package (GEDAP) wave synthesis software.

4.10 Physical Modelling Tests

Before constructing the model in the Coastal Wave Basin, a number of calibration and verification tests were undertaken to assure that the target conditions were achieved at the testing site. Calibration consisted of adjusting the command signals used to generate the waves, and establishing the correct thruster settings required to maintain the desired depth averaged flow velocity. The calibration process took a number of trials in order to obtain the desired parameters, however for brevity, only the finalized calibrations are shown herein.

4.10.1 Calibration of Currents

Numerous physical model tests were performed in which currents were simulated on their own and in combination with waves. Although their effects are not studied in this thesis, a summary of their calibration is presented for explanatory purposes, and also to give an idea of the velocity magnitudes of a current compared with wave-induced velocities. A summary of the low frequency component of the velocities measured at all five current meters is presented in

Table 4.2,

Table 4.3. and Table 4.4. The low frequency portion of the measured velocities (defined as less than 1/30 Hz) pertains to the flow-induced velocity, whereas the high frequency portion pertains to wave-induced velocities. The velocity was fairly uniform with depth and across the width of the test channel along the axis of the tunnel. The current was also fairly steady and the standard deviation of the temporal fluctuations was small; roughly 14% of the mean velocity.

Table 4.2 - Vertical location of flow velocity measurements

Test Name	Target Velocity (m/s)	Elevation of the current measurement (m)				
		ADV01	ADV02	ADV03	ECM01	ECM02
CAL_CURRENT_Z18	1.2	−25.0	−25.0	−25.0	−17.5	−17.5
CAL_CURRENT_Z33	1.2	−17.5	−17.5	−17.5	−17.5	−17.5
CAL_CURRENT_Z48	1.2	−10.0	−10.0	−10.0	−17.5	−17.5

Table 4.3 - Summary of time-averaged flow velocities

Test Name	Averaged Measured Velocity (m/s)						
	ADV01	ADV02	ADV03	ECM01	ECM02	**Transversal Average (m/s)**	**Cross-Sectional Variation**
CAL_CURRENT_Z18	1.13	1.26	1.11	1.32	1.27	1.165	7%
CAL_CURRENT_Z33	1.14	1.27	1.31	1.32	1.30	1.242	7%
CAL_CURRENT_Z48	1.14	1.21	1.26	1.33	1.31	1.205	5%
Vertical Average (m/s)	**1.135**	**1.251**	**1.227**	-	-	**1.204**	**5%**

Table 4.4 - Summary of standard deviations of flow velocities

Test Name	Standard Deviation Measured Velocity					
	ADV01	ADV02	ADV03	ECM01	ECM02	**Cross-Sectional Average**
CAL_CURRENT_Z18	0.14	0.12	0.17	0.10	0.12	0.142
CAL_CURRENT_Z33	0.12	0.10	0.18	0.09	0.09	0.130
CAL_CURRENT_Z48	0.12	0.13	0.19	0.11	0.11	0.147
Vertical Average	**0.127**	**0.113**	**0.179**	-	-	**0.140**

4.10.2 Calibration of Waves

Table 4.5 indicates the target parameters used for calibration of the waves at the test section.

Table 4.5 - Target wave calibration parameters

Test Name	Target Parameters		
	Water Level (m)	H_{m0} (m)	T_p (s)
CAL_T16_H4P5	−1.55	4.5	16.2
CAL_T20_H5P0	−1.72	5.0	20.1
CAL_T20_H6P0	−1.72	6.0	20.1

A summary of the wave conditions measured at all gauges is presented in Table 4.6 and Table 4.7. The maximum errors in H_{m0} and T_p, relative to the target parameters, were found to be 2.5% and 2% respectively. As can be observed, the wave height and period are both reproduced with a high degree of accuracy. Figure 4.48 shows an example of the measured and target spectra during the CAL_T16_H4P5 calibration test at the axis of the structure, shown in black and red lines respectively. It is seen that the target spectra are reproduced quite well, with a minor overestimation of the spectral peak. Similar spectral observances were made for the other calibration cases.

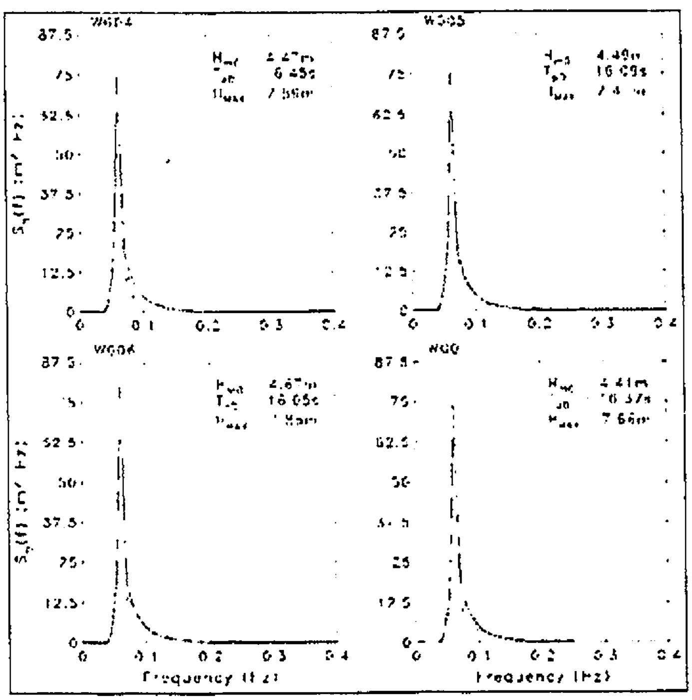

Figure 4.48 - Measured and target calibration wave spectra at structure axis

For comparison purposes, the measured average wave-induced horizontal velocities are presented in Table 4.8. One can notice that wave-induced peak velocities measured from the 6 m design wave test are nearly as large as the design current of 1.2 m/s.

Table 4.6 - Measured significant wave heights

Test Name	Measured Spectral Parameter: Significant Wave Height H_{mo} (m)										
	WG01	WG02	WG03	WG04	WG05	WG06	WG07	WG08	WG09	WG10	Average WG04-WG07
CAL_T16_H4P5	4.39	4.68	4.48	4.47	4.49	4.67	4.41	4.22	4.38	4.25	**4.51**
CAL_T20_H5P0	4.99	5.38	5.06	5.01	4.91	5.06	5.09	4.63	5.31	4.77	**5.02**
CAL_T20_H6P0	5.99	6.42	5.96	6.05	5.90	6.01	6.02	5.56	6.42	5.59	**5.99**
Location	Up-wave Row (South)			Tunnel Axis				Down-wave Row (North)			Axis

Table 4.7 - Measured peak periods

Test Name	Measured Spectral Parameter: Peak Period T_p (s)										
	WG01	WG02	WG03	WG04	WG05	WG06	WG07	WG08	WG09	WG10	Average WG04-WG07
CAL_T16_H4P5	16.57	16.45	16.59	16.45	16.09	16.05	16.37	15.52	15.29	15.36	**16.24**
CAL_T20_H5P0	20.33	20.74	20.31	20.71	19.99	20.01	20.74	19.79	20.25	20.77	**20.36**
CAL_T20_H6P0	20.37	20.74	20.34	20.72	20.07	20.09	20.75	19.94	20.24	20.90	**20.41**
Location	Up-wave Row (South)			Tunnel Axis				Down-wave Row (North)			Axis

Table 4.8 - Measured averaged wave-induced peak horizontal velocities

Test Name	Averaged Wave-Induced Peak Horizontal Velocities (m/s)									
	Wave Crest (positive Northward current)					Wave Trough (negative Southward current)				
	ADV01	ADV02	ADV03	ECM01	ECM02	ADV01	ADV02	ADV03	ECM01	ECM02
CAL_T16_H4P5	0.63	0.66	0.68	0.68	0.63	−0.60	−0.63	−0.65	−0.60	−0.55
CAL_T20_H5P0	0.79	0.78	0.83	0.76	0.71	−0.69	−0.71	−0.74	−0.62	−0.60
CAL_T20_H6P0	0.96	0.97	1.01	0.91	0.85	−0.82	−0.84	−0.87	−0.72	−0.70

4.10.3 Combined Waves and Currents

As previously mentioned, the combined effects of waves and currents were used in the physical modelling study. Following the calibration tests for waves and currents alone, additional tests were undertaken employing both waves and currents to determine the undisturbed conditions at the test location before the structure was placed. No adjustments were made to account for the wave-current interaction effects; however they are hereby briefly described.

For waves alone, a small wave-induced current (Stokes drift) is observed, on top of the wave-induced velocities mentioned previously. For the combined waves and current tests, compared with the tests of current alone, it was observed that the averaged current velocity was reduced, due to the presence of the waves, by approximately 6%. The mean current at the test site remained roughly uniform and very close to the target current speed of 1.2 m/s. In a comparison for tests of waves alone versus combined waves and current, the wave height is reduced in the combined waves and current tests, since a following current superimposed in a wave field reduces the wave steepness because the wavelength becomes longer. In order to maintain the total energy flux, the wave height is reduced accordingly, and was observed to be roughly 15%.

As mentioned, the effects of current are not included in the scope of this thesis, and these remarks have been included simply for a better understanding of the overall experimental program.

4.10.4 Physical Modelling Testing Series

Many tests were performed during the physical model study, however only five of these, all conducted with waves and without current, are considered in this thesis. The target water levels and wave conditions for these five tests are summarized in Table 4.9. The model setup is such that the design waves are collinear and perpendicular to the longitudinal axis of the tunnel. The average water depth is −34 m Mean Sea Level (MSL) at the location where the tunnel is to be laid.

Table 4.9 - Physical experiment testing series

Test ID	H_{m0} (m)	T_p (s)	Water Level (m)	Duration (hrs)	Presence of Tunnel
Case 0	4.5	16.2	−1.55	5	No
Case 1	4.5	16.2	−1.55	5	Yes
Case 2	6.0	20.1	−1.72	5	Yes
Case 3	6.0	20.1	−5.00	5	Yes
Case 4	7.0	20.1	−5.00	5	Yes

Case 0 corresponds to the calibration case, using the same parameters as Case 1 but without the structure in place. As stated previously, a number of other physical model tests were performed incorporating the effects of currents; however this work is not considered in this thesis.

The submerged structure was continuously monitored by the researchers, and numerous digital images and video were captured before, during, and following each test. Figure 4.49 shows the author observing the model during one test. For the extreme wave events in the drive signals, wave breaking was actually observed at the shallow side (see red arrow in Figure 4.49), when the wave height was nearly as large as the submergence depth over the tunnel. Figure 4.50 shows the author, along with fellow researchers. Detailed observations of the structure were made following each test to assess and document the damage to the structure's armour and toe protection layers. However, the response of the structure to the waves is not considered in this thesis.

The measurements and results of the physical modelling work are presented in Section 7.

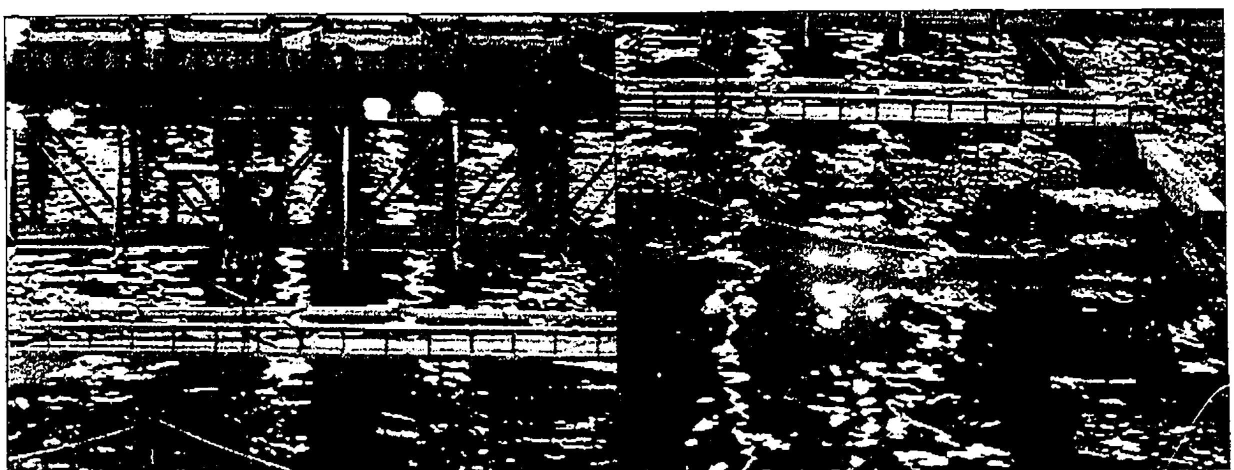

Figure 4.49 - The author observing wave breaking during the physical model experiments

Figure 4.50 - Researchers observing the submerged structure after the testing series

5 Numerical Modelling

5.1 Introduction

The second phase of research was a series of numerical simulations based on the physical modelling tests described earlier. Section 5 provides a detailed depiction of the study.

As will be described in Sections 5.2 and 5.3, Shoal2-D is the name of the actual numerical model for simulating the propagation and transformation of waves, while WaveSim is the environment designed to work with it. For explanatory purposes, the model and the interface will be referred to by their specific names for these mentioned sections, however for ease of reference, the numerical model and the interface combined will be referred to simply as "WaveSim" in all following sections. It should be noted that WaveSim is also the name of the model used for commercial purposes by which it is most commonly known.

5.2 Shoal2-D Numerical Model

The following sub-sections (Sections 5.2.1 to 5.2.10) contain partially modified excerpts from the WaveSim Manual (McDonald, 2001).

5.2.1 Introduction

Shoal2-D is a numerical model for simulating the propagation and transformation of ocean waves in coastal regions and harbours. The numerical model is based on a time domain solution of the Boussinesq-type equations, which represent the vertically integrated equations for the conservation of mass and momentum for nonlinear dispersive waves, propagating in water of variable depth.

The classical two-dimensional form of the Boussinesq equations for water of variable depth was originally derived by Peregrine (1967). The mass and momentum equations were expressed in terms of the free surface elevation and depth-averaged velocity. Boussinesq-type equations are particularly useful for coastal engineering problems since they are able to describe the transformation of irregular multidirectional wave fields due to the effects of shoaling, refraction, diffraction, reflection and weakly nonlinear interactions.

The classical form of the Boussinesq equations is restricted to relatively shallow water depths because of the weak frequency dispersion characteristics of the equations. In order to keep errors in the phase velocity less than 5%, the water depth has to be less than one-fifth of the wavelength. In 1993, Nwogu extended the range of applicability of Boussinesq-type equations to deeper water by recasting the equations in terms of the velocity at an arbitrary distance z_α from the still water level, instead of the commonly used depth-averaged velocity. The elevation of the velocity variable, u_α, becomes a free parameter, which is chosen to optimize the linear dispersion characteristics of the equations.

According to Nwogu (1993), the new form of the equations has errors of less than 2% in the phase velocity from shallow water depths up to the deep water limit (i.e. one-half the wavelength). Despite the improvement in the frequency dispersion characteristics of the equations, the assumption of weak nonlinearity still limits its application to weakly nonlinear waves in intermediate and shallow water depths. This led Wei *et al.* (1995) to derive a fully nonlinear variant of the equations. The fully nonlinear equations are particularly useful for simulating highly asymmetric waves in shallow water, wave setup close to the shoreline, and wave-current interaction.

In nearshore regions, the processes of wave breaking and the associated generation of currents are important driving mechanisms for the transport of sediments and pollutants. In 1996, Nwogu extended the fully nonlinear form of the Boussinesq equations to the surf and swash zones, by coupling the mass and momentum equations with a one-equation model for the temporal and spatial evolution of the turbulent kinetic energy produced by wave breaking. The waves are assumed to start breaking when the horizontal velocity at the free surface exceeds the phase velocity of the waves. The equations were also modified to include the effects of bottom friction and flow through porous structures. The modified equations can simulate most of the phenomena of interest in coastal regions and harbour basins, including:

- Shoaling,
- Refraction,
- Diffraction,
- Full/partial reflection and transmission,

- Bottom friction,
- Multidirectional ocean waves,
- Nonlinear wave-wave interactions,
- Wave breaking and runup, and
- Wave-induced currents.

The governing equations, expressed in terms of the water surface elevation and orthogonal components of the horizontal velocity at a specified depth below the still water level have been solved using a time-domain, finite difference method. The area of interest is discretized using a rectangular grid with the equation variables defined at every grid node in a staggered manner.

Along offshore or internal boundaries, time histories of velocity fluxes corresponding to an incident storm condition are input. The incident wave conditions may be periodic or non-periodic, unidirectional or multidirectional. Damping layers are placed around the perimeter of the computational domain to absorb outgoing waves. Damping and porosity layers are also used to model the reflection and transmission characteristics of breakwaters and harbour structures. The damping and porosity characteristics are initially calibrated in a one-dimensional numerical flume to match the desired reflection and transmission characteristics of the breakwaters or harbour structures.

The model can be applied to a wide variety of coastal and ocean engineering problems including:

- Nearshore wave climate studies,
- Wave agitation and harbour resonance studies,
- Wave transformation around artificial islands,
- Wave loading and runup on large gravity-based structures,
- Wave breaking over submerged obstacles,
- Wave-induced nearshore circulation patterns, and
- Infragravity wave generation by groups of short waves.

5.2.2 Governing Equations

The wave transformation model is based on Boussinesq-type equations derived by Nwogu (1993, 1996). The equations represent depth-integrated continuity and conservation of momentum and can be considered to be a perturbation from non-dispersive long wave theory to include the effect of weak frequency dispersion. For dispersive waves, the horizontal and vertical velocities are no longer uniform over depth. The vertical profile of the velocity field is obtained by expanding the velocity potential as a Taylor series about an arbitrary depth z_α in the water column. By truncating the series at second order, this results in a linear variation of the vertical velocity a quadratic variation for the horizontal velocity over depth. For weakly nonlinear waves, the depth-integrated equations for the conservation of mass and momentum can be expressed in terms of the water surface elevation $\eta(x,t)$ and horizontal velocity $u_\alpha(x,t)$ at a distance z_α from the still water level to yield:

$$\eta_t + \nabla\cdot[(h+\eta)u_\alpha] + \nabla\cdot\left[\left(\frac{z_\alpha^2}{2}-\frac{h^2}{6}\right)h\nabla(\nabla\cdot u_\alpha)+\left(z_\alpha+\frac{h}{2}\right)h\nabla[\nabla\cdot(hu_\alpha)]\right]+F_{d\eta}=F_{wave} \tag{5-1}$$

$$\frac{1}{n}u_{\alpha t}+g\nabla\eta+\frac{1}{n^2}(u_\alpha\cdot\nabla)u_\alpha + \frac{1}{n}\left[\frac{z_\alpha^2}{2}\nabla(\nabla\cdot u_{\alpha t})+z_\alpha\nabla[\nabla\cdot(hu_{\alpha t})]\right]+\tau_{br}+\tau_{bf}+F_{du}+F_p=0 \tag{5-2}$$

where h(x) represents the water depth, g the gravitational acceleration, n is the porosity (1 for open water), and τ_{br}, τ_{bf}, F_{du}, $F_{d\eta}$, F_p and F_{wave} are terms used to incorporate the effects of wave breaking, bottom friction, wave energy damping, porous structures and internal wave generation respectively. The elevation of the velocity variable, z_α, is a free parameter and is chosen to minimize the differences between the linear dispersion characteristics of the Boussinesq model and the exact dispersion relation for small amplitude waves.

5.2.3 Linear Dispersion Properties

The linear dispersion relation for the model's governing equations is given by Nwogu (1993) as:

$$C^2 = \frac{\omega^2}{k^2} = gh\left[\frac{1-(\alpha+1/3)(kh)^2}{1-\alpha(kh)^2}\right] \qquad (5\text{-}3)$$
$$\text{where } \alpha = (z_\alpha/h)^2/2 + (z_\alpha/h)$$

and where ω is the angular frequency and k is the wave number. Depending on the elevation of the velocity variable or the value of α, different dispersion relations are obtained. If the velocity at the seabed ($z_\alpha = -h$) is used, $\alpha = -1/2$. Alternatively, if the velocity at the still water level ($z_\alpha = 0$) is used, $\alpha = 0$. The classical form of the Boussinesq equations which uses the depth-averaged velocity corresponds to $\alpha = -1/3$. The value of $\alpha = -2/5$ was obtained by Witting (1984) using a (2,2) Padé approximant of tanh kh. The phase speeds for different values of α, normalized with respect to the linear theory phase speed are plotted as a function of relative depth in Figure 5.1 (WaveSim Manual, 2001).

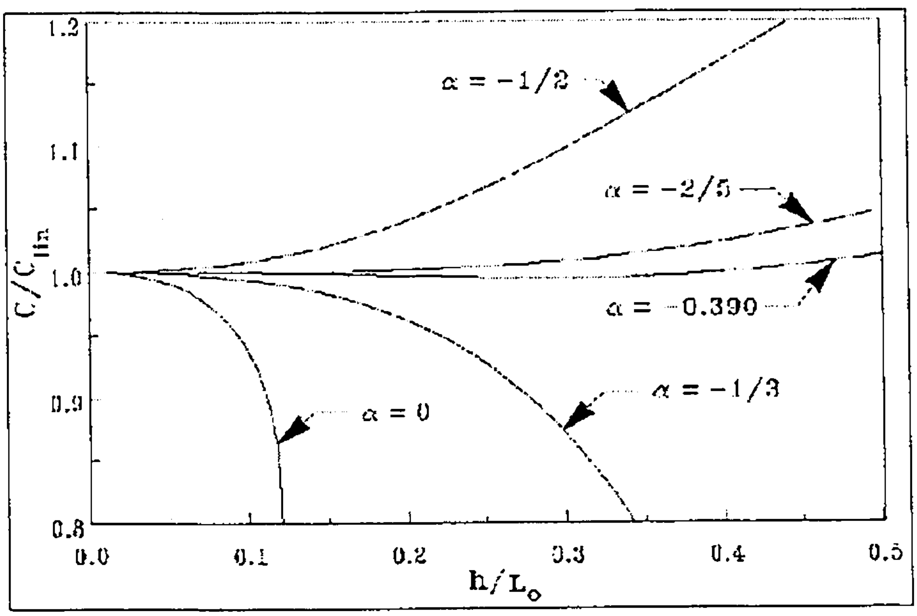

Figure 5.1 - Comparison of normalized phase speeds for different values of α (McDonald, 2001)

The relative depth is defined as the ratio of the water depth, h, to the equivalent deep-water wavelength, $L_0 = 2\pi g/\omega^2$. The deep-water depth limit corresponds to $h/L = 0.5$. The different dispersion equations are all equivalent in relatively shallow water ($h/L < 0.02$), but gradually depart from the exact solution with increasing depth. An optimal depth, $z_\alpha = -0.53h$ (i.e., $\alpha = -$

0.390), gives errors of less than 2% in the phase velocity from shallow water depths up to the deep water limit.

5.2.4 Nonlinear Properties

In an irregular sea state, different frequency components interact to generate forced waves at the sum and difference frequencies of the primary waves because of the nonlinear boundary conditions at the free surface. Longuet-Higgins and Stewart (1962) derived expressions for the magnitude of the low frequency component of the forced waves based on second-order Stokes theory. Sharma and Dean (1981) derived similar expressions for both the lower and higher harmonics in the multidirectional wave fields. Nwogu (1993) derived expressions for the magnitude of the second-order forced waves in water of constant depth for the weakly nonlinear form of the Boussinesq equations. Wei and Kirby (1994) derived similar expressions for the fully nonlinear model. The quadratic transfer function for the weakly nonlinear model is given by:

$$G_{\pm}(\omega_1,\omega_2)=\frac{f_{\pm}k_{\pm}h\left[1-\alpha(k_{\pm}h)^2\right]\left[f_1k_2'h+f_2k_1'h\right]+A}{\left\{f_{\pm}^{\,2}\left[1-\alpha(k_{\pm}h)^2\right]-gk_{\pm}^2h\left[1-(\alpha+1/3)(k_{\pm}h)^2\right]\right\}2k_1'k_2'h^3} \qquad \text{(5-4)}$$

$$\text{where } A = f_1f_2(k_{\pm}h)^2\left[1-(\alpha+1/3)(k_{\pm}h)^2\right]$$

where frequency $f_{\pm} = f_1 \pm f_2$, wave number $k_{\pm} = k_1 \pm k_2$, and $k' = k[1-(\alpha+1/3)(kh)^2]$. Figure 5.2 (WaveSim Manual, 2001) shows a comparison of the quadratic transfer function of the weakly nonlinear Boussinesq model with that of second-order Stokes theory for an example where the period of the wave group is ten times the average of the individual wave periods. The weakly nonlinear Boussinesq model underestimates the magnitude of the set-down wave and second harmonic at the deep-water depth limit by 65% and 45%, respectively. This suggests it cannot accurately simulate nonlinear effects in deep water. In order to be able to reasonably simulate nonlinear effects, the weakly nonlinear model should be restricted to the range $0 < h/L < 0.3$.

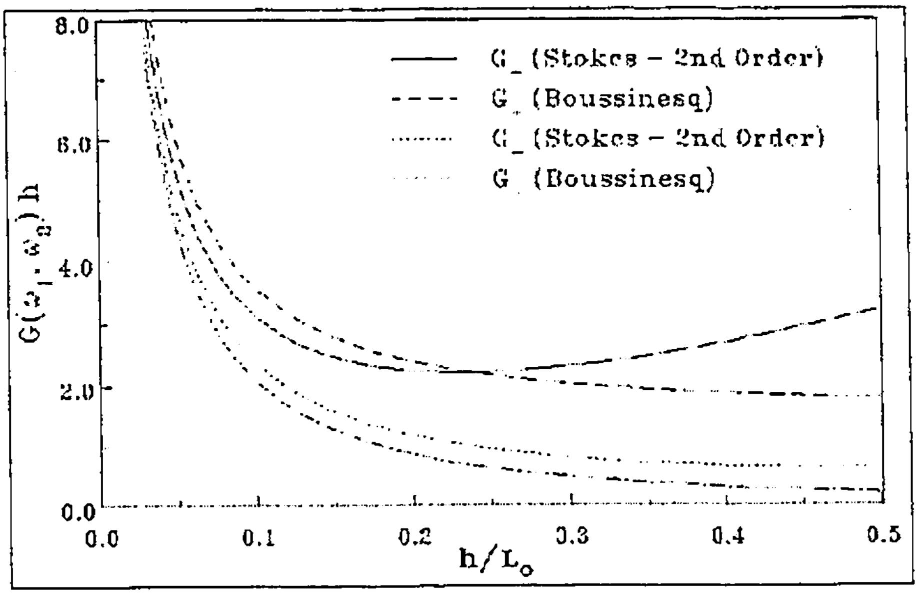

Figure 5.2 - Comparison of the quadratic transfer function for Boussinesq and Stokes (McDonald, 2001)

5.2.5 Simulation of Wave Breaking

The effect of energy dissipation due to wave breaking is simulated in the numerical model by introducing an eddy viscosity term, $\tau_{br} = \upsilon_t\nabla(\nabla\cdot u_\alpha)$, into the momentum equation. The eddy viscosity, υ_t, is related to the turbulent kinetic energy, k_t, and a turbulence length scale, l_t, by $\upsilon_t = \sqrt{k_t}l_t$. A one-equation turbulence model is used to describe the temporal and spatial evolution of the turbulent kinetic energy produced by wave breaking:

$$\frac{\partial k_t}{\partial t} + u_\eta \cdot \nabla k_t = \sigma\upsilon_t\nabla^2 k_t + B\upsilon_t\left[\left(\frac{\partial u}{\partial z}\right)^2 + \left(\frac{\partial \upsilon}{\partial z}\right)^2\right]_{z=\eta} - C_D\frac{k_t^{3/2}}{l_t} \tag{5-5}$$

The transport equation includes terms for the production, advection, diffusion and dissipation of turbulent kinetic energy. The second term on the right hand side represents the production of turbulent kinetic energy due to wave breaking, while the last term represents the dissipation of turbulent kinetic energy into heat. The waves are assumed to start breaking when the horizontal component of the orbital velocity at the wave crest exceeds the phase velocity of the waves. The length scale, l_t, is chosen to be the only free parameter in the turbulence model and is determined from comparisons of numerical model results with experimental results.

5.2.6 Damping Regions

Waves propagating out of the computational domain are absorbed in damping regions placed around the perimeter of the computational domain. Damping layers can also be used to model the partial reflection from harbour structures inside the computational area. Artificial dissipation of wave energy in damping layers is achieved through the introduction of terms, which are out of phase with free surface velocity and fluid acceleration, into the mass and momentum equations respectively:

$$F_{d\eta} = \mu\eta, \ F_{du} = \mu u_{\alpha} \tag{5-6}$$

where $\mu(x)$ is the damping strength (units of 1/s). Extensive tests of the performance of the damping layer shows that waves could be effectively damped out in a layer half a wavelength wide by employing a quadratic variation of $\mu(x)$, with a peak strength of 30/T (T = wave period). The damping strength has thus been non-dimensionalized with 30/T so that a damping coefficient of 1.0 corresponds to μ = 30/T. Figure 5.3 (WaveSim Manual, 2001) shows the variation of the reflection coefficient with damping coefficient for different relative widths of the damping layer.

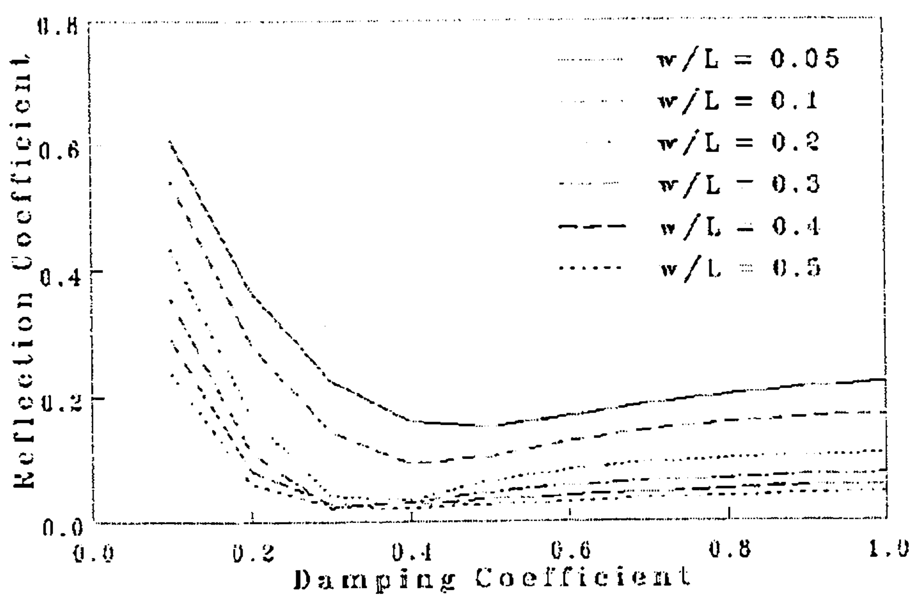

Figure 5.3 - Variation of reflection coefficient with damping coefficient (McDonald, 2001)

5.2.7 Flow through Porous Structures

Porosity layers are used to simulate partial reflection and transmission through porous structures such as breakwaters. The unsteady Dupuit-Forchheimer equation is used to describe the flow resistance in the porous layer:

$$F_p = f_1 \frac{(1-n)^3}{n^2} u_\alpha + f_2 \frac{(1-n)}{n^3} u_\alpha |u_\alpha| \tag{5-7}$$

where f_1 and f_2 are laminar and turbulent friction factors respectively. Empirical values of the laminar and turbulent friction factors for porous media with a characteristic stone size, D, were given by Engelund (1953) as:

$$f_1 = \alpha_0 v / D^2, \ f_2 = \beta_0 / D \tag{5-8}$$

where v is the kinematic viscosity of water and the empirical constant α_0 ranges from 780 to 1500 and β_0 ranges from 1.8 to 3.6. Figure 5.4 (WaveSim Manual, 2001) shows the typical variation of the reflection coefficient with porosity for different relative widths of a porous structure. Default values of the laminar and turbulent friction factors were used in the simulations.

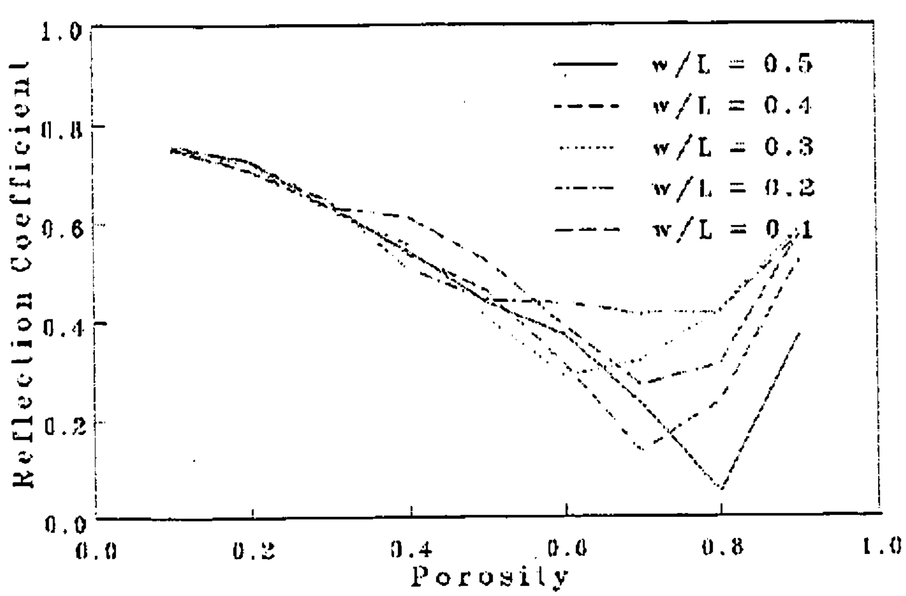

Figure 5.4 - Variation of reflection coefficient with porosity (McDonald, 2001)

5.2.8 Bottom Friction

The effect of the turbulent boundary layer at the seabed on the wave field has been modelled using a quadratic friction term with a Chezy coefficient, Ch:

$$\tau_{bf} = \frac{g}{Ch^2(h+\eta)} u_\alpha |u_\alpha| \tag{5-9}$$

In wave-induced flow fields, the bottom boundary layer is typically confined to a tiny region above the seabed unlike river and tidal flows where it extends all the way up to the free surface. There is, thus, very little wave energy attenuation due to bottom friction over typical wave propagation distances (on the order of 1 km) used in Boussinesq-type models. The bottom friction factor plays a more important role in wave transformation close to the shoreline and in wave-induced currents.

5.2.9 Numerical Solution

The numerical model solves the governing equations, expressed in terms of surface elevation, η, and two components of the horizontal velocity (u_α, v_α) at a specified depth z_α below the still water level, using a time-domain finite difference method. The iterative Crank-Nicolson method used by Nwogu (1993) was extended to spatial dimensions by using a line by line technique. The area of interest is discretized using a rectangular grid with the equation variables defined at every grid point in a staggered manner. The grid sizes in the x and y directions are Δx and Δy, respectively, and Δt is the time step size. The partial derivatives are approximated using a forward difference scheme for time and central difference schemes for the spatial variables.

The numerical solution scheme consists of three stages. The first one is the predictor stage in which the values of the variables at an intermediate time step $t = (i + ½)\Delta t$ are determined using known values at $t = i\,\Delta t$. The second one is the corrector stage in which the predicted values at $t = (i + ½)\Delta t$ are used to calculate an initial estimate of the values at $t = (i + 1)\Delta t$. The final stage is an iterative Crank-Nicolson scheme, which is repeated until convergence.

The numerical solution procedure consists of solving an algebraic expression for η at all grid points and tridiagonal equations for u_α, along lines in the x direction and v_α along lines in the y-direction at every time step.

5.2.10 Boundary Conditions

The external boundaries of the computational domain may be specified as wave generation boundaries or solid walls. Along wave generation boundaries, time histories of velocity fluxes corresponding to an incident storm condition are input. The incident wave conditions may be periodic or non-periodic, unidirectional or multidirectional. For multidirectional sea states, time histories of the velocity fluxes are derived from target directional wave spectra using the single summation, random phase method of wave synthesis (Miles and Funke, 1987). Outgoing waves are absorbed in damping layers placed next to solid wall boundaries. All model simulations start in the non-slip boundary condition, that is, all velocities are equal to zero. The water surface begins at the mean sea level. A ramping up stage, mentioned in Section 5.6.6, ensures that the simulation proceeds smoothly from the initial static condition.

5.3 Modelling Environment

Developed at CHC, EnSim was designed as an advanced numerical modelling environment, as well as a general purpose data handling and visualization system that could easily be adapted for any class of environmental data. EnSim provides an ideal framework for the integration of environmental data, GIS information and model data. An EnSim application can be designed to run a simple numerical model or a suite of numerical models providing a variety of pre- and post- processing tools. It is designed as a generic toolkit from which a system developer chooses components to create an application.

For the modeller, EnSim creates a virtual environment where simulation results can be viewed, animated and analysed in one, two, and three-dimensions. This allows the user to observe complex interactions of various phenomena in an intuitive manner, providing a realistic view of simulation results. Presentation of simulation results to non-technical audiences are greatly improved by providing seamless integration with other Windows applications such as word-processors, spreadsheets and multimedia tools (Farr, 2005).

The WaveSim environment then is essentially the graphical user interface (GUI) used for interacting with the Shoal2-D numerical model.

As aforementioned, the combined model and interface (Shoal2-D and WaveSim) will henceforth be referred to solely as WaveSim.

5.4 Computational Domain

Figure 5.5 shows the computational domain in its final configuration as compared to the physical modelling domain. Only the central test channel was reproduced in the numerical model since WaveSim is unable to produce currents within the domain. Section 5.5 discusses alternate configurations and testing that led up to this configuration. Figure 5.6 shows the computational domain both with and without the submerged structure. Figure 5.7 shows the arrangement of the numerical model with the locations of extracted simulation results (refer also to Figure 4.47). The extra probes will be discussed in Section 6.2.

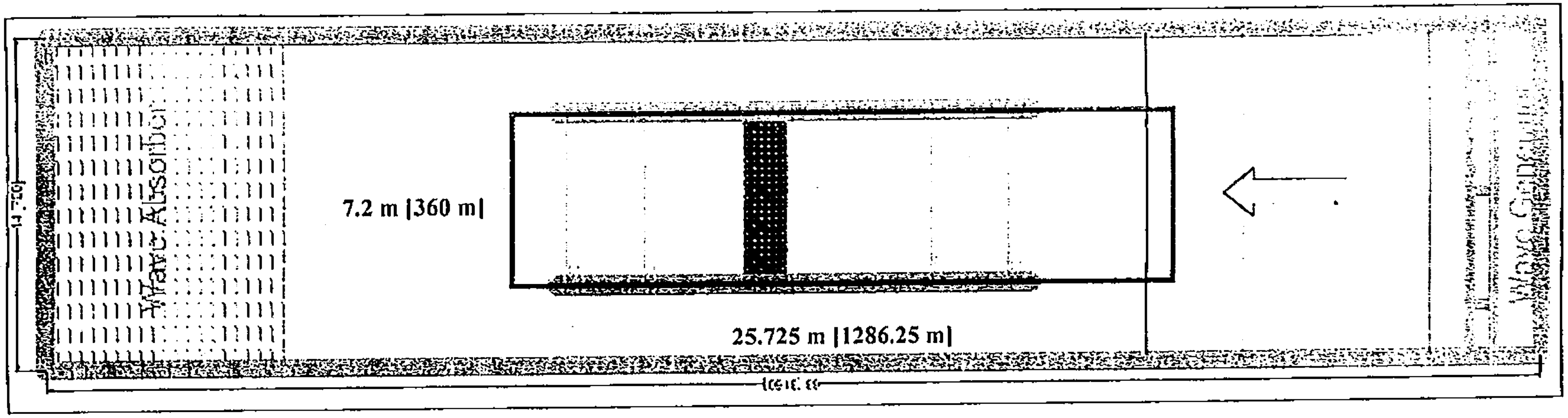

Figure 5.5 - Domain used for numerical modelling (denoted by the red outline)

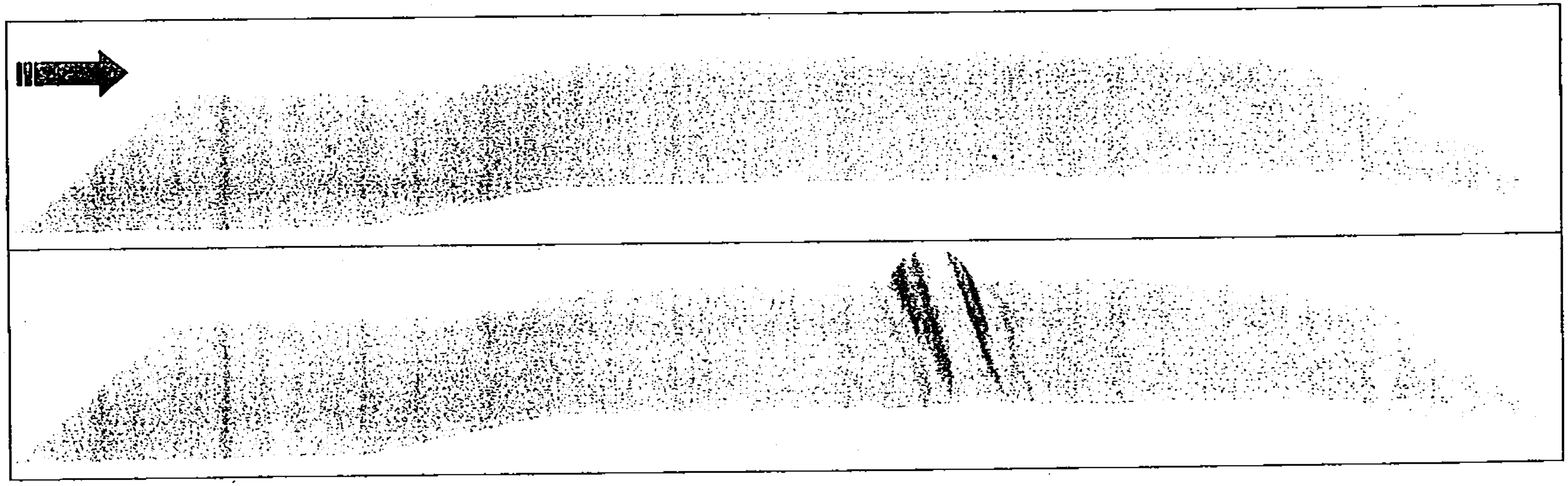

Figure 5.6 - Computational domain with and without the submerged structure

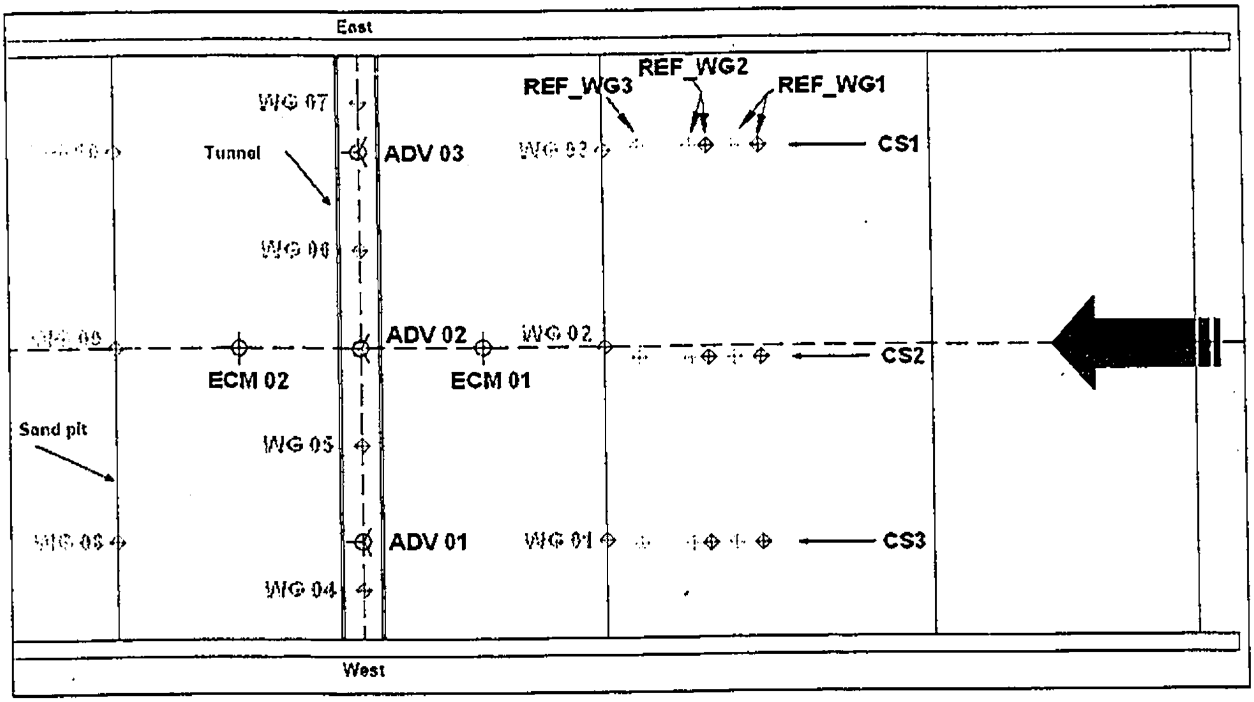

Figure 5.7 - Arrangement of the extracted simulation results in the numerical model
WG = Wave Gauges, ECM = Electromagnetic Current Meter, ADV = Acoustic Doppler Velocimeter

5.5 Model Testing and Calibration

Numerous "trial runs" were undertaken, firstly to train in the use of the model and the software environment, but more importantly to optimize the various model parameters and learn their effects on the results. The procedures described in Section 5.6 were finalized by the knowledge gained through the simulation trials.

5.5.1 Trial Series 1

The first approach to the numerical modelling was to work at model scale, identical to the physical experiments, and also to use the entire length of the Coastal Wave Basin (minus the side channels) in the computational domain. The first trial series comprised 10 simulations using coarser to finer grids, while other parameters remained essentially the same. The main focus of this series was to become more confident using the model and to observe the wave fields progressing through the domain before the structure was put in place.

5.5.2 Trial Series 2

In the second trial series, it was suggested to the author to try using a one dimensional flume to aid in determining further model parameters before attempting the full three dimensional simulations. A narrow "strip" down the centre of the wave basin was modelled, for the first time including the tunnel bathymetry. A series of 30 simulations were conducted using a number of different time steps and also experimenting with the porosity field. In fact, it is quite common for researchers using the WaveSim model to employ such a process when setting up numerical modelling simulations. The WaveSim Manual (McDonald, 2001) suggests that the damping and porosity characteristics should initially be calibrated in a one-dimensional numerical flume to match the desired reflection and transmission characteristics of the breakwaters or harbour structures.

5.5.3 Trial Series 3

In the third trial series, simulations of the three-dimensional tunnel were undertaken. A series of 28 simulations with a relatively fine time step was used, using coarser and finer spatial grid densities to varying success. When a coarse grid was used, the model was generally more stable; however the shape of the submerged structure was not captured very well. When a finer grid was used, the model sometimes behaved more erratically, with frequent instabilities developing almost exclusively at the deeper side just at or beyond the crest of the structure.

It was at first thought that the model was simply developing these instabilities as an unexpected boundary effect, and measures were attempted to abate the instabilities. After consultations with the thesis supervisors, it was suggested that the instabilities may have been caused by the relatively steep slopes of the structure, particularly at the "trenches" at the deep side of the submerged structure. At this point, a slightly modified structure bathymetry was created, in which the sharp depressions near the deep end of the structure were removed. Figure 5.8 shows the before and after images for the modified bathymetry. As shown, the crest elevation was maintained. However, the existing side slopes and toe protection were extended from partway along the structure, denoted by the red arrow (Note: the vertical (z) scale is exaggerated by a factor of 2).

These modifications to the shape of submerged structure greatly improved the overall stability of the simulations, and the earlier problems encountered were almost non-existent afterwards. Although modifying the structure geometry was not desirable, it was necessary in order to ensure the stability of the numerical simulations. As the geometry changes were relatively minor compared with the overall structure shape, the actual changes in the behaviour of waves passing over the structure are assumed negligible. Actually, the modification to the toe protection would have little effect on the observed flow conditions, and it is primarily the bulk of the submerged structure that is influencing the wave climate.

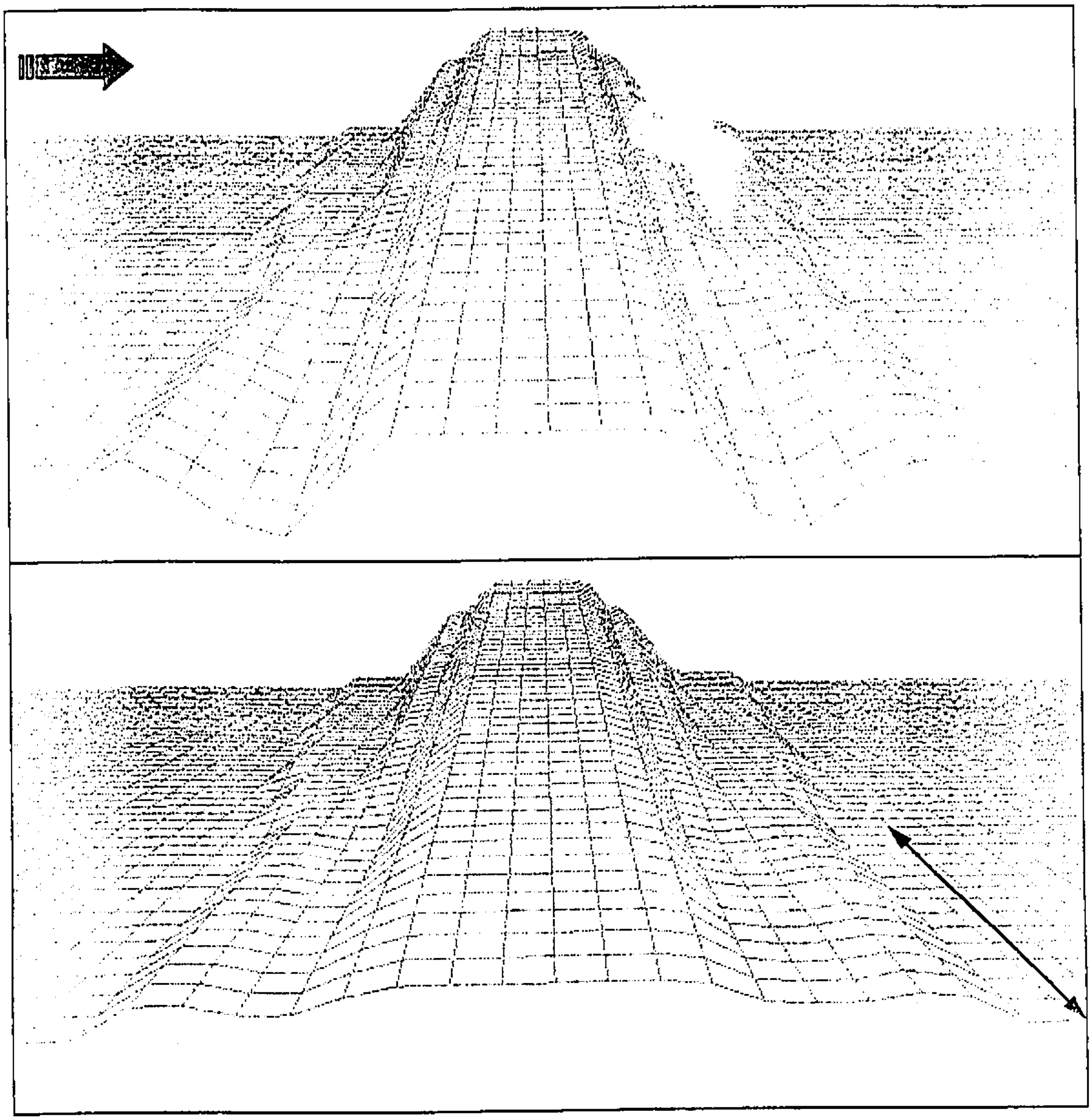

Figure 5.8 - Minor modification to the shape of the submerged structure

5.5.4 Trial Series 4

In the fourth trial series, some 13 simulations with the modified bathymetry and a slightly coarser time step were performed. These runs proved much more stable at the structure crest than the previous attempts. However, it was observed that minute noise-like instabilities were collecting near the numerical wave generator. It was initially thought that this noise might be due to extremely short wave reflection from the structure, and that if the modelling was done at full scale, these extremely small waves would disappear in the prototype sea. A further 10 simulations were conducted at full scale. However, the apparent reflection issue did not disappear. For this reason, an extra damping field was added behind the wave generator to absorb any waves that might be reflected from the structure.

It should be noted that the use of an extra damping layer behind the wave generator (i.e. internal wave generation) is a common technique in numerical modelling of wave propagation.

5.5.5 Trial Series 5

All simulations before this trial series used the same "base case" for the wave heights and periods. In the fifth trial series, additional simulations were conducted, using the actual various wave parameters required by the testing program. Longer duration simulations were also conducted to try and simulate the actual storm lengths used in the physical modelling. It was observed that instabilities eventually arose in the longer duration simulations, especially for the severe wave cases. Although it was undesirable to shorten the simulation times, the amount of data collected was indeed long enough, providing enough waves to ensure a reliable statistical analysis in comparison to the physical model data.

Further discussion on the various issues encountered is found in Section 7.3.1.

5.6 Numerical Modelling Procedures

5.6.1 Model Setup

Creating and running a simulation with WaveSim requires several different files. First, a WaveSim parameter file (.wsp file type) is automatically created by the application itself for each simulation. This file contains nearly all the information regarding a particular simulation, namely the:

- Full description of the simulation as defined by the user,
- Filename of the grid (bathymetry) data (.r2s file type),
- Filename of the damping data (.r2m file type),
- Filename of the porosity file data (.r2m file type),
- Location and details of up to 2 wave generators
- Simulation parameters, and
- Output options.

Figure 5.9 shows an example of the simulation information tab within WaveSim.

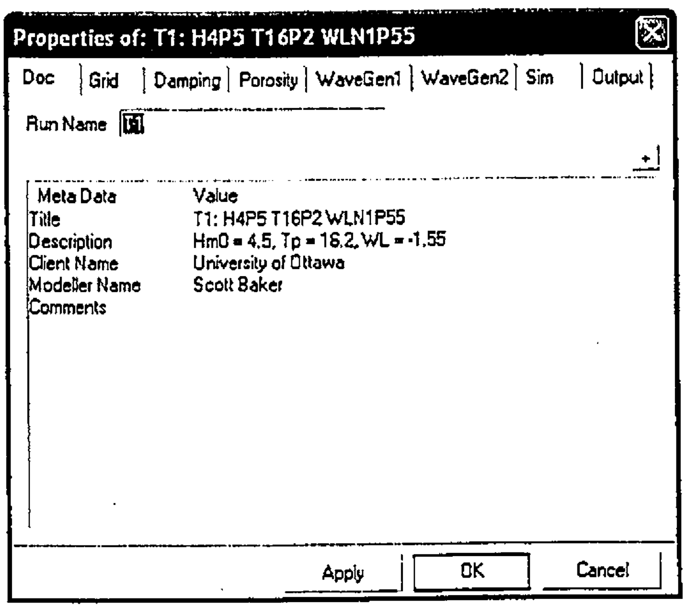

Figure 5.9 - WaveSim simulation information dialog box

5.6.2 Numerical Grid

After the description of the simulation is prepared, the next step is to establish a data point file (*.xyz file type), containing three columns of data with X, Y, and Z coordinates for each noteworthy point within the grid (i.e. slope changes, the domain boundaries and the profiles of the submerged structure). In order to accurately describe the shape of the submerged structure, cross-sections were extracted every 5 meters (prototype scale) from the AutoCAD drawings. WaveSim contains an internal grid generator to create a full three dimensional rectangular grid containing the bottom elevation information at each node of the grid. The WaveSim Manual (McDonald, 2001) states several rules with which the grid should comply:

- Land nodes should be defined as positive elevations, while water nodes should be defined as negative.
- Grid spacing (Δx, Δy) should be selected such that there are ten to twenty nodes per wavelength at the peak wave period, and at least six nodes per wavelength at the minimum wave period in the shallowest areas of the grid.
- Points of interest in the computational domain should be kept at least one wavelength away from the boundaries to minimize the effect of diffraction into the damping layers.
- The grid should be rotated such that the predominant wave direction is within ± 30 degrees of the normal to the wave generation boundary. Typically, the grid is rotated to align the grid axes with the predominant wave direction.
- The grid should not have steep slopes between nodes.

The most severe testing condition has a peak wave period of 20.1 seconds, corresponding to a wavelength of approximately 323 m (for a depth of 29 m). The grid node spacing along the direction of wave propagation should therefore be between approximately 16 and 33 meters to satisfy the first rule pertaining to the spacing. The minimum wave period considered by the numerical model is set as 3.6 seconds. However, for practical purposes, the minimum period considered is 6.66 seconds (0.15 Hz). This decision was made after analyzing the wave data and observing that hardly any spectral energy was appearing beyond this threshold. A frequency of 0.15 Hz yields a wavelength of approximately 69 m (for a depth of 29 m). The second rule then suggests a grid spacing of less than 12 m.

In order to capture the details of the submerged structure, however, it is necessary to implement a finer grid. The structure features a berm just over 5 meters in size, and the entire structure itself is only 91 meters wide (not including the scour protection) at its widest point. After numerous trial runs (described in Section 5.5), a grid size of 5.25 meters was selected for the direction of wave propagation. The cross-sectional variation of the structure is much more gradual in the direction perpendicular to the wave propagation. 25 grid spaces (grid size of 14.4 m) provided adequate detail and thus chosen. The model then computes and creates the grid required using the input data described above, seen in Figure 5.11.

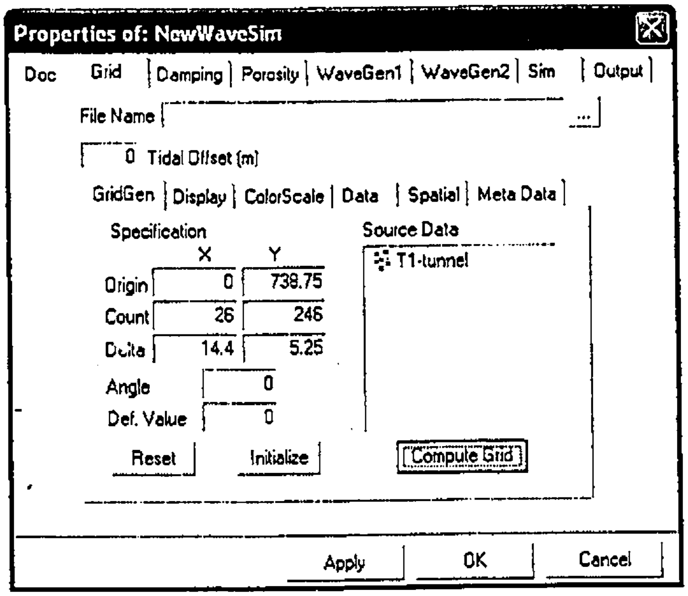

Figure 5.10 - WaveSim grid generation dialog box

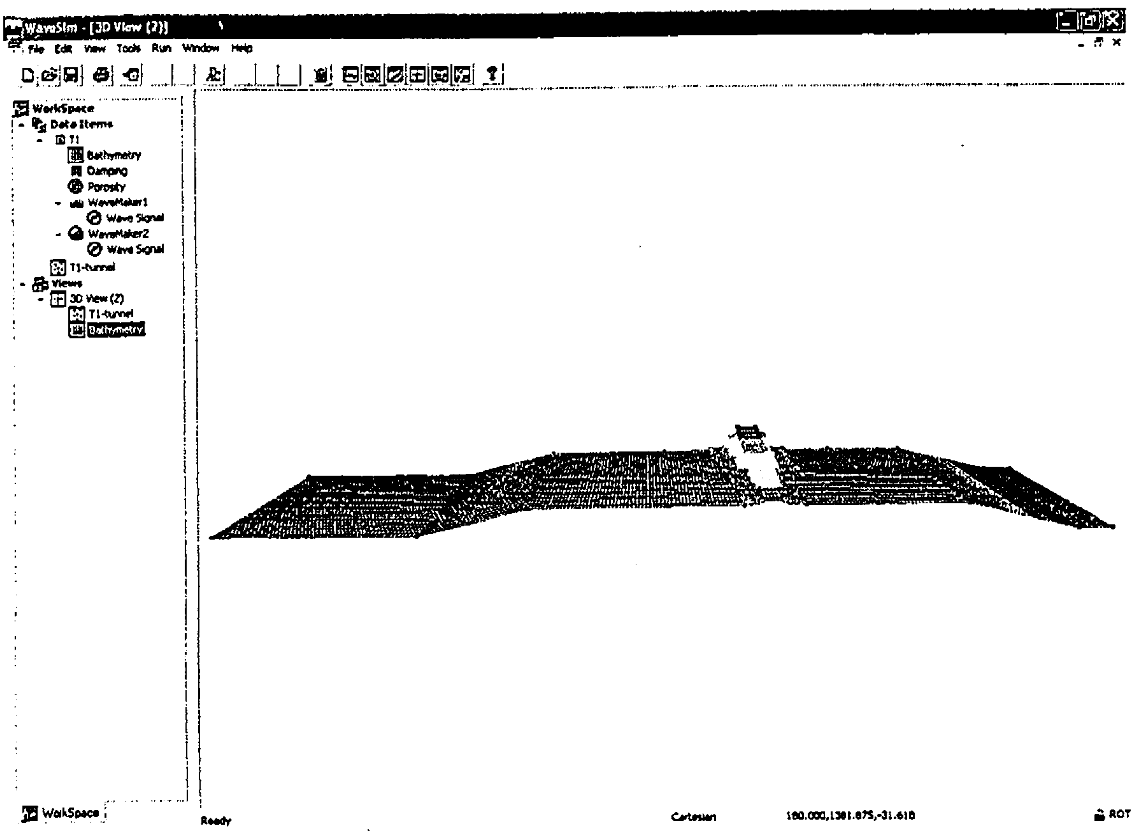

Figure 5.11 - WaveSim figure showing the computational domain and grid

5.6.3 Wave Damping

The next step is to establish the damping zones (numerical wave absorbers). Figure 5.12 and Figure 5.13 show the damping settings and overview of the damping in the numerical domain. The WaveSim Manual (McDonald, 2001) suggests that a damping coefficient of 1 (0 corresponds to no damping, 1 is full damping) and a width of half a wavelength should be used to absorb outgoing waves on the radiation boundaries. The worst case scenario has a 20.1 second wave propagating in 50 m of water, corresponding to a wavelength of just over 400 meters. Thus, damping layers with a width of 200 m should provide the desired effects. Through the trials (Section 5.5) and also learning information about how WaveSim is best suited to run by checking how simulations were setup for previous work, it was determined that the model is more stable when the numerical wave generator is not located directly on the boundary of the numerical domain. It is common practice to utilize another damping layer behind the wave generator. For this reason, the damping layers were set up such that boundaries 1 and 3 (corresponding to the front and back walls) have a 200 m damping layer with a coefficient of 1. Boundaries 0 and 2 (corresponding to the side walls) were left as solid walls, identical to the physical model.

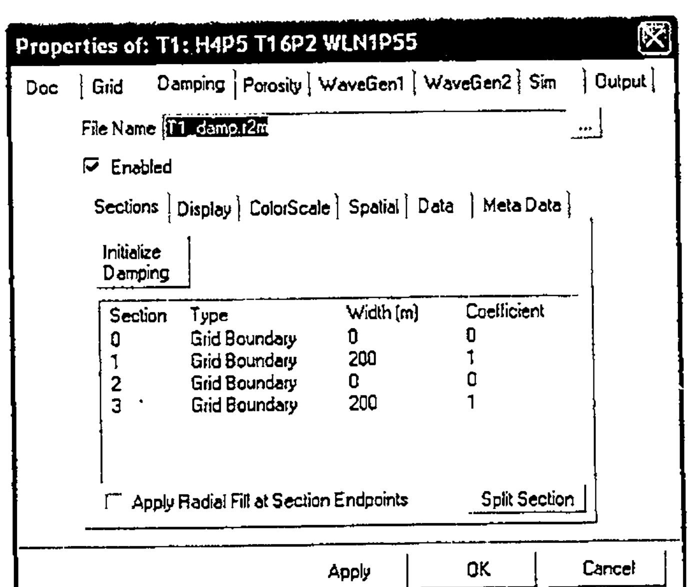

Figure 5.12 - WaveSim damping dialog box

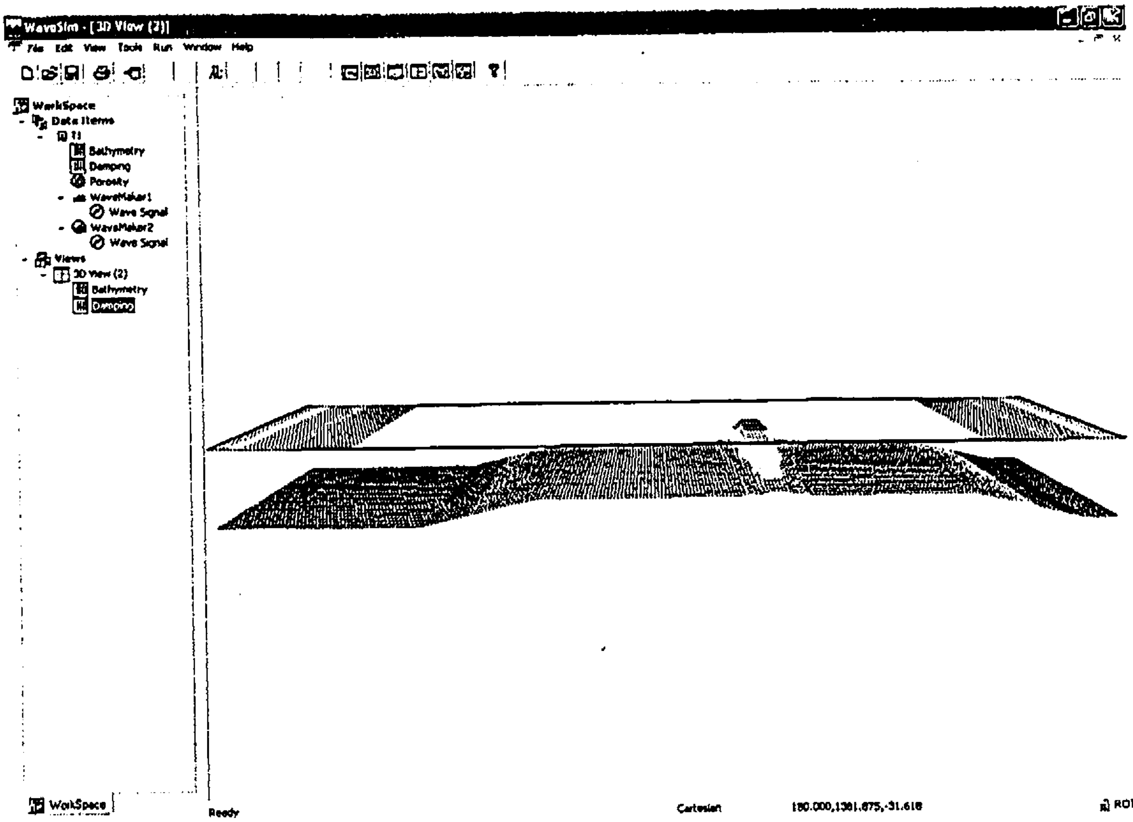

Figure 5.13 - WaveSim figure showing the damping fields for the computational domain

5.6.4 Structure Porosity

Including porosity fields in the model is optional. During the trials (Section 5.5), a narrow two-dimensional (quasi-1D) flume was considered and the effects of the porosity were tested as suggested in the WaveSim Manual (McDonald, 2001). A typical porosity coefficient for breakwaters is 0.4 (0 corresponds to highest effects, 1 to no effects). It was determined that the porosity layer is essentially considered as a rectangular sponge affecting the entire water column. In the case of a normal breakwater that rises out of the water, the effects of such a porosity layer would be highly representative of the actual effects. However, for the case of a structure that does not occupy the full water column, such a damping field would force unrealistic behaviour.

The prototype tunnel, constructed from steel, is impervious and occupies nearly the entire centre section of the structure; there would be a significant decrease in energy transmission through the submerged structure versus the case of a normal rubblemound structure of similar cross-section. Therefore, modelling the structure as simply part of the seabed would produce the most realistic results, since the numerical seabed is essentially impervious. For this reason, the porosity option was not enabled for the numerical simulations, as seen in Figure 5.14.

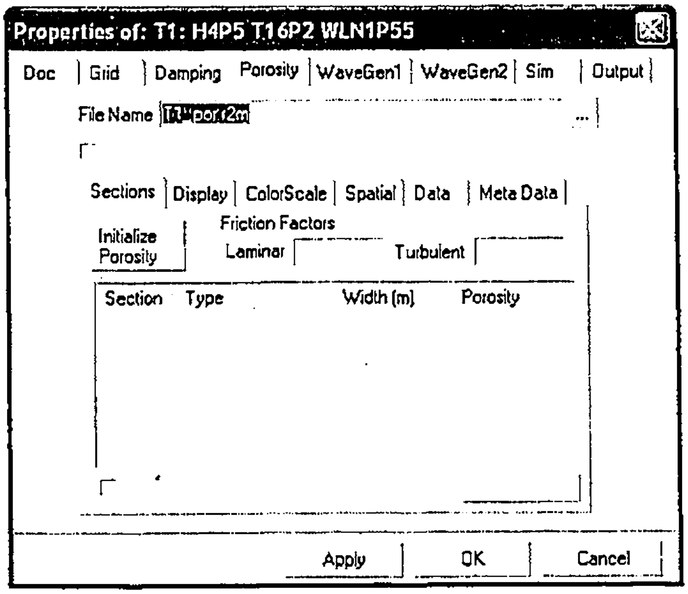

Figure 5.14 - WaveSim porosity dialog box

5.6.5 Wave Generation

The numerical model supports two possible wave generators. Since modelling the entire length of the basin was unnecessary, the numerical wave generator was placed closer to the bathymetry. Once the wavemaker is positioned, a series of options are available to specify additional parameters related to synthesized waves, as seen in Figure 5.15. In this instance, an irregular unidirectional wave was selected. The waves propagate along the basin, corresponding to a direction of 180 degrees. A random number seed can also be specified to produce different wave trains, however this option was not utilized, and the default value was used in all cases.

The drive signals used for the physical tests were each 2.5 hours long (1275 seconds at model scale). Extra time was added to ensure that waves generated at the end of the drive signal would have time to propagate past the test section and be measured, yielding an effective time of 1300 seconds (model scale). Converted to full scale, this corresponds to a test duration of approximately 9200 seconds. However from the trials (Section 5.5) it was determined that this relatively long test length duration could not be simulated numerically due to instability issues, especially for the worst case scenarios. The simulation durations for the first two cases was 4600 seconds, while for the remaining three cases, it was 2300 seconds. The numerical simulation durations were truncated, compared with the physical tests, in order to avoid numerical instabilities. Further discussion on this matter is found in Section 7.3.1.

Since the JONSWAP spectrum was used in the physical modelling, it was also used for the numerical modelling. The appropriate significant wave heights and peak wave periods were input for each test. Based on the significant wave height and period input, the model automatically calculates the minimum wave period it will consider which was used in each case. The maximum wave period considered is set as 1000 seconds as a default value, which was also used in each case. The model includes an option to rescale the spectrum, giving the user a choice to deal with high-frequency wave energy beyond the frequency cut-off limit. If selected, the truncated energy is redistributed uniformly across the useful frequency band (maintaining the H_s), but if not selected the truncated energy is lost (leading to a lower H_s). In this case, the option was not required since the wave energy was within the frequency limits. The peak-enhancement factor, gamma (γ) was set as 3.3 corresponding to fully developed seas. As γ increases, the spectrum becomes higher and narrower around the spectral peak (Onorato *et al.*, 2001).

The Phillips constant (α_p), also known as the equilibrium-range parameter (not shown in Figure 5.15), has a default value of 0.0081 of the JONSWAP spectrum, which was used in all cases. The influence of the parameter α consists in increasing the energy content of the time series and, therefore as α_p increases, the wave amplitude and consequently the wave steepness also increases (Onorato *et al.*, 2001).

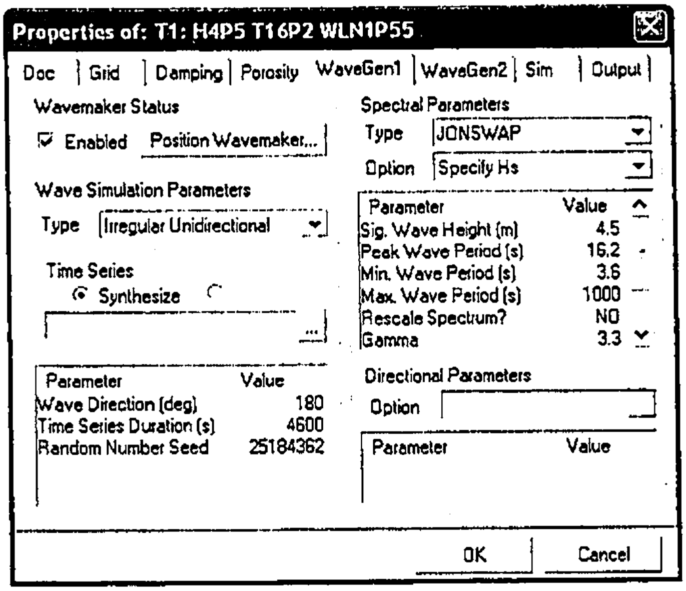

Figure 5.15 - WaveSim wave generation setup

The location of the wave generator after all parameters have been input can be seen in Figure 5.16.

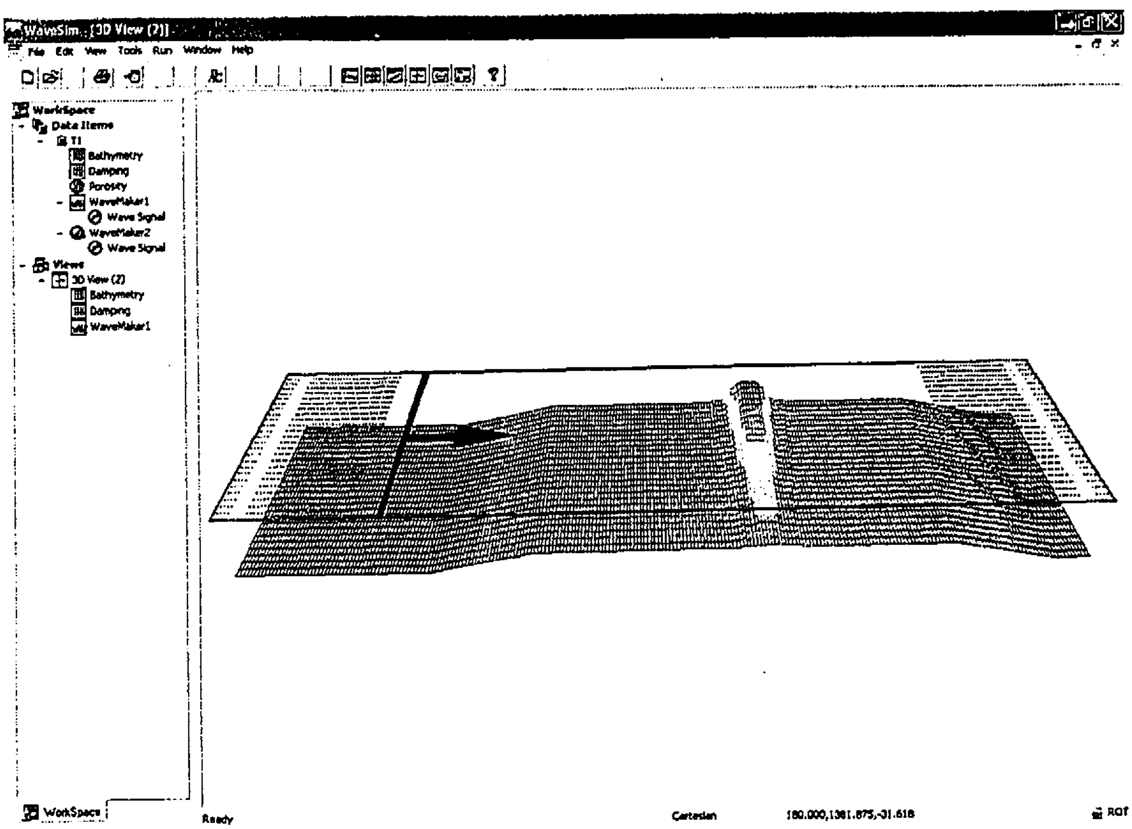

Figure 5.16 - WaveSim figure showing the wave generation and damping fields

5.6.6 Simulation Parameters

The next requirement of the model is selecting the runtime parameters. The run duration was set the same as the drive signal duration for all cases. The time step chosen was based on the numerous trials (see Section 5.5) attempted to determine an appropriate value, in this case 0.1 seconds. The model automatically calculates an estimate of the Courant number based on the following formula:

$$Cr = \sqrt{C^2 \Delta t' \left(\frac{1}{\Delta x^2} + \frac{1}{\Delta y^2} \right)} \qquad \textbf{(5-10)}$$

where C is the phase velocity calculated using the maximum water depth and the average zero-crossing period of the incident waves. Discussion on the calculated Courant number can be found in Section 7.3.1. Ramp duration is a time period over which the boundary conditions are ramped up from zero to their full respective values. This is typically set to one or two wave periods, and in this case the model defaults to two times the peak wave period, which was used in all cases. The default Chezy coefficient is 30, which was used for all cases.

The model allows for the use of either a weak or strong option for nonlinearity, each corresponding with the respective model of Nwogu from either 1993 or 1996. Since strong nonlinear behaviour is expected in the shallow regions of the structure and wave-induced currents, the strongly nonlinear option was selected, despite the warning about it being more computationally intensive. Wave runup was not a factor to be considered, and therefore this option was not selected. The wave breaking option, however, was selected, and the turbulent length scale was left at the default value of H_s. Figure 5.17 shows an example of the simulation parameters. Table 5.1 also presents a summary of the simulation parameters used for each run.

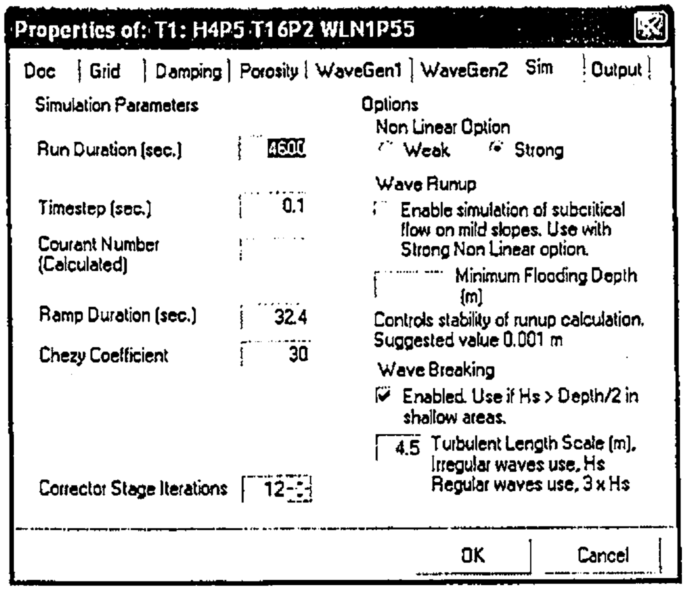

Figure 5.17 - WaveSim simulation parameters

Table 5.1 - Summary of simulation parameters

Case #	Run Duration (sec)	Time Step (sec)	Courant Number	Ramp Duration (sec)	Chezy Coefficient	Corrector Stage Iterations	Non Linear Option	Wave Breaking Option & Turbulent Length Scale (m)
0	4600	0.1	0.39	32.4	30	12	Strong	Enabled (4.5)
1	4600	0.1	0.39	32.4	30	12	Strong	Enabled (4.5)
2	2300	0.1	0.39	40.2	30	12	Strong	Enabled (6.0)
3	2300	0.1	0.39	40.2	30	12	Strong	Enabled (6.0)
4	2300	0.1	0.39	40.2	30	12	Strong	Enabled (7.0)

5.6.7 Output Options

The final task before running a simulation is to select the desired output options. The significant wave height option produces a time averaged plot over the entire simulation length of the significant wave height ($H_s(x,y)$) calculated as four times the standard deviation of the water level fluctuations ($\eta(x,y,t)$). The mean currents option produces a plot of the depth and time averaged current components $u(x,y)$ and $v(x,y)$. The surface elevation and velocity options produce instantaneous output for surface elevation ($\eta(x,y,t)$) and velocities ($u(x,y,t)$, $v(x,y,t)$) for a specified time period and time step. These files provide animations of the wave and current fields during the simulation. Although the model output data every 0.1 seconds (once for each time step), data was only used once every 0.5 seconds for the purposes of creating an animation. This resulted in a much smaller file size, yet still produced a smooth animation.

The final output option is to create specific data probes located at particular grid points. The model will automatically output the time series of water surface elevation ($\eta(t)$) and the horizontal velocity components ($u_a(t)$ and $v_a(t)$) at the selected point in both American Standard Code for Information Interchange (ASCII) and binary data formats, the latter being useful for the eventual data processing via GEDAP. The data probe locations were selected to match, as closely as possible, the location of the probes in the physical model. Figure 5.18 shows an example of the output options. Figure 5.19 and Figure 5.20 give examples of simulated wave and velocity records (compare with Figure 4.43 and Figure 4.46.)

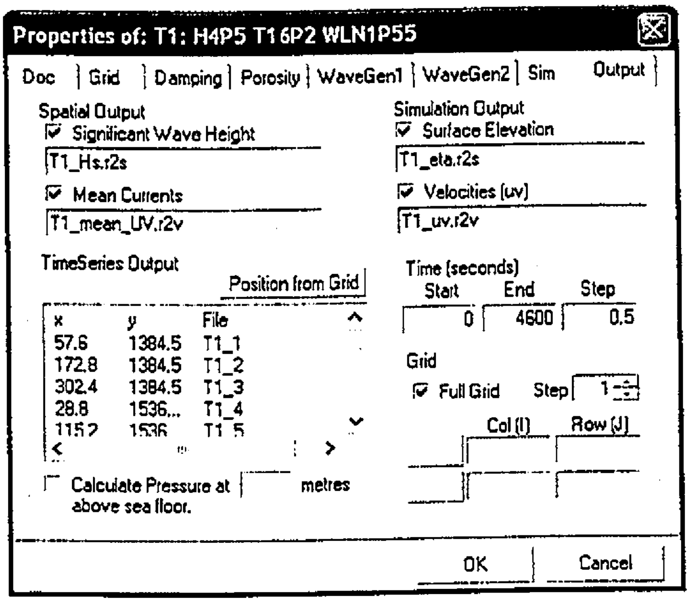

Figure 5.18 - WaveSim output options

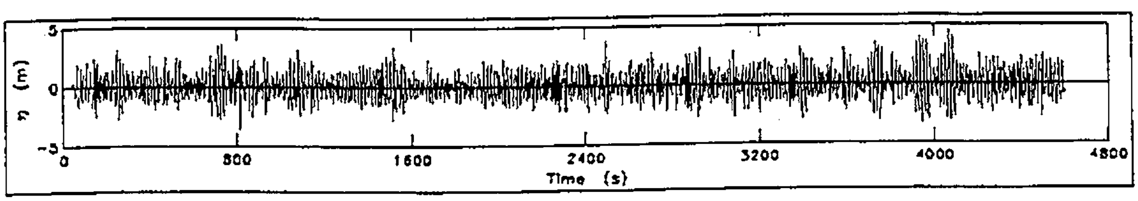

Figure 5.19 - Simulated wave record example (WG05 from Case 0)

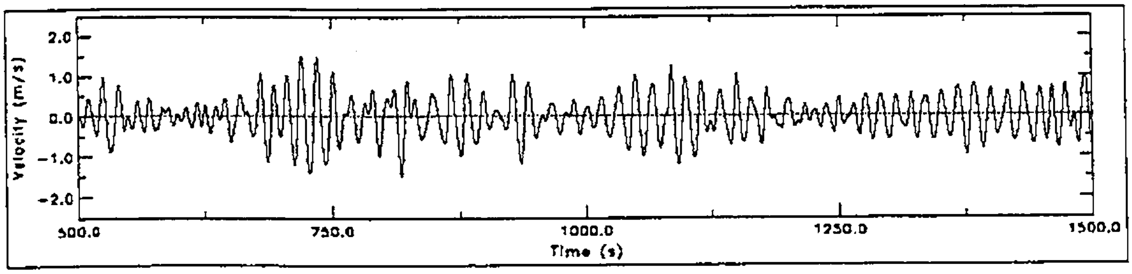

Figure 5.20 - Simulated velocity record example (ECM02 from Case 0)

5.6.8 Numerical Model Tests

Before executing the model simulation, WaveSim makes a simple check of the parameters for any obvious errors. The simulation can then be launched, starting in an MS-DOS command prompt window as an independent process.

The model first runs a sub-process that generates a file called wavegen_eta.001, containing the information for the wave generator based on the parameters defined previously. The model checks to see if the generated waves are in the linear regime. In this case, the tests with an H_{m0} of 4.5 meters are within the linear regime, however the remaining tests have wave heights that fall into the nonlinear regime (refer to Table 5.2). Figure 5.21 shows the warning message that is displayed. It should be noted that the model is quite capable of generating very large waves as would be expected, and this warning message should simply be a note to the user that free and forced nonlinear waves will be generated along the numerical wave generator, because linear wave generation theory has been used.

```
*** Warning: Incident wave height is in the nonlinear regime
             Free and forced nonlinear waves will be generated at
             the boundary since using linear wave generation theory
```

Figure 5.21 - WaveSim nonlinearity warning

After processing the wave generation data, the model reads in the bathymetry, damping and porosity grids. It then performs a calculation over the entire bathymetry grid to check for steep slopes. If slopes greater than 0.5 are detected, the model gives a warning, indicating the locations of these steep slopes. Figure 5.22 shows an example of the warning received for the simulations (the image was modified for brevity, since the steep slopes are occurring on the grid points along the entire structure). Discussion regarding the testing of other slopes is found in Section 7.3.1.

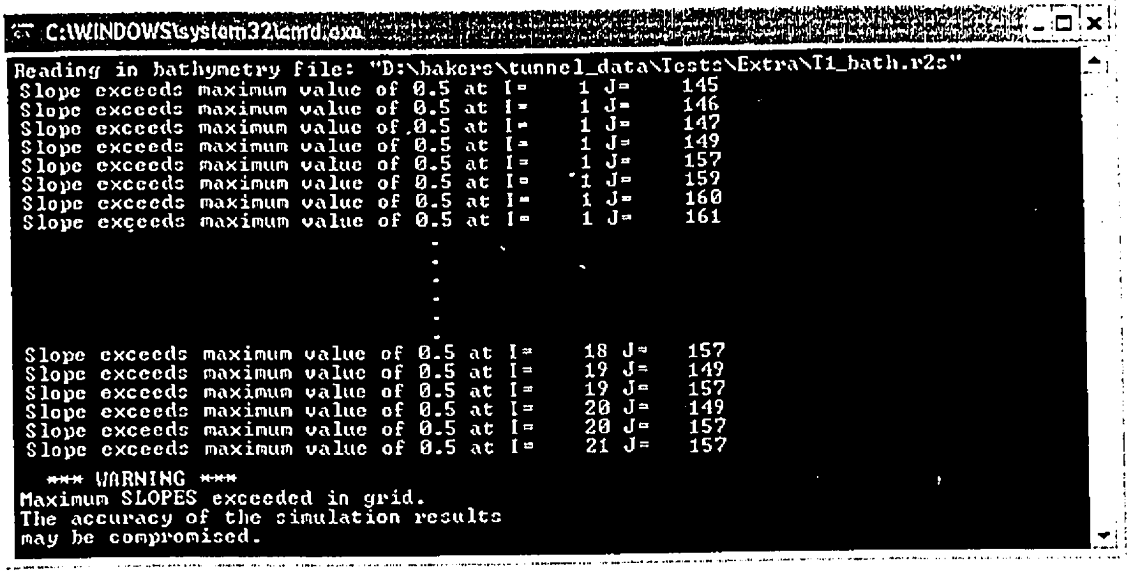

Figure 5.22 - WaveSim steep slope warning

After every ten time steps, the model makes an estimate of the remaining run time, which can vary depending on other processes being run on the computer at the same time. The 4600 second duration tests took approximately 90 minutes to run, while the 2300 second duration tests took approximately 45 minutes.

5.7 Numerical Modelling Simulations

5.7.1 Numerical Modelling Testing Series

The numerical modelling test series, presented in Table 5.2, was derived directly from the previous physical modelling work. As much as possible, the numerical simulations were setup to mimic one of the physical model tests. However, the numerical modelling tests were conducted at prototype scale as discussed earlier in Section 5.5.

Table 5.2 - Numerical experiment test cases

Test ID	H_{m0} (m)	T_p (s)	Water Level (m)	Simulation Duration (s)	Presence of Tunnel
Case 0	4.5	16.2	−1.55	4600	No
Case 1	4.5	16.2	−1.55	4600	Yes
Case 2	6.0	20.1	−1.72	2300	Yes
Case 3	6.0	20.1	−5.00	2300	Yes
Case 4	7.0	20.1	−5.00	2300	Yes

Case 0 corresponds to the calibration case with no structure in place, corresponding with the equivalent physical experiment Case 0. Numerical simulation Cases 1-4 correspond with the equivalent physical experiment Cases 1-4 (see Table 4.9).

5.7.2 Numerical Model Results

Figure 5.23 shows the representation of the submerged structure in the numerical model in its initial equilibrium condition. This image is true to scale, giving a feel for the relative size and shape of the structure and its relative submergence below the mean sea level. Figure 5.24 shows a snapshot of the model results at one instant during the simulation. The results of the numerical model can be played back to watch the full history of the waves and their transformations over the submerged structure.

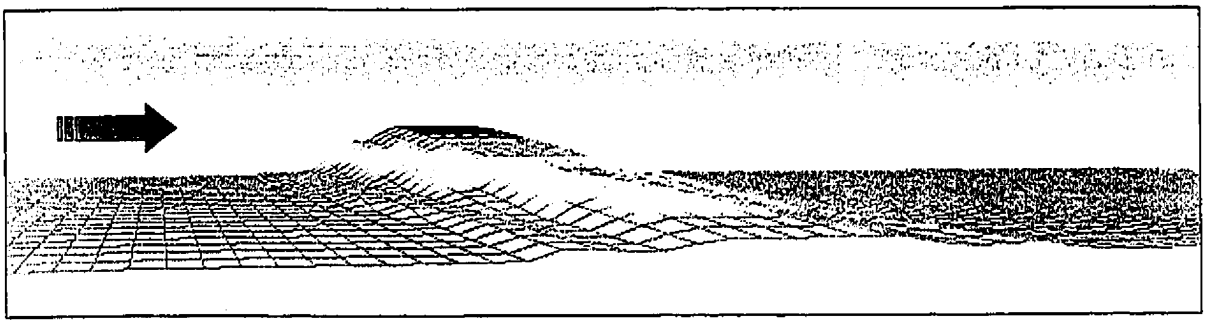

Figure 5.23 - Image of simulation in starting condition

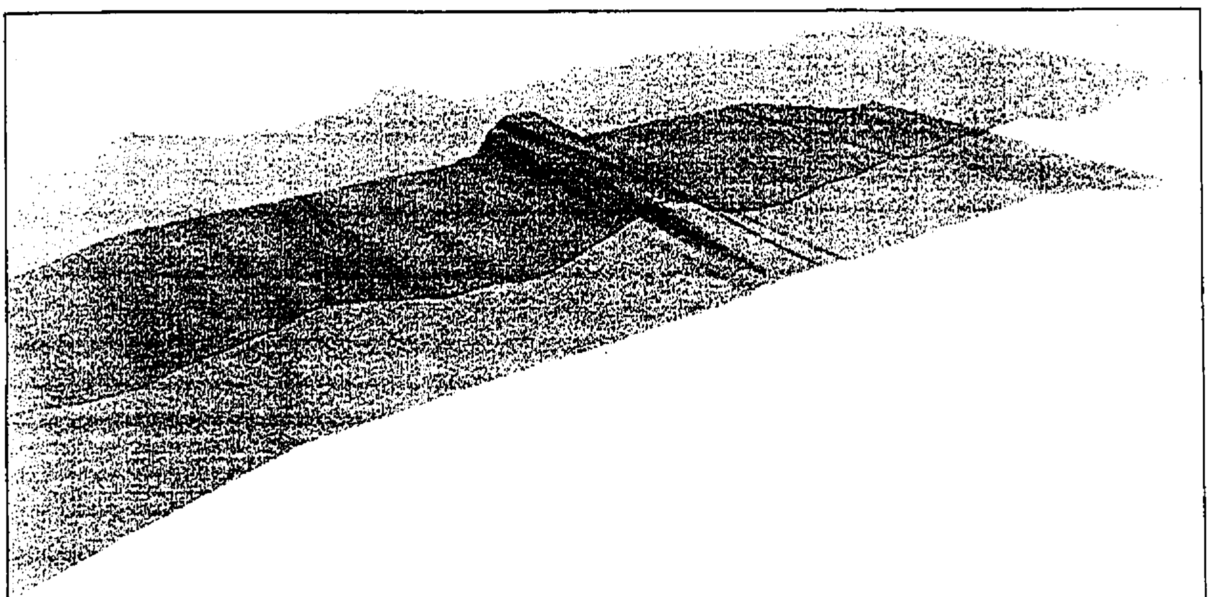

Figure 5.24 - Numerical modelling simulation in progress

6 Data Analysis

6.1 Introduction

CHC's GEDAP software was used for all data analysis. The basic organization of the system is shown in Figure 6.1. The NDAC package provides real-time data acquisition and control for both analog and digital signals. GPLOT is an extensive interactive graphics package that allows data to be easily examined at any stage of the analysis process. The ANALYSIS package contains a comprehensive set of more than 150 data analysis programs organized in eight groups as shown. Since GEDAP is an open system, users can also easily add their own analysis programs by taking advantage of more than 350 subroutines available in the various GEDAP libraries (Miles, 1997).

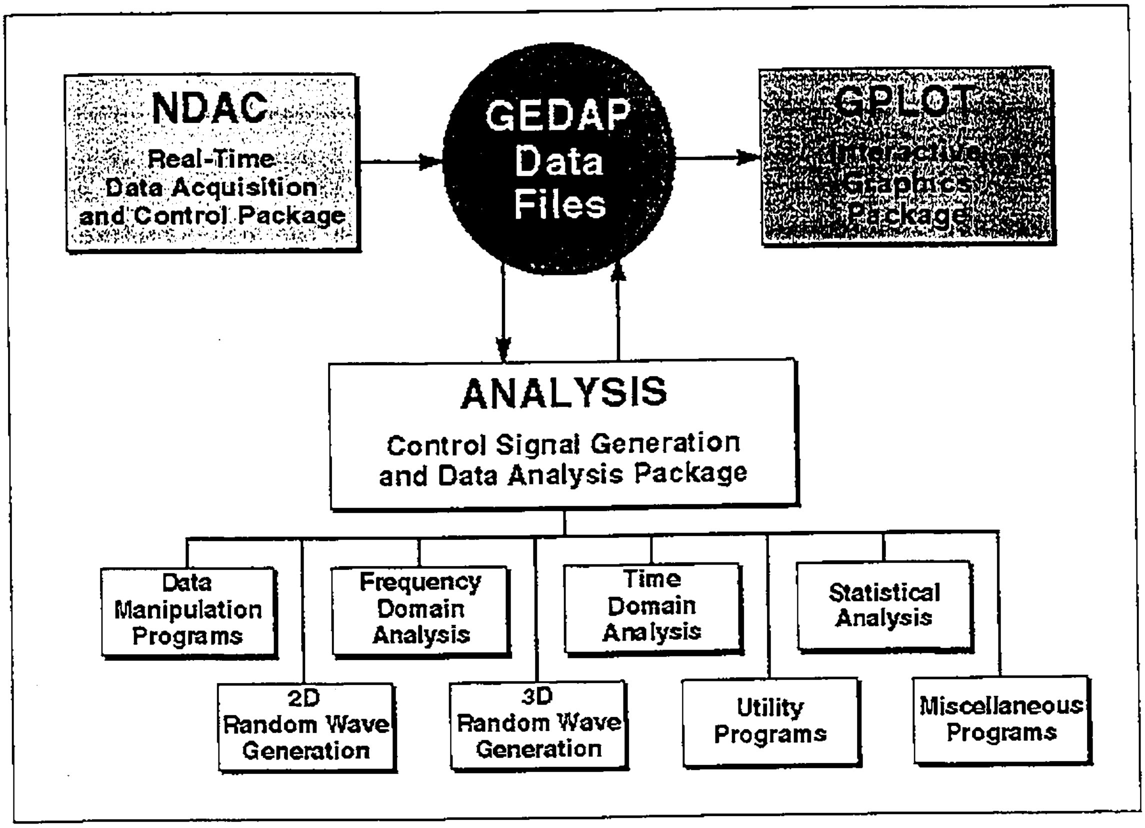

Figure 6.1 - GEDAP block diagram

6.2 Data Analysis Programs

Standard GEDAP time-domain and frequency-domain analysis algorithms were applied to analyse the wave conditions measured in both the physical and numerical models in considerable detail. The following sub-sections (Sections 6.2.1 to 6.2.13) each contain partially modified excerpts from the GEDAP documentation (Miles, 1997), as well as information about the input, runtime parameters and output for the data analysis routines.

6.2.1 GEDAP Program STAT1

STAT1 computes the following basic statistics for any record:

1. Minimum value,
2. Maximum value,
3. Mean value,
4. Standard Deviation from the mean, and
5. RMS value (including the mean).

The file to be analyzed is passed to the program, which then calculates the statistics and subsequently places the information back into the header of the same file.

6.2.2 GEDAP Program STAT5

STAT5 computes a probability density histogram and a cumulative distribution histogram along with corresponding fitted curves for a set of independent samples. The histograms are computed using constant-width cells defined as $(X_{max}-X_{min})/N_{cells}$ where X_{max} and X_{min} are the maximum and minimum values of the data. The program fits the equivalent theoretical probability density to the input data, in this case on the Rayleigh distribution fitted on the basis of the mean of the data. A χ^2 goodness-of-fit test is also performed.

6.2.3 GEDAP Program FILT_FFT

FILT_FFT applies a rectangular bandpass filter to a time series signal. This filter removes all energy in the signal that occurs at frequencies below f_1 Hz and at frequencies above f_2 Hz which are specified by the user. The Fourier transform of the input signal is computed by FFT and the rectangular bandpass filter is applied in the frequency domain. An inverse FFT is then used to obtain the filtered output signal.

FILT_FFT removes the mean value of the input signal prior to applying the filter. The original mean value can also be added to the filtered output signal as an option.

6.2.4 GEDAP Program POLAR_2-D

POLAR_2-D converts a 2-D vector time series defined by x(t) and y(t) components into polar coordinates defined by R(t) and θ(t) where:

$$R(t) = \sqrt{x(t)^2 + y(t)^2}$$
$$\theta(t) = \arctan(y(t)/x(t)) \tag{6-1}$$

POLAR_2-D can be used to convert velocity data from z-axis current meters into polar coordinates. The Fortran ATAN2 function is used to compute θ(t) so that the resulting angle will be calculated correctly in all four quadrants from -180 to 180 degrees depending on the signs of the x(t) and y(t) components. θ(t) is measured in the counter-clockwise positive direction relative to the x axis. Thus, $\theta = 0°$ when the velocity is in the +x direction, and $\theta = 90°$ when the velocity is in the +y direction.

6.2.5 GEDAP Program ZCA

ZCA performs a detailed zero crossing analysis on a time series signal. It is designed primarily for wave elevation records but it may also be used to analyse other types of data such as force records. ZCA performs both zero up-crossing and zero down-crossing analyses. Figure 6.2 (IAHR, 1986) depicts how the zero crossing analysis is performed on a typical wave record, in this case a zero up-crossing.

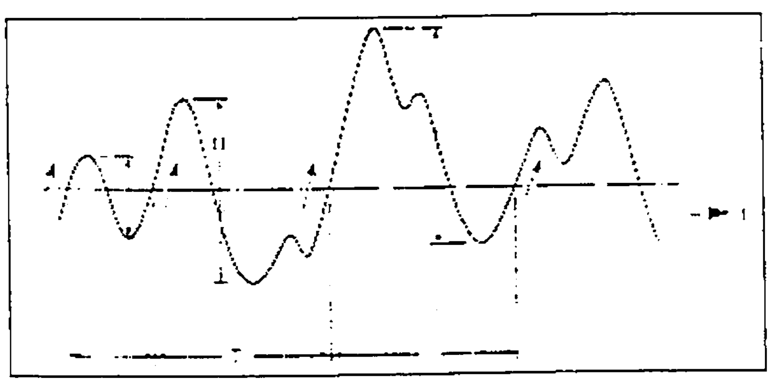

Figure 6.2 - Definition of zero crossing analysis

Two different classes of wave parameters are calculated from the analysis. Class 1 consists of parameters which are defined for each individual wave cycle in the record, such as crest height, wave steepness, and asymmetry, and are stored as data vectors. Class 2 consists of parameters which apply to the entire wave record, such as significant wave height, maximum wave height, and average period. ZCA checks the time spacing of the input signal to make sure that the sampling rate is high enough for accurate zero crossing analysis.

The file to be analyzed is passed to the program, which then asks for the water depth at the location of the wave gauge. Alpha is the amplitude threshold used to detect a zero crossing wave cycle. This prevents small amplitude noise ripples from being counted improperly. It is defined as a percentage of the standard deviation of the input wave record. In this case the default value of 2% was used, which the program describes as satisfactory in most cases. T_{min} is the minimum wave period threshold for wave cycle detection. The default value is 0.0 seconds meaning that all cycles which exceed the Alpha amplitude will be counted regardless of how short their periods are. The option to remove trends in the data is selected, in this case Option 1, to remove the mean value prior to analysis. Finally, an option for the vertical asymmetry factor is used. The program then performs its analysis and outputs optional files as selected by the user.

6.2.6 GEDAP Program ZCA3

ZCA3 performs a zero down-crossing analysis on time series records. It detects the peaks and troughs of the signal and stores them in output files for subsequent analysis by programs such as STAT5. Zero down-crossings are used to define cycles, thus a cycle consists of a trough followed by a peak. The zero crossing analysis is performed relative to a reference level specified by the user. Amplitude and period thresholds are defined by the user similar to ZCA.

6.2.7 GEDAP Program PEAKS

PEAKS performs a peak detection on a time series signal. In contrast to programs ZCA and ZCA3, the peaks are not defined by zero crossing analysis but are defined by the local maxima of the signal instead. A peak is detected whenever a local maximum of the signal exceeds the local minima on each side of it by a threshold level chosen by the user. The main purpose of this peak amplitude threshold is to prevent small ripples due to noise in the signal from being counted as valid peaks.

In some cases, peaks which are too close together in time cannot be considered to be independent, and in order to handle this situation, PEAKS also allows the user to specify a minimum time permitted between two peaks. If any two peaks are closer together than the specified time, then the smaller peak is discarded and the larger peak is retained.

6.2.8 GEDAP Program VSD

VSD is a general purpose program for variance spectral density analysis. The spectral density is obtained by smoothing the modified periodogram of the total record. The modified periodogram is obtained by multiplying the signal by a data window prior to taking the FFT. The purpose of the data window is to reduce leakage when processing noncyclic data. The data window option allows for a trapezoidal or cosine bell, in this case the former is used. The data window can be bypassed when processing cyclic data by setting alpha = 0.0 where alpha is the non-dimensional data window transition length. The modified periodogram is smoothed by using a simple moving average filter. The length of this filter is set to obtain either a specified filter bandwidth or a specified number of degrees of freedom per spectral estimate. For the analysis, the filter bandwidth was specified as 0.005 Hz.

6.2.9 GEDAP Program VSD_WAVE

VSD_WAVE is a modified version of program VSD which is used for analysis of water surface wave elevation records. It calculates the following four spectra of a wave elevation record:

1. The main wave variance spectrum $S_\eta(f)$
2. The long wave variance spectrum $S_{lw}(f)$
3. The main wave power spectrum $S_{pwr}(f)$
4. The long wave power spectrum $S_{lw\text{-}pwr}(f)$

The first two spectra are the variance spectra of the two major frequency bands on the input wave elevation time series record. Each wave power spectrum is computed from the corresponding wave variance spectrum as follows:

$$S_{pwr}(f) = \left((\rho_w \cdot g)/1000\right) \cdot c_g(f) \cdot S_\eta(f)$$
$$c_g(f) = \text{group velocity of waves at frequency } f \qquad \text{(6-2)}$$

Thus, the wave power spectrum has units of (kW/m)/Hz and is the wave power (or energy flux) per unit width of wave crest per unit frequency interval. The integral of $S_{pwr}(f)$ over all frequencies is the total wave power per unit crest width.

The long-wave spectrum extends for f_1 to f_2 Hz, and the primary spectrum extends from f_2 to f_3 Hz, specified by the user. The spectral density is obtained in a similar fashion as VSD described in Section 6.2.8.

6.2.10 GEDAP Program TRFRA

TRFRA computes the amplitude of the transfer function of a linear system from the variance spectra of its input and output signals. If the input signal is x(t) and the output signal is y(t), then the amplitude of the transfer function $H_{xy}(f)$ of the linear system is given by the following:

$$\left|H_{xy}(f)\right|^2 = \frac{S_y(f)}{S_x(f)} \tag{6-3}$$

where $S_x(f)$ is the auto spectrum of the input signal x(t) and $S_y(f)$ is the auto spectrum of the output signal y(t). It can only compute the amplitude of $H_{xy}(f)$ but not the phase.

6.2.11 GEDAP Program REFLS

REFLS performs wave reflection analysis for the case of two irregular wave trains travelling in opposite directions in a wave flume or basin. A linear array of three wave probes is used to measure the wave elevation at three positions near the reflecting structure. Each probe measures the total wave elevation due to the sum of the incident wave train moving towards the structure and the reflected wave train moving away from the structure. The incident wave train travels in the direction from probe 1, to probe 2, to probe 3, and the reflected wave train travels in the opposite direction. Thus, probe 1 is the one nearest to the wave generator and probe 3 is the one nearest to the reflecting structure. The spacing of the probes is a factor in the results, and should be based on the following recommendations:

$$\begin{aligned} &X_{12} = L_p/10 \\ &L_p/6 < X_{13} < L_p/3 \end{aligned} \tag{6-4}$$

where L_p is the wavelength of the peak frequency, X_{12} is the distance between probes 1 and 2, and X_{13} is the distance between probes 1 and 3.

For simplification, wave probe 3 was selected at a fixed location in front of the structure for all cases of reflection analysis. The spacing of probes 1 and 2 were then calculated based on of the parameters laid out in Equation ((6-4). The locations of the three probes were optimized such that they were generally centered between the submerged structure and the beginning of the bathymetry at the same elevation as the base of the structure (i.e. centered on the flat section in front of the structure).

For Cases 0 and 1, the water depth of 32.45 m and peak period of 16.2 s yields a wavelength of 264.91 m. Placing the probes at the closest grid nodes produced spacings of X_{12} = 26.25 m and X_{13} = 57.75 m.

For Case 2, the water depth of 32.28 m and peak period of 20.1 s yields a wavelength of 338.38 m. Placing the probes at the closest grid nodes produced spacings of X_{12} = 42 m and X_{13} = 73.5 m.

For Cases 3 and 4, the water depth of 29 m and a peak period of 20.1 s yields a wavelength of 322.58 m. Placing the probes at the closest grid nodes produced spacings of X_{12} = 42 m and X_{13} = 73.5 m.

The program uses the 3-probe wave reflection analysis method of Mansard and Funke (1980). This method is based on linear wave theory and uses three complex transfer functions to compute the Fourier transforms of the incident and reflected wave trains in the frequency domain. The corresponding time series for the incident and reflected wave trains are then computed by using the inverse FFT. The average reflection coefficient C_r is also computed as follows:

$$C_r = \frac{\sigma_r}{\sigma_i} \tag{6-5}$$

where σ_r is the standard deviation of the reflected wave train $\eta_r(t)$ and σ_i is the standard deviation of the incident wave train $\eta_i(t)$.

The incident and reflected wave trains are computed over the frequency range from f_1 to f_2 where f_1 and f_2 are specified lower and upper frequency limits. These limits are used to avoid frequencies where the wave energy is too small to allow accurate determination of the incident and reflected components. They are also used to avoid the singular frequencies associated with the wave probe spacing. In this case, the lower and upper frequency limits were chosen by the non-dimensional ratios of f_1/f_p and f_2/f_p of 0.6 and 2 respectively, which are commonly used values.

The program also calculates a tapering down to zero at each end of the wave signal to prevent oscillations in the FFT operations. The taper length has a recommended value of $(2/f_p)$, in this case a taper length of 50 seconds was applied in all cases. The program outputs the incident and reflected wave trains in two files with the reflection coefficient information in the header.

6.2.12 GEDAP Program XSPEC1

XSPEC1 computes the complex cross-spectrum $S_{xy}(f)$ of two time series signals named x(t) and y(t), representing the input and output signals from a linear system. The frequency response of the linear system is defined by a complex transfer function $H_{xy}(f)$ that is related to the cross-spectrum $S_{xy}(f)$ as follows:

$$S_{xy}(f) = H_{xy}(f) \times S_x(f) \tag{6-6}$$

where $S_x(f)$ is the auto-spectrum of the input signal x(t). The following functions are created and stored in output files:

1	$\lvert S_{xy}(f)\rvert$	magnitude of cross-spectrum $S_{xy}(f)$,
2	$\varphi(f)$	phase lag of cross-spectrum $S_{xy}(f)$,
3	$S_x(f)$	auto-spectrum of signal x(t),
4	$S_y(f)$	auto-spectrum of signal y(t), and
5	$G_{xy}(f)$	coherence function of x(t) and y(t).

The phase $\varphi(f)$ is defined as a lag so that it will have positive values for typical linear systems, thus:

$$S_{xy}(f) = \left|S_{xy}(f)\right| \times \exp^{(-i\cdot\varphi(f))} \tag{6-7}$$

These five functions are computed for frequencies between F_1 and F_2 Hz which are the lower and upper cut-off frequencies. By default these frequencies are set at the upper and lower 1% power limits of the spectrum input signal.

The coherence function is related to the auto and cross spectra as follows:

$$G_{xy}(f) = \frac{|S_{xy}(f)|}{\sqrt{S_x(f) \times S_y(f)}} \tag{6-8}$$

$G_{xy}(f) = 1$ by definition if x(t) and y(t) are the input and output signals of a perfectly linear system with constant parameters. Conversely, if x(t) and y(t) are completely unrelated, then the coherence function will be zero. The auto-spectra and the cross-spectrum are calculated by the Welch method.

6.2.13 GEDAP Program REFLA

REFLA separates the incident and the reflected spectra from a measured random sea state. This method is based on the least-squares analysis using data from 3 probes. A wave train sampled at three probe locations must first be processed by the program XSPEC1 to obtain the cross spectra between probes 1 and 2, and also between probes 1 and 3. Probes 1, 2, and 3 are located in the same fashion as described in the program REFLS. The cross-spectral density files from XSPEC1 are then used as input files to this program. Digital filter limits can be applied so that the components with little or no energy content need not be analysed.

6.3 Data Analysis Routines

The GEDAP software provides the ability to perform batch processing of data. A number of routines were coded to perform a range of analysis on all the measured data from the various experiments and simulations. These results are discussed in considerable detail in Section 7.

7 Results and Discussion

A substantial amount of data was collected from the physical and numerical modelling undertaken in this research project in order to study and analyze the transformation of the wave and wave-induced velocity climate over a submerged structure. This data analysis is now presented and thoroughly discussed.

7.1 Comparison between Experimental Data and Numerical Results

A significant amount of comparison can be made between the physical experiments and numerical simulations, namely a study of the wave climate, the transfer function over the structure and an investigation of the wave-induced velocities.

Figure 7.1 presents a summary of the physical and numerical modelling boundaries and domains. Before comparisons can be made between these two methods, it is necessary to examine the possible sources for error in the measurements. In this figure, the blue arrow denotes long crested unidirectional waves propagating from the respective wave generators. For the numerical domain, the simplified basin eliminates several possible sources of error, since this domain will behave essentially as a wide flume with no disruptions from internal objects, aside from the submerged structure itself. Arrow #1 denotes possible reflection due to the damping sponge layer used to absorb the outgoing waves. The reflection in this case is considered quite small, on the order of less than 5% (calculated from an additional simulation), since the numerical damping is done gradually, much like a long mildly sloped beach absorbing the wave energy. The numerical domain is effectively as close to the perfect conditions for studying the true effects of the submerged structure on the wave climate as possible.

A significant potential source of error for the numerical modelling is the actual model itself. The results can only be as accurate as the conceptual model, based on the Boussinesq equations, used to generate the numerical model and all the parameter assumptions. The WaveSim model has undergone a lengthy process of development to its current state, and although it is not perfect, it is still an excellent tool for modelling the propagation of ocean waves.

The physical modelling domain is far more complicated, presenting a number of possible sources which could contaminate to a certain extent the measured data. Similar to the numerical modelling case, Arrow #2 denotes possible reflection due to the main wave absorbers located at the back of the basin. Unlike the numerical case though, the physical wave absorbers would have less of a gradual effect, and there exists a strong likelihood that a reflection on the order of 5-10% (based on the experience of CHC researchers) would be observed. Some of this reflected energy could undoubtedly travel back towards the submerged structure. Similarly, the extra wave absorber employed just behind the submerged structure to balance the current in the test channel could potentially produce a similar level of reflection. One of the main differences between the numerical and physical domains is the main test channel and side channels. Because the bathymetry is present in the main channel, the propagation speed of the wave crests would be faster in the side channels, causing the crests to become out of phase, as previously mentioned. When the wave crests in the side channels reach the ends of the masonry wall, diffraction occurs causing some wave energy to bend around the wall. The diffracted waves coming from both side channels would eventually meet near the middle of the central testing channel, forming a standing wave pattern. Although it is difficult to quantify the amount of error this could introduce into the readings, there would undoubtedly be some effect.

Finally, a possible, though very minor, source of error are the gauges themselves. Calibration error on the physical model gauges was less than 0.5%, however the numerical model should ideally have zero measurement error. Although this may not be entirely true, as in the case of round-off error within the numerical model, there is still a likely difference in the relative precision of measurements from the numerical and physical models such that the physical readings would be considered slightly less reliable than the numerical readings.

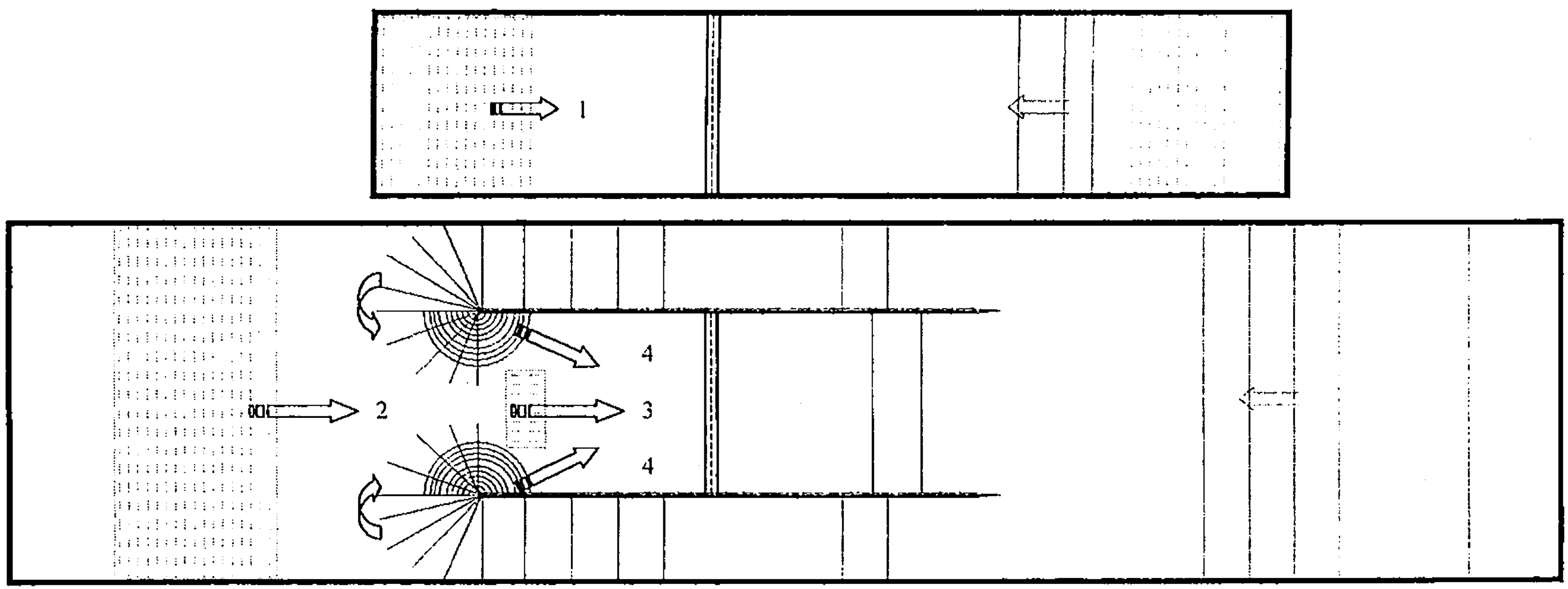

Figure 7.1 - Sketch of possible error sources for the numerical (top) and physical (bottom) domains

7.1.1 Wave Analysis

A general analysis was performed on each of the wave gauge records for all the physical experiments and numerical simulations. First, STAT1 was performed to generate basic statistics of each time series. This was followed by VSD to obtain a frequency domain spectral analysis of the waves and VSD_WAVE to compute wave power. A ZCA time domain zero crossing analysis was performed to calculate a number of wave parameters. Finally, STAT5 was run on the resulting zero crossing analysis to generate further statistical information.

Figure 7.2 gives an example of an analysis plot used to view the results from a particular gauge in the physical model experiments (refer to the wave record presented in Figure 4.43). Figure 7.3 presents the same case from the numerical simulations (refer to the wave record presented in Figure 5.19).

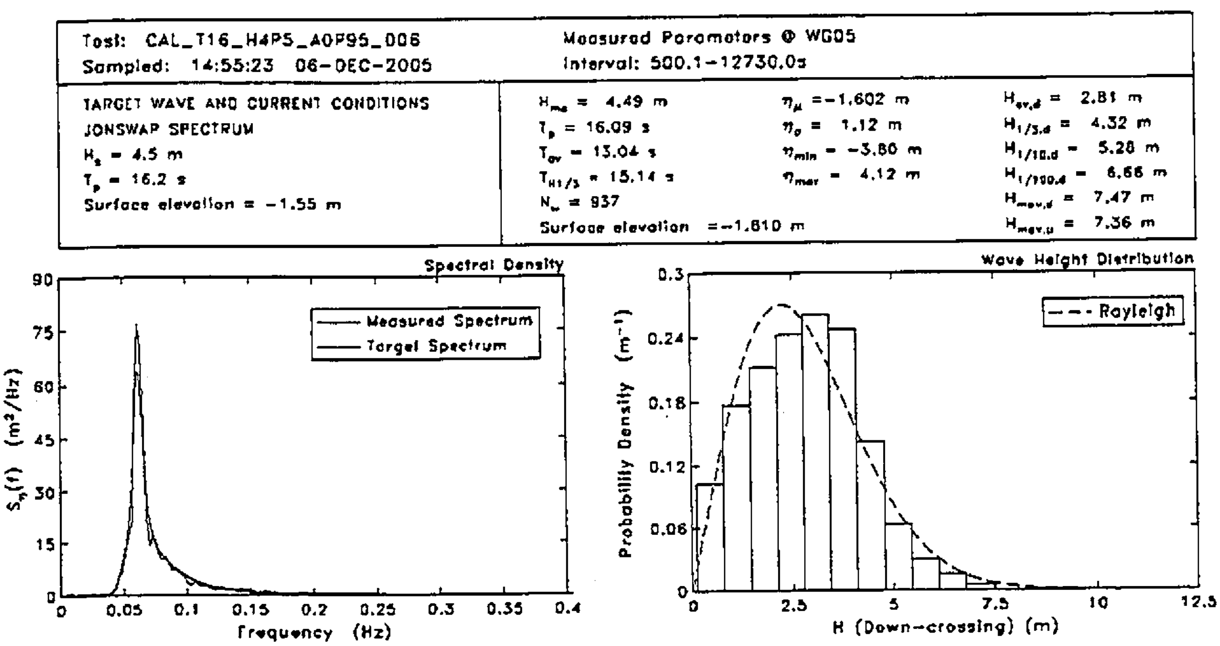

Figure 7.2 - Example of wave record analysis (WG05 from Physical Case 0)

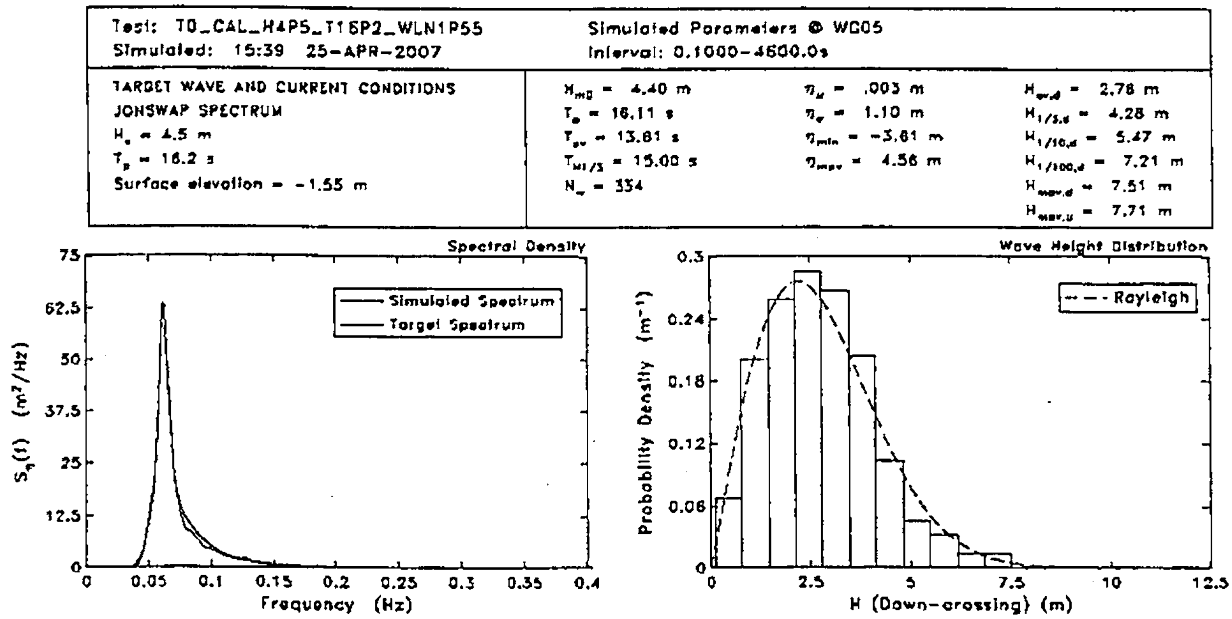

Figure 7.3 - Example of simulated wave record analysis (WG05 from Numerical Case 0)

Table 7.1 provides a summary of the target parameters and for reference includes the number of waves measured in each of these tests. Table 7.2 provides a comparison of the measured versus simulated significant wave heights, while Table 7.3 compares the measured versus simulated peak periods. Both the physical modelling and numerical simulations were quite capable of achieving a high degree of accuracy in reproducing the prescribed target parameters. For physical Case 0 without the submerged structure, the maximum deviations in H_{m0} and T_p were a mere 6.2% and 5.6% respectively, and usually much less. Similarly for the numerical simulations, the maximum deviations in H_{m0} and T_p were an impressive 2.5% and 0.5% respectively. The average deviations in H_{m0} at the structures axis were 1.7% and 2.2% for the measured and simulated results respectively. The average deviations in T_p at the structure axis were 1.0% and 0.5% for the measured and simulated results, respectively.

Table 7.1 - Target parameters for Cases 0 – 4 and observed waves

Test Name	H_{m0} (m)	T_p (s)	Water Depth (m)	Presence of Structure	Number of Waves Physical (Numerical)
Case 0	4.5	16.2	−1.55	No	953 (334)
Case 1	4.5	16.2	−1.55	Yes	1345 (335)
Case 2	6.0	20.1	−1.72	Yes	1120 (145)
Case 3	6.0	20.1	−5.00	Yes	1125 (134)
Case 4	7.0	20.1	−5.00	Yes	1122 (143)

Table 7.2 - Comparison of measured and simulated significant wave heights

Test Name	Measured and Simulated Significant Wave Height H_{m0} (m)										
	WG01	WG02	WG03	WG04	WG05	WG06	WG07	WG08	WG09	WG10	Average WG04-WG07
Case 0 Physical	4.39	4.68	4.48	4.47	4.49	4.67	4.41	4.22	4.38	4.25	**4.51**
Case 0 Numerical	4.41	4.41	4.41	4.40	4.40	4.40	4.40	4.39	4.39	4.39	**4.40**
Case 1 Physical	4.80	4.83	4.65	5.25	4.94	4.87	4.51	4.30	4.31	4.22	**4.90**
Case 1 Numerical	5.35	4.94	4.61	5.58	4.86	4.32	4.36	4.63	3.96	4.16	**4.78**
Case 2 Physical	6.07	6.35	6.47	6.89	6.58	6.61	6.40	5.84	6.43	5.98	**6.62**
Case 2 Numerical	6.50	6.56	6.59	7.77	7.03	6.42	6.43	6.71	5.84	6.13	**6.91**
Case 3 Physical	6.71	6.73	6.51	7.94	7.21	6.58	6.42	6.35	6.34	5.73	**7.04**
Case 3 Numerical	6.53	6.35	6.22	7.67	6.63	6.09	6.01	6.10	5.38	5.73	**6.60**
Case 4 Physical	7.53	7.64	7.39	8.84	8.13	7.51	7.36	7.07	7.34	6.57	**7.96**
Case 4 Numerical	7.31	7.24	7.08	8.28	7.68	6.91	6.80	6.72	6.19	6.39	**7.42**
Location	Up-wave Row (South)			Tunnel Axis				Down-wave Row (North)			Axis

Table 7.3 - Comparison of measured and simulated peak periods

Test Name	Measured and Simulated Peak Period T_p (s)										
	WG01	WG02	WG03	WG04	WG05	WG06	WG07	WG08	WG09	WG10	Average WG04-WG07
Case 0 Physical	16.57	16.45	16.59	16.45	16.09	16.05	16.37	15.52	15.29	15.36	**16.24**
Case 0 Numerical	16.13	16.13	16.13	16.11	16.11	16.11	16.11	16.12	16.12	16.12	**16.11**
Case 1 Physical	16.64	16.46	16.56	16.40	16.08	16.10	16.29	15.47	15.29	15.65	**16.22**
Case 1 Numerical	16.07	16.10	16.08	16.15	16.08	16.25	16.00	16.15	16.18	16.10	**16.12**
Case 2 Physical	19.02	20.56	20.29	19.96	20.01	20.22	20.78	20.79	19.98	20.57	**20.24**
Case 2 Numerical	18.92	20.20	20.34	20.10	20.27	20.34	20.27	20.23	20.08	20.23	**20.24**
Case 3 Physical	19.00	19.48	19.70	18.97	20.07	20.32	19.34	19.52	20.46	19.65	**19.67**
Case 3 Numerical	19.32	19.73	20.05	19.88	19.87	20.11	20.25	20.10	19.80	20.21	**20.03**
Case 4 Physical	19.15	19.50	19.81	19.04	20.11	20.37	19.36	19.49	20.53	19.62	**19.72**
Case 4 Numerical	19.24	19.55	19.85	19.68	19.79	20.12	20.20	20.23	19.76	20.26	**19.95**
Location	Up-wave Row (South)			Tunnel Axis				Down-wave Row (North)			Axis

Figure 7.4 through Figure 7.8 depict the direct comparison of wave conditions and energy spectra between the physical and numerical tests. The target parameters for each case are presented in the top-right corner. The black and red lines denote the spectra for the numerical and physical cases respectively. Specific data are denoted using subscript p $_{(p)}$ and subscript n $_{(n)}$ for the physical and numerical results, respectively.

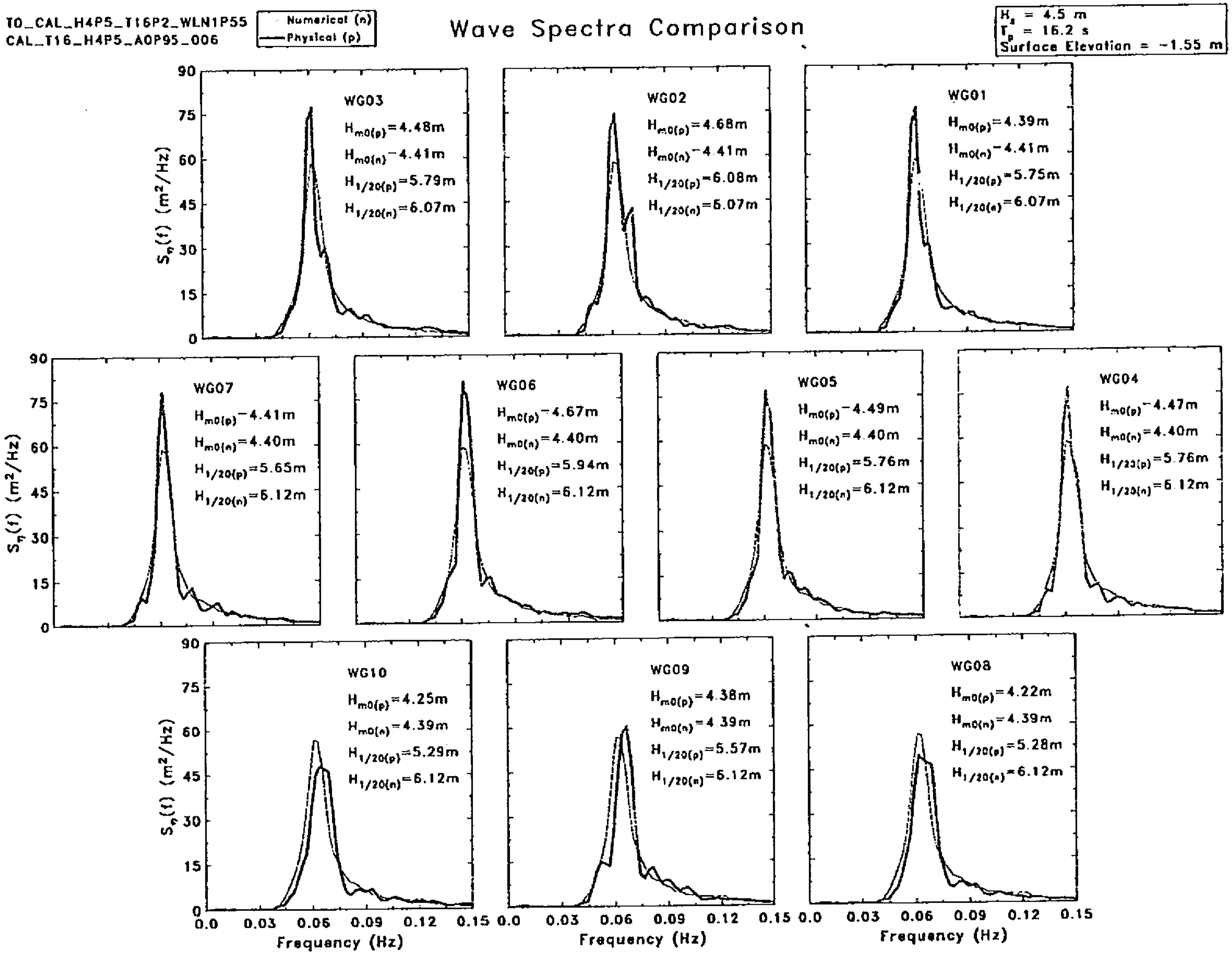

Figure 7.4 - Wave spectra comparison: Case 0

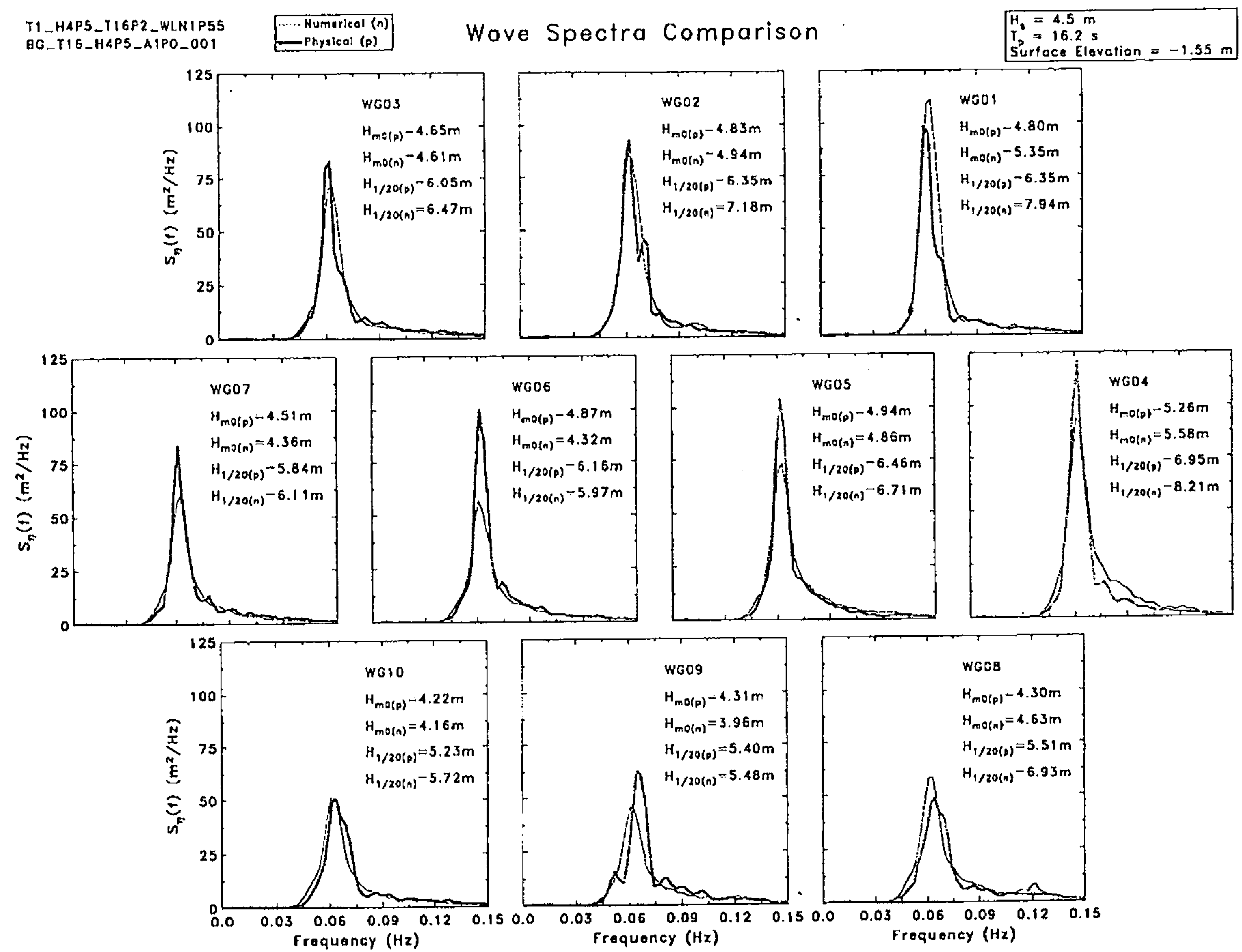

Figure 7.5 - Wave spectra comparison: Case 1

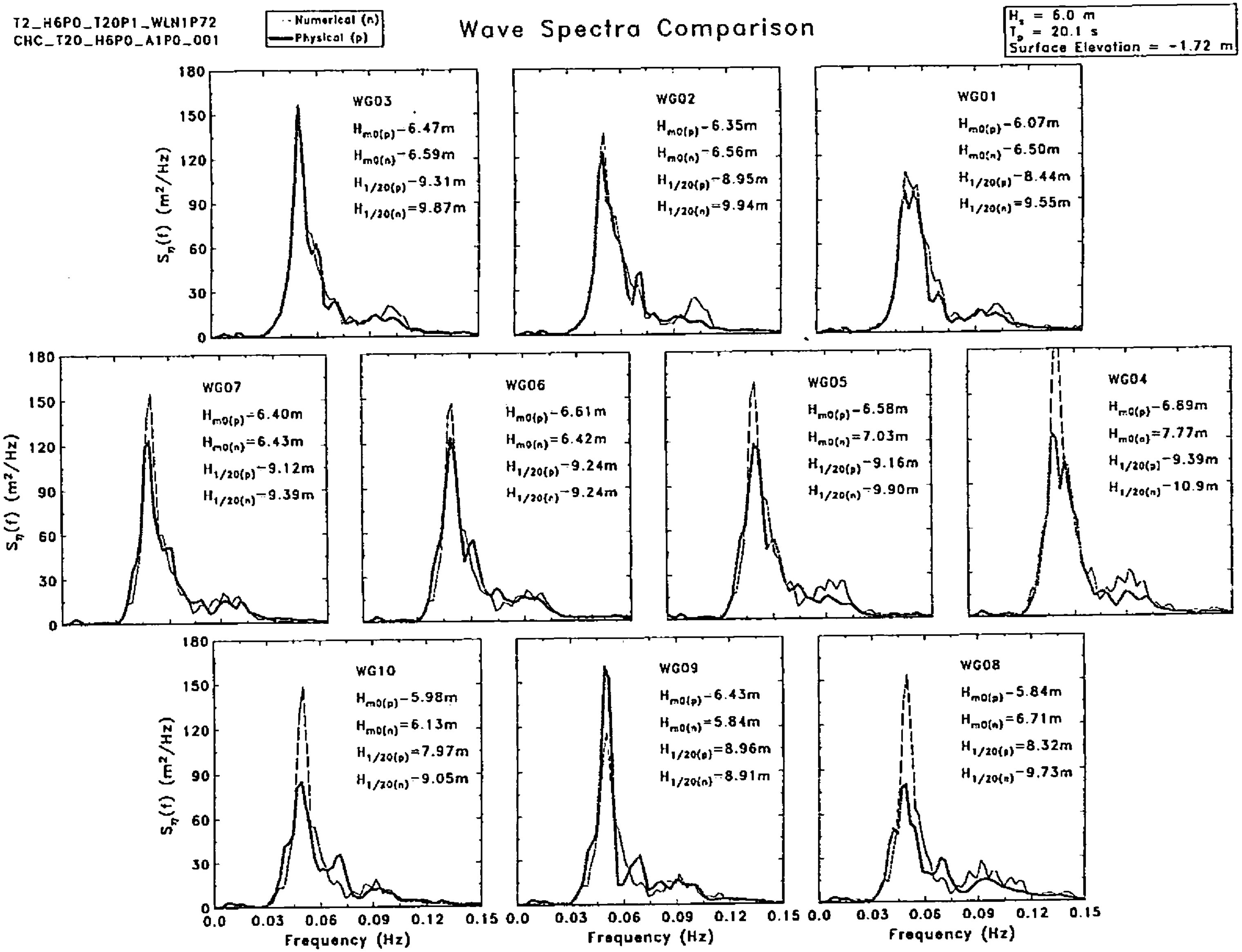

Figure 7.6 - Wave spectra comparison: Case 2

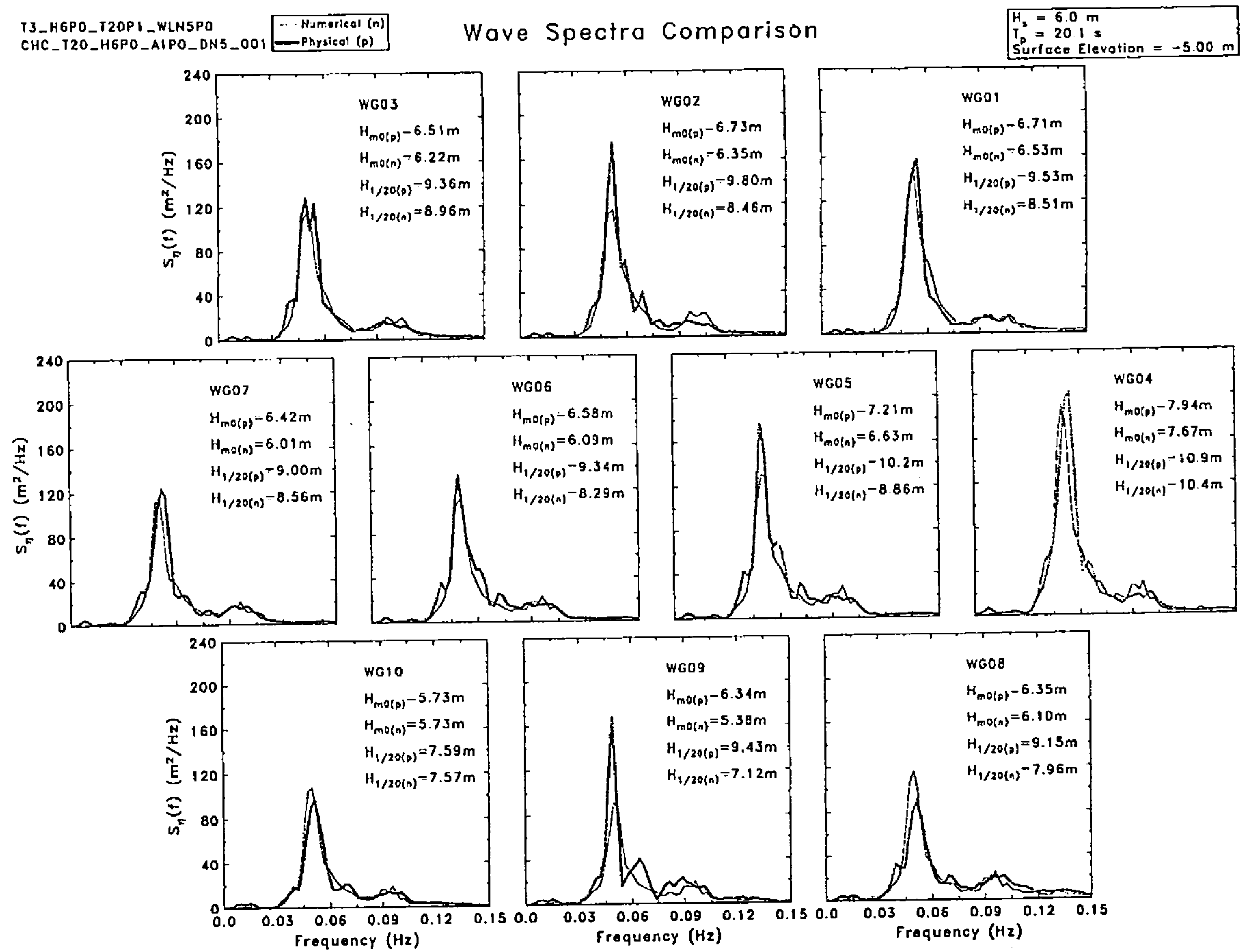

Figure 7.7 - Wave spectra comparison: Case 3

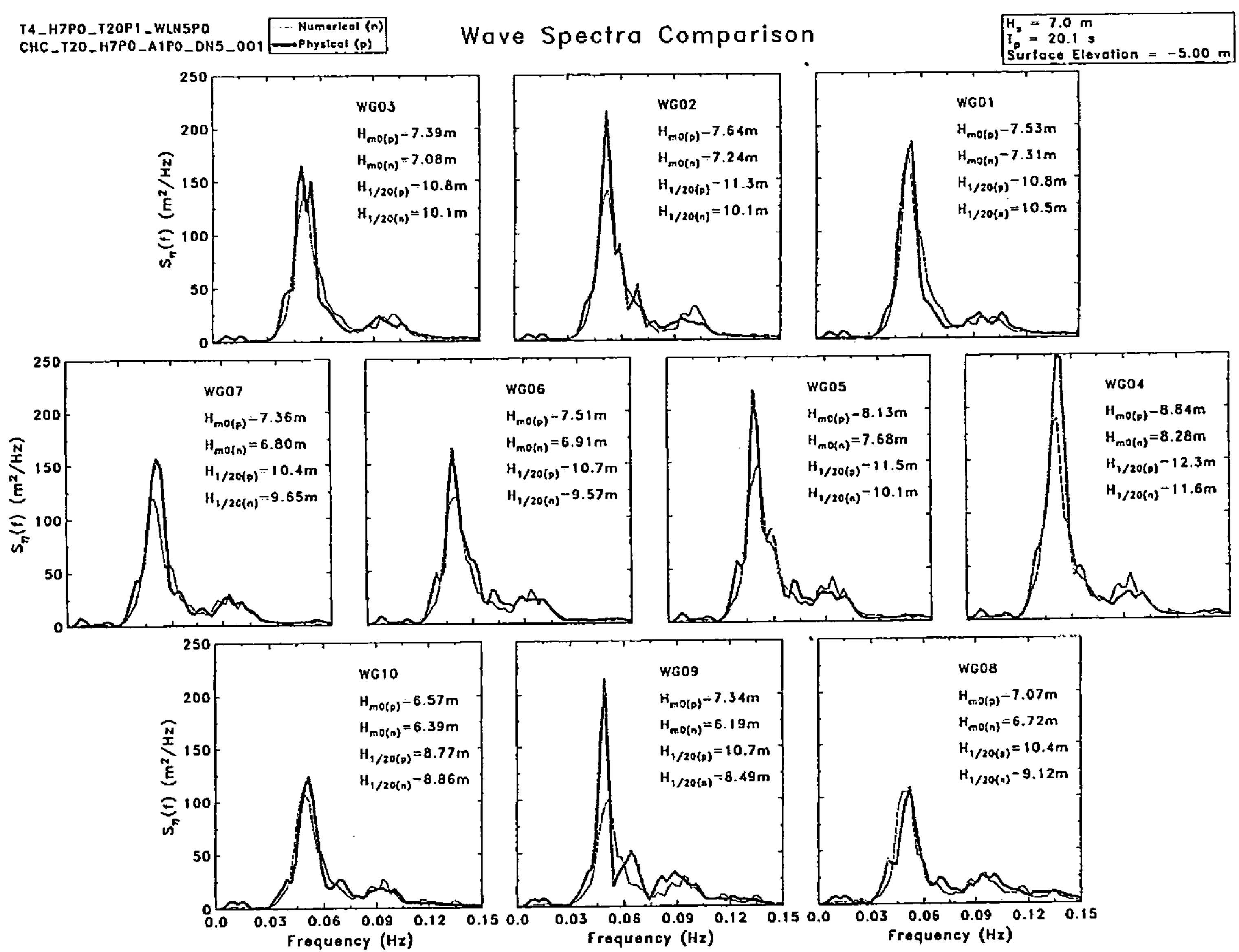

Figure 7.8 - Wave spectra comparison: Case 4

In Figure 7.4, the calibration case without the submerged structure, it is observed that the H_{m0} for the most part are quite well matched between the numerical and physical data. In general, the physical spectra are more peaked than the numerical spectra, however the peak locations do match up quite suitably. It is also observed that the numerical model is displaying nearly perfect symmetrical behaviour. Although the spectral shapes vary slightly, nearly all the spectral parameters are exactly the same across each row of gauges. The same cannot be said for the experimental data. Even across the first row of gauges where the disturbances should be least, there are some minor discrepancies with the spectral shapes and parameters, indicating that other factors are causing minor distortions. This will become more important for larger waves in the presence of the structure, and will be discussed again for these cases.

Most evident with the numerical data, and to a lesser degree, the physical data, the higher frequency portions of the spectra (~0.09 Hz and up) is a relatively smooth curve, indicating a gradual decline in higher energy waves. It is also noted that the differences between the top 1/20th waves agree reasonably well, although a few larger discrepancies are observed.

In Figure 7.5 (Case 1), it is possible to see a significant influence from the structure on the wave climate, as compared to the previous (Case 0). Wave energy is partially reflected from the structure, causing the up-wave row of gauges to show significantly higher waves. As would be expected, the readings show that the influence is larger at the right side, where the tunnel is higher into the flow. A similar trend is observed in the gauges at the structure crest. The submerged structure forces the approaching waves to shoal as they pass over it. Breaking was even observed at the far left side (refer to Figure 4.49), suggesting that the largest waves are nearly as tall as the submergence depth since breaking typically occurs when the wave height is 0.8 of the water depth. Breaking was observed more often with each progressive test case, as would be expected. The wave height observed at each of the down-wave row of gauges for both the numerical and physical tests is nearly the same (except for the physical data from WG09) suggesting that the structure influences higher energy dissipation as the submergence depth decreases. The physical data from WG09 shows a notable discrepancy.

Comparing the spectral shapes to the calibration case, it is possible to identify some variations in the upper range beyond ~0.09 Hz, possibly due to the growth of higher frequency harmonics. This is particularly noticeable for the numerical data from WG08, where the spectral peak occurs at approximately 0.065 Hz, and a secondary peak is evident at approximately 0.12 Hz, the "first harmonic".

In Figure 7.6 (Case 2), an unexpected pattern is observed in the up-wave row of gauges. Both the physical and numerical analysis seem to show that the wave climate is more severe at the left side, where the anticipated reflection from the structure should be least. The fact that the numerical and physical data are in good agreement indicates perhaps there is a valid reason for this result. The explanation for this observation is that the up-wave gauges are falling at a node or anti-node of a partial standing wave system created by the reflected energy from the submerged structure. The gauges at the structure axis show a more expected trend, with higher waves appearing at the right side where the influence of the structure is greatest.

Figure 7.6, Figure 7.7, and Figure 7.8 show similar trends in regards to higher harmonic formation. It is generally apparent for both the physical and numerical data that secondary spectral peaks can be observed, normally at about twice the spectral peak frequency in each situation.

Figure 7.7 (Case 3) generally shows the expected trends. Notice again that for the physical data, WG02 and WG09 both demonstrate inexplicably high spectral peaks. The same pattern is observed in Figure 7.8 (Case 4). In these larger wave tests, greater contamination from sources of error is observed in the physical model results. As previously mentioned, the most likely explanation for this occurrence is the difference between the numerical and physical modelling domains. The diffracted energy from the masonry walls as well as some undesired reflection from the wave absorbers would meet each other near the center of the basin (WG02 and WG09).

To investigate this hypothesis further, an extra numerical simulation (referred to as "Full_Basin") was setup. In this case, the entire Coastal Wave Basin was included in the domain, along with the concrete block walls. The tunnel was again put in place and the equivalent Case 1 was run in the new domain. In this setup, the model was somewhat troublesome, with instabilities turning up partway through the simulation. In order to avoid the instabilities, a simulation duration of 1150 seconds was used (similar to Cases 2-4). Analysis of the wave data from the Full_Basin test showed that the wave conditions (except WG02 and WG09) were reasonably comparable to the equivalent results from Case 1. However, the simulated conditions at WG02 and WG09 showed a similar trend as seen in the physical data such that the spectral peaks were greatly overpredicted (see Figure 7.9).

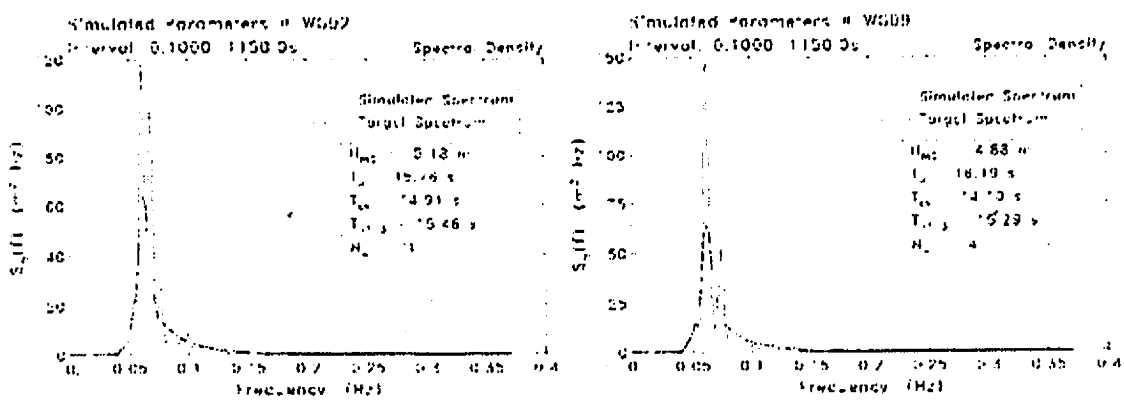

Figure 7.9 - Wave analysis for WG02 and WG09 from the Full Basin simulation

The $H_{1/20}$ parameter is a measure of the highest 1/20th waves, useful in describing the likely possible damage to an armoured structure caused by the wave climate. Regarding this parameter, in general the numerical and physical data match to a reasonable degree for Cases 0-1 and less so for Cases 2-4. The length of the wave train in each case likely has a bearing on the statistics involved with the $H_{1/20}$ parameter. The physical tests contained approximately 3.5 and 8 times as many waves in Cases 0-1 and 2-4 respectively. This is a probable reason that the numerical and physical data do not match nearly as well for the latter cases. Unfortunately, the numerical tests Cases 2-4 do not contain as many waves as would be desired to provide a more reliable statistical comparison.

Figure 7.10 through Figure 7.14 present the significant wave height data in a graphical fashion. In these plots, the blue and purples lines denote the physical and numerical results respectively. For Cases 1-4, a green line denotes additional numerical results for the same target parameters but without the submerged structure. These figures should be read from right-to-left, with the numbers on the x-axis indicating the wave gauge number. The first group on the right is the up-wave row of gauges, the middle group is at the structure's crest, and the final group on the left is the down-wave row of gauges.

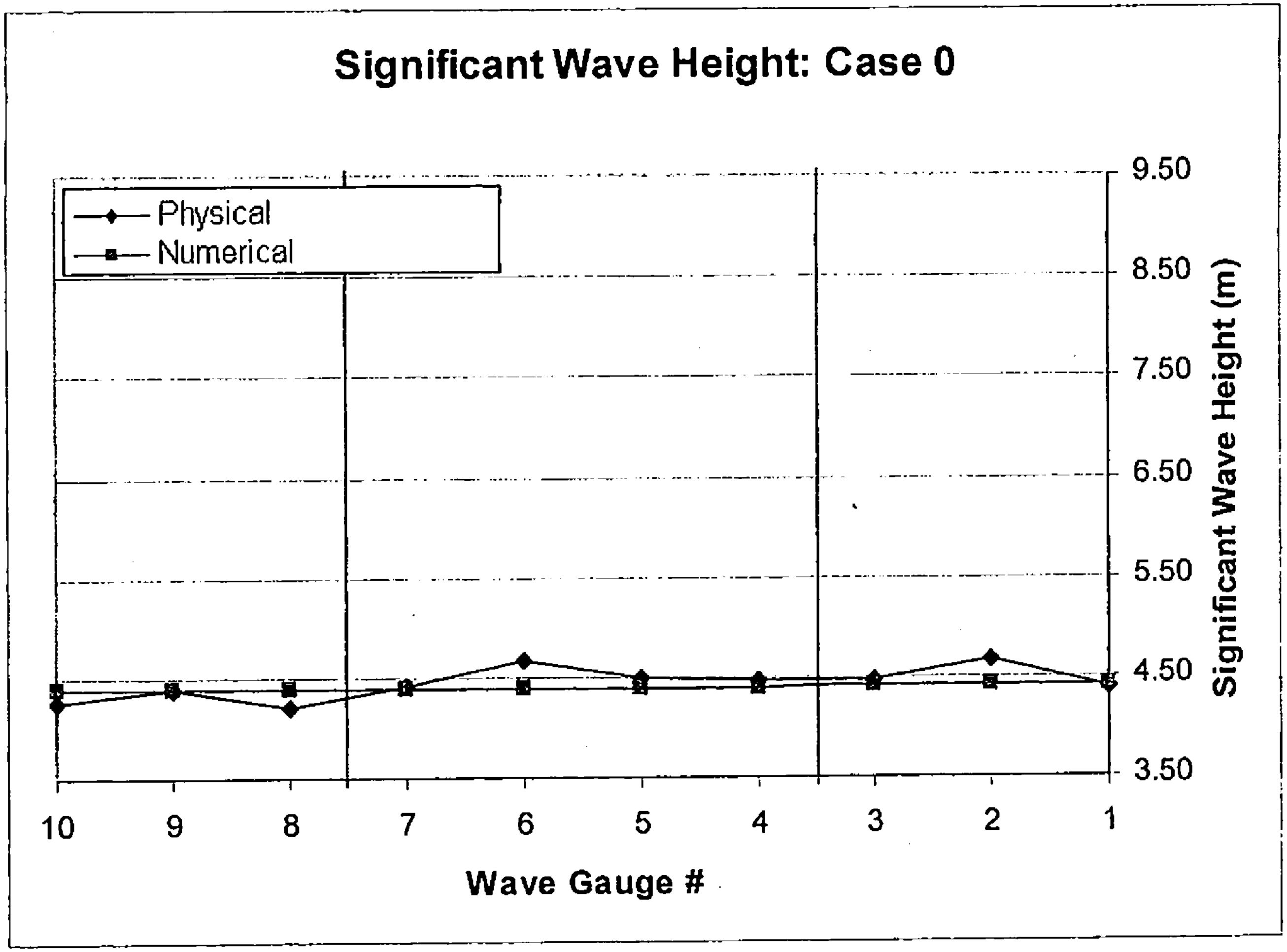

Figure 7.10 - Significant wave height comparison: Case 0

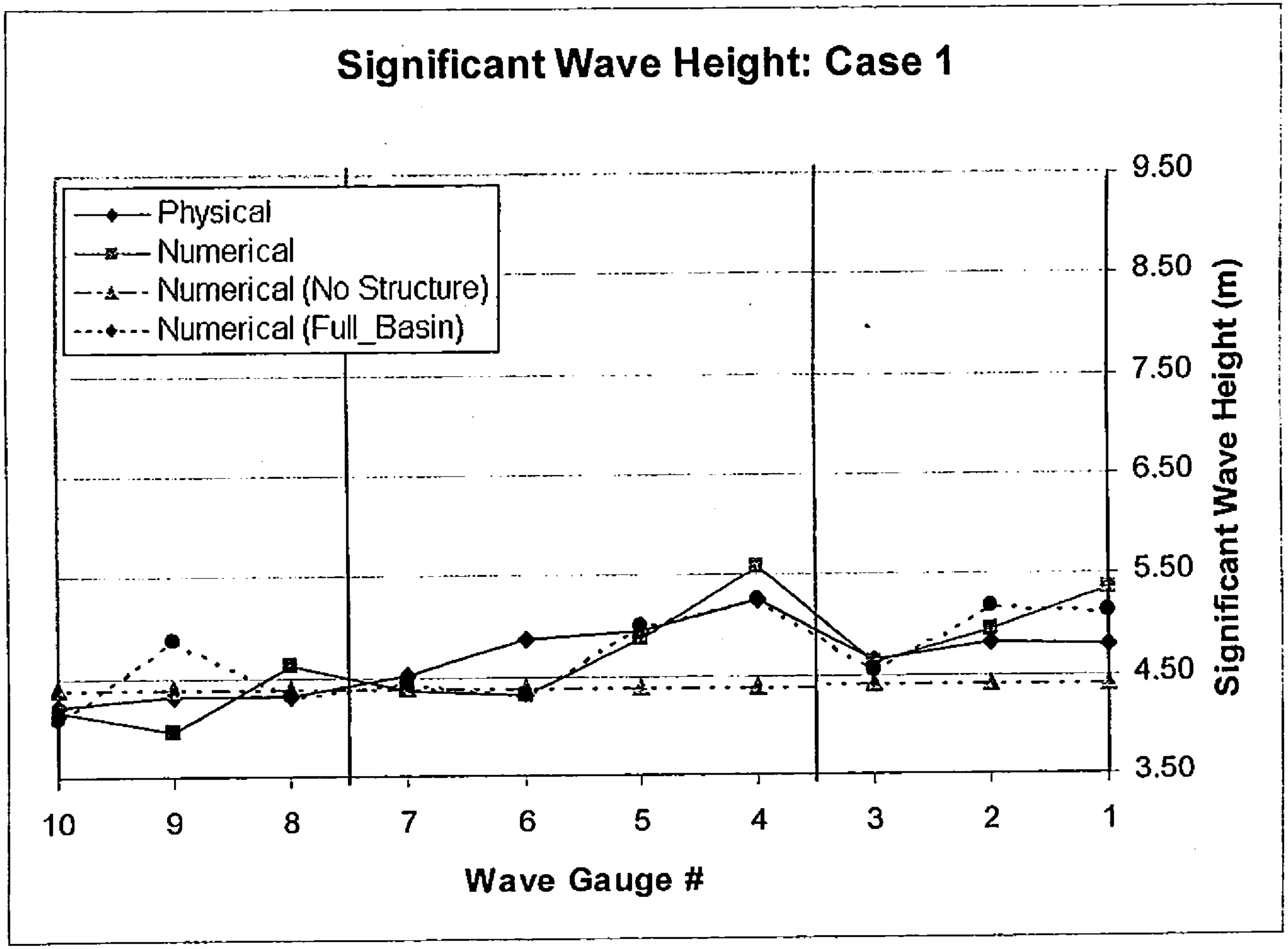

Figure 7.11 - Significant wave height comparison: Case 1

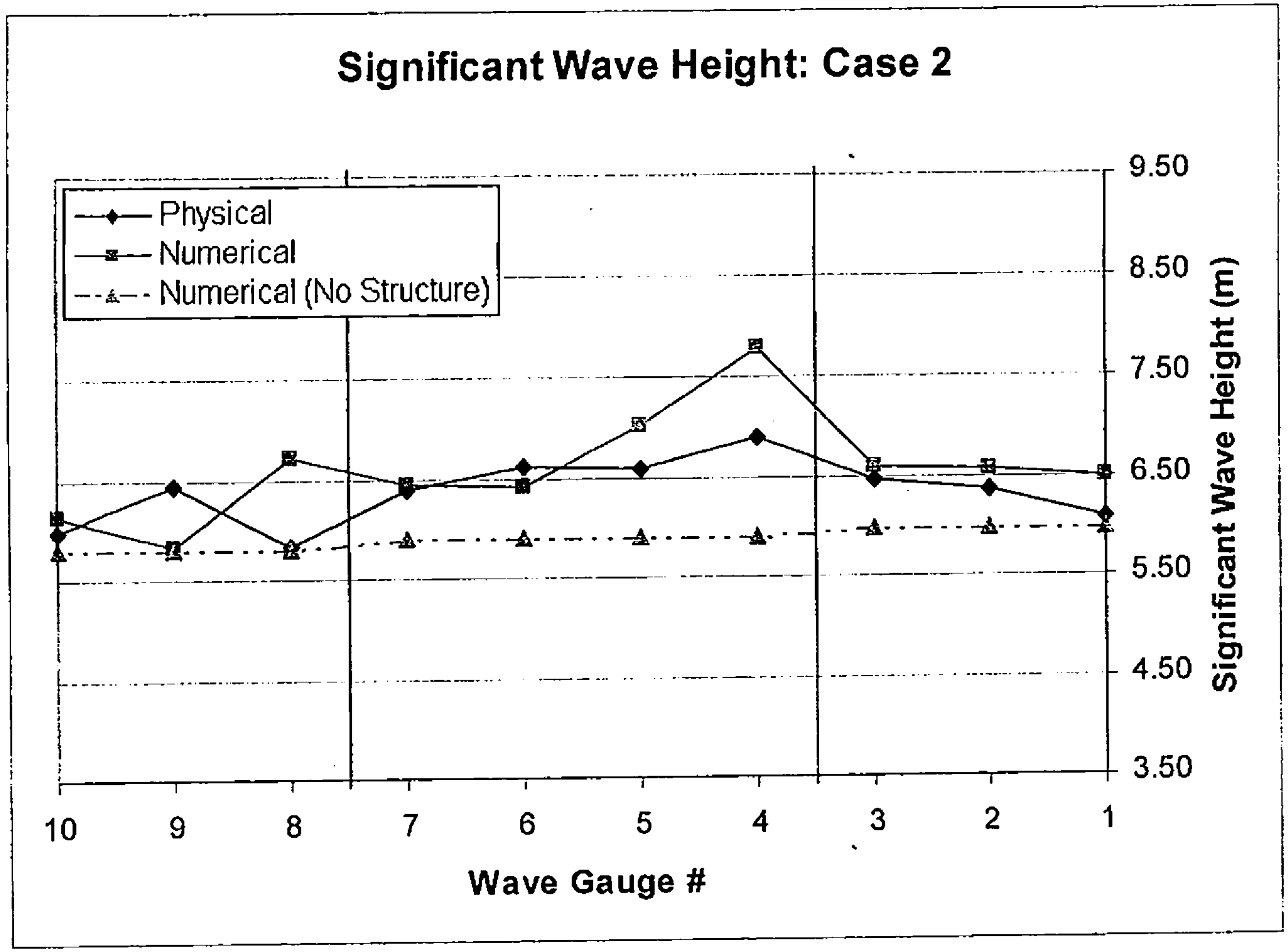

Figure 7.12 - Significant wave height comparison: Case 2

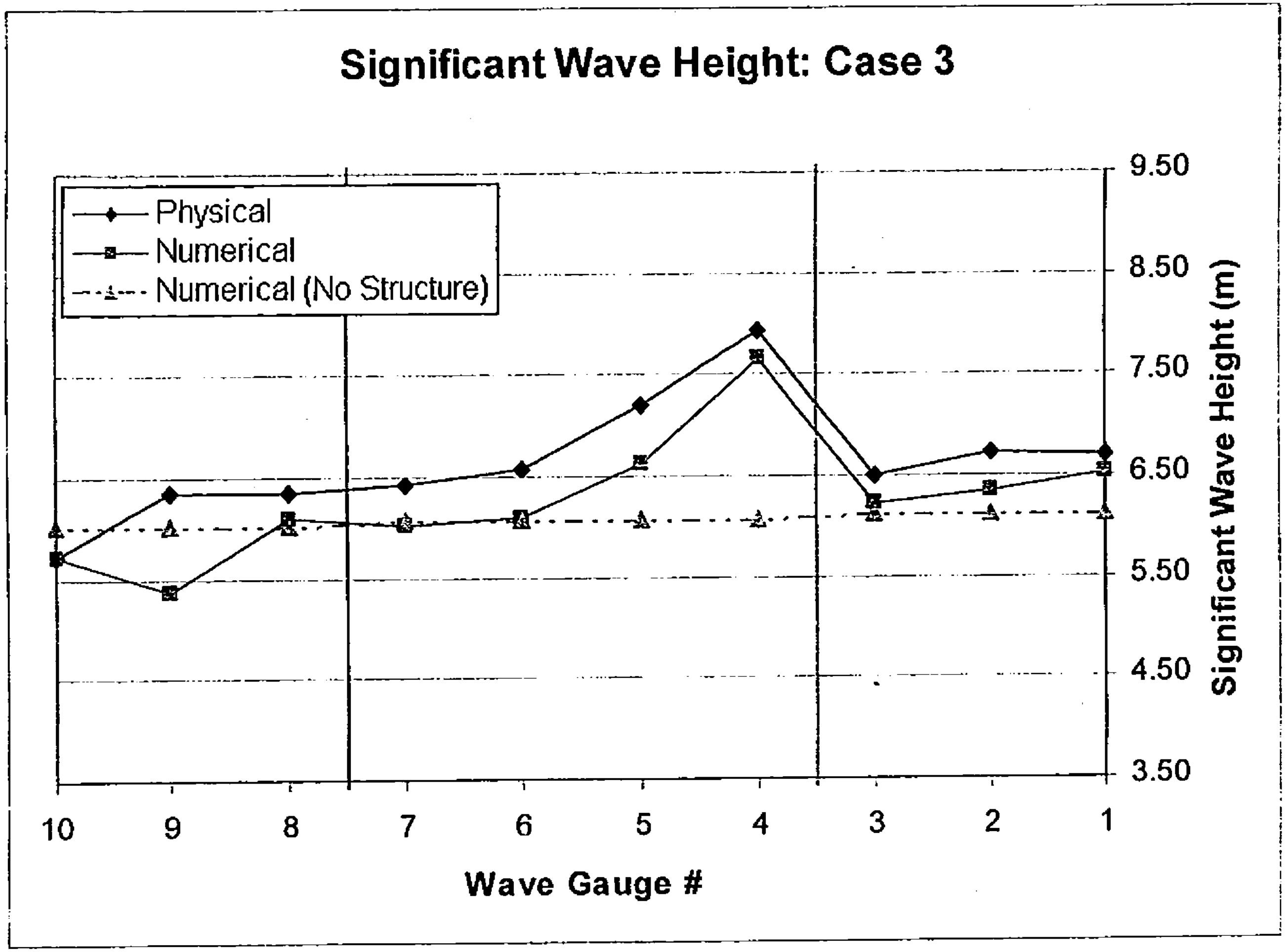

Figure 7.13 - Significant wave height comparison: Case 3

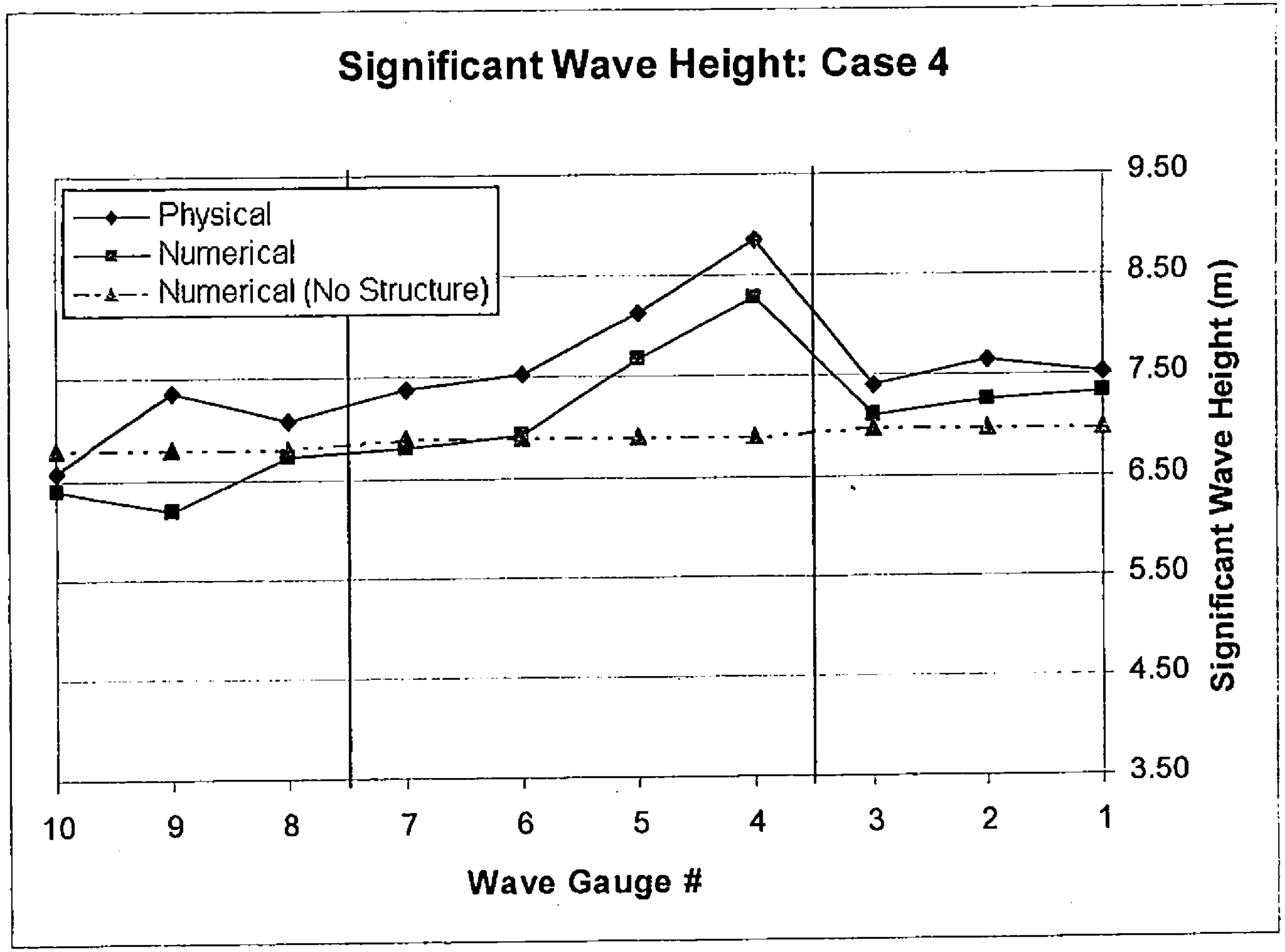

Figure 7.14 - Significant wave height comparison: Case 4

In Figure 7.10 through Figure 7.14, it is observed that the numerical model results pertaining to the submerged structure demonstrate fairly consistent trends. The up-wave row of gauges displays a decreasing slope, again demonstrating that the reflected waves are larger in front of the structure where the freeboard is smallest. For the row of gauges along the structural axis, another decreasing slope is observed. In general, a linear slope is observed between WG 04 and 06, indicating that the shoaling waves passing over the structure varies in a linear fashion. It is observed that there are only small differences between the results for WG 06 and 07, indicating that the submerged structure is perhaps no longer having a significant effect on the wave climate due to its increased freeboard. It should be noted that the results for WG 06 and 07 are essentially the same for both numerical situations (with and without structure) with the exception of Case 2. Again, this would indicate that the submerged structure has only a small impact on the wave climate after a certain freeboard is met. The numerical results (with structure) for the down-wave row of gauges fairly consistently show a notably smaller wave height at WG09.

It is noted that significant wave heights in the physical model are consistently larger than the ones generated from numerical data for Cases 3 and 4. This is due to the fact that the numerical model simulation times used were significantly shorter than the temporal length of the physical model simulations due to the aforementioned issue with numerical instabilities observed with the cases dealing with larger waves. The wave trains from the physical model tests were much longer than the ones in the numerical model simulations, which means that the number of very large waves appearing in the numerical model would have been significantly smaller than for the physical model, thereby explaining the smaller average of the 1/3rd highest waves (significant wave height).

The physical model results are less consistent, but they too generally show similar trends to those seen in the numerical results. Notable discrepancies between the numerical and physical results is observed at WG09 where the physical results consistently show an increase in wave height compared to WG 08 and 10 whereas the numerical results consistently show the opposite.

Comparing the unobstructed numerical case to the case with structure, the simulations consistently show an increased wave height at the up-wave gauge and along the structures axis (notably more when the freeboard is smallest). With the exception of Case 2, the simulations generally show a decreased wave height behind the structure compared to the unobstructed case. Similar comparisons between the physical modelling results and the numerical unobstructed case are difficult to make. The results are less logically consistent, likely due to the possible error sources described previously.

7.1.2 Transfer Function Analysis

The transfer function analysis provides a means to observe the transfer of energy into and out of a system. The transfer function was calculated from the variance spectra of the wave conditions up-wave and down-wave of the structure. TRFRA was run for each of the 3 cross-sections for both the physical and numerical data presented in Figure 7.15 through Figure 7.19. In these figures, the submerged structure has the most freeboard at the left (Cross-Section 1), and the least freeboard at the right (Cross-Section 3). For reference, the wave spectra from the gauges up-wave and down-wave of the structure are shown respectively above and below the transfer function. The dotted blue lines denote the major trend in the numerical data.

In Figure 7.15, the calibration case, there is no structure obstructing the flow, and therefore the up-wave and down-wave spectra should be identical, meaning the theoretical transfer function should be 1.00, indicating 100% energy transfer at all frequencies from the input to the output. For the case of the numerical data, it is observed that the transfer function is nearly 1.00 for the frequency band containing most wave energy between approximately 0.04 to 0.08 Hz. Some minor fluctuations are observed in the higher frequency range. The physical data however does not follow a similar trend as would be expected, and it is quite difficult to explain the unexpected results. As described previously, the contamination from different sources of error within the physical model would be a likely explanation for the observed discrepancies.

In Figure 7.16, the numerical transfer function shows a significant reduction in energy around the peak frequency, f_p and significant increase in energy around twice the peak frequency, $2f_p$. The physical transfer function, although not quite as consistent as the numerical data, also shows similar trends in energy transfer from lower to higher frequencies. The trend appears strongest where the structure is highest (Cross-Section 3).

Figure 7.17, Figure 7.18, and Figure 7.19 demonstrate definite patterns in the transfer function, similar in all test cases, denoted by the blue dotted lines. Although the physical model transfer functions are not always as consistent with each other, in general the numerical and physical results do show a reasonably good comparison. It is evident that the freeboard of the structure holds a significant influence over the transfer of energy.

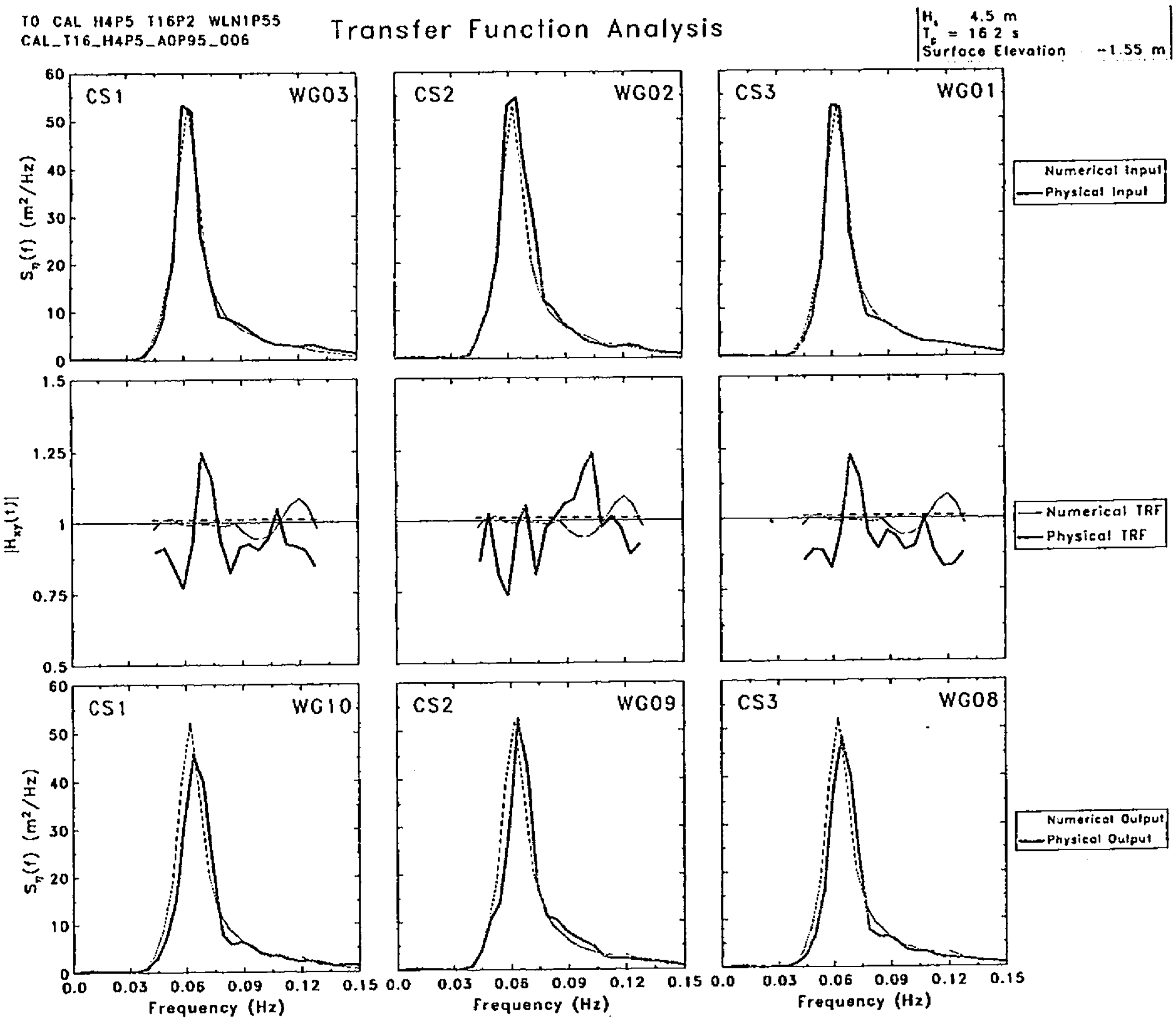

Figure 7.15 - Transfer function analysis: Case 0

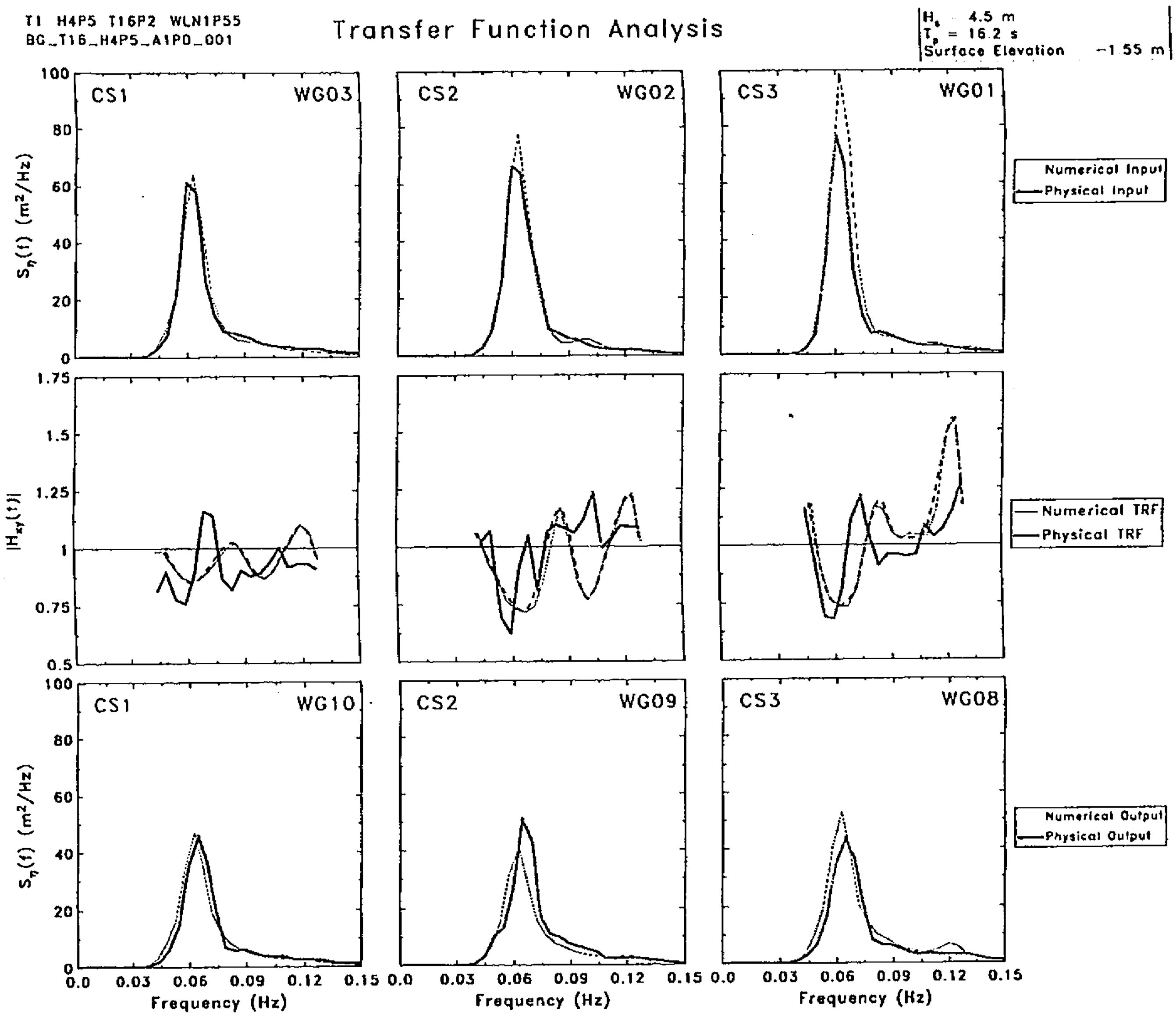

Figure 7.16 - Transfer function analysis: Case 1

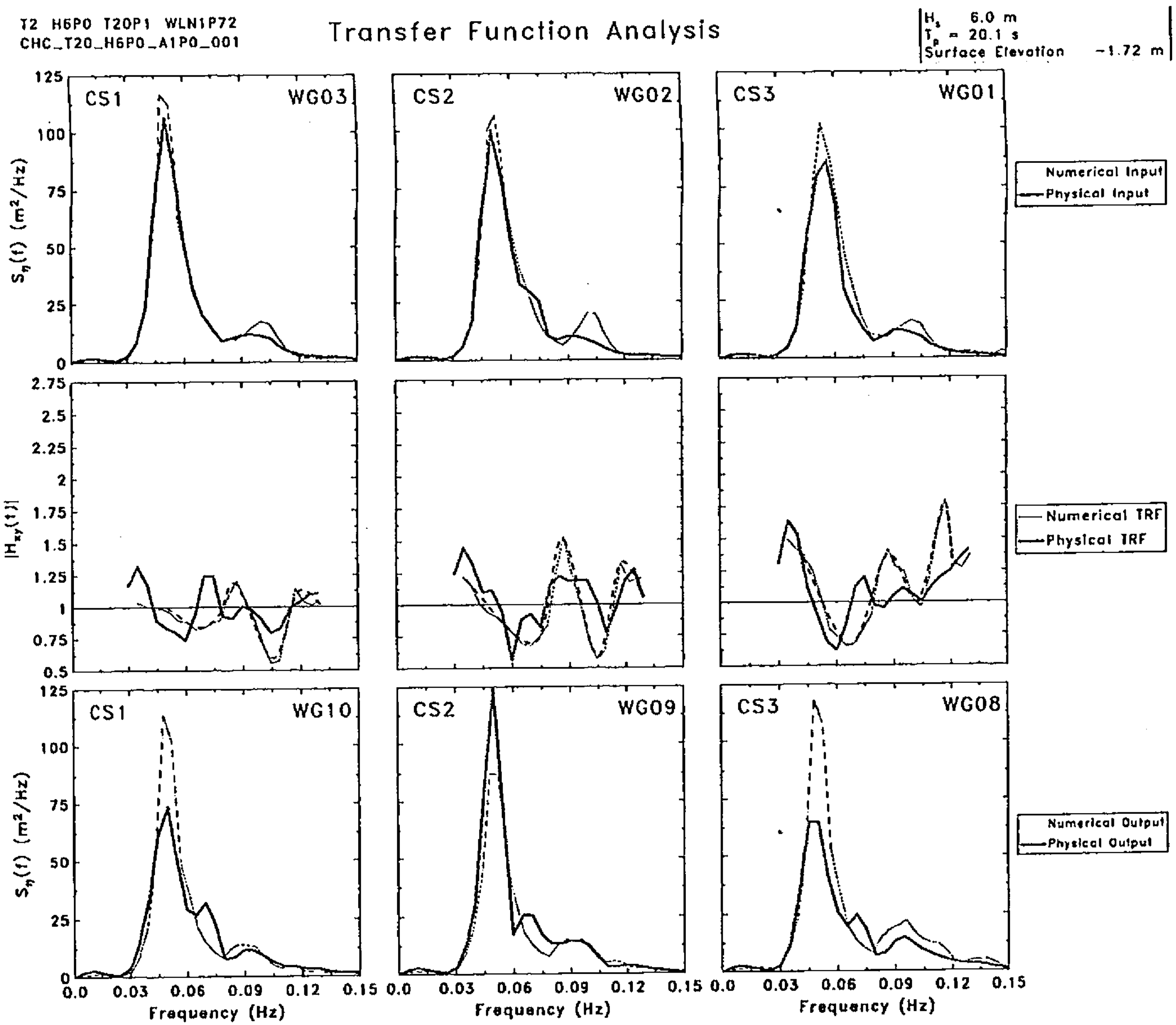

Figure 7.17 - Transfer function analysis: Case 2

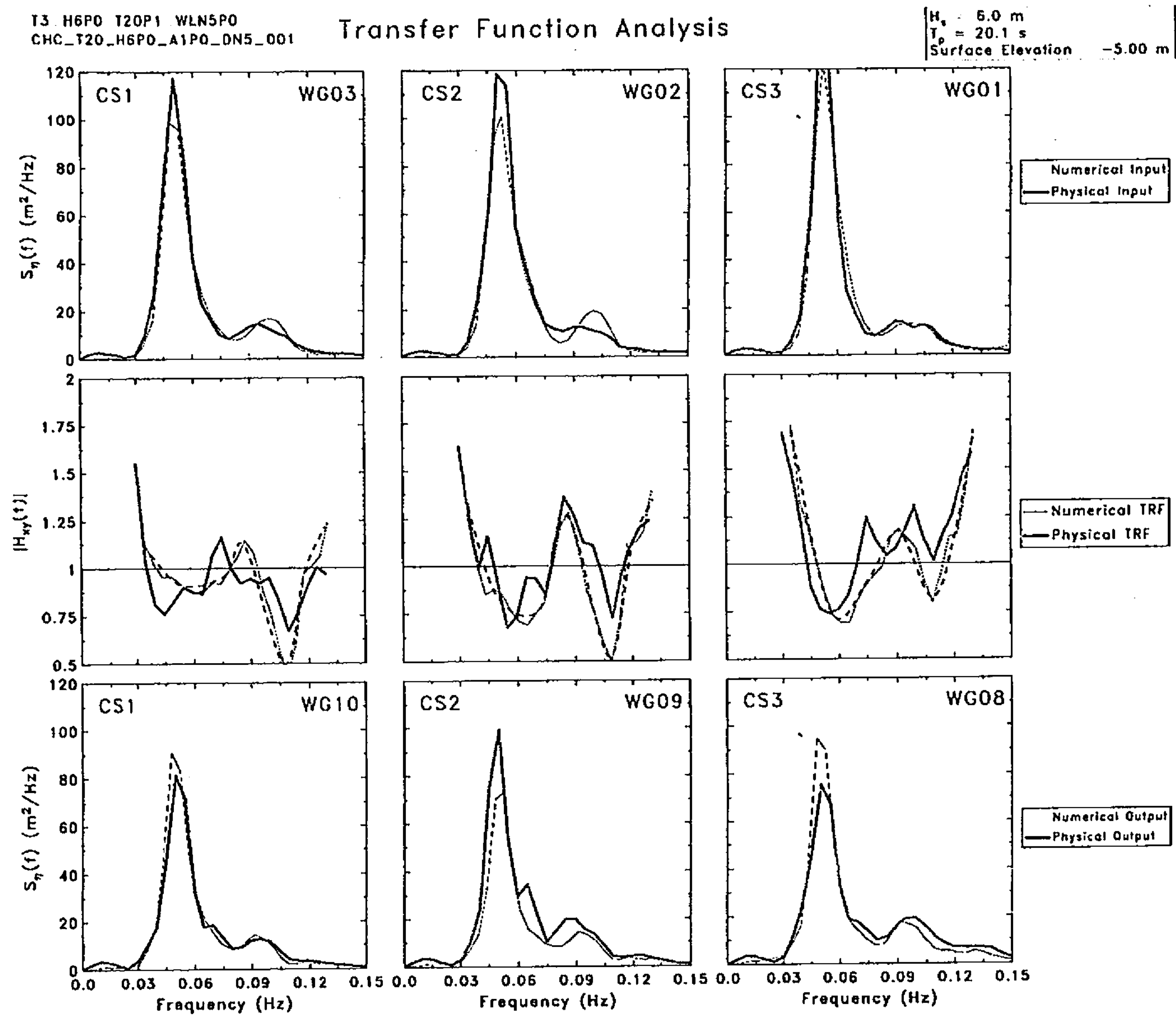

Figure 7.18 - Transfer function analysis: Case 3

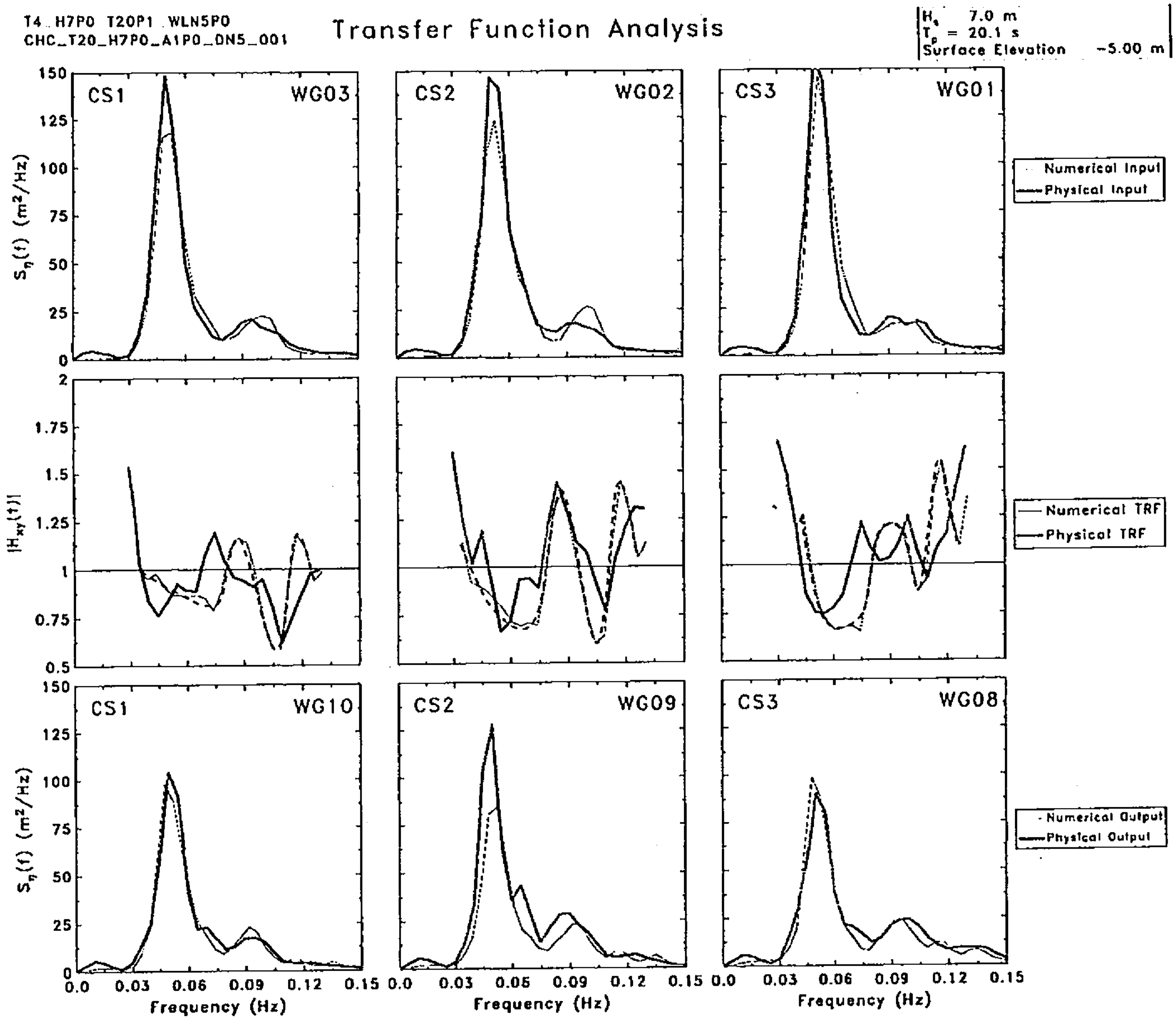

Figure 7.19 - Transfer function analysis: Case 4

7.1.3 Wave-Induced Velocity Analysis

The measured and simulated wave-induced velocities were analyzed to determine the effects of the submerged structure on surrounding flows. FILT_FFT was run to remove noise from the physical model readings, retaining only the data between 0 and 0.2 Hz (prototype scale). STAT1 was then performed to generate basic statistics for each velocity gauge time series. POLAR_2-D was run on the respective x and y components for each of the velocity gauges to obtain the resultant magnitude and direction of the velocity vector. PEAKS was then performed on each of the resultants, and finally STAT5 was run to obtain probability statistics.

Figure 7.20 through Figure 7.24 depict the results this analysis on the velocity measurements. It should be noted that in the physical model, velocities were measured at a particular elevation above the seabed or submerged structure, whereas the numerical model yields depth-averaged velocities. Because the numerical model gives depth-averaged velocities, it is expected results would generally show larger velocities than the ones recorded in the physical model. Note that ECM01 is located up-wave of the submerged structure at the center of the channel, while ECM02 is located down-wave. ADV01 is located at the crest of the structure, over the side of least submergence. ADV02 is located directly over the middle of the structure, and ADV03 is located over the side of greatest submergence (Refer to Figure 4.3 and Figure 4.47).

In Figure 7.20, the unobstructed case, it is observed that the simulated velocities are very similar at all locations, again showing the uniformity of the numerical model. The experimental data is also fairly consistent, however some minor spatial variations can be observed. In Figure 7.21, the influence of the submerged structure can clearly be seen, specifically in the ADVs. Both the physical measurements and the numerical simulations show that the velocities measured over the crest of the structure are larger where the freeboard is smallest. This result is as expected since the water is forced to flow through a smaller area. An overall reduction in the wave-induced velocity is observed between the up-wave and down-wave ECMs. The numerical Full_Basin simulations compare reasonably well with both the normal numerical simulations as well as the physical measurements although some minor spatial variations are noticeable.

Figure 7.22, Figure 7.23, and Figure 7.24 show similar trends to those observed in Case 1. As the wave height increases in each further case, the wave-induced velocities are also observed to increase in magnitude. Significant velocities are observed over the submerged structure at Cross-Section 3. In general, the numerical probability curves match reasonably well to the experimental probability curves, although some discrepancies are typically observed at ADV03. As mentioned above, this difference is mostly due to the fact that the wave-induced velocities are not measured at the exact same elevation in both the numerical and physical models.

It is clear that the submerged structure has a greater impact on the wave-induced velocities over the sections of least freeboard, as the difference between simulated results for the structure and no-structure cases at ADV03 is very little.

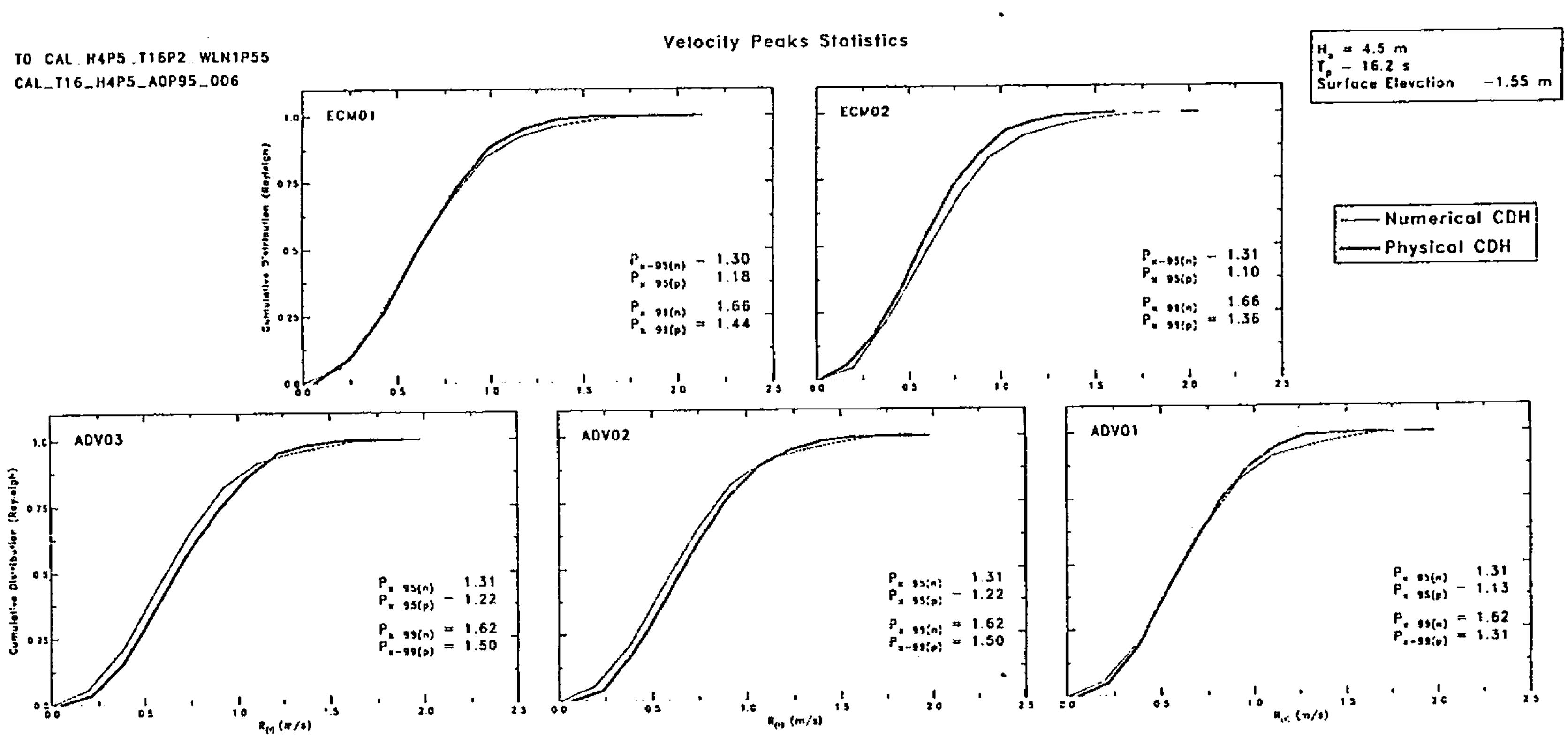

Figure 7.20 - Velocity peaks analysis: Case 0

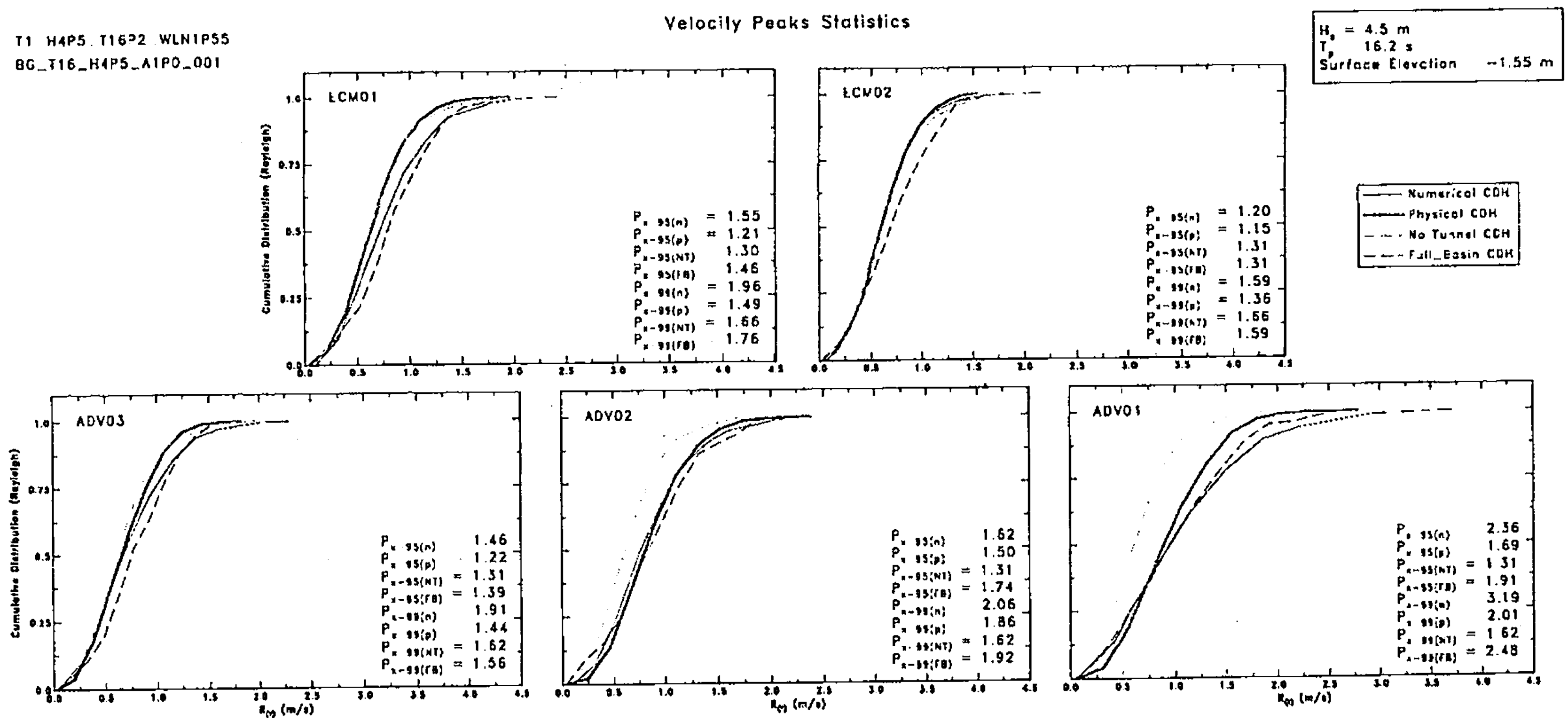

Figure 7.21 - Velocity peaks analysis: Case 1

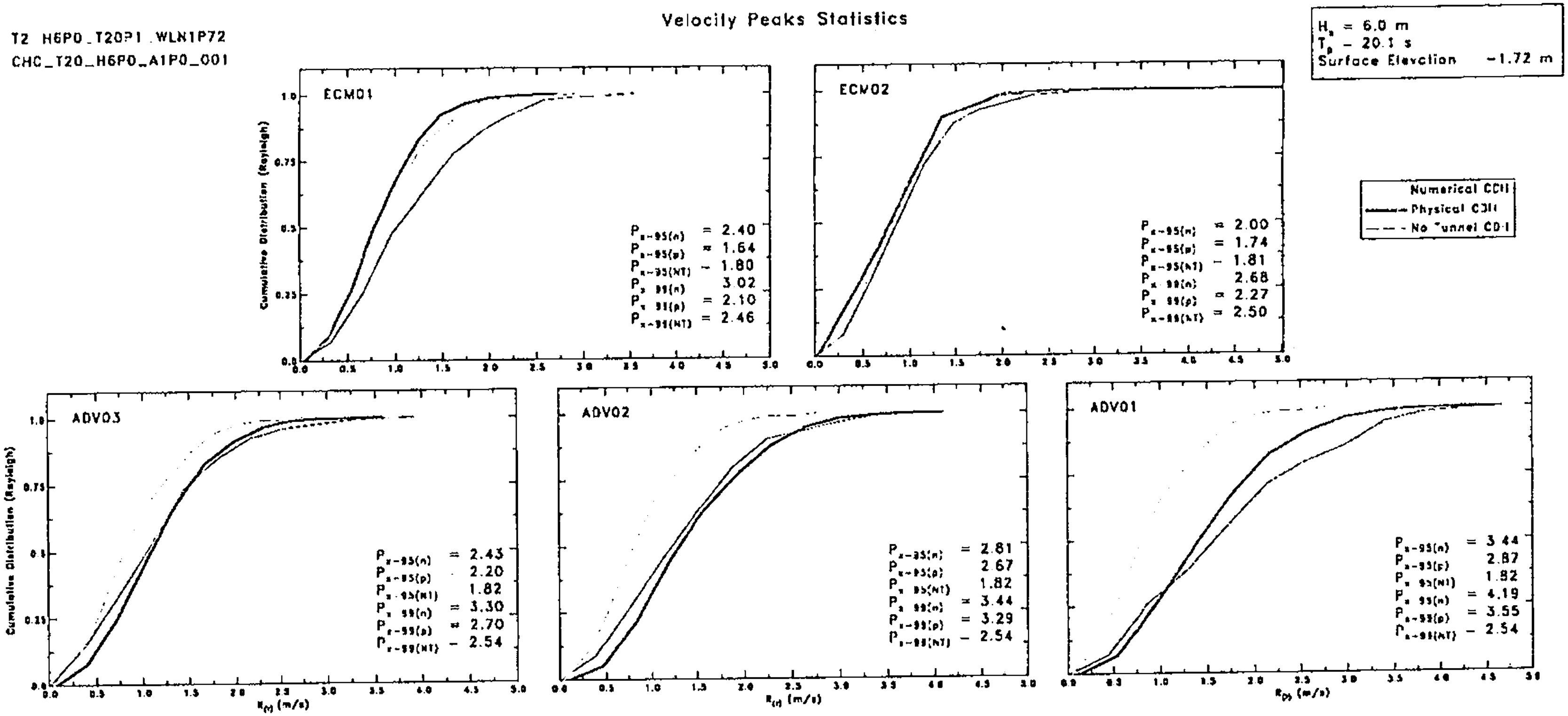

Figure 7.22 - Velocity peaks analysis: Case 2

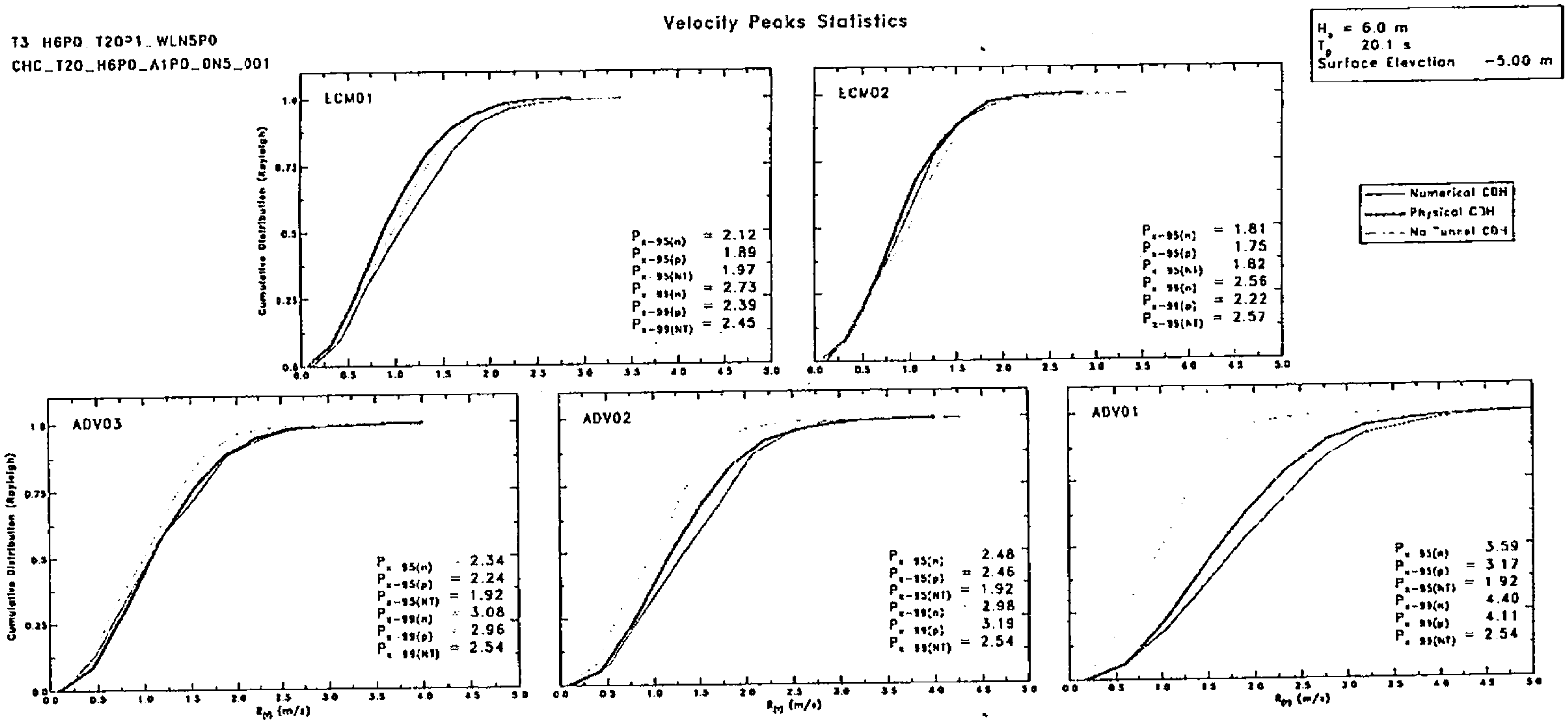

Figure 7.23 - Velocity peaks analysis: Case 3

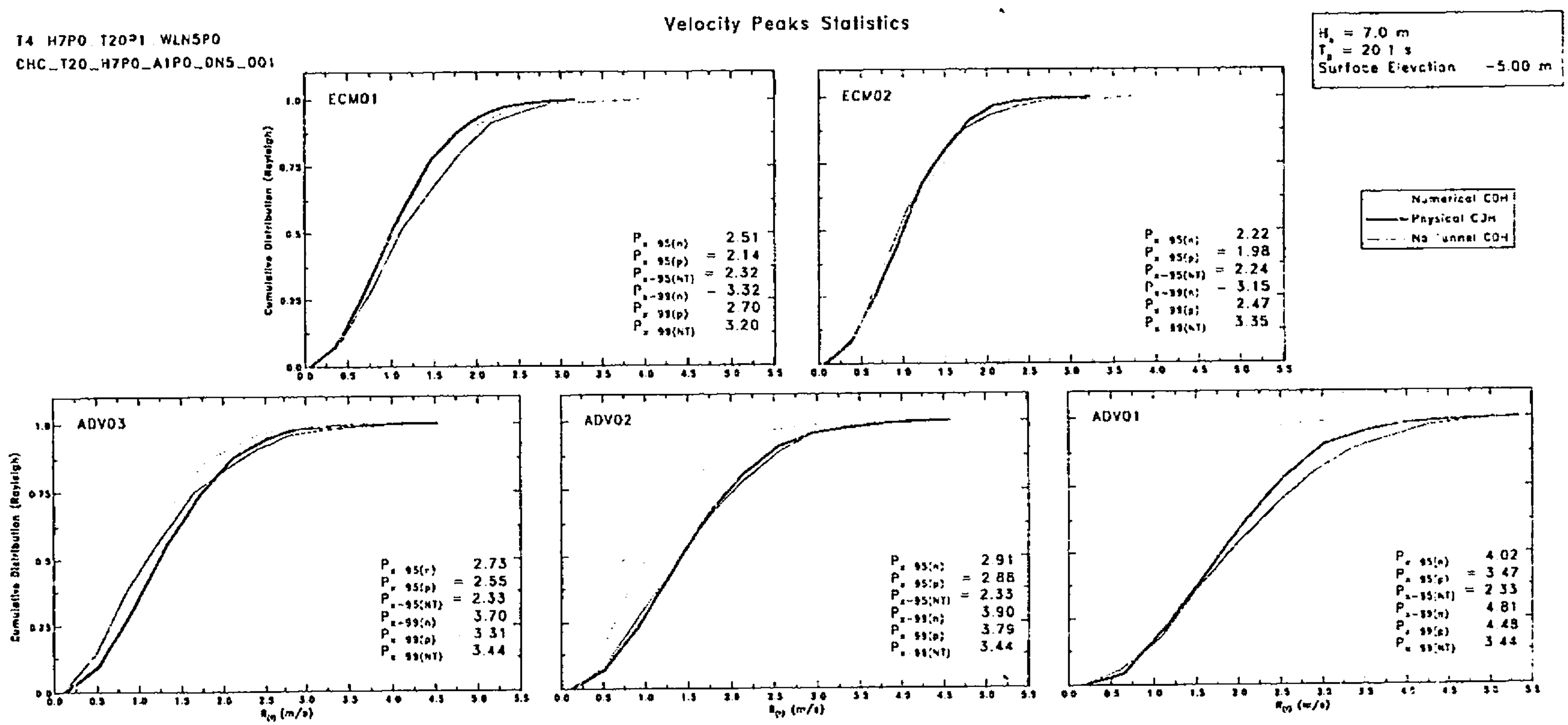

Figure 7.24 - Velocity peaks analysis: Case 4

7.2 Analysis of Numerical Results

One of the most beneficial aspects of numerical modelling is the ease of analyzing numerical results. It is quite simple to place new data probes at any desired location within the domain of the simulation. Doing the same for physical modelling is much more time consuming and requires more resources and equipment. Numerical models can also offer time-averaged snapshots of the entire domain giving researchers an idea as to the general patterns or trends occurring within the domain.

7.2.1 Significant Wave Height Analysis

The WaveSim numerical model allows the option to output the time-averaged significant wave heights distributed over the domain. Figure 7.25 through Figure 7.29 depict the results for each of the simulations (units are in prototype meters). In each of these figures, a partial section of the computational domain is presented. The bottom of each image is the location of the wave generator, and the top is at the edge of the damping layer. At 1025 m (y-axis scale), the dark line indicates the location of the −50 m elevation, the beginning of the concrete bathymetry. At 1185 m, this dark line indicates the location of the −34 m plateau of the concrete bathymetry. At 1815 m near the top of each image, this dark line indicates the location of the −34 m mark where the bathymetry again slopes down on the opposite side. For Cases 1-4, the outline of the tunnel is also overlaid onto each image, depicting the toe protection and the structures crest.

In Figure 7.25, the calibration case, the significant wave height is notably uniform across the entire domain as would be expected, demonstrating the uniformity of the numerical model.

In Figure 7.26, the effects of the submerged structure on the wave climate are obvious. A significant shoaling is observed at the up-wave crest of the structure. This effect is seen to diminish across the submerged structure where the freeboard increases. A distinct pattern of reflection can be observed in front of the structure, repeating at steady intervals back towards the wave generator (see Table 7.4). An area of increased wave activity is also seen down-wave of the structure, primarily at the location of least freeboard.

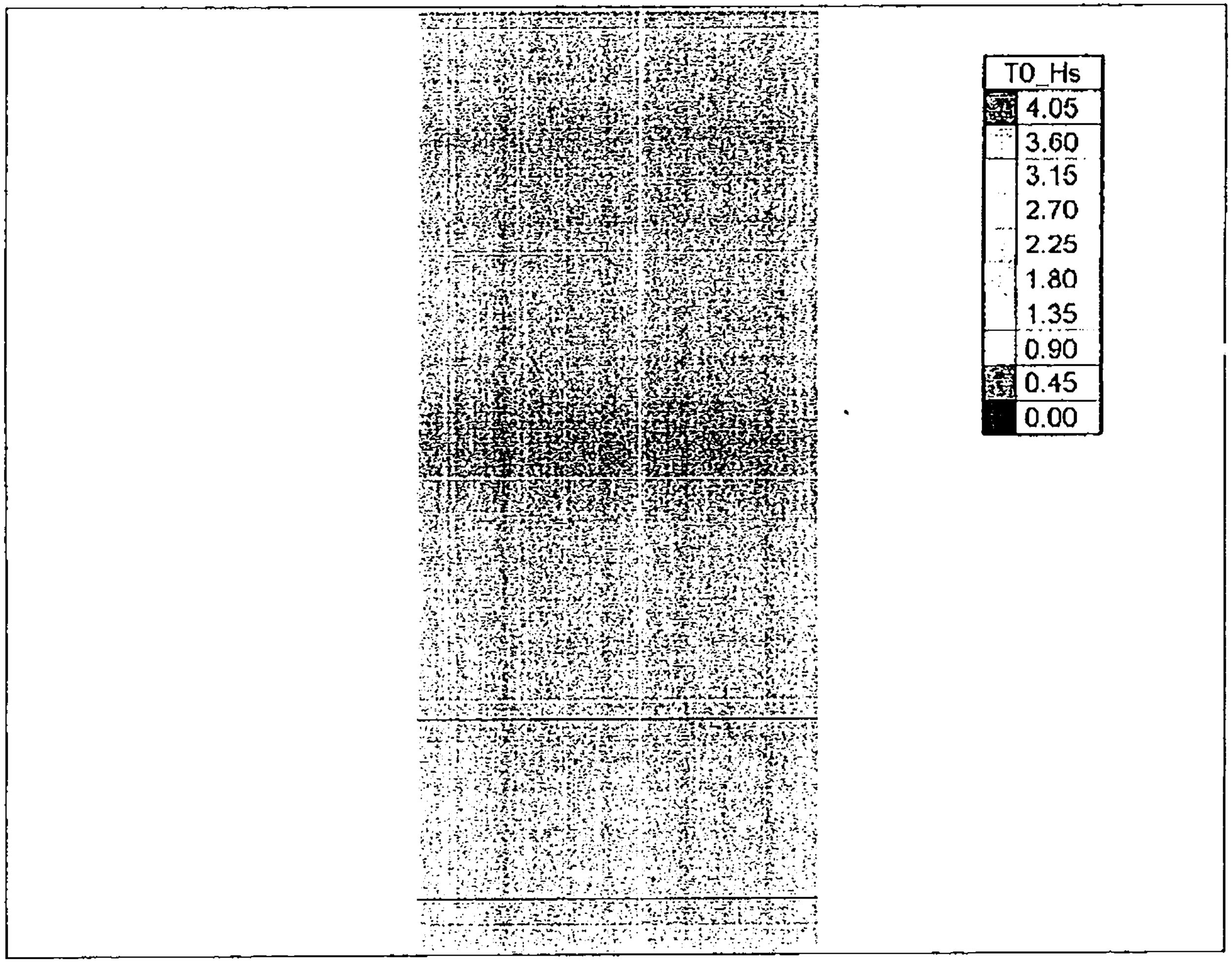

Figure 7.25 - Significant wave height distribution: Case 0

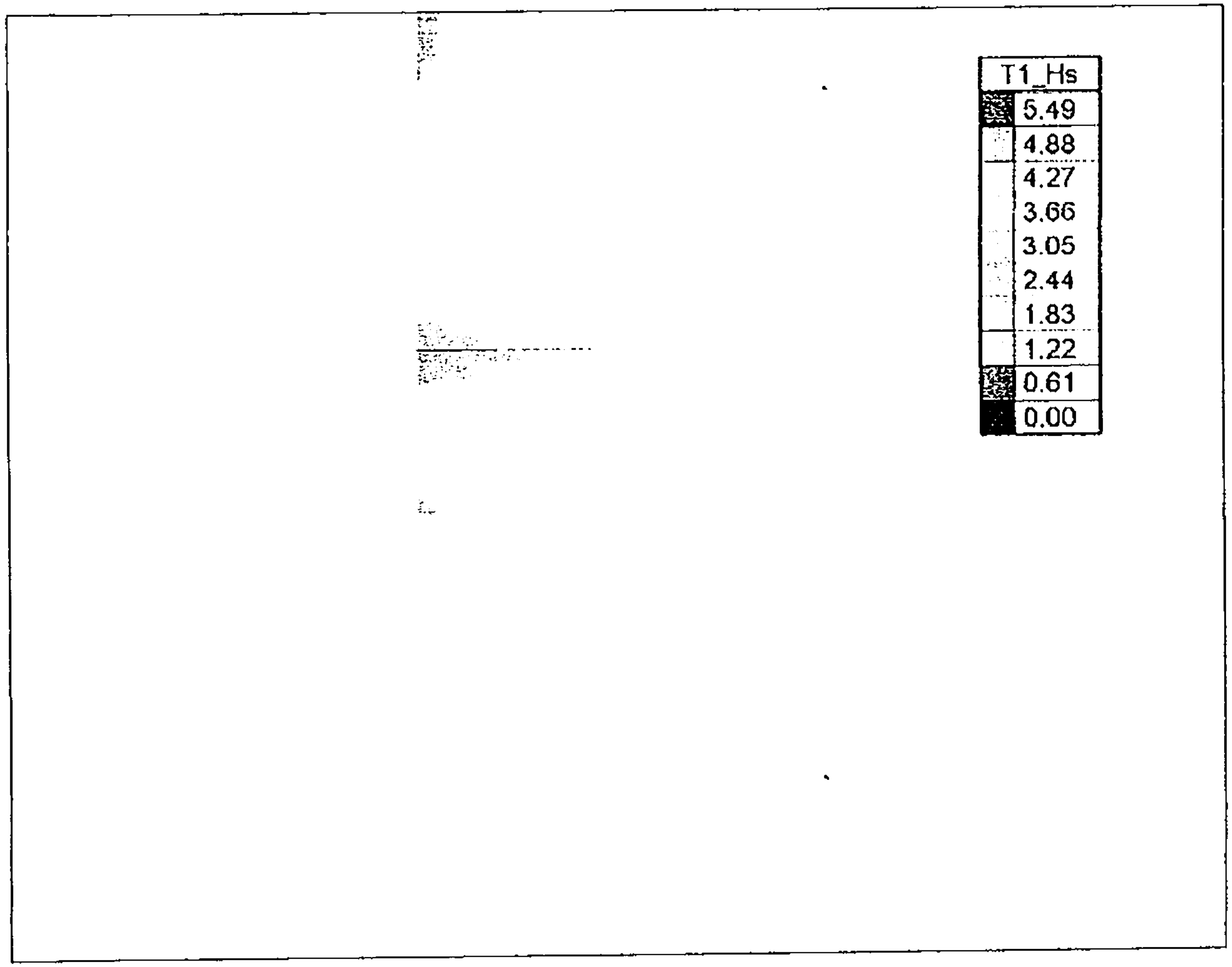

Figure 7.26 - Significant wave height distribution: Case 1

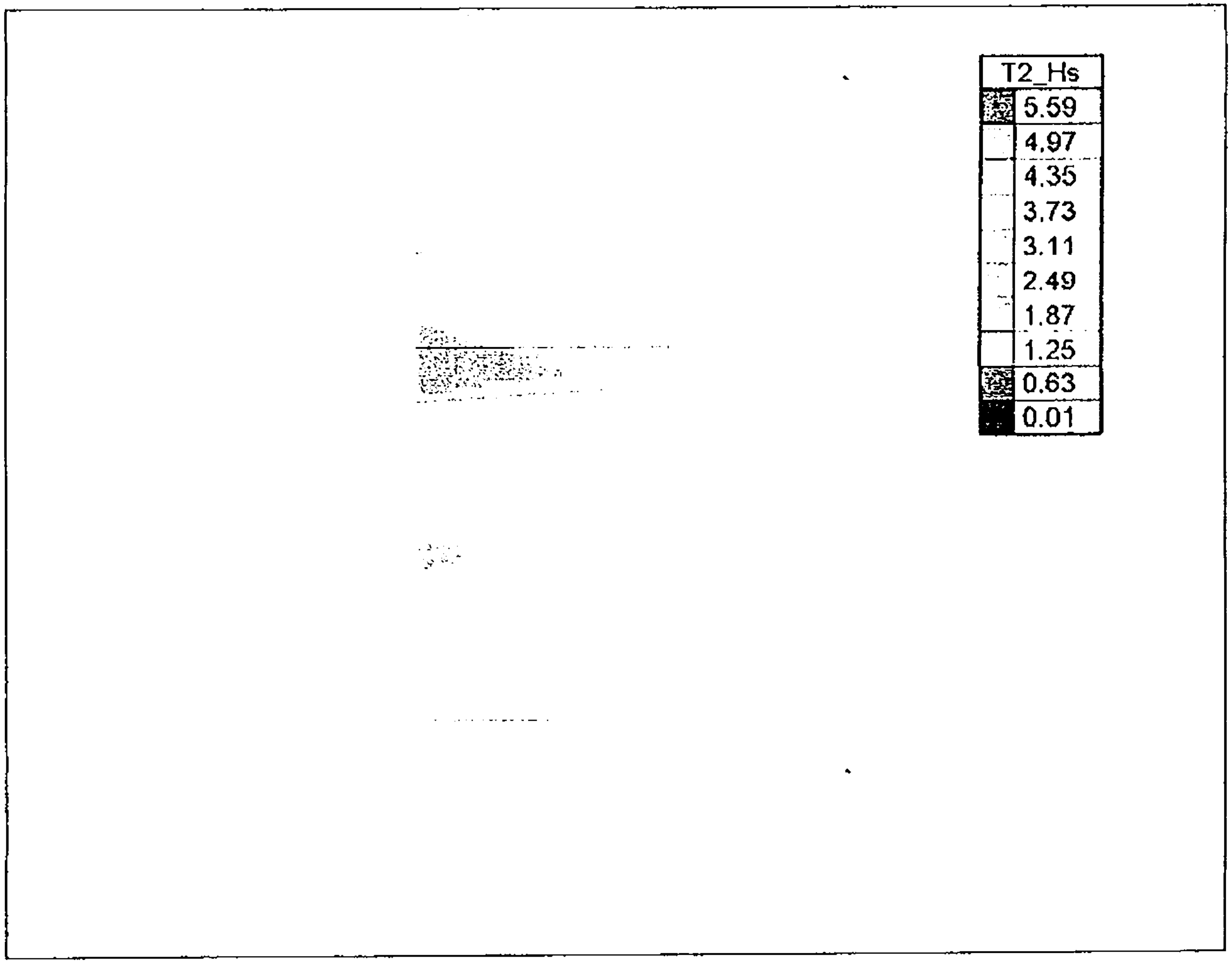

Figure 7.27 - Significant wave height distribution: Case 2

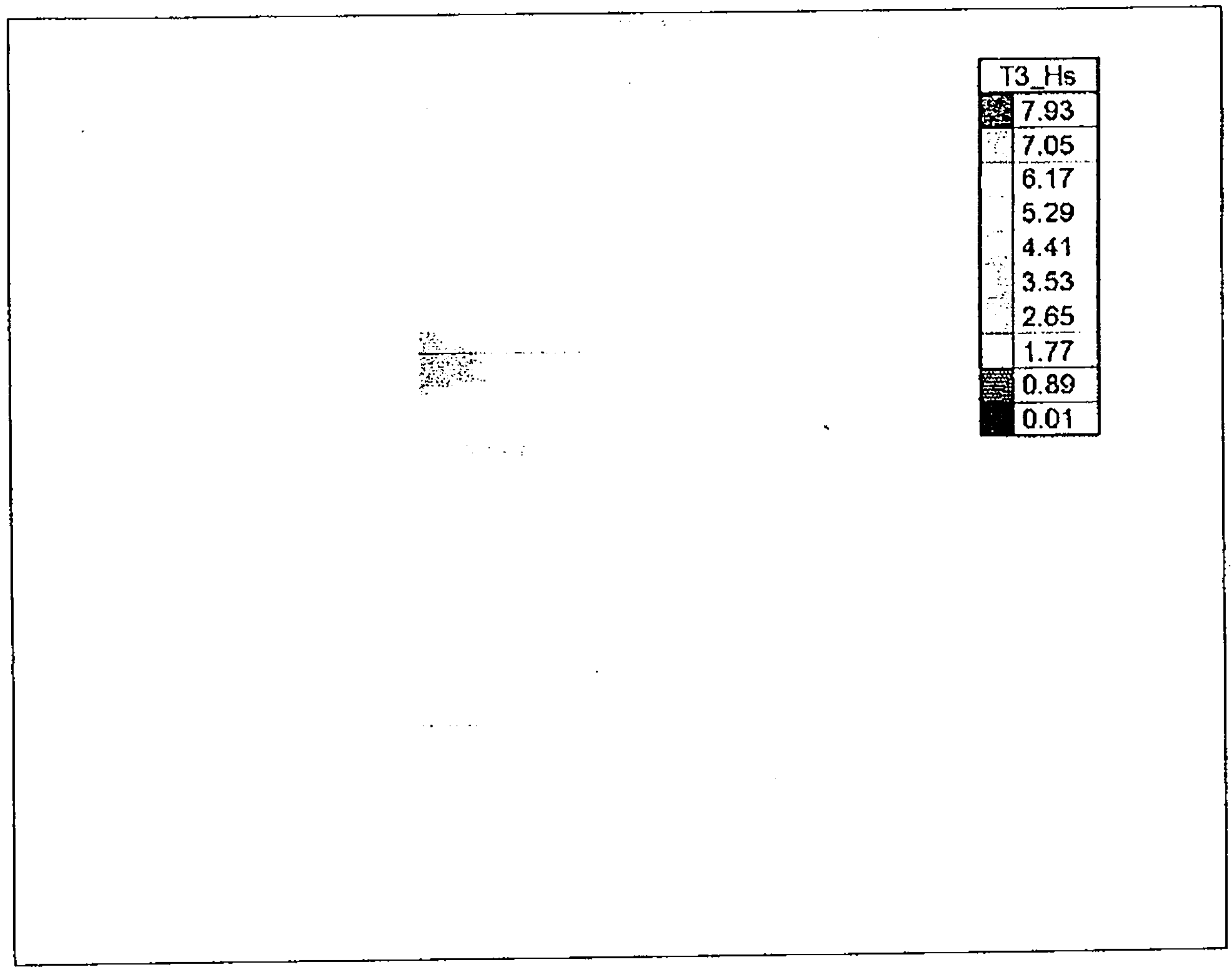

Figure 7.28 - Significant wave height distribution: Case 3

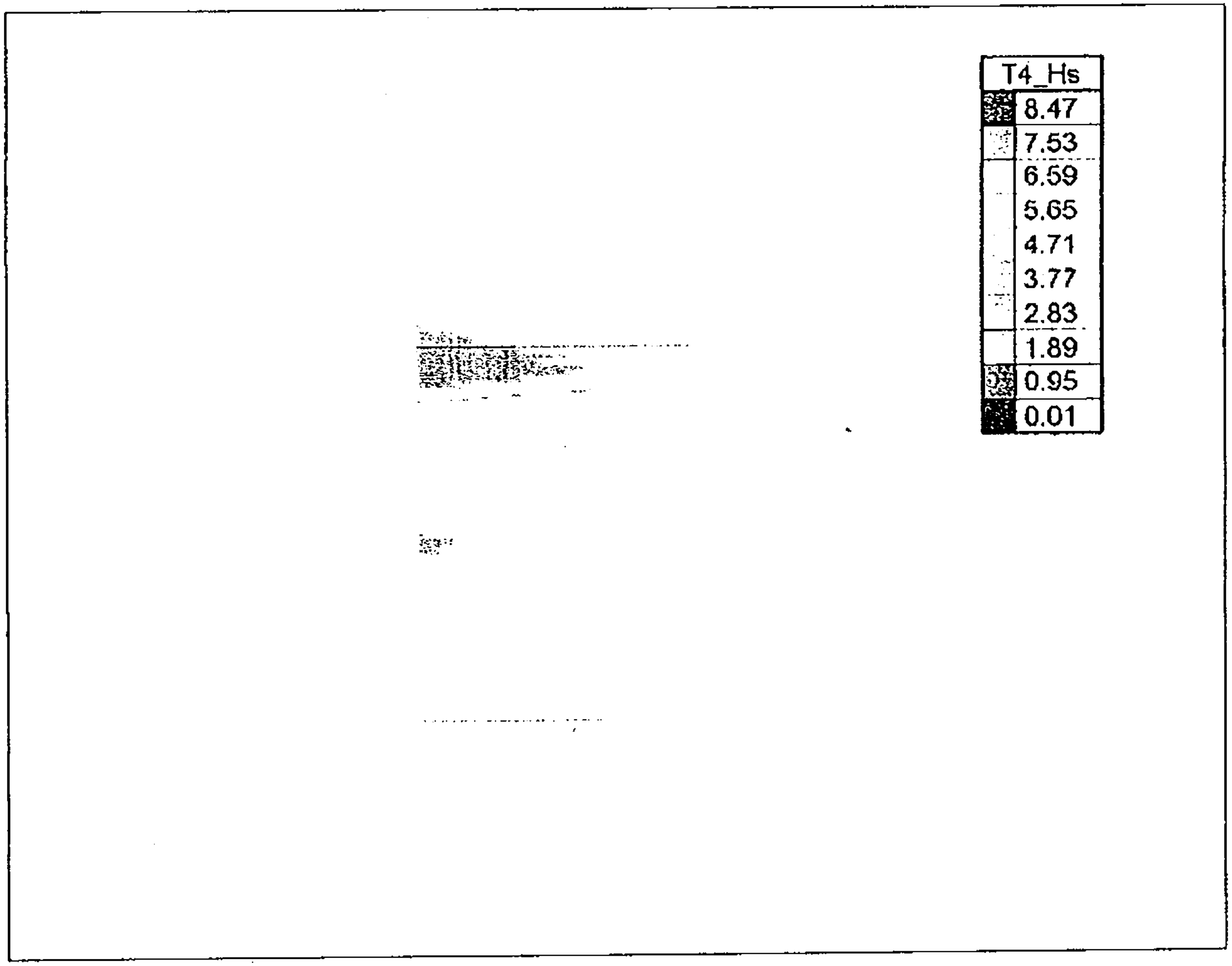

Figure 7.29 - Significant wave height distribution: Case 4

In Figure 7.27, Figure 7.28, and Figure 7.29, similar effects are observed as previously observed. The shoaling section at the up-wave crest of the submerged structure generally increases in magnitude for each case, and its area of influence reaches farther along the structures axis to the section of increased freeboard. The reflection patterns, again showing steady intervals, also increase their area of influence with each case.

Table 7.4 enumerates the distances measured between each "peak" in the significant wave heights observed in Figure 7.25 through Figure 7.29. The "main" peak is the increase in wave heights measured right near the front crest of the submerged structure. This main peak is followed by a number of other repetitions (denoted first, second, etc.). The wavelength of the reflected wave along Cross-Section 3 (where the freeboard is least) is also noted in the table. The final column presents a calculation of the reflected wavelength versus the measured distances between each successive peak in the significant wave height.

It is observed that in general, the distance between these peaks has a high correlation to the reflected wavelength, specifically half of this wavelength.

Table 7.4 - Significant wave height peaks

Test	Reflected Wavelength at CS3 (m)	Distance between Significant Wave Height Peaks (m)		$L_{reflected}$ / Distance between Peaks
Case 1	263.92	131.40	Main ↔ First	2.0
		140.10	First ↔ Second	1.9
		121.80	Second ↔ Third	2.2
Case 2	333.76	156.50	Main ↔ First	2.1
		176.20	First ↔ Second	1.9
Case 3	319.88	157.80	Main ↔ First	2.0
		178.80	First ↔ Second	1.8
Case 4	321.01	164.60	Main ↔ First	2.0
		182.70	First ↔ Second	1.8

7.2.2 Current Field Analysis

The WaveSim numerical model allows the option to output the depth and time averaged current distributed over the entire grid. Figure 7.30 through Figure 7.34 depict the results for each of the simulations (units are in meters per second). In each of these figures, a partial section of the computational domain is presented. The bottom of each image is the location of the wave generator, and the top is at the edge of the damping layer. At 1025 m (y-axis scale), the dark line indicates the location of the −50 m, the beginning of the concrete bathymetry. At 1185 m, this dark line indicates the location of the −34 m plateau of the concrete bathymetry. At 1815 m near the top of each image, this dark line indicates the location of the −34 m mark where the bathymetry again slopes down on the opposite side. For Cases 1-4, the outline of the tunnel is also overlaid onto each image, depicting the toe protection and the structures crest. In each of these figures, the vectors have been exaggerated by 150 times to better view the flow circulations.

In Figure 7.30, the calibration case, it is observed that there is effectively no current development, and that the velocities are essentially uniform in the entire domain.

As seen in Figure 7.31, the submerged structure has a strong effect on the time-averaged current within the computational domain. In general it is observed that a large circulatory flow has developed. A medium strength current is driving the flow down-wave at the right side where the freeboard is greatest. This is counterbalanced by a more intense up-wave flow over the left side of the tunnel where the freeboard is least. As would then be expected, a location of zero current is observed near the middle of the structure about which the current is rotating.

In order to ensure that the observed circulatory flow was not a function of the boundary conditions, an additional simulation was run using the "Full Basin" computational domain. A similar pattern was observed, thus indicating that the circulation is indeed a phenomenon induced by the submerged structure and not merely an artifact of the numerical model.

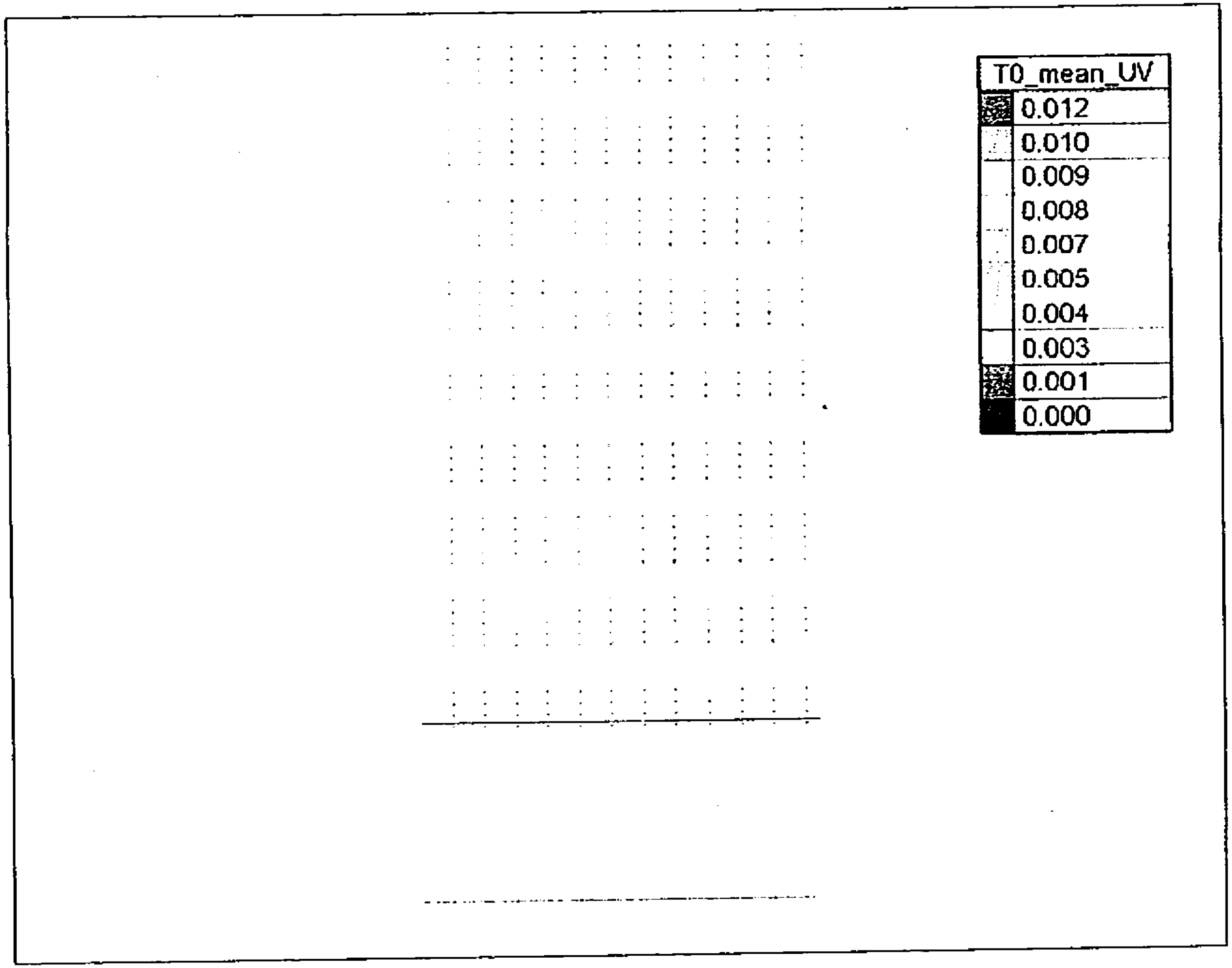

Figure 7.30 - Mean current distribution: Case 0

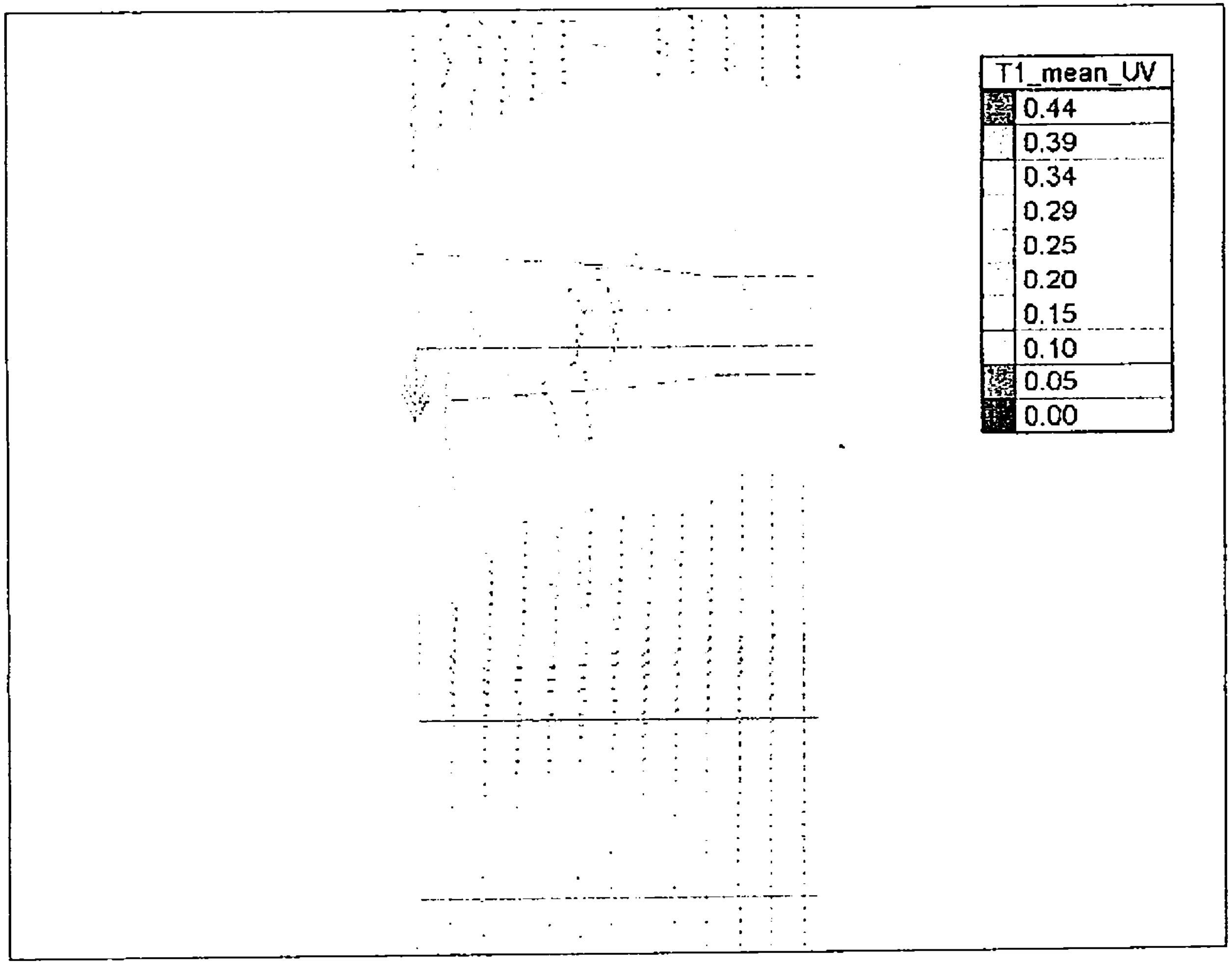

Figure 7.31 - Mean current distribution: Case 1

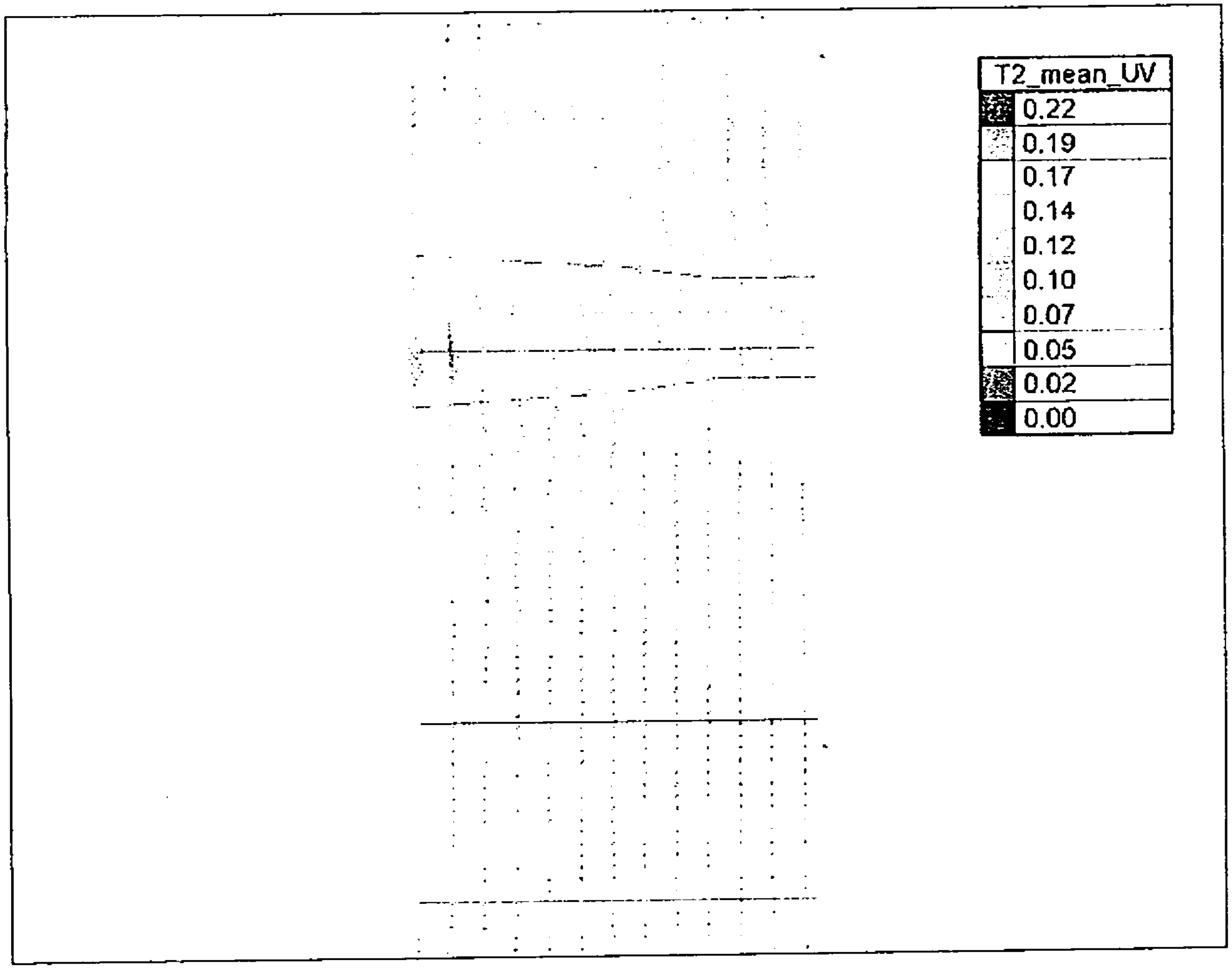

Figure 7.32 - Mean current distribution: Case 2

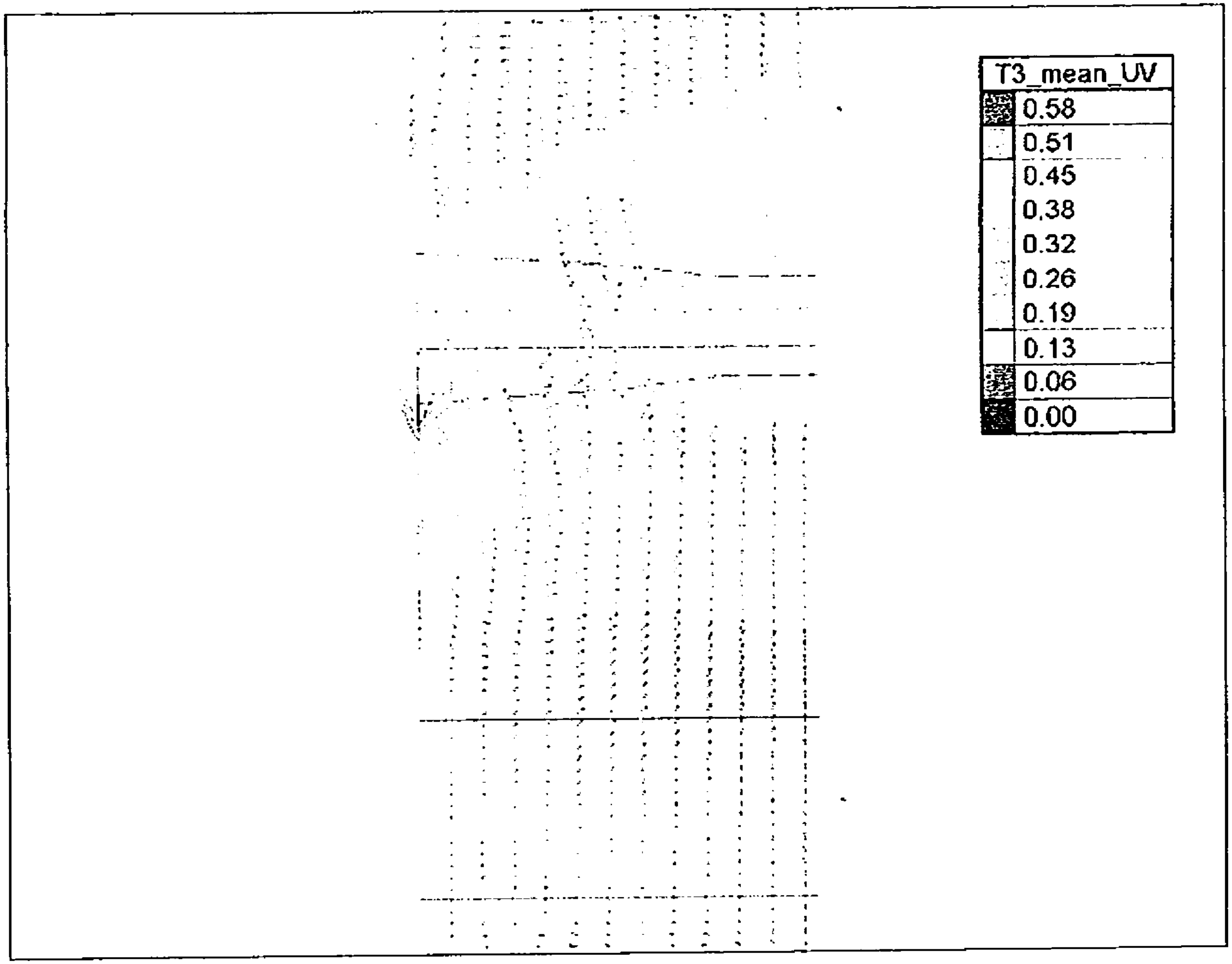

Figure 7.33 - Mean current distribution: Case 3

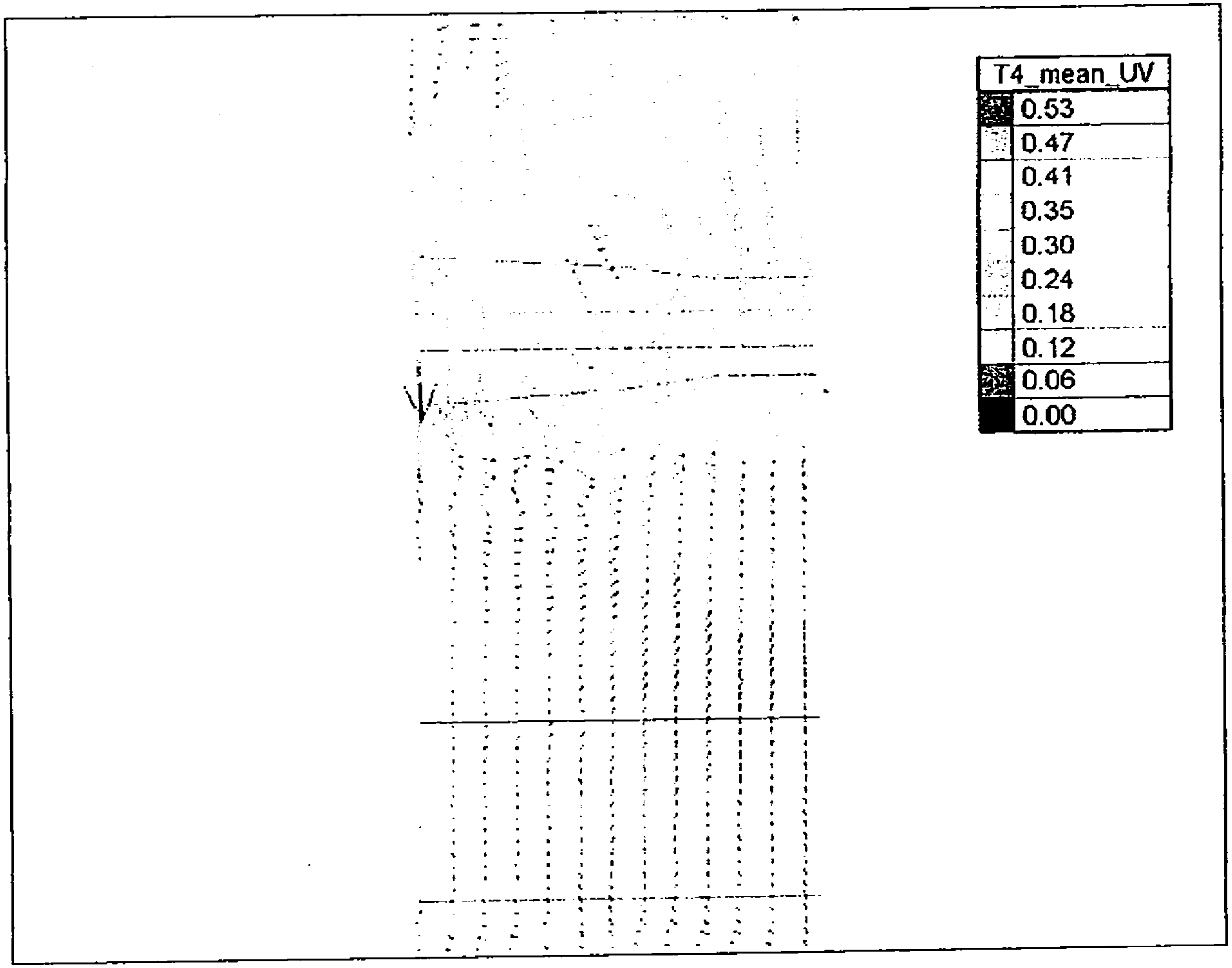

Figure 7.34 - Mean current distribution: Case 4

In Figure 7.32, Figure 7.33, and Figure 7.34, similar patterns are observed. In general it appears that the more energetic wave conditions produce stronger circulations. In general, the axis of the rotational flow is generally in the same location for each case.

7.2.3 Reflection Analysis

A reflection analysis was undertaken in the numerical model with the placement of additional probes as discussed earlier in Section 6.2.11 and 6.2.13. The analysis was performed using two GEDAP programs, although they both use the same calculation process to compute the reflection. The first method outputs the results in the time domain, while the second method outputs the results in the frequency domain. The reflection analysis was performed for each of the 3 cross-sections.

Figure 7.35 through Figure 7.39 depict the reflection analysis results in the time domain at each of the three cross-sections. CS1 is where the freeboard is greatest, and CS3 is where the freeboard is smallest.

In Figure 7.35, the calibration case, it is observed that there is effectively no reflection since there is no obstruction to the flow. The reflection coefficients in this case show only 2.3%. The uniformity of the numerical model is seen by comparing the three incident wave trains, which are virtually identical. Although it would be expected that there should be zero reflected energy, the explanation for the 2.3% reflection is partially due to possible reflection from the damping layer at the end of the numerical domain, and potentially due to error in the method of calculating reflection itself at extremely low reflection values.

In Figure 7.36, it is observed again that the incident wave trains appear nearly identical across each of the three cross-sections. The reflected wave trains magnificently demonstrate the impact of the submerged structure on the flow. A steady increase in the reflection is observed as the structure's freeboard decreases.

Figure 7.37, Figure 7.38, and Figure 7.39 each show similar trends in the reflection as would be expected. In general, the reflections at each cross-section are fairly consistent despite the changing wave conditions. At the location of largest freeboard (Cross-Section 1), the reflection coefficient is observed to be approximately 14%. At the middle of the submerged structure (Cross-Section 2), the reflection coefficient is observed to be approximately 26%. Finally, the location of least freeboard (Cross-Section 3) shows a reflection coefficient of approximately 36%.

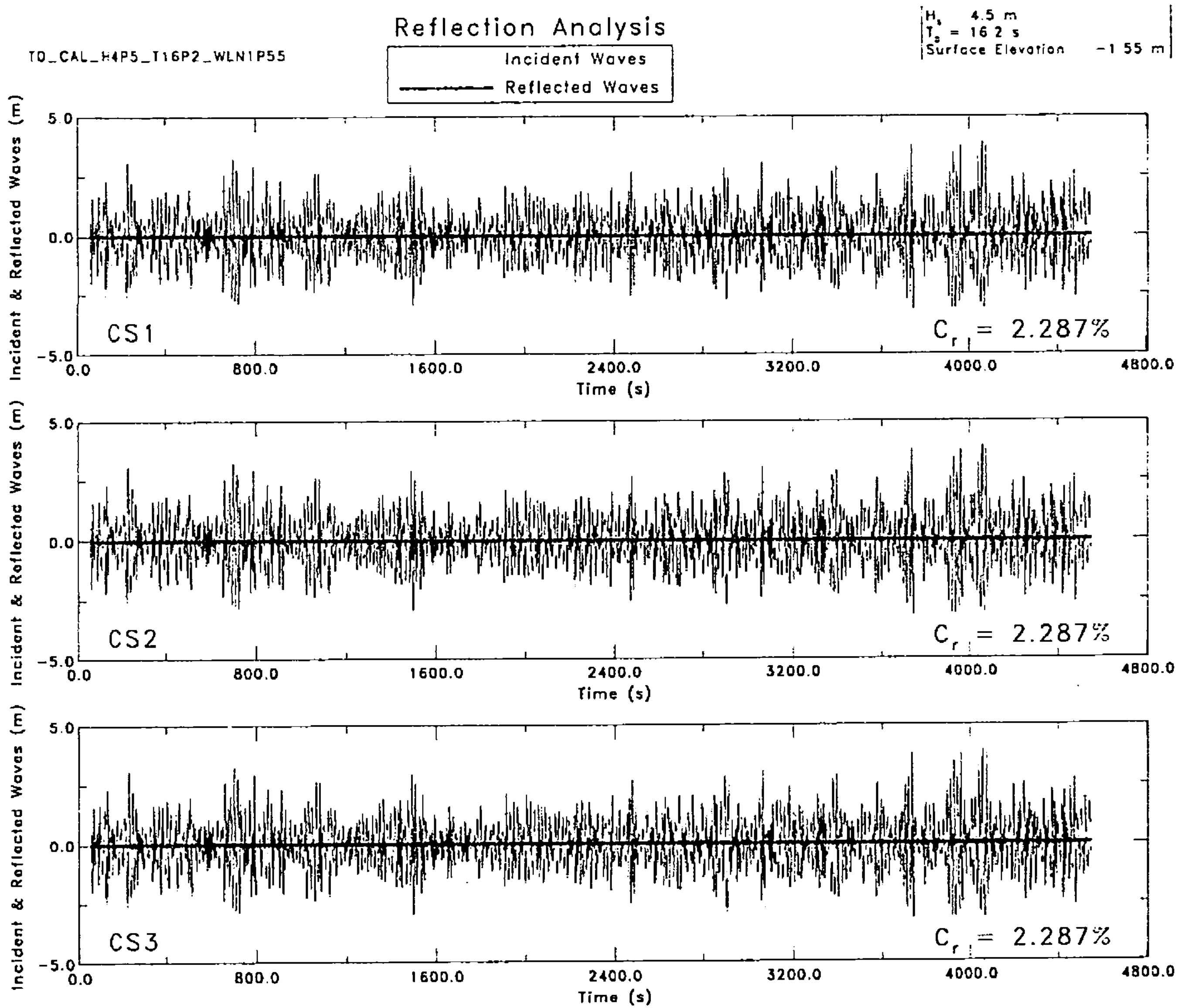

Figure 7.35 - Reflection analysis (time domain): Case 0

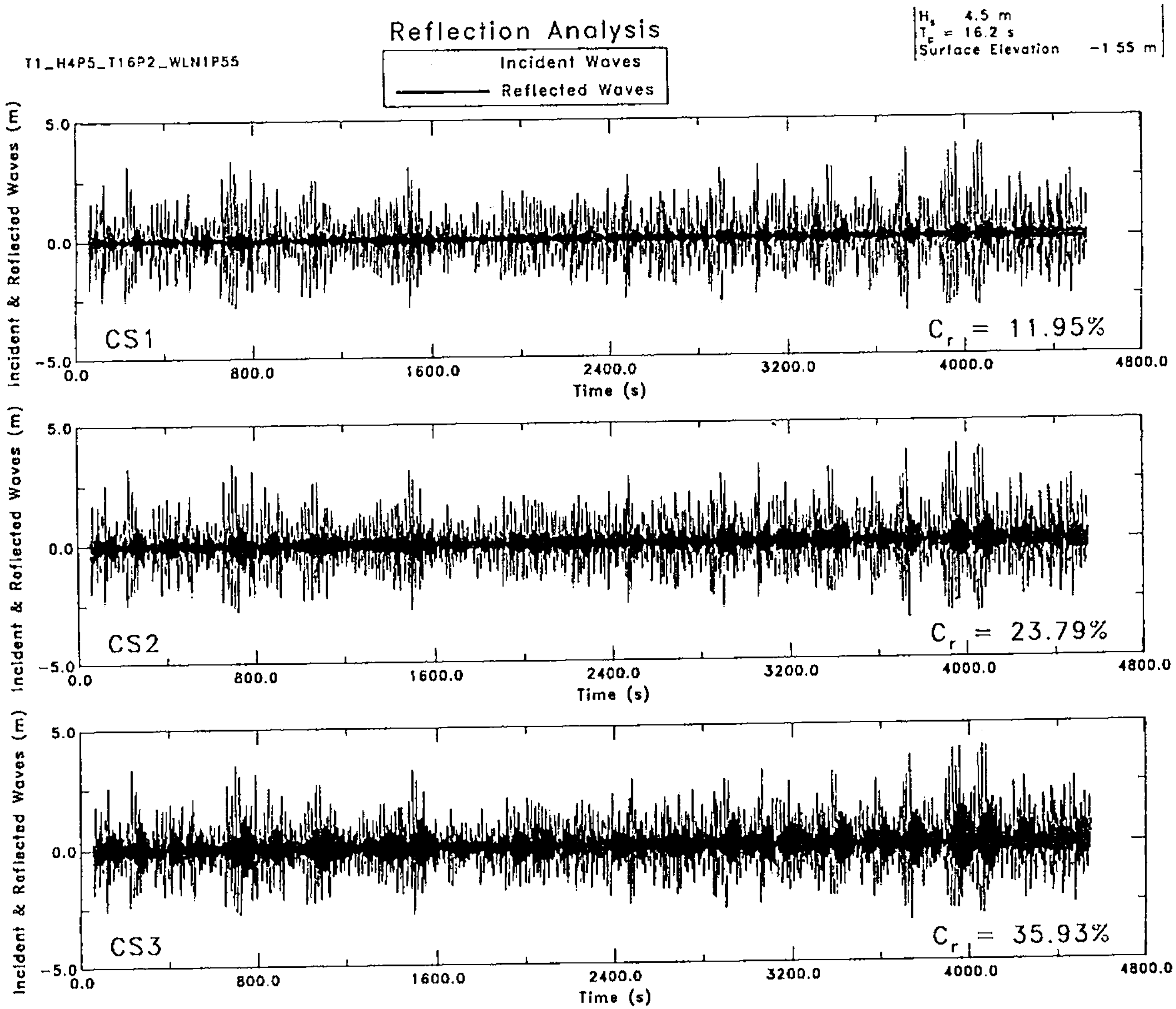

Figure 7.36 - Reflection analysis (time domain): Case 1

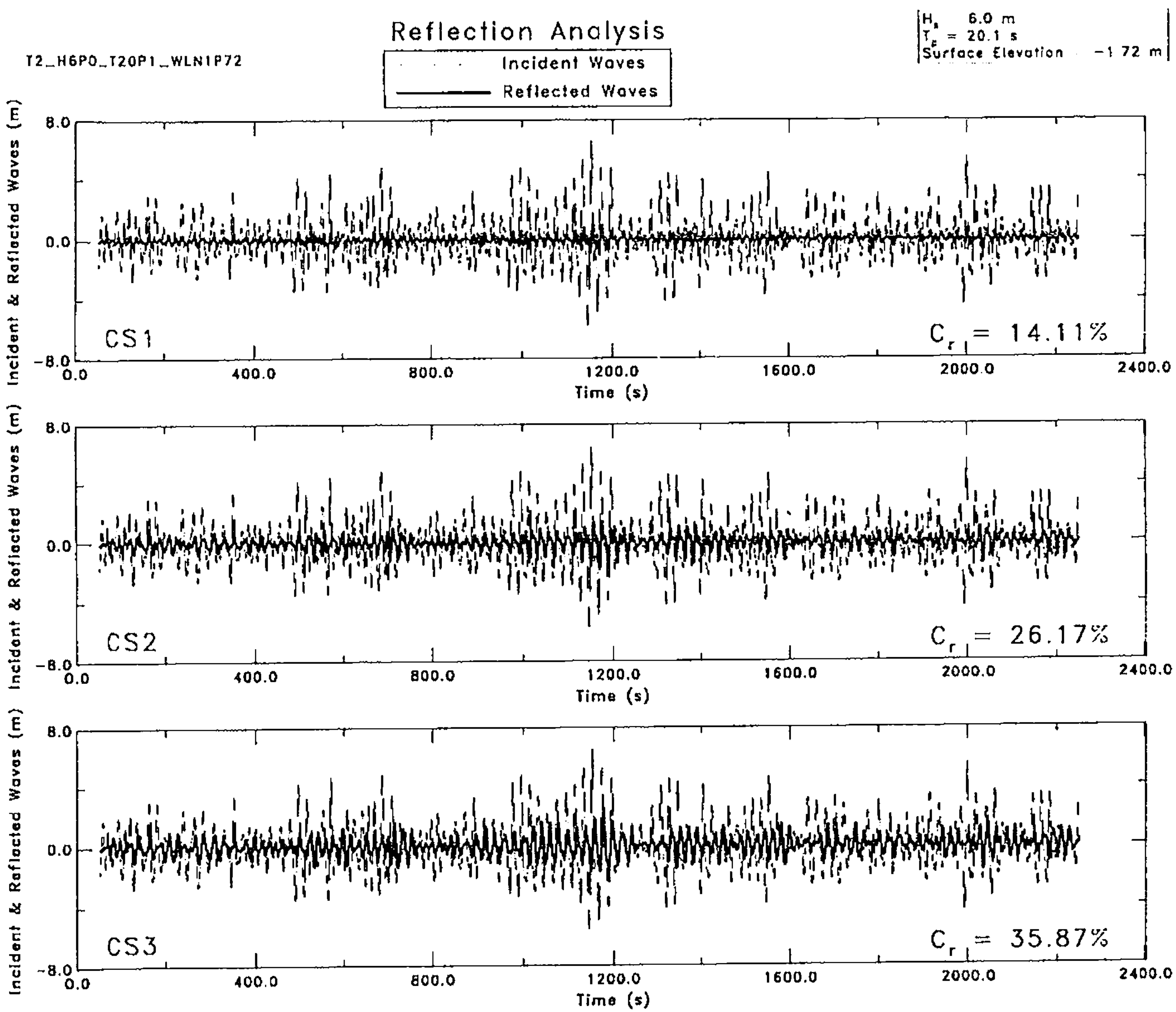

Figure 7.37 - Reflection analysis (time domain): Case 2

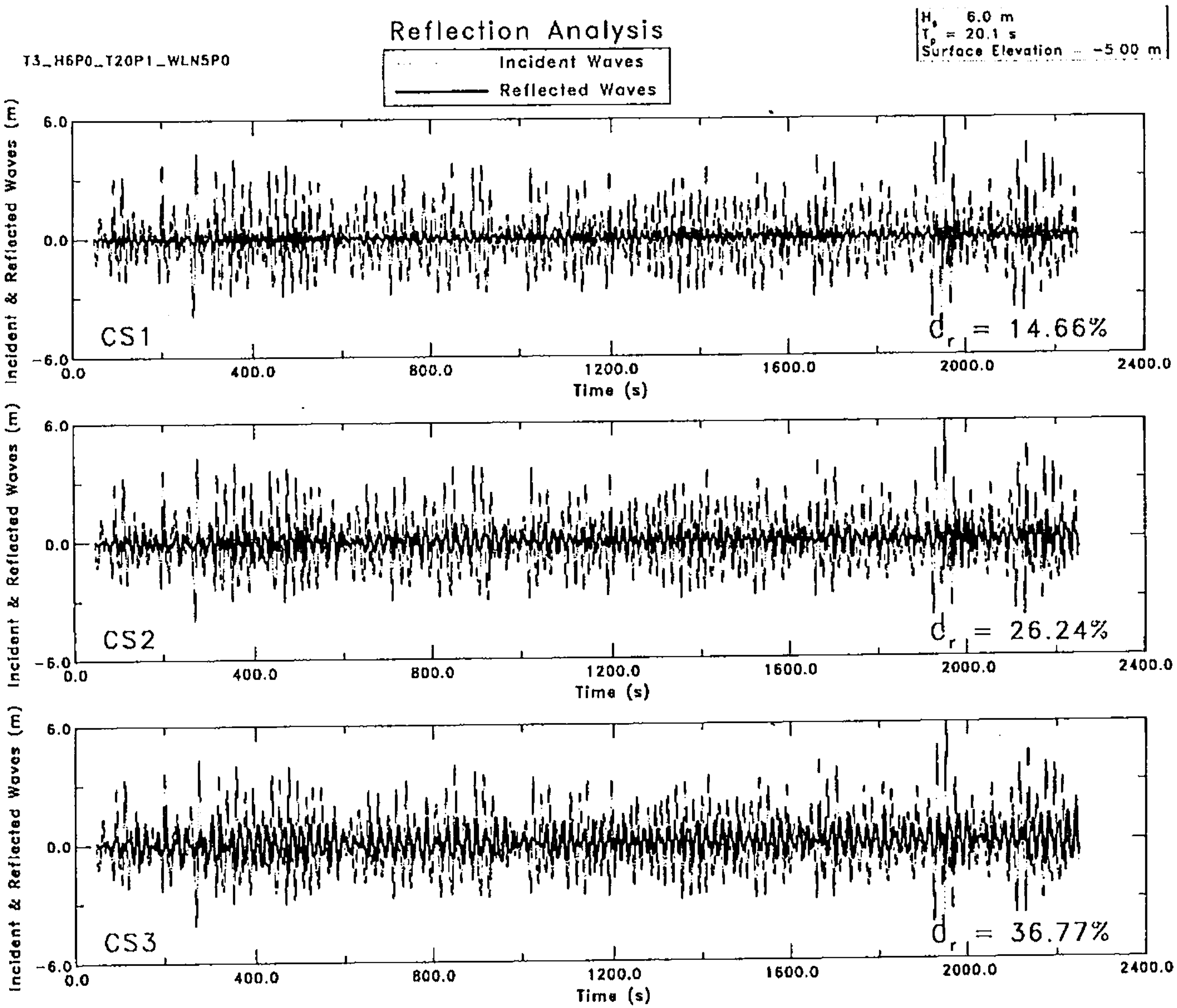

Figure 7.38 - Reflection analysis (time domain): Case 3

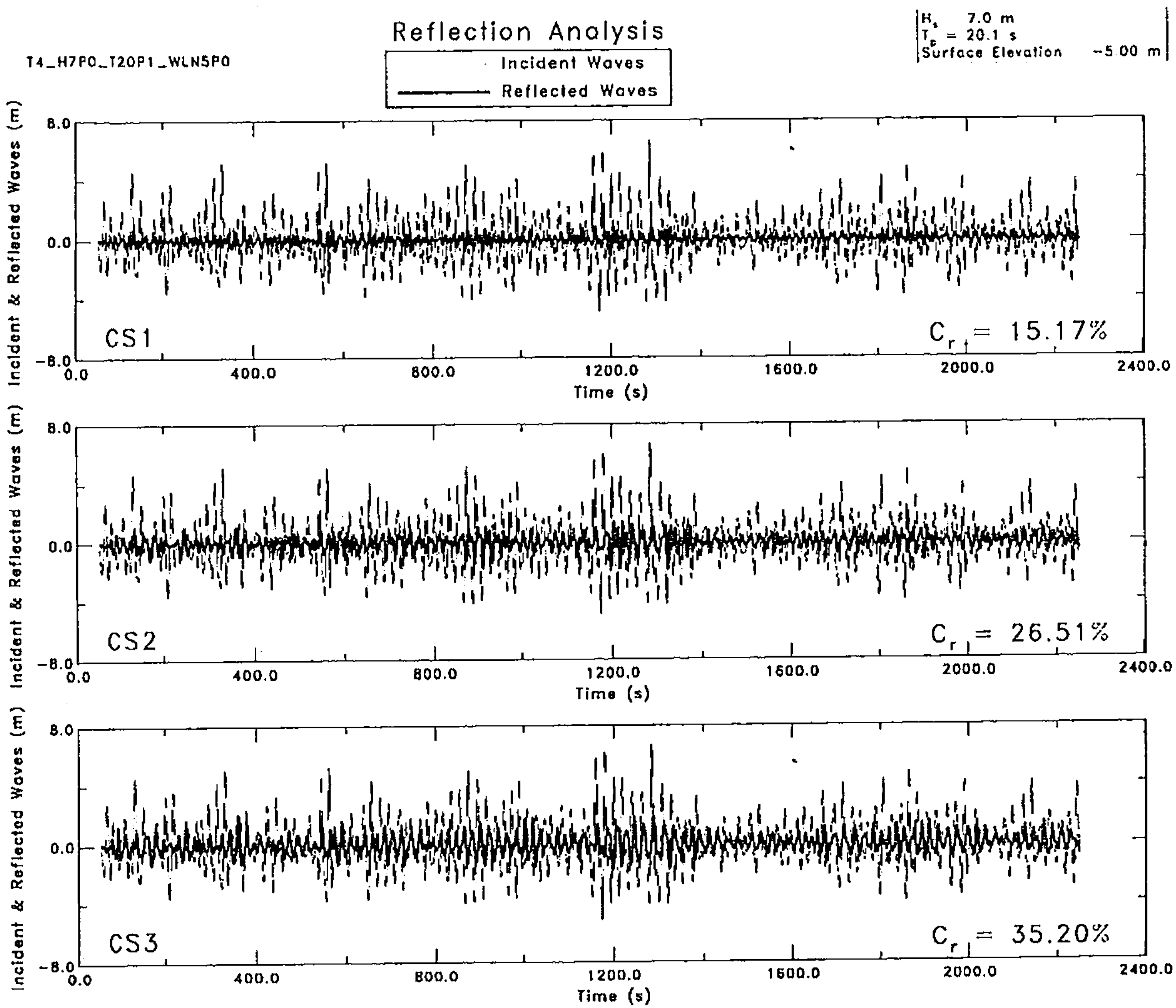

Figure 7.39 - Reflection analysis (time domain): Case 4

Figure 7.40 shows the results of the wave record reflection analysis compared with the relative submergence, defined as the incident wave height over the water depth at the crest of the structure for each cross-section. Distinct trends are visible for each case, meaning that a reasonable estimate of expected reflection could be calculated for alternate submergence depths along the submerged structure.

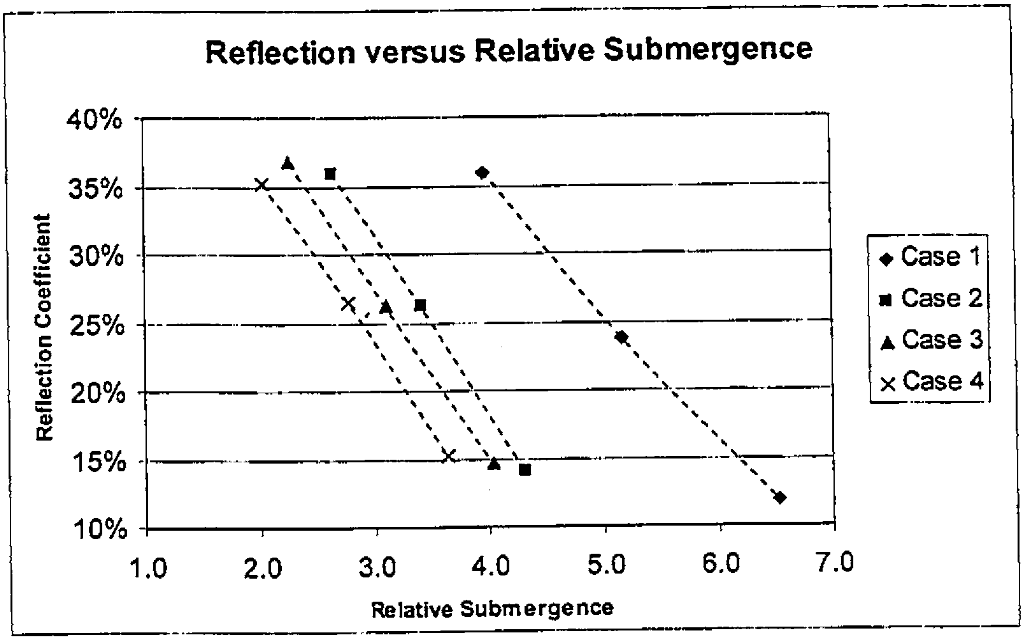

Figure 7.40 - Reflection versus relative submergence

Figure 7.41 through Figure 7.45 depict the reflection analysis results in the frequency domain at each of the three cross-sections. CS1 is where the freeboard is greatest, and CS3 is where the freeboard is smallest. These figures also show the reflection coefficient functions and error thresholds over the analysis frequencies.

In Figure 7.41, the calibration case, we can see the incident and reflected wave spectra for each cross-section. As would be expected, there is effectively zero reflected energy since there is no flow obstruction. Again, a comparison of the three images shows they are virtually identical, showing the uniformity of the numerical model.

In Figure 7.42, the reflected wave spectra are clearly shown. The bulk of the reflected energy matches the main frequency band of the incident spectral shape. Figure 7.43, Figure 7.44, and

Figure 7.45 show similar patterns of reflected energy. An error threshold of approximately 10% is observed around the peak frequency, however beyond ~0.11 Hz, the error threshold starts to become larger, indicating that the analysis method is starting to have difficulties resolving the reflection from these shorter waves. The error threshold is calculated by checking the input data to see if it is consistent with the calculated wave reflection coefficient, and if the threshold is exceeded, the reflection coefficient is obtained by interpolation from adjacent frequencies.

As should be expected, the reflection coefficients from the two reflection analyses methods match within approximately 2% at the worst case, since they are effectively using the same calculation for reflection.

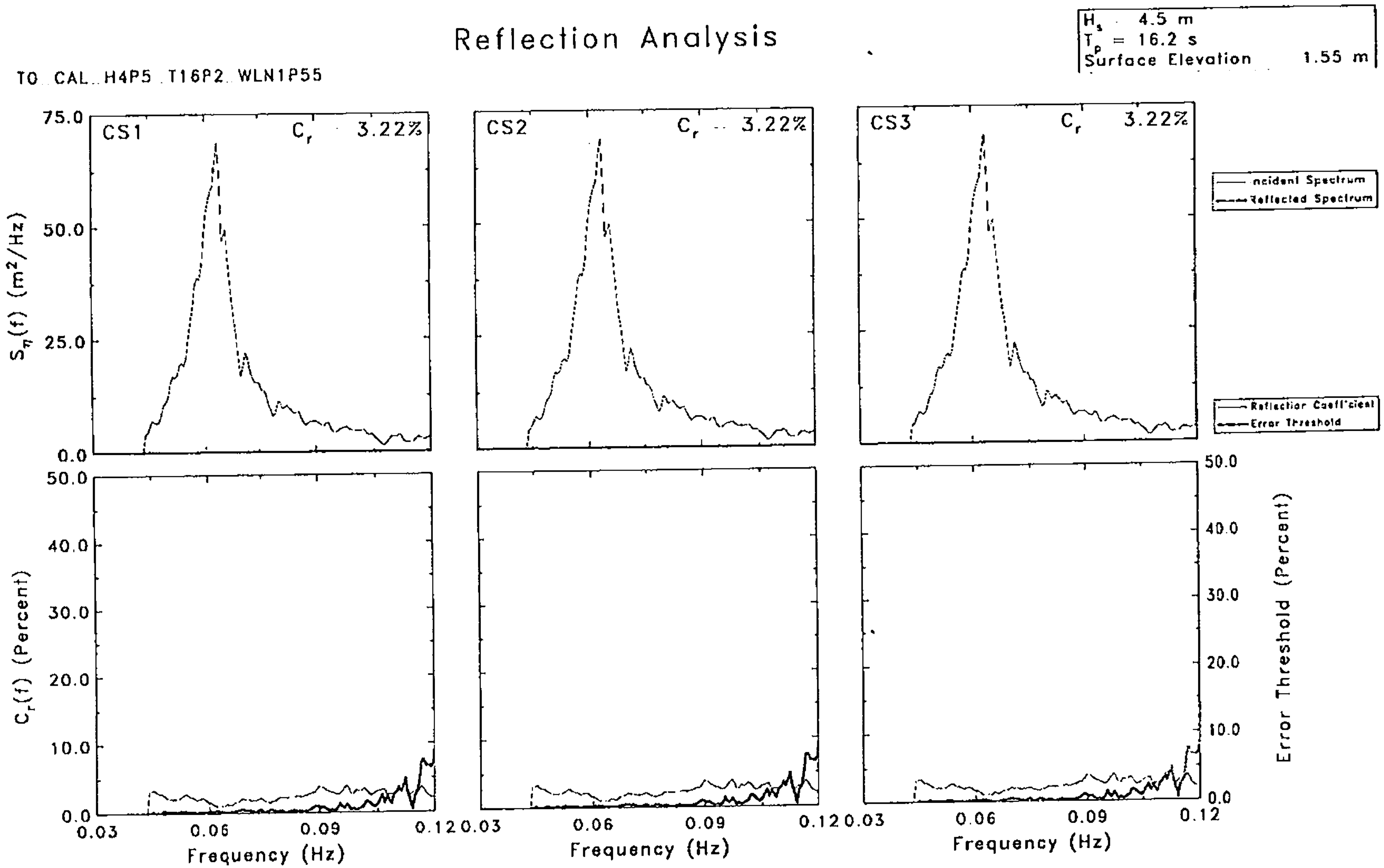

Figure 7.41 - Reflection analysis (frequency domain): Case 0

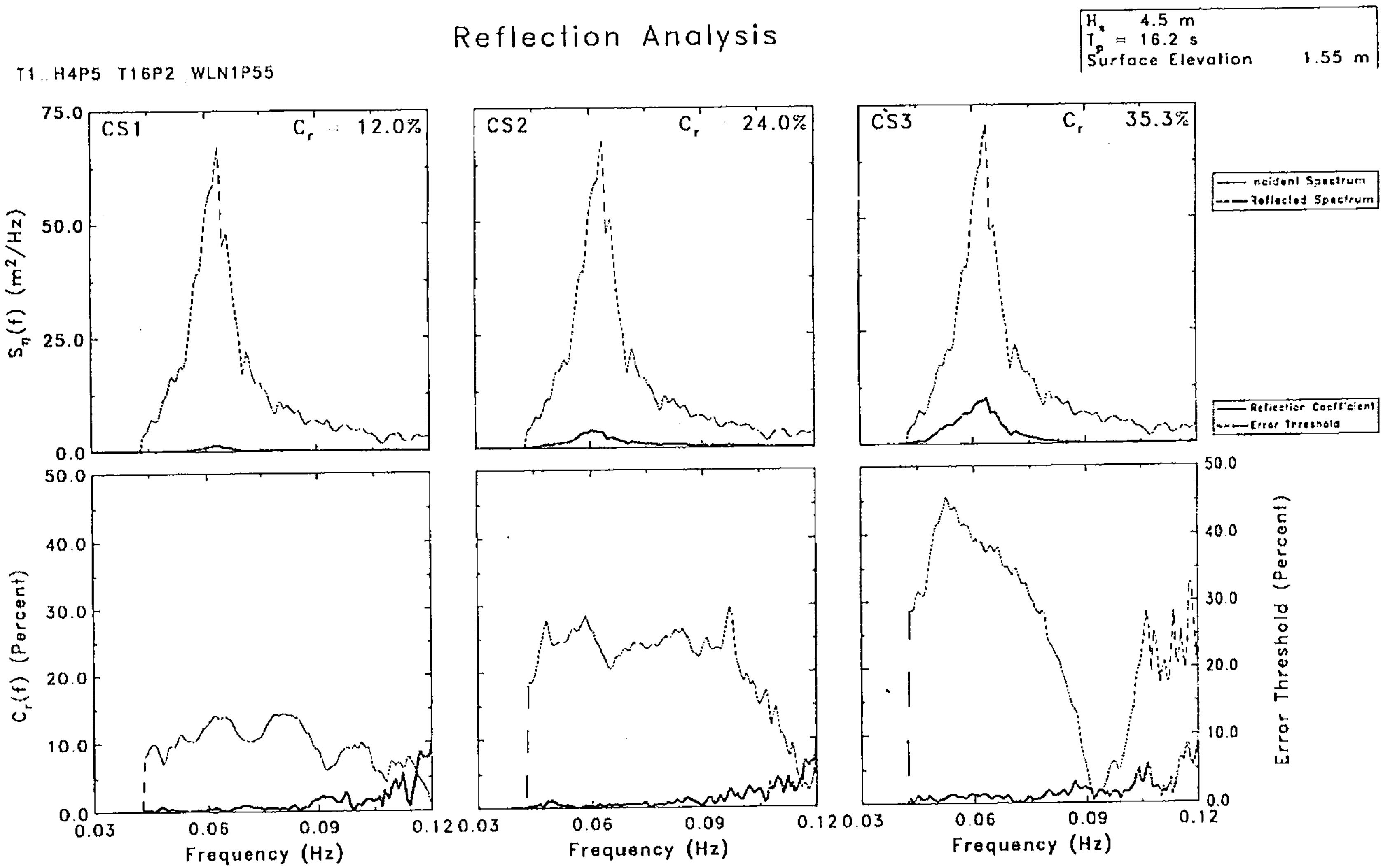

Figure 7.42 - Reflection analysis (frequency domain): Case 1

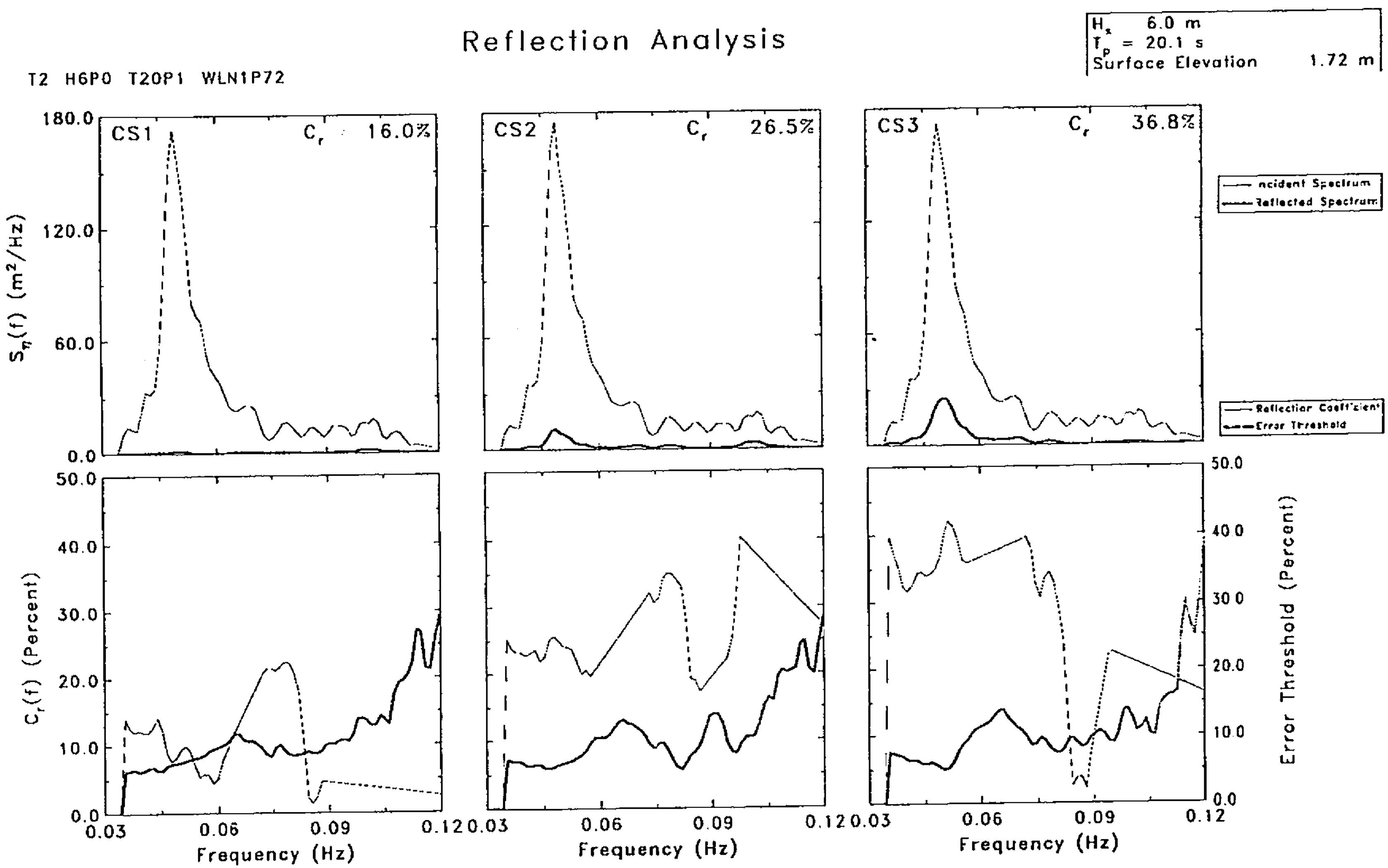

Figure 7.43 - Reflection analysis (frequency domain): Case 2

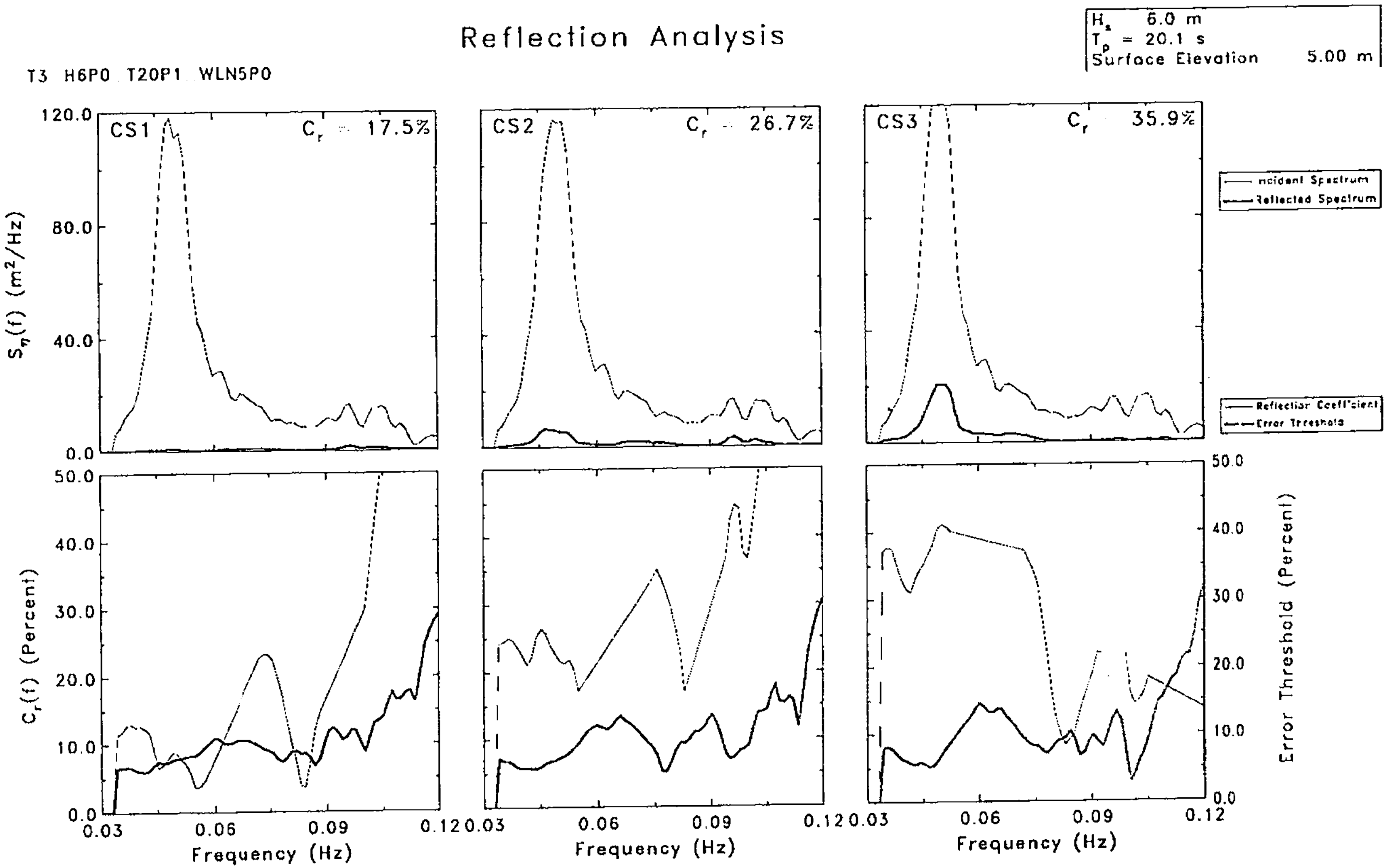

Figure 7.44 - Reflection analysis (frequency domain): Case 3

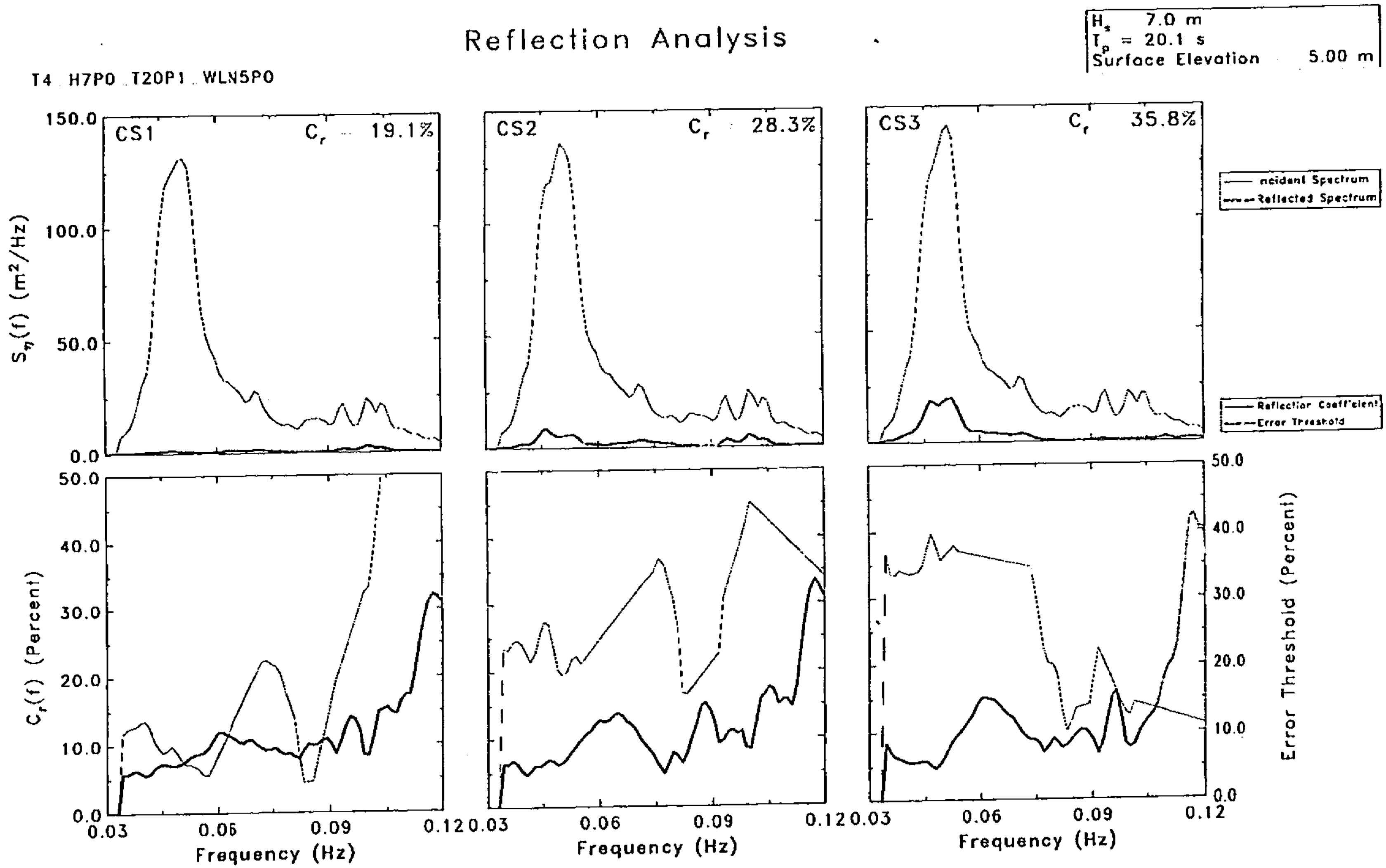

Figure 7.45 - Reflection analysis (frequency domain): Case 4

7.3 Discussion

7.3.1 Damage Analysis

Although a full analysis of the damage to the submerged structure will not be considered within the scope of this research, it did comprise a major portion of the original physical modelling project, and thus a brief commentary is provided.

The water velocity passing over the submerged structure, induced by the motion of the waves, is one of the major causes of damage to the armoured structure. These velocities tend to grab at the outer armour layer, forcing the rocks to dislodge, shake in place, loosen, and eventually roll out of position and down the side slope. Certain minimal levels of damage are normally acceptable for armoured structures, however the size of the armour used must be large enough such that the entire structure is not in danger of any severe damage.

The prescribed current in the physical modelling was 1.2 m/s, and on its own it appeared to have essentially no effect on the armour stability of the submerged structure. However, as seen earlier in Figure 7.20 through Figure 7.24, there were measured velocities much greater than 1.2 m/s in cases where current was not involved. The 99th percentile velocities reached to a maximum of approximately 4.8 and 4.5 m/s for the numerical and physical models respectively in the worst case scenario (Case 4), measured at ADV01 where the submerged structure has the least freeboard and intuitively where the maximum velocities would be found. Indeed velocities of such magnitude were observed to have significant effects on the armour protection of the structure.

In the physical modelling project, the assessment of stability or damage was performed qualitatively, based on the location, extent and number of stone layers displaced. The observed level of damage was rated on a scale of 1 to 6, according to the following classification system:

1. No damage,
2. Initiation of damage (when the armour or scour protection stones are overturned, showing the un-painted side and/or the second armour layer),
3. Light damage (when the first armour layer is removed and the second armour layer presents an initiation of damage),

4. Moderate damage (several armour layers removed, without exposing the tunnel or the backfill),
5. Heavy damage (backfill or tunnel exposure), and
6. Destruction or structure's failure (backfill erosion or scour protection removal).

Following the CHC tests that corresponded with the contract to the client, a full damage analysis was undertaken, pictured in Figure 7.46. The armour protection overall sustained light damage under the action of the design waves and current considered in the study. The worst damage occurred, as expected, near the West side of the model, where the tunnel is highest and the freeboard was smallest. At this location, the shoulders of the armour protection crest and berm were reshaped and became slightly rounded by the more severe velocities. The damage was not even on both sides of the structure, as the down-wave (North) shoulders sustained slightly more damage than did the up-wave (South) shoulders. The final cross-section profile of the structure featured rounded shoulders that are typical at the end of prototype construction works. In general, the structure showed a satisfactory performance and robustness since it maintained its intended purpose even after testing in severe design conditions.

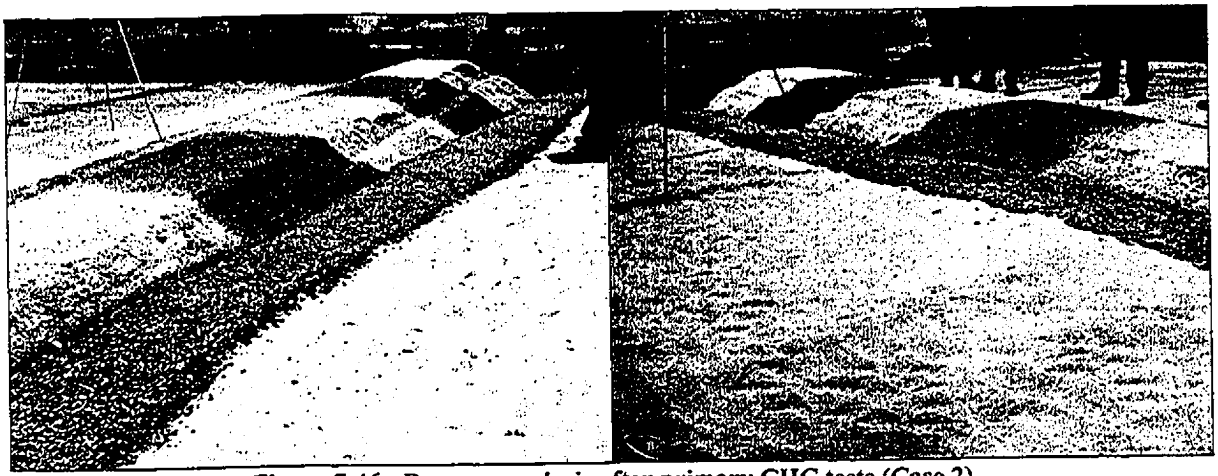

Figure 7.46 - Damage analysis after primary CHC tests (Case 2)
View of North (left) and South (right) sides. Waves travel from left-to-right in both images.

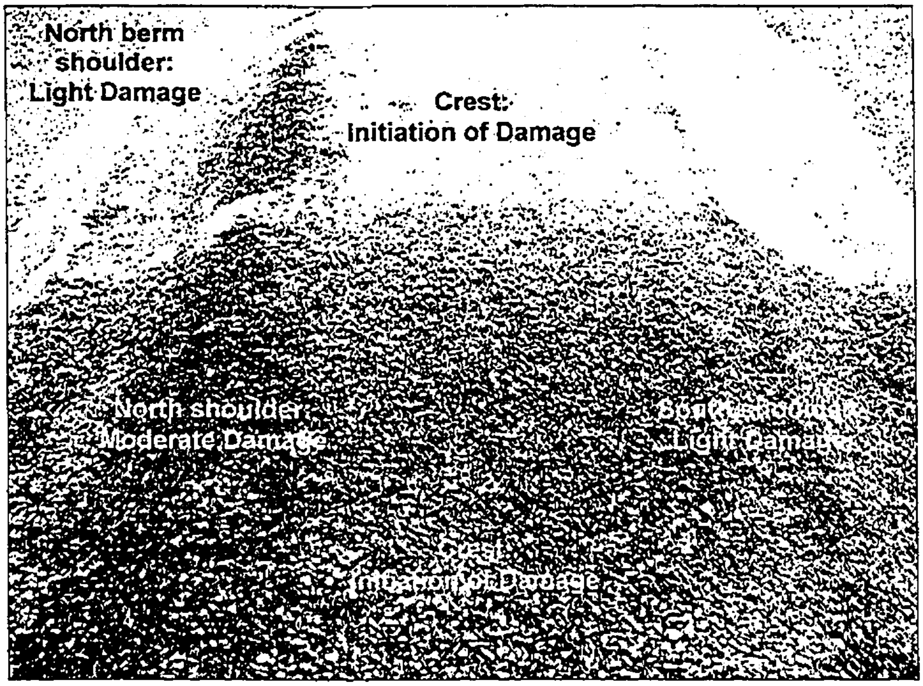

Figure 7.47 - Tunnel protection after primary CHC tests (Case 2)
Observed Damage at West end of Structure (Sta. 5+100 to 5+200). Waves travel from right-to-left.

Following the primary CHC tests (namely corresponding with Cases 0-2), a number of additional or secondary tests were performed (namely corresponding with Cases 3-4). These extra tests would be considered as extreme over-design scenarios, and the end objective was simply to increase the wave magnitude until a total failure was observed. Figure 7.48 demonstrates the final condition of the submerged structure following Case 4. The extreme velocities induced by the larger waves caused the total failure of the structure at the West side of the model, where all the armour was stripped away, revealing the tunnel beneath. Damage to the down-wave shoulder was significant, extending farther along to the East side despite the increasing freeboard.

Figure 7.48 - Damage analysis after secondary CHC tests (Case 4)
View from East (bottom) to West (top). Waves travel from left-to-right.

Losada *et al.* (1996a) revealed that the maximum pressure values measured were located at the front slope while velocities and accelerations take their maximum value at the beginning of the breakwater crest. The slope of the submerged structure used in the paper was considerably less than that of this research. The general findings of this research would suggest that velocities are quite high over the down-wave shoulder since this is the location where most damage occurred.

7.3.2 WaveSim Numerical Model

The WaveSim numerical model provides a powerful tool for simulating the propagation and transformation of waves. In general, it is capable of providing comparable results to physical modelling approaches, and also allows for more in-depth investigation. Certain limitations are still inherent in this and all numerical models. A discussion follows on this topic.

The mild-slope equations, as their name implies, are quite restricted in terms of the bathymetry over which they can effectively compute the wave transformation. Boussinesq equations, used in the WaveSim model, are able to handle steeper slopes, however they too have limitations. Nwogu (1996) set a limit for slopes of 0.5 (vertical over horizontal) before a warning would be issued, however it is unknown if any specific testing was done to determine the strict limit of the model with regards to the slope. This research involved using a slope beyond the warning limit (approximately 0.667). From the simulations that were run, it is clear that the model is capable of handling steeper slopes such as those used, however the possibility that instabilities could appear in the simulation is greatly increased. Most instabilities were found to occur at the side where the structure is deepest, where it would not intuitively be expected. Although the side-slopes of the submerged structure are essentially the same along the entire length, a logical reason for the observance of the instabilities at the deep side could be that the overall structure is also narrower at the deep side (from toe to toe). Therefore the overall length of the slope is occurring over fewer grid points in the deeper end than the shallow end, and it might be too few for the model to capture the transformation processes properly, however for the shallow end, it is occurring over a slightly longer distance which the model can handle. In theory, using a denser grid would allow the model an increased number of nodes along the slope with which to ease in the calculated gradients between each grid step. In practice, this measure was not reliably able to reduce the observed instabilities. As seen in Section 5.5.3, the elimination of the "trenches" seemed to increase the model stability substantially.

The issues encountered in Section 5.5.4 regarding the observance of a strange build-up near the wave generator was perhaps occurring to a similar degree in the physical model, however due to fact that the physical basin was much larger as compared to the computational domain, the problem did not develop.

One of the most notable deficiencies in the WaveSim numerical model is the lack of support for the introduction of currents into the computational domain. The physical modelling tests performed as part of this research contained several other tests pertaining to the combined action of waves and currents on the submerged structure. Ideally, the numerical model would have allowed the introduction of currents as well as waves in the domain, and thus a more comprehensive comparison could have been performed between the physical and numerical modelling. Chawla and Kirby (2000) made improvements on a previous numerical model by introducing an alternate formulation for wave generation in weakly dispersive wave models using two spatially distributed source functions. This formulation allowed for the existence of an underlying current field, allowing the model to be utilized in studies involving interaction of waves with a strong current. This formulation also generated waves travelling in only one direction, the advantage that it greatly reduced the required damping layer behind the source region.

The choice to limit the computational domain of the numerical model to include only the central test channel versus modelling the entire wave basin was complex. On one hand, setting up the numerical model to match exactly the conditions of the physical model would allow for a more reliable comparison between the two modelling methods, however doing so would have been extremely challenging and some parts would simply not be possible due to limitations with WaveSim. As previously mentioned, it would have been ideal to involve currents in the numerical model. However, installing the waveguides in the numerical domain would have been quite tricky. The waveguides used in the physical model were steel plates that were effectively not visible to the waves approaching perpendicular. However, they were required in order to help direct the flow down the central channel. In the numerical model, having vertical walls within the computational domain is not possible. In order to work properly, the plates would have to occupy several grid spaces wide at the base so that they could extend high enough to rise above the water surface in the shape of a pyramid. Having this much more obtrusive object would certainly cause significant flow disturbances for waves approaching the central test channel. Modelling the extra wave absorber installed down-wave of the submerged structure would also involve some difficulty, mainly in determining the proper damping adjustment to replicate the effects of the wave absorber in the physical model. As mentioned in Section 7.1.1, trials using the full basin proved challenging, and instabilities were seen to develop far sooner than for the other test cases. By maintaining a simpler computational domain in only modelling the central test channel, far more reliable results were obtained.

It was unfortunate that longer simulation times could be not used in some of the larger wave tests, as instabilities were seen to arise in these cases. Statistically, for a longer wave train, a larger H_{max} will be observed. Therefore, in the cases with large waves, it is assumed that over the duration of the simulation, a significantly large wave formed; that eventually caused instabilities in the simulation, as it propagated over the submerged structure. Hence, for a shorter simulation, there is less likelihood for such a particularly large wave to form. This is the reason why a shorter simulation did not crash due to instabilities, yet provided reliable data over the duration of the simulation. For a proper statistical comparison, it is normally desired to have at least 300 samples (i.e. waves) in the data. In the case of the first two tests, this amount was achieved, however the final three cases had fewer, approximately 140 in each situation. However, looking at the data afterwards suggests that this amount was sufficient to perform a valid comparison as the spectral data do not look jagged or bumpy, but instead appear to measure up well with the physical experiment data.

The WaveSim Manual (McDonald, 2001) suggests that Courant number should be kept between 0.5 and 0.7, however in order to maintain a stable performance from the model, a notably smaller time step was used (0.1 sec), corresponding with a Courant number of approximately 0.35. The important factor is that the Courant number does remain below 1, meaning that the model is able to calculate the occurrences at each grid node before the phenomena have a chance to pass it by.

Some additional simulations were also setup to test if a slightly different slope would affect the simulations. For these trials, the small berms on each side of the submerged structure were removed, thereby decreasing the relative slopes by several degrees. These trials appeared to behave identically to the normal cases, which also eventually had instabilities that would arise after an extended period of simulation time. Given that the changed slopes did not increase the stability of the model, they were not used since the bathymetry that did include the berms would provide a more realistic simulation to compare with the physical model data.

The greatest deficiency of the numerical model is the numerical scheme. Being an explicit, finite difference scheme, it is unconditionally unstable, and it is essentially too simple for the complex bathymetries forced upon it in this research. The model manages to do a notable job of simulating the prescribed conditions, however perhaps if a more robust numerical scheme was employed, the long-term instabilities that kept appearing would become increasingly stable. Simply because the numerical modelling simulations eventually crashed does not invalidate the results obtained while the model was performing in a stable manner. This numerical model is quite powerful, but it, like any computer model, has its limitations.

7.3.3 Further Discussion

A number of the research papers found in the Literature Review (Section 2) have been generally compared to the results of this work, and discussed as follows. Other general discussion on the results is also included.

Seabrook & Hall (1998), based on the work of d'Angremond *et al.* (1996), provided Equation (2-1) for the calculation of wave transmission. For all of Cases 1-4, the 3rd and 4th terms of the equation are outside the bounds dictated, and hence the calculated values of transmission based on this equation cannot be considered as reliable. Calabrese *et al.* (2002), also based on the work of d'Angremond, provided Equation (2-2) as a different calculation for wave transmission. The bounds of the first condition (R_c/B) and second condition (B/H_i) are met by Cases 1-4, however they are not met for the third or fourth conditions (H_i/h and ξ), again explaining the erroneous results when using the data from the current research. The definition of transmission by d'Angremond is more analogous to overtopping. Most of the research was aimed at low-crested structures with crest elevations at or slightly above the mean sea level, specifically in relatively shallow water conditions. Wave overtopping for these types of structures would occur very frequently, as compared to some larger breakwaters that are designed with higher crests to limit the amount of overtopping. The works of Seabrook & Hall (1998) and Calabrese *et al.* (2002) slightly extended to different types of structures, however they would still be more considered as low-crested structures rather than actual deeply submerged structures. The resulting formulae therefore are more intended for emergent low-crested breakwaters in shallow water, not submerged breakwaters.

Nwogu and Demirbilek (2001) presented the numerical model BOUSS-2-D. Upon examining further, it would appear that BOUSS-2-D is essentially identical to the WaveSim model used in this research. Nwogu took the code developed in his previous works (1993 and 1996) and repackaged the model, presumably with some minor changes or upgrades. Although WaveSim might appear to be an older model, with its basis on work from 1996, it should be noted that indeed the same model is still in use beyond 2001 for works of the US Army Corps of Engineers, a notable player in the field of Coastal Engineering. Although newer software may be available to perform this type of research, the fact that other noted laboratories are still employing this very model is a testament to the abilities of the model.

Twu *et al.* (2001), in contrast, conducted research specifically on deeply submerged breakwaters, developing Equation (2-3) for calculating wave reflection and transmission. Table 7.5 presents the comparison of the calculated reflection coefficients by three different methods. In general, the equation of Twu *et al.* (2001) corresponds very well with the calculated reflection based on the data analysis methods. Discrepancies are however observed for Cases 2-4 at CS1. For these cases, the observed peak period of the reflected waves was significantly shorter than the prescribed period for the test (see Table 7.6). The Twu *et al.* (2001) formula uses the wavelength which corresponds to the peak period, thus giving a calculated coefficient that differed quite a bit from the other two analysis methods. Aside from these observed differences though, the Twu *et al.* (2001) equation provides an exceptionally good estimate of reflection.

Table 7.5 - Comparison of reflection coefficients

Case #	Cross-Section	Water Level (m)	Coefficient of Reflection, C_r (%)		
			Time Domain (REFLS)	Frequency Domain (REFLA)	Twu *et al.* (2001)
0	CS1	−1.55	2.29	3.22	2.61
	CS2	−1.55	2.29	3.22	2.61
	CS3	−1.55	2.29	3.22	2.61
1	CS1	−1.55	12.0	12.0	11.7
	CS2	−1.55	23.8	24.0	24.5
	CS3	−1.55	35.9	35.3	36.0
2	CS1	−1.72	14.1	16.0	6.14
	CS2	−1.72	26.2	26.5	26.4
	CS3	−1.72	35.9	36.8	35.0
3	CS1	−5.00	14.7	17.5	3.99
	CS2	−5.00	26.2	26.7	26.7
	CS3	−5.00	36.8	35.9	35.6
4	CS1	−5.00	15.2	19.1	3.66
	CS2	−5.00	26.5	28.3	28.3
	CS3	−5.00	35.2	35.8	34.3

Figure 7.49 depicts the information found in Table 7.5 in a graphical fashion. Again, it is observed that a significant difference is apparent for the envelope of the first cross-section, however the data envelopes for the second and third cross-sections are quite narrow.

Table 7.6 - Simulated wave results for reflection and transmission

Case #	Cross-Section	Water Level (m)	Simulated Up-wave			Simulated Reflection		Simulated Incident			Simulated Down-wave		
			H_{m0} (m)	T_p (s)	Power (kW/m)	H_{m0} (m)	T_p (s)	H_{m0} (m)	T_p (s)	Power (kW/m)	H_{m0} (m)	T_p (s)	Power (kW/m)
0	CS1	-1.55	4.41	16.13	151.0	0.10	17.56	4.30	16.11	147.2	4.39	16.12	149.8
	CS2	-1.55	4.41	16.13	151.0	0.10	17.56	4.30	16.11	147.2	4.39	16.12	149.8
	CS3	-1.55	4.41	16.13	151.0	0.10	17.56	4.30	16.11	147.2	4.39	16.12	149.8
1	CS1	-1.55	4.61	16.08	166.7	0.51	15.96	4.28	16.14	145.5	4.16	16.10	134.9
	CS2	-1.55	4.94	16.10	192.1	1.03	16.41	4.31	16.12	147.8	3.96	16.18	120.8
	CS3	-1.55	5.35	16.07	226.4	1.57	16.15	4.36	16.14	150.8	4.63	16.15	160.0
2	CS1	-1.72	6.59	20.34	360.9	0.91	12.30	6.42	20.22	349.9	6.13	20.23	319.3
	CS2	-1.72	6.56	20.20	352.5	1.69	20.49	6.45	20.34	353.2	5.84	20.08	283.2
	CS3	-1.72	6.50	18.92	343.1	2.32	19.85	6.48	20.19	356.9	6.71	20.23	361.6
3	CS1	-5.00	6.22	20.05	309.9	0.89	10.33	6.05	20.04	299.9	5.73	20.21	268.2
	CS2	-5.00	6.35	19.73	320.0	1.59	20.73	6.07	19.91	302.0	5.38	19.80	230.1
	CS3	-5.00	6.53	19.32	339.9	2.25	19.95	6.12	19.90	308.3	6.10	20.10	291.1
4	CS1	-5.00	7.08	19.85	397.9	1.02	9.94	6.72	20.13	369.2	6.39	20.26	327.9
	CS2	-5.00	7.24	19.55	411.8	1.79	21.68	6.75	20.15	372.8	6.19	19.76	299.1
	CS3	-5.00	7.31	19.24	423.1	2.39	20.01	6.79	19.85	377.9	6.72	20.23	341.1

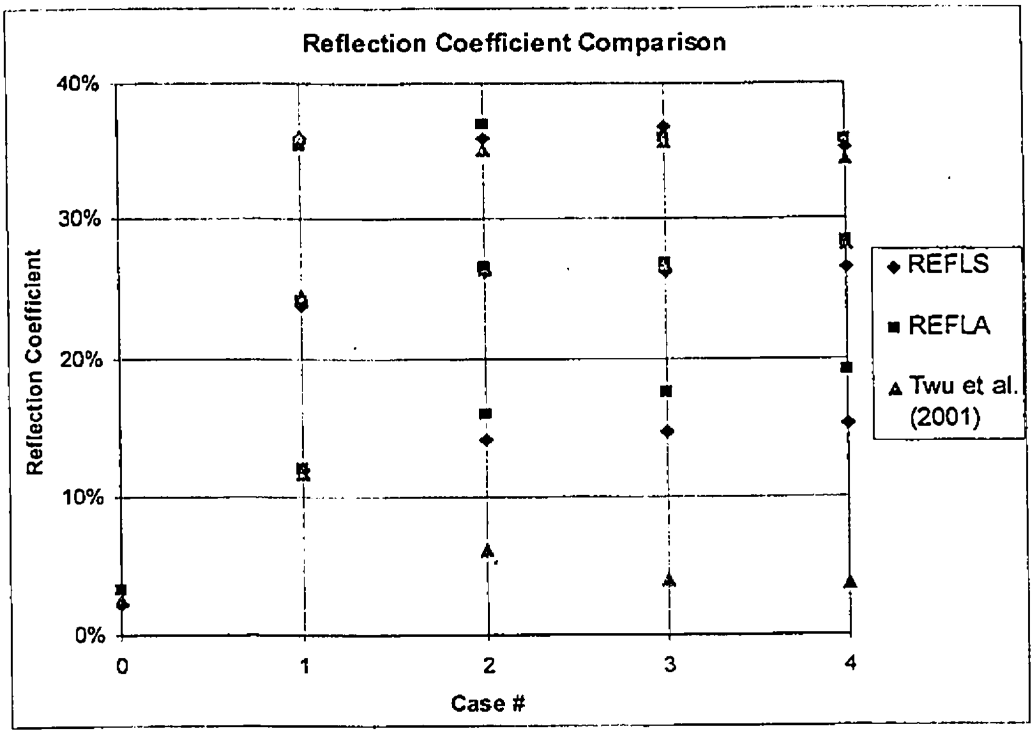

Figure 7.49 - Comparison of reflection coefficients

Wave transmission for the case of submerged breakwaters is a complicated topic. The greater the submergence of the breakwater, the lesser effect it will incur on the surrounding wave climate. It would be expected that wave transmission should be smaller at the location of smaller freeboard, and larger at the location of greater freeboard. Table 7.7 shows the comparison of transmission coefficients calculated by three different methods (data from Table 7.6). Although the Twu formula again delivers very comparable results, it is difficult to understand what this data is showing. A significant amount of energy is seen to reflect from the submerged structure, therefore it would be expected that the waves on the lee side of the structure should be somewhat smaller than the incident waves. However, the results seem to show that in fact very little damping of the wave heights seems to be occurring, and in several instances, the transmitted wave height is larger than the incident. In a study of nonlinear waves passing over a submerged shelf, Ohyama and Nadaoka (1994) observed that on the trailing side of the shelf, the energy in bound harmonics is abruptly transferred into free higher harmonics, resulting in a drastic change of wave form and a greater height of transmitted waves than that predicted by linear wave theory.

It is possible therefore that the observations of the transmitted waves do in fact make sense, although further understanding of the matter is warranted.

Table 7.7 - Comparison of transmission coefficients

Case #	Cross-Section	Water Level (m)	Coefficient of Transmission, C_t (%)		
			H_{m0} transmitted / incident	Wave Power transmitted / incident	Twu *et al.* (2001)
0	CS1	−1.55	102	98	102
	CS2	−1.55	102	98	102
	CS3	−1.55	102	98	102
1	CS1	−1.55	97	108	97
	CS2	−1.55	92	122	92
	CS3	−1.55	106	94	106
2	CS1	−1.72	95	110	95
	CS2	−1.72	91	125	89
	CS3	−1.72	104	99	104
3	CS1	−5.00	95	112	96
	CS2	−5.00	89	131	88
	CS3	−5.00	100	106	101
4	CS1	−5.00	95	113	96
	CS2	−5.00	92	125	89
	CS3	−5.00	99	111	101

Weston *et al.* (2004) modelled wavegroups passing over a shoal and observed the release of free waves as the wavegroup returned to deeper water. This phenomenon was superbly observed in the WaveSim numerical model as well. As particularly large event waves passed over the submerged structure, the change in water depth induced the waves to steepen, and thus form larger high frequency harmonics. A portion of these harmonics was then released as a free wave as the wave rapidly returned to deeper water after the structure's crest. Upon observation of the numerical model results, it is apparent that this phenomenon is also occurring in the simulations. Figure 7.50 shows 6 subsequent images (progression is left-to-right) in which the bathymetry scale is exaggerated twice and the waves are exaggerated 5 times in the vertical (z) direction. Each subsequent image is 4 frames later than the previous. In the first image, a fairly large wave is about to pass over the submerged structure. A steepening of the wave can be observed in the following images. As the wave "spills" over the structure in the 3rd and 4th images, the mentioned harmonics are released. This secondary wave, released from the primary wave, is clearly visible in the 5th and 6th images as it travels behind the primary wave. In these images, it is also possible to notice that the wave crest down-wave of the structure is no longer perpendicular to the structure's crest, as the wave celerity is affected more on the side with lesser freeboard.

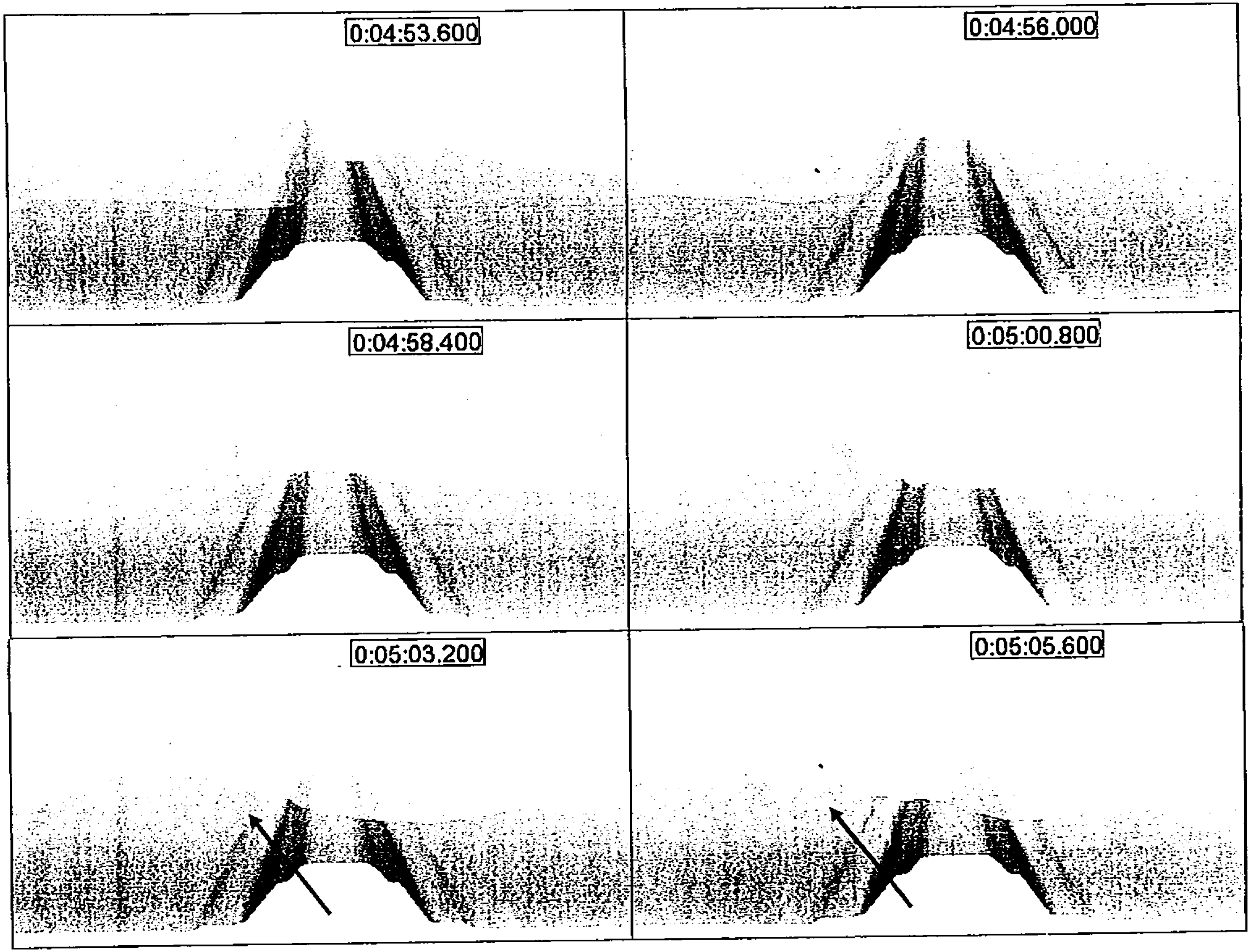

Figure 7.50 - Observation of free wave release

Wang *et al.* (2005) concluded that the reflected peak period is quite close to the incident peak period. The results of this present research highly agrees with this finding (refer to Table 7.6 and Figure 7.41 through Figure 7.45). In general, it was observed that the computed reflection spectra had peak periods that matched very closely with the calculated incident spectra.

Burcharth *et al.* (2006) observed that the freeboard has a large influence in regards to the initiation of damage for low-crested structures. As discussed briefly, the observed damage to the physical model structure highly agreed with these results. Although the submerged structure in this research did an adequate job of protecting the tunnel, there was noticeable damage to the outer armour layers. A significant increase of damage was observed as the freeboard decreases.

In a comparison of the data in

Table 4.3 and Table 4.8, it is noticed that the force of wave action alone can cause significant instantaneous velocities. In the case of the calibration (

Table 4.3), the currents attained were measured at approximately 1.2 m/s, whereas the peak measured velocities (Table 4.8) were in the vicinity of 1.0 m/s for the 6 m wave test named CAL_T20_H6P0, corresponding with Test Cases 2 and 3.

8 Conclusions

Submerged structures are becoming more frequently considered for use in coastal engineering applications. In the past, a great deal of research has been undertaken on low-crested structures, and far less work dealt with deeply submerged structures. Also, the majority of existing research focused on lightly sloped, uniform cross-sectioned structures with specific crest elevations.

The objective of this research was to improve the understanding of wave and wave-induced velocity transformations in the presence of a steeply sloped submerged structure with a non-uniform cross-section. Moreover, the depth of submergence was not uniform. This task was undertaken through two means.

A large-scale three-dimensional physical modelling study was performed, followed by a numerical modelling study using the WaveSim wave modelling software. Both the physical and numerical models were able to reproduce the target wave parameters with a high degree of accuracy. In general, the effect of the submerged structure on the wave and wave-induced velocities could be more easily identified from the numerical data. This was due to the fact that the numerical simulations were conducted over a smaller domain which eliminated several sources of error affecting the physical data. This statement does not endorse the use of numerical models to the detriment of physical models. It merely states that the complexities of the physical model phenomena are not always included in the formulation of the numerical model.

It was observed that the submerged structure considered in this research imparted significant transformations to the wave climate and generated substantial wave-induced velocities at the crest. The wave heights increased over the structure, and the increase was greatest where the submergence depth was least. The wave-induced velocities were also increased by the presence of the structure, and the increase was again greatest where the structure was highest. These increases in wave height and wave-induced velocity were also greater when the incident waves were more energetic. The transfer function analysis showed distinct patterns in energy transfer between the up-wave and down-wave gauges, specifically a significant reduction in energy around the spectral peak frequency (f_p) and a significant increase in energy around twice the spectral peak frequency ($2f_p$). This is consistent with a transfer of energy to higher harmonics and the generation of high-frequency free waves. The distribution of the significant wave height was found to occur in a distinct pattern, with peaks occurring at approximately every half wavelength.

Reflection analysis from the submerged structure displays a clear trend in the amount of reflected energy in relation to the submergence depth. A reasonable estimate of the expected reflection could be calculated for different submergence depths along the submerged structure.

The sloping submerged structure also induced a circular time-averaged current, flowing up-wave over the higher part of the structure, and flowing down-wave over the lower part.

The analysis and results of this research have shown that although the WaveSim model may have its limitations, it provides an excellent means for studying wave transformation over 3-D submerged structures.

9 Recommendations for Future Work

Based on the analysis conducted in the present study, the conclusions drawn, and the shortcomings of the work, several recommendations for future work are given.

As discussed previously, the possibility definitely exists within WaveSim to extend its abilities to incorporate currents. This would likely involve a substantial amount of work; however, it could dramatically improve the capability of the model. Using an improved version of WaveSim or the use of another numerical model capable of dealing with the complex interaction between waves and currents would be recommended. In this scenario, a more rigorous comparison could be performed between the experimental data collected in this research and the results of a numerical model.

To better understand the effects of a submerged structure on the nearby wave and current climates, the use of different cross-sections would be recommended. Much of the former research involving breakwater shapes has involved various 2-D cross-sections, however little work has been performed with 3-D submerged structures, such as in this research. To increase the complexity further, alternate shapes and slopes could be applied to the submerged structure used in this study to further comprehend the complex flow-structure interactions.

One of the main objectives for the original physical modelling work was to perform an analysis of the damage to the structure after being subjected to various storms conditions in the presence of both waves and currents. The author noticed that there is a lack of methods and a standard assessment tool destined to assess the potential damage to an armoured structure based on specified storm conditions. The development of such methods would be highly complex, and will require the gathering of an extensive field and physical modelling data needed to develop such a tool; hence, there are many steps along the way which will need to be examined in order to attain this objective.

10 Bibliography

As mentioned in Section 3.1, the physical experiments and subsequent reports connected with a Canadian Hydraulics Centre project are confidential. Several of the following references have details omitted in order to maintain the appropriate discretion.

Avgeris, I., Karambas, T.V., & Prinos, P. (2004). "Boussinesq Modeling of Wave Interaction with Porous Submerged Breakwaters." *Proceedings, Twenty-Ninth International Conference on Coastal Engineering*, ASCE, Lisbon, Portugal, 604-616.

Bosboom, J., Klopman, G., Roelvink, J.A., & Battjes, J.A. (1997). "Boussinesq Modelling of Wave-Induced Horizontal Particle Velocities." *Coastal Engineering*, 32, 163-180.

Bredmose, H., Schäffer, H.A., & Madsen, P.A. (2004). "Boussinesq Evolution Equations: Numerical Efficiency, Breaking and Amplitude Dispersion." *Coastal Engineering*, 51, 1117-1142.

Briganti, R., Van der Meer, J., Buccino, M., & Calabrese, M. (2003). "Wave Transmission Behind Low-Crested Structures." *Proceedings, Conference on Coastal Structures*, ASCE, Portland, Oregon, 580-592.

Bruehl, M. & Oumeraci, H. (2005). "Comparative Analysis of Wave Transmission over an Artificial Reef using FFT, Wavelet and Hilbert-Huang-Transform." *Proceedings, Fifth International Symposium on Ocean Waves Measurements and Analysis*, Madrid, Spain, Paper 23, 10 pp.

Brunone, B., & Tomasicchio, G.R. (1997). "Wave Kinematics at Steep Slopes: Second-Order Model." *Journal of Waterway, Port, Coastal, and Ocean Engineering*, 123(5), 223-232.

Buccino, M., & Calabrese, M. (2007). "Conceptual Approach for Prediction of Wave Transmission at Low-Crested Breakwaters." *Journal of Waterway, Port, Coastal, and Ocean Engineering*, 133(3), 213-224.

Burcharth, H.F., Kramer, M., Lamberti, A., & Zanuttigh, B. (2006). "Structural Stability of Detached Low Crested Breakwaters." *Coastal Engineering*, 53, 381-394.

Cáceras, I., Sáchez-Arcilla, A., Alsina, J-M., González-Marco, D., & Sierra, J.P. (2005). "Coastal Dynamics around a Submerged Barrier." *Proceedings, Fifth International Conference on Coastal Dynamics*, ASCE, Barcelona, Spain, 14 pp.

Calabrese, M., Vicinanza, D., & Buccino, M. (2002). "Large-Scale Experiments on the Behaviour of Low-Crested and Submerged Breakwaters in Presence of Broken Waves." *Proceedings, Twenty-Eighth International Conference on Coastal Engineering*, ASCE, Cardiff, Wales, 1900-1912.

Chapra, S.C., & Canale, R.P. (2002). *Numerical Methods for Engineers*, 4th edition, McGraw-Hill, New York, USA, 926 pp.

Chawla, A., & Kirby, J.T. (2000). "A Source Function Method for Generation of Waves on Currents in Boussinesq Models." *Applied Ocean Research*, 22, 75-83.

CHC (Canadian Hydraulics Centre). (2007). *National Research Council of Canada, Canadian Hydraulics Centre*. http://chc.nrc-cnrc.gc.ca/main_e.html [Accessed July 2007].

Chen, Q., Kirby, J.T., Dalrymple, R.A., Kennedy, A.B., & Chawla, A. (2000). "Boussinesq Modeling of Wave Transformation, Breaking, and Runup. II: 2-D." *Journal of Waterway, Port, Coastal, and Ocean Engineering*, 126(1), 48-56.

Christensen, E.D., Zanuttigh, B., & Zyserman, J.A. (2003). "Validation of Numerical Models Against Laboratory Measurements of Waves and Currents Around Low-Crested Structures." *Proceedings, Conference on Coastal Structures*, ASCE, Portland, Oregon, 876-888.

Cox, R.J., & Tajziehchi, M. (2005). "2-D Experimental Modelling of Hydrodynamic Effects of Submerged Breakwaters". *Proceedings, Fifth International Conference on Coastal Dynamics*, ASCE, Barcelona, Spain, 12 pp.

Crowe, C.T., Elger, D.F., & Roberson, J.A. (2001). *Engineering Fluid Mechanics*, 7th edition, John Wiley & Sons, Inc., New York, USA, 714 pp.

d'Angremond, K., Van der Meer, J.W., & de Jong, R.J. (1996). "Wave Transmission at Low-Crested Structures." *Proceedings, Twenty-Fifth International Conference on Coastal Engineering*, ASCE, Orlando, Florida, 2418-2427.

Davies, M.H., Mansard, E.P.D., & Cornett, A.M. (1995). "Damage Analysis for Rubble-Mound Breakwaters." *National Research Council of Canada, Institute Report IR-1995-09*, Ottawa, Canada, 15 pp.

Dean, R.G. (1985). "Physical Modeling of Littoral Processes." *Physical Modelling in Coastal Engineering*. Rotterdam, The Netherlands, 119-139.

Dean, R.G., & Dalrymple, R.A. (1984). *Water Wave Mechanics for Engineers and Scientists*, Prentice-Hall, Inc., New Jersey, USA, 353 pp.

Dean, R.G., Chen, R., & Browder, A.E. (1997). "Full Scale Monitoring Study of a Submerged Breakwater, Palm Beach, Florida, USA." *Coastal Engineering*, 29, 291-315.

Engelund, F. (1953). "On the Laminar and Turbulent Flows of Groundwater Through Homogeneous Sand." *Bulletin No. 4, Technical University of Denmark*, Copenhagen, Denmark.

Farr, D. (2005). "EnSim Core Reference Manual." *National Research Council of Canada*, Ottawa, Canada, 125pp.

Figueres, M., & Medina, J.R. (2004). "Estimating Incident and Reflected Waves Using a Fully Nonlinear Wave Model." *Proceedings, Twenty-Ninth International Conference on Coastal Engineering*, ASCE, Lisbon, Portugal, 594-603.

Funke, E.R., & Mansard, E.P.D. (1984). "The NRCC Random Wave Generation Package." *National Research Council of Canada, Technical Report TR-HY-002*, Ottawa, Canada.

Garcia, N., Lara, J.L., Lomonaco, P., & Losada, I.J. (2004). "Flow at Low-Crested Structures under Breaking Conditions." *Proceedings, Twenty-Ninth International Conference on Coastal Engineering*, ASCE, Lisbon, Portugal, 4240-4252.

Goda, Y. (1985). *Random Seas and Design of Maritime Structures*, University of Tokyo Press, Tokyo, Japan, 323 pp.

Harris, L.E. (2003). "Submerged Reef Structures for Beach Erosion Control." *Proceedings, Conference on Coastal Structures*, ASCE, Portland, Oregon, 1155-1163.

Hauge, L., Kim, C.-H., Kim, Y.-M., & Galmarini, A. (2004). "Design of the *BG Fixed Link Bridges Considering Extreme Loads." 12 pp. [* *details omitted*]

Horikawa, K., ed. (1988). *Nearshore Dynamics and Coastal Processes*, University of Tokyo Press, Tokyo, Japan, 522 pp.

Huang, C.-J., & Dong, C.M. (1999). "Wave Deformation and Vortex Generation in Water Waves Propagating over a Submerged Dike." *Coastal Engineering*, 37, 123-148.

Hughes, S.A. (1993). *Physical Models and Laboratory Techniques in Coastal Engineering*. World Scientific, New Jersey, USA, 568 pp.

Hur, D.-S., & Mizutani, N. (2003). "Numerical Estimation of the Wave Forces acting on a Three-Dimensional Body on Submerged Breakwater." *Coastal Engineering*, 47, 329-345.

I.A.H.R./P.I.A.N.C. (1986). "List of Sea State Parameters, Supplement to Bulletin 52." *Permanent International Association of Navigation Congresses*, Brussels, Belgium, 24 pp.

Jensen, O.J., & Klinting, P. (1983). "Evaluation of Scale Effects in Hydraulic Models By Analysis of Laminar and Turbulent Flows." *Coastal Engineering*, 7, 319-329.

Johnson, H.K., Karambas, T.V., Avgeris, I., Zanuttigh, B., Gonzalez-Marco, D., & Caceres, I. (2005). "Modelling of Waves and Currents Around Submerged Breakwaters." *Coastal Engineering*, 52, 949-969.

Johnson, H.K. (2006). "Wave Modelling in the Vicinity of Submerged Breakwaters." *Coastal Engineering*, 53, 39-48.

Kaihatu, J.M. & Kirby, J.T. (1998). "Two-Dimensional Parabolic Modeling of Extended Boussinesq Equations." *Journal of Waterway, Port, Coastal, and Ocean Engineering*, 124(2), 57-67.

Kamphuis, J.W. (2000). *Introduction to Coastal Engineering and Management*, World Scientific, New Jersey, USA, 437 pp.

Karambas, T.V., & Koutitas, C. (1992). "A Breaking Wave Propagation Model based on the Boussinesq Equations." *Coastal Engineering*, 18, 1-19.

Kennedy, A.B., Chen, Q., Kirby, J.T., & Dalrymple, R.A. (2000). "Boussinesq Modeling of Wave Transformation, Breaking, and Runup. I: 1D." *Journal of Waterway, Port, Coastal, and Ocean Engineering*, 126(1), 39-47.

Klopman, G., & Van der Meer, J.W. (1999). "Random Wave Measurements in Front of Reflective Structures." *Journal of Waterway, Port, Coastal, and Ocean Engineering*, 125(1), 39-45.

Kobayashi, N., Meigs, L.E., Ota, T., & Melby, J.A. (2007). "Irregular Breaking Wave Transmission over Submerged Porous Breakwater." *Journal of Waterway, Port, Coastal, and Ocean Engineering*, 133(2), 104-116.

Kramer, M., Zanuttigh, B., Van der Meer, J.W., Vidal, C., & Gironella, F.X. (2005). "Laboratory Experiments on Low-Crested Breakwaters." *Coastal Engineering*, 52, 867-885.

Lamberti, A., Zanuttigh, B., & Kramer, M. (2003). "Wave and Current Flows around Low-Crested Structures." *Proceedings, Conference on Coastal Structures*, ASCE, Portland, Oregon, 850-862.

Lee, C., Cho, Y.-S., & Yum, K. (2001). "Internal Generation of Waves for Extended Boussinesq Equations." *Coastal Engineering*, 42, 155-162.

Lomonaco, P., & Cornett, A. (2006a). "Stability of Rock Protection for the BG* Fixed Link Immersed Tunnel." *National Research Council of Canada*, Ottawa, Canada, 1 pp. [*details omitted*]

Lomonaco, P., & Cornett, A. (2006b). "Physical Model Study on the Stability of the Rock Protection for the BG* Fixed Link Immersed Tunnel." *National Research Council of Canada, Technical Report CHC-CTR-049*, Ottawa, Canada, 100 pp. [*details omitted*]

Lomonaco, P., Vidal, C., Losada, I.J., & Mendez, F.J. (2003). "Wave Height, Pressure and Velocity CDF's around Rubble Mound Protections for Submarine Outfalls." *Proceedings, Conference on Coastal Structures*, ASCE, Portland, Oregon, 889-901.

Longuet-Higgins, M.S., & Stewart, R.W. (1962). "Radiation Stress and Mass Transport in Surface Gravity Waves with Applications to Surf Beats." *Journal of Fluid Mechanics*, 13(4), 481-504.

Losada, I.J., Silva, R., & Losada, M.A. (1996a). "3-D Non-Breaking Regular Wave Interaction with Submerged Breakwaters." *Coastal Engineering*, 28, 229-248.

Losada, I.J., Silva, R., & Losada, M.A. (1996b). "Interaction of Non-Breaking Directional Random Waves with Submerged Breakwaters." *Coastal Engineering*, 28, 249-266.

Losada, I.J., Patterson, M.D., & Losada, M.A. (1997). "Harmonic Generation past a Submerged Porous Step." *Coastal Engineering*, 31, 281-304.

Losada, I.J., Lara, J.L., & Garcia, N. (2003). "2-D Experimental and Numerical Analysis of Wave Interaction with Low-Crested Breakwaters including Breaking and Flow Recirculation." *Proceedings, Conference on Coastal Structures*, ASCE, Portland, Oregon, 863-875.

Losada, I.J., Lara, J.L., Christensen, E.D., & Garcia, N. (2005). "Modelling of Velocity and Turbulence Fields Around and Within Low-Crested Rubble-Mound Breakwaters." *Coastal Engineering*, 52, 887-913.

Lynett, P.J. (2006). "Nearshore Wave Modeling with High-Order Boussinesq-Type Equations." *Journal of Waterway, Port, Coastal, and Ocean Engineering*, 132(5), 348-357.

Madsen, P.A., Murray, R. & Sørensen, O.R. (1991). "A New Form of the Boussinesq Equations with Improved Linear Dispersion Characteristics." *Coastal Engineering*, 15, 371-388.

Madsen, P.A., Fuhrman, D.R., & Wang, B. (2006). "A Boussinesq-type Method for Fully Nonlinear Waves Interacting with a Rapidly Varying Bathymetry." *Coastal Engineering*, 53, 487-504.

Mansard, E.P.D. (1995). "On the Estimation of the Incident Wave Train from Reflection Analysis." *National Research Council of Canada, Institute Report IR-1995-07*, St. John's, Canada, 8 pp.

Mansard, E.P.D., & Funke, E.R. (1980). "The Measurement of Incident and Reflected Spectra using a Least Squares Method." *Proceedings, Seventeenth Coastal Engineering Conference*, ASCE, Sydney, Australia, 154-172.

Mansard, E.P.D., & Funke, E.R. (1987). "On the Reflection Analysis of Irregular Waves." *National Research Council of Canada, Technical Report TR-HY-017*, Ottawa, Canada, 46 pp.

McDonald, B. (2001). "WaveSim Reference Manual." *National Research Council of Canada*, Ottawa, Canada, 169 pp.

Méndez, F.J., Losada, I.J., & Losada, M.A. (2001). "Wave-Induced Mean Magnitudes in Permeable Submerged Breakwaters." *Journal of Waterway, Port, Coastal, and Ocean Engineering*, 127(1), 7-15.

Miles, M.D. (1997). "GEDAP User's Guide for Windows NT." *National Research Council of Canada, Technical Report HYD-TR-021*, Ottawa, Canada, 96 pp.

Miles, M.D. (2001). "Release Notes for GEDAP Version 7.5 for Windows NT." *National Research Council of Canada*, Ottawa, Canada, 3 pp.

Miles, M.D., & Funke, E.R. (1987). "Comparison of Methods for Synthesis of Directional Seas." *Proceedings, Sixth International Offshore Mechanics and Arctic Engineering Symposium*, ASME, Houston, Texas, 247-255.

Miles, M.D., & Pelletier, D. (2001). "User Guide for GEDAP Wave Generation Software: Update to Windows NT4 / Windows 2000 Version." *National Research Council of Canada*, Ottawa, Canada, 24 pp.

Nwogu, O. (1993). "Alternative Form of Boussinesq Equations for Nearshore Wave Propagation." *Journal of Waterway, Port, Coastal, and Ocean Engineering*, 119(6), 618-638.

Nwogu, O.G. (1996). "Numerical Prediction of Breaking Waves and Currents with a Boussinesq Model." *Proceedings, Twenty-Fifth International Conference on Coastal Engineering*, ASCE, Orlando, Florida, 4807-4820.

Nwogu, O.G., & Demirbilek, Z. (2001). "BOUSS-2-D: A Boussinesq Wave Model for Coastal Regions and Harbors. Report 1: Theoretical Background and User's Manual." *US Army Corps of Engineers, Engineer Research and Development Center, Coastal and Hydraulics Laboratory TR-01-25*, Washington, DC, USA, 90 pp.

Ohyama, T., & Nadaoka, K. (1994). "Transformation of a Nonlinear Wave Train Passing over a Submerged Shelf Without Breaking." *Coastal Engineering*, 24, 1-22.

Onorato, M., Osborne, A.R., Marina, S., & Bertone, S. (2001). "Freak Waves in Random Oceanic Sea States." *Physical Review Letters*, 86(25), 5831-5834.

Pelletier, D. (1997). "GDAC Release Notes." *National Research Council of Canada*, Ottawa, Canada.

Pelletier, D. (2001). "NDAC User's Guide for Windows NT." *National Research Council of Canada, Technical Report CHC-TR-008*, Ottawa, Canada, 32 pp.

Peregrine, D.H. (1967). "Long Waves on a Beach." *Journal of Fluid Mechanics*, 27, 815-827.

Pinto, F.T., & Neves, A.C. (2005). "Wave Shoaling Analysis Near Submerged Breakwaters." *Proceedings, Fifth International Symposium on Ocean Waves Measurements and Analysis*, Madrid, Spain, Paper 136, 10 pp.

Prasuhn, A.L. (1992). *Fundamentals of Hydraulic Engineering*, Oxford University Press, New York, USA, 509 pp.

Sarpkaya, T., & Isaacson, M. (1981). *Mechanics of Wave Forces on Offshore Structures*, Van Nostrand Reinhold Company, New York, USA, 651 pp.

Seabrook, S.R., & Hall, K.R. (1998). "Wave Transmission at Submerged Rubblemound Breakwaters." *Proceedings, Twenty-Sixth International Conference on Coastal Engineering*, ASCE, Copenhagen, Denmark, 2000-2013.

Sharma, J.N., & Dean, R.G. (1981). "Second-Order Directional Seas and Associated Wave Forces." *Society of Petroleum Engineers Journal*, 21(1), 129-140.

Shi, F., Dalrymple, R.A., Kirby, J.T., Chen, Q., & Kennedy, A. (2001). "A Fully Nonlinear Boussinesq Model in Generalized Curvilinear Coordinates." *Coastal Engineering*, 42, 337-358.

Shi, F., Kirby, J.T., Dalrymple, R.A., & Chen, Q. (2003). "Wave Simulations in Ponce de Leon Inlet Using Boussinesq Model." *Journal of Waterway, Port, Coastal, and Ocean Engineering*, 129(3), 124-135.

Shibayama, T. (1991). *Coastal Processes: Concepts in Coastal Engineering and their Application to Coastal Processes*, Asian Institute of Technology, Bangkok, Thailand, 335 pp.

Sørensen, O.R., Schäffer, H.A., & Sørensen, L.S. (2004). "Boussinesq-type Modelling using an Unstructured Finite Element Technique." *Coastal Engineering*, 50, 181-198.

Sumer, B.M., Fresøe, J., Lamberti, A., Zanuttigh, B., Dixen, M., Gislason, K., & Di Penta, A.F. (2005). "Local Scour at Roundhead and along the Trunk of Low Crested Structures." *Coastal Engineering*, 52, 995-1025.

Sutherland, J. & O'Donoghue, T. (1998). "Characteristics of Wave Reflection Spectra." *Journal of Waterway, Port, Coastal, and Ocean Engineering*, 124(6), 303-311.

Twu, S.-W., Liu, C.-C., & Hsu, W.-H. (2001). "Wave Damping Characteristics of Deeply Submerged Breakwaters." *Journal of Waterway, Port, Coastal, and Ocean Engineering*, 127(2), 97-105.

U.S. Army Corps of Engineers. (2002). *Coastal Engineering Manual*. Engineer Manual 1110-2-1100, U.S. Army Corps of Engineers, Washington, USA, (in 6 volumes).

Van der Meer, J.W., & Daemen, I.F.R. (1994). "Stability and Wave Transmission at Low-Crested Rubble-Mound Structures." *Journal of Waterway, Port, Coastal, and Ocean Engineering*, 120(1), 19 pp.

Van der Meer, J.W., Wang, B., Wolters, A., Zanuttigh, B. & Kramer, M. (2003). "Oblique Wave Transmission over Low-Crested Structures." *Proceedings, Conference on Coastal Structures*, ASCE, Portland, Oregon, 567-579.

Van Gent, M.R.A. (1994). "The Modelling of Wave Action on and in Coastal Structures." *Coastal Engineering*, 22, 311-339.

Van Rijn, L.C. (1993). *Principles of Sediment Transport in Rivers, Estuaries and Coastal Seas*. Aqua Publishing, The Netherlands.

Vidal, C., Losada, M.A., & Mansard, E.P.D. (1995). "Suitable Wave-Height Parameter for Characterizing Breakwater Stability." *Journal of Waterway, Port, Coastal, and Ocean Engineering*, 121(2), 88-97.

Vidal, C., Medina, R., & Lomónaco, P. (2006). "Wave Height Parameter for Damage Description of Rubble-Mound Breakwaters." *Coastal Engineering*, 53, 711-722.

Wang, B., Van der Meer, J.W., Otta, A.K., Chadwick, A.J. & Horrillo-Caraballo, J. (2005). "Reflection of Obliquely Incident Waves at Low-Crested Structures". *Proceedings, Fifth International Conference on Coastal Dynamics*, ASCE, Barcelona, Spain, 12 pp.

Wei, G. & Kirby, J.T. (1994). "Time-Dependent Numerical Code for Extended Boussinesq Equations." *Journal of Waterway, Port, Coastal, and Ocean Engineering*, 121(5), 251-261.

Wei, G., & Kirby, J.T. (1995). "Time-Dependent Numerical Code for Extended Boussinesq Equations." *Journal of Waterway, Port, Coastal, and Ocean Engineering*, 121(5), 251-261.

Wei, G., Kirby, J.T., Grilli, S.T., & Subramanya, R. (1995). *Journal of Fluid Mechanics*, 294, 71-92.

Weston, B.P., Taylor, P.H., Borthwick, A.G.L., Hunt, A.C., & Stansby, P.K. (2004). "Boussinesq Modelling of Wavegroup Propagation over a Shallow Shoal and the Release of Second Order and Higher Harmonics." *Proceedings, Twenty-Ninth International Conference on Coastal Engineering*, ASCE, Lisbon, Portugal, 1277-1289.

Witting, J.M. (1984). "A Unified Model for the Evolution of Nonlinear Water Waves." *Journal of Computational Physics*, 56(2), 203-239.

Woo, S.-B., & Liu, P.L.-F. (2004a). "Finite-Element Model for Modified Boussinesq Equations. I: Model Development." *Journal of Waterway, Port, Coastal, and Ocean Engineering*, 130(1), 1-16.

Woo, S.-B., & Liu, P.L.-F. (2004b). "Finite-Element Model for Modified Boussinesq Equations. II: Applications to Nonlinear Harbor Oscillations." *Journal of Waterway, Port, Coastal, and Ocean Engineering*, 130(1), 17-28.

Zanuttigh, B. (2007). *DELOS: Environmental Design of Low Crested Coastal Defence Structures*. http://www.delos.unibo.it [Accessed July 2007].

Zanuttigh, B., & Lamberti, A. (2006). "Experimental Analysis and Numerical Simulations of Waves and Current Flows Around Low-Crested Rubble-Mound Structures." *Journal of Waterway, Port, Coastal, and Ocean Engineering*, 132(1), 10-27.